



Scott, Jamie (2001) *Characterisation of MFM Tip Stray Fields using Lorentz Electron Tomography*. PhD thesis.

<http://theses.gla.ac.uk/3561/>

Copyright and moral rights for this thesis are retained by the author

A copy can be downloaded for personal non-commercial research or study, without prior permission or charge

This thesis cannot be reproduced or quoted extensively from without first obtaining permission in writing from the Author

The content must not be changed in any way or sold commercially in any format or medium without the formal permission of the Author

When referring to this work, full bibliographic details including the author, title, awarding institution and date of the thesis must be given

# Characterisation of MFM Tip Stray Fields using Lorentz Electron Tomography

by Jamie Scott



UNIVERSITY  
*of*  
GLASGOW

Submitted for the degree of Doctor of Philosophy at the Department of Physics and  
Astronomy, University of Glasgow.

September 2001

© Jamie Scott 2001

## Summary

The work presented in this thesis is a study of the magnetic properties of various magnetic force microscopy (MFM) tips using Lorentz electron microscopy and tomography. The implementation of tomography and differential phase contrast (DPC) microscopy allows the stray field distribution in the half space in front of MFM tips to be measured with a spatial resolution of  $<30$  nm and a field resolution of  $<2$  mT. This information will allow the development of better models for MFM imaging performance and, potentially, the quantification of MFM images.

In Chapter 1 the properties of ferromagnetic materials are reviewed. The various energy contributions that govern magnetism in these materials are reviewed, leading on to the formulation of the micromagnetic equations. The use of these equations in numerical simulations of magnetic elements is discussed. Finally, the type of magnetic domain structure specific to thin films is discussed, with particular focus on domain walls in thin films and the behaviour of small magnetic elements.

In Chapter 2 the general principles of electron microscopy are briefly reviewed, and the main methods of observing phase contrast in samples are covered. Special attention is given to the DPC imaging mode, and its implementation on the Philips CM20 field emission gun (FEG) electron microscope at Glasgow. It is shown that DPC imaging by itself only yields the projection of the MFM tip stray field distribution, and so to obtain the three-dimensional field distribution a tomographic method must be used. The collection and calibration of the tomographic data series is discussed, including the special sample mounting methods required.

To understand the principles behind MFM, the theory behind atomic force microscopy (AFM) is discussed at length in Chapter 3. The extension of AFM to MFM is covered, and the simple point charge analysis of the MFM imaging process is reviewed. A more sophisticated analysis is then presented, based on the knowledge of the MFM point-response function. It is demonstrated that in some cases, the magnetic charge distribution of a sample can be extracted provided that the response function of the MFM tip (related directly to the stray field distribution from the tip) is known. Finally, some specialised MFM techniques are briefly reviewed.

In Chapter 4, prototype tips (produced at Sheffield University) coated with a low-coercivity amorphous ferromagnetic alloy (METGLAS<sup>®</sup>2605SC) are characterised by Lorentz tomography. Planar thin films of the same alloy are also characterised by Fresnel imaging, and the response of both the planar films and the coated tips to external fields is shown. The results indicate that these tips, while possessing finite coercivity, can be

considered as very ‘soft’ tips when coated with  $>50$  nm of METGLAS alloy. Thus these tips are shown to be well suited for imaging samples with very strong stray fields, where the use of a normal (CoCr) tip would result in hysteretic artefacts in the MFM image.

In Chapter 5 other special purpose MFM tips are investigated using Lorentz tomography. The tips investigated comprise two examples modified by focused ion beam (FIB) milling to form ‘spike’ tips, a tip intended to measure magnetic moments several orders of magnitude smaller than is currently possible with MFM, and a tip coated with a high-coercivity coating for imaging samples with strong stray fields. Tomographic reconstructions for all of these tips are presented, and the effects of the various tip modifications on the character of the tip stray fields are discussed.

One of the problems that arises when performing DPC imaging of MFM tips is the electrostatic charging of the tips by the electron beam. In Chapter 6 the effects of electrostatic charging on the tomographic field reconstructions are simulated numerically, and it is demonstrated that the effect on the reconstruction is a characteristic smearing of the field distribution. A method for separating the magnetic and electrostatic effects is proposed, and is shown to work in an experimental case study. The effect of DPC detector misalignment is also investigated, and is found not to be a critical problem.

In Chapter 7 the future of MFM tip design and MFM operation is considered in the light of the results in this thesis, and some improved tip designs are suggested. The separation of the electrostatic (arising from the inner potential) and magnetic effects from DPC images of thin-film samples is also considered, as is a possible improved design of DPC detector.

## Declaration

This thesis is a record of experiments carried out by myself in the Department of Physics and Astronomy at the University of Glasgow during 1997-2000. The work described herein is my own apart from the following exceptions; the samples were prepared by Drs Dion Song, Liesl Folks, Dieter Weller, John Mamin and Greg Heydon, the Radon transform tomography program was initially provided by Profs. Kubalek and Balk at the University of Duisburg in Germany and was modified by Prof. R. P. Ferrier, the modified sample rod and mounting stubs were provided by Prof. R P. Ferrier and Mr Ian McVicar, and the simulated DPC data used in Chapter 6 was provided by Dr Andrew Gallacher.

Some of the work contained in this thesis can be found in the following papers:

- Heydon G P, Rainforth W M, Gibbs M R J, Davies H A, McVitie S, Ferrier R P, Scott J, Tucker J W and Bishop J E L (1999), "Preparation and characterisation of a new amorphous tip coating for application in magnetic force microscopy", *J. Magn. Magn. Mater.*, **205**, L131 – 135
- Scott J, McVitie S, Ferrier R P, Heydon G P, Rainforth W M, Gibbs M R J, Tucker J W, Davies H A and Bishop J E L (1999), "Characterisation of FeBSiC coated MFM tips using Lorentz electron tomography and MFM", *IEEE Trans. Mag.* **35**, 3986-3988
- McVitie S, Ferrier R P, Scott J, White G S and Gallagher A (2001), "Quantitative field measurements from magnetic force microscope tips and comparison with point and extended charge models", *J. Appl. Phys.*, **89**, 3656-3661
- Scott J, McVitie S, Ferrier R P and Gallagher A (2001) "Electrostatic charging artefacts in Lorentz electron tomography of MFM tip stray fields", *J Phys. D – Appl. Phys.*, **34**, 1326-1332

This thesis has not previously been submitted for a higher degree.

## Acknowledgements

Firstly I would like to thank my supervisor Dr Stephen McVitie, and my second supervisor Prof. Robert P. Ferrier for their guidance and help over the course of the last few years. I am also indebted to Prof. John Chapman for the provision of the research facilities in the Solid State Physics group in the University of Glasgow. Thanks are also due to Drs W. A. Patrick Nicholson and Sam Mcfadzean for their work in maintaining the IT and research infrastructure of the group.

I am grateful to Dr Peter Aitchison for his assistance when learning to operate the Philips CM20 and for keeping this microscope in good working order. I would also like to thank Mr Colin How and Mr William Smith for keeping the JEOL microscopes in order, and Mr Ian McVicar for manufacturing the tomographic mounting stubs.

This thesis would not have been possible without samples to examine, and these have come from a variety of sources. I would like to thank Dion Song of Seagate Research, Liesl Folks, Dieter Weller and John Mamin of IBM Almaden for the samples that are examined in Chapter 5. All the samples examined in Chapter 4 were produced at Sheffield University, and thanks are due to Prof. Mike Gibbs, Dr Mark Rainforth and Dr Greg Heydon for their collaboration in the work presented here.

I am particularly grateful to Dr Greg Heydon for his help and support, especially during my stay in Sheffield.

No research group could run without a good secretary, and so I am grateful to Miss Beverley Lynn for her organisational skills, whether applied to work matters or social events. Thanks also to Miss Lucy Murray for taking up the load so efficiently.

I would like to acknowledge the support and friendship of my colleagues in the SSP group and the Physics department, without whom the last few years would have seemed dull and grey. In particular, thanks to Brian, Margit, Tommy, Patrick, Philippe, Peter and Christine for their (sometimes literal) support. Thanks are also due to my parents for their support and encouragement.

And finally, this thesis was only possible with the support of a studentship from the Engineering and Physics Science Research Council.

# Contents

<b>Summary</b>	<b>I</b>
<b>Declaration</b>	<b>III</b>
<b>Acknowledgements</b>	<b>IV</b>
<b>Chapter 1. Ferromagnetism and ferromagnetic materials</b>	<b>1</b>
1.1 Introduction	1
1.2 General characteristics of ferromagnetism and ferromagnetic materials	1
1.3 Energetics of ferromagnetic materials	3
1.3.1 Exchange energy	3
1.3.2 Magnetostatic stray field energy	5
1.3.3 Zeeman energy	6
1.3.4 Anisotropy energy	6
1.3.5 Magneto-elastic energy	7
1.3.6 The micromagnetic equations	8
1.3.7 Micromagnetic simulation	9
1.4 Domains and domain walls	11
1.4.1 Domains in thin films	11
1.4.2 Domain walls in thin films	13
1.4.3 Other magnetic configurations of thin films	16
1.5 Conclusions.	17
<b>Chapter 2. Lorentz electron microscopy and tomography</b>	<b>19</b>
2.1 Introduction	19
2.2 Electron microscopy	19
2.2.1 The electron gun	21
2.2.2 Electron optical lenses	22
2.2.3 Lenses for imaging magnetic materials	23
2.2.4 Magnetic lens aberrations	23
2.2.5 Detection of electrons	24
2.2.6 Lorentz microscopy – classical description	25
2.2.7 Lorentz microscopy – quantum mechanical description	25
2.2.8 Electrostatic phase microscopy	26
2.3 Imaging phase objects in the (S)TEM	27

2.3.1	Fresnel imaging mode	27
2.3.2	Foucault contrast	28
2.3.3	Coherent Foucault contrast	29
2.3.4	Electron holography	29
2.3.5	Differential phase contrast	30
2.3.6	Modified DPC	33
2.4	<i>Lorentz electron tomography</i>	34
2.4.1	Tomography fundamentals	34
2.4.2	Conventional ART algorithm	36
2.4.3	RTM algorithm	38
2.4.4	Magnetic ART algorithm	39
2.5	<i>Implementation of tomography on the CM20</i>	39
2.5.1	Alignment of the DPC detector and the scan axes	40
2.5.2	Sample mounting for tomography	40
2.5.3	Extraction and alignment of linescans	42
2.5.4	Calibration of reconstructions	43
2.6	<i>Conclusion</i>	44
<b>Chapter 3.</b>	<b>Scanning Probe Microscopy</b>	<b>46</b>
3.1	<i>Introduction</i>	46
3.2	<i>The SPM scanning system</i>	46
3.3	<i>Scanning Tunnelling Microscopy</i>	48
3.4	<i>Atomic Force Microscopy</i>	49
3.4.1	AFM detection techniques	50
3.4.2	Surface forces acting on AFM probes	52
3.4.3	AFM imaging modes	53
3.5	<i>Probe manufacture for AFM</i>	55
3.5.1	Wire-based probes	55
3.5.2	Silicon Nitride probes	55
3.5.3	Monolithic silicon probes	56
3.5.4	Probe modifications for force detection	57
3.6	<i>Magnetic force microscopy</i>	57
3.6.1	MFM probe types	58
3.6.2	Basic MFM imaging theory	59
3.6.3	Separation of topographic and magnetic effects in MFM	61
3.6.4	Interaction problems	62
3.6.5	MFM analysis using the point probe approximation	63



3.6.6	MFM analysis using reciprocity and the charge formulation	64
3.6.7	Deconvolution of sample charge distribution	65
3.6.8	Magnetisation reconstruction from MFM and DPC data	66
3.7	<i>Further uses of MFM</i>	68
3.7.1	Magnetic Dissipation Microscopy	68
3.7.2	Magnetoresistance Sensitivity Mapping	68
3.8	<i>Scanning Hall Probe Microscopy</i>	69
3.9	<i>Conclusions</i>	69
<b>Chapter 4.</b>	<b>Physical and magnetic properties of METGLAS coated MFM tips</b>	<b>74</b>
4.1	<i>Introduction</i>	74
4.2	<i>Physical and magnetic properties of METGLAS</i>	75
4.3	<i>Fresnel imaging of METGLAS films</i>	77
4.3.1	Measurement of anisotropy and coercivity	77
4.3.2	Magnetisation processes in METGLAS films	78
4.4	<i>TEM studies of METGLAS tips</i>	82
4.5	<i>DPC studies of METGLAS tip response to external field</i>	84
4.5.1	30 and 50 nm tips	85
4.5.2	70 and 100 nm tips	88
4.6	<i>Tomography of METGLAS tips</i>	89
4.6.1	30 nm tip #1	91
4.6.2	30nm tip #2	92
4.6.3	50 nm tip #1	94
4.6.4	50 nm tip #2	96
4.6.5	Analysis of tomographic reconstructions	97
4.7	<i>Application of METGLAS tips to MFM</i>	98
4.8	<i>Conclusions</i>	103
<b>Chapter 5.</b>	<b>Special purpose MFM tips</b>	<b>106</b>
5.1	<i>Introduction</i>	106
5.2	<i>Seagate ion beam milled tips</i>	106
5.3	<i>IBM ion milled spike tips</i>	112
5.3.1	Spike tip 1	114
5.3.2	Spike tip 2	115
5.3.3	Conclusions	116
5.4	<i>IBM ultrasensitive tip</i>	116
5.5	<i>High <math>H_c</math> tip</i>	120

5.6	<i>Conclusions</i>	122
<b>Chapter 6.</b>	<b>Artefacts in Lorentz electron tomography</b>	<b>125</b>
6.1	<i>Introduction</i>	125
6.2	<i>Modelling electrostatic charging artefacts</i>	125
6.2.1	The model MFM tip	126
6.2.2	The electrostatic model	127
6.2.3	Effect on tomographic reconstruction	130
6.3	<i>Separation of magnetic and electrostatic effects</i>	131
6.4	<i>Experimental case study</i>	133
6.5	<i>DPC detector misalignment</i>	140
6.5.1	Effect on DPC data	140
6.5.2	Effect on tomographic reconstructions	141
6.5.3	Determination of misalignment angle	143
6.6	<i>Similarity between charging and misalignment</i>	144
6.7	<i>Conclusions</i>	145
<b>Chapter 7.</b>	<b>Conclusions and future work</b>	<b>147</b>
7.1	<i>Conclusions</i>	147
7.2	<i>Future work on DPC imaging</i>	148
7.2.1	Separation of magnetic and electrostatic DPC data	148
7.2.2	Improved DPC detectors	149
7.3	<i>Tomography</i>	149
7.4	<i>Future directions in MFM</i>	150
7.4.1	Creating approximations to point or line charge MFM tips	150
7.4.2	Active Q factor control	153
<b>Appendix A.</b>	<b>Analysis of charging and detector rotation in Lorentz microscopy</b>	<b>155</b>
A.1	<i>Separation of electrostatic and magnetic DPC signals</i>	155
A.1.1	Simple argument	155
A.1.2	A more quantitative argument.	156
A.2	<i>Effects of angular misalignment of DPC detector</i>	158
A.3	<i>Effects of charging and detector rotation</i>	159

## Chapter 1. Ferromagnetism and ferromagnetic materials

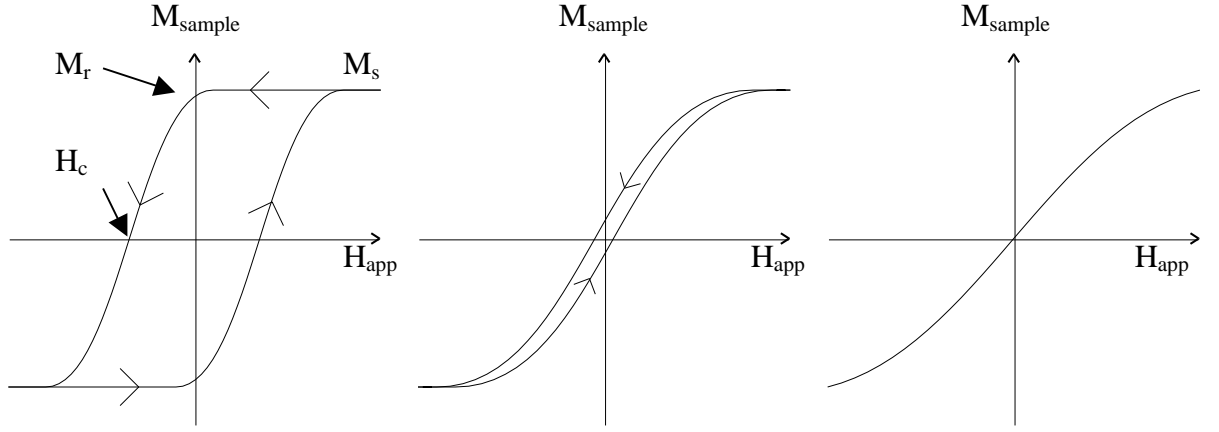
### 1.1 Introduction

This chapter describes the phenomenon of ferromagnetism that occurs in some technologically important materials (section 1.2). Ferromagnetic materials are used in a large variety of devices, including recording systems (tape and hard disk), position sensors and mechanical actuators (solenoids and electric motors). In particular, the recording industry is dependent on the characterisation of ferromagnetic materials to deliver improvements in the areal density of magnetic recording devices. As the scale of magnetic devices reduces to micron and even nanometer dimensions, microscopy of magnetic materials has become increasingly important. Two microscopy techniques are discussed in Chapters 2 and 3. In this chapter the characteristics of ferromagnetism are discussed (section 1.2). The origin of ferromagnetism is covered in section 1.3, along with the energy considerations that govern the distribution of magnetisation in an object. The properties of magnetic domains and domain walls are covered in section 1.4, and a brief conclusion is given in section 1.5.

### 1.2 General characteristics of ferromagnetism and ferromagnetic materials

Ferromagnetic materials are defined as materials that possess spontaneous magnetisation  $\mathbf{M}$  with no external field  $\mathbf{H}$  present. This magnetisation is temperature dependant, and disappears at a material-dependant temperature known as the Curie temperature  $T_c$ . Ferromagnetic materials often have high susceptibilities, that is, a small external field  $\mathbf{H}_{app}$  results in a large magnetic induction  $\mathbf{B}$ . Ferromagnetic elements are found in the transition and rare earth sections of the periodic table. Many of the compounds and alloys that include these elements are also ferromagnetic.

The response of the magnetisation in ferromagnetic materials to an external field can be measured by a vibrating sample magnetometer (VSM), alternating gradient force magnetometer (AGFM) or by the magneto-optical Kerr effect (MOKE), amongst other methods. Fig. 1.1 shows the typical response of the magnetisation as the external field applied to a ferromagnetic sample is varied between large negative to positive values and back again.



**Figure 1.1.** Typical hysteresis loops of (a) a hard ferromagnetic material, (b) a soft ferromagnetic material and (c) a paramagnetic material (e.g. a ferromagnetic material above the Curie temperature).

As can be seen from Fig. 1.1, the magnetisation of ferromagnetic materials depends not only on  $H$ , but also the previous magnetic history of the material. In other words, the magnetisation of the material exhibits hysteresis. The maximum magnetisation possible is called the saturation magnetisation ( $M_s$ ). The remanent magnetisation ( $M_r$ ) is the value of the magnetisation when the external field is reduced to zero, and the coercivity of the material ( $H_c$ ) is the field needed to bring the magnetisation to zero after saturation. The loops shown in Fig. 1.1 are the major hysteresis loops of the material, and most ferromagnetic materials are characterised by the major hysteresis loop. Cycling between smaller field values results in smaller (minor) hysteresis loops, of which there can be an infinite number. Magnetic materials are often anisotropic in nature, and so the direction of applied field may also be important. For complete characterisation of a sample it is often necessary to measure the hysteresis loop for different directions of applied field. The causes and nature of magnetic anisotropy are discussed in the following sections.

Materials that have a high coercivity are often referred to as ‘hard’, while low-coercivity materials are called ‘soft’. Above the Curie temperature  $M_r$  and  $H_c$  are zero. In all cases the magnetic induction  $B$  in the material is given by

$$B = \mu_o (M + H) \quad (1.1)$$

where  $\mu_o$  is the permeability of free space ( $4\pi \times 10^{-7} \text{ Hm}^{-1}$  in S.I. units).

### 1.3 Energetics of ferromagnetic materials

#### 1.3.1 Exchange energy

Ferromagnetic elements have magnetic moments associated with their constituent atoms; these moments primarily arise from the spin of unpaired electrons in the 3d or 4f atomic shells. In ferromagnetic materials these moments are aligned parallel to each other, resulting in a net spontaneous magnetisation. An attempt was made to explain this ordering by means of a molecular field theory by Weiss (1907). In this theory a molecular field internal to the material acts on each atomic moment. In ferromagnetic materials this field is strong enough to align each moment nearly parallel to a common direction, and has a value of the order of  $3 \times 10^9 \text{ Am}^{-1}$  ( $\sim 4 \times 10^7 \text{ Oe}$ ). The problem with this theory was that it does not explain the origin of the molecular field. Also, the extremely high value of the molecular field would seem to suggest that any external applied field would be insignificant and would not affect the system at all. Heisenberg (1928) gave an explanation using quantum mechanical theory. The energy associated with the overlap of two electron spins is given by

$$E_{ex} = -2JS_i \bullet S_j \quad (1.2)$$

where  $E_{ex}$  is the exchange energy,  $S_i$  and  $S_j$  are the spins of the two electron wavefunctions and  $J$  is the exchange integral, calculated by integrating over the overlap of the two electron wavefunctions. An important point of this theory is that the interactions are primarily electrostatic in nature, not magnetic and so a very large magnetic molecular field is not required. Usually only the overlap between two adjacent atoms gives an appreciable value for  $J$ , so only nearest-neighbour interactions need be considered. This simplifies the calculation of the exchange energy considerably. We first define a stiffness constant  $A$  as

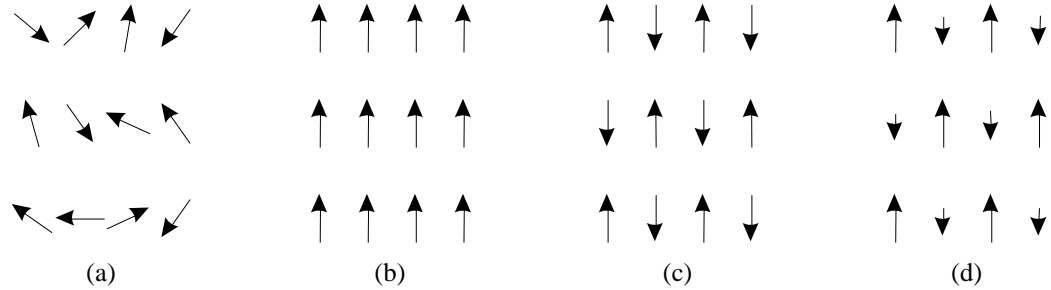
$$A = \frac{kJS^2}{a} \quad (1.3)$$

where  $k$  is a structure-dependant constant (1 for simple cubic, 2 for body centred cubic and 4 for face centred cubic materials),  $a$  is the crystal lattice parameter and  $S$  is the magnetic spin moment of the atom. The exchange energy can then be written as

$$E_{ex} = \mu_o A \int (\nabla \mathbf{M})^2 dV \quad (1.4)$$

where the integral is performed over the volume of magnetic material.

Ferromagnetic materials have a positive value of  $J$ , so the lowest energy state occurs when the spins  $S_i$  and  $S_j$  are parallel. When  $J$  is negative the lowest energy state occurs when adjacent spins are antiparallel, and materials for which this occurs are classified as antiferromagnets. Although the spins in antiferromagnetic materials are ordered, there is no net magnetisation present. A more complex state can arise when there are two types of magnetic species present with different moments. If these two species are coupled antiferromagnetically the result is a material with a net magnetic moment; this is termed a ferrimagnet. These different types of states are illustrated in Fig. 1.2.



**Figure 1.2. Illustrations of different types of magnetic order. (a) is a material above the Curie temperature, i.e. no magnetic order present. (b) is a ferromagnetic system, (c) is a antiferromagnetic system and (d) is a ferrimagnetic system.**

When thermal energy is present in a ferromagnetic system the effect is to perturb the perfect arrangement of spins, decreasing the value of the net magnetisation. The Curie temperature is defined as the temperature where the average thermal energy is equal to the exchange energy. At this point the spin directions are in a completely disordered state (in the absence of an external field), and hence the net magnetisation vanishes (Fig. 1.2a). In this case the material is said to be paramagnetic. In this state the magnetisation of the material depends purely on the external field, and the remanent magnetisation and coercivity are both zero (Fig. 1.1c).

Although ferromagnetic materials have net magnetic moments on the atomic scale, macroscopic blocks of material can possess little or no net magnetisation. This is explained by the formation of domains, which are areas of the material that are magnetised uniformly but in varying directions. Thus the net magnetisation of a block of material can range from the maximum possible ( $M_s$ ) to zero. The effect of the exchange interaction alone cannot explain this behaviour, so a consideration of the other contributions to the magnetic energy of the material is required.

### 1.3.2 Magnetostatic stray field energy

The magnetostatic energy of a magnetic object arises from the interaction of the magnetisation and the magnetic field arising from the magnetisation distribution. The energy due to the stray field is

$$E_d = \frac{1}{2} \mu_o \int_{all.space} \mathbf{H}_d^2 dV = -\frac{1}{2} \mu_o \int_{object} \mathbf{H}_d \bullet \mathbf{M} dV. \quad (1.5)$$

Note that the  $\frac{1}{2}$  in this expression is necessary to avoid double counting. To calculate the field generated by the magnetisation of the object the concept of free magnetic poles (or magnetic charge) is introduced. These poles occur where the magnetisation vector of the object encounters an interface, or where the divergence of the magnetisation is non-zero. The surface magnetic charge density  $\sigma$  is given by

$$\sigma = \mathbf{M} \bullet \mathbf{n} \quad (1.6)$$

where  $\mathbf{M}$  is the magnetisation vector and  $\mathbf{n}$  is the outward pointing surface normal unit vector. The volume magnetic charge density  $\rho$  is given by

$$\rho = -\nabla \bullet \mathbf{M}. \quad (1.7)$$

The field generated by these poles can be internal and external to the magnetic object. The internal field is often opposed to the magnetisation of the object, and hence reduces the stability of the magnetisation distribution. For this reason the magnetostatic field is often termed the demagnetising field ( $\mathbf{H}_d$ ). The magnetic scalar potential  $\phi_d$  of this field at a point  $\mathbf{r}$  is given by integration over  $\mathbf{r}'$  as follows

$$\phi_d(\mathbf{r}) = \frac{1}{4\pi} \left( \int \frac{\rho(\mathbf{r}')}{|\mathbf{r} - \mathbf{r}'|} dV' + \int \frac{\sigma(\mathbf{r}')}{|\mathbf{r} - \mathbf{r}'|} dS' \right) \quad (1.8)$$

where the integrations are performed over the volume  $V'$  and the surface  $S'$  of the magnetic material. The stray field is then derived using

$$\mathbf{H}_d(\mathbf{r}) = -\nabla \phi_d(\mathbf{r}). \quad (1.9)$$

Thus, using Eqn. 1.5, the energy associated with the demagnetising field can be shown to be

$$E_d = \int_V \rho(\mathbf{r}) \phi_d(\mathbf{r}) dV + \int_S \sigma(\mathbf{r}) \phi_d(\mathbf{r}) dS \quad (1.10)$$

where the integrations are again performed over the volume  $V$  and surface  $S$  of the object.

### 1.3.3 Zeeman energy

If a magnetic object is placed in an external magnetic field, the interaction between the field and object magnetisation also affects the energy of the magnetisation distribution. The energy  $E_z$  due to an external field  $\mathbf{H}_{ext}$  is

$$E_z = -\mu_o \int_V \mathbf{M} \cdot \mathbf{H}_{ext} dV \quad (1.11)$$

where  $V$  is the volume of space occupied by the object. Note that unlike Eqn. 1.5 there is no  $\frac{1}{2}$  in this expression as in this case the field and the magnetisation are independent.

### 1.3.4 Anisotropy energy

The atomic structure of a ferromagnet can give rise to preferred directions of magnetisation, due ultimately to spin-orbit interactions. This form of anisotropy is called magnetocrystalline anisotropy. Due to the symmetry of crystalline structures, the expressions for this energy are usually expansions of spherical harmonic terms. For most materials only the first two terms of the expansion are required and higher orders can be neglected. For example, the anisotropy energy  $E_K$  of a cubic crystal is given by

$$E_K = \int_V \{K_1(\alpha^2\beta^2 + \beta^2\gamma^2 + \gamma^2\alpha^2) + K_2\alpha^2\beta^2\gamma^2\} dV \quad (1.12)$$

where  $K_1$  and  $K_2$  are the first and second order material-dependant anisotropy constants. The terms  $\alpha$ ,  $\beta$  and  $\gamma$  are the direction cosines of the magnetisation vector directed along the cubic axes. The integration is performed over the volume  $V$  of the material. The preferred magnetisation directions (the easy axes) are governed by  $K_1$  and  $K_2$ , and can lie in the  $\langle 100 \rangle$ ,  $\langle 110 \rangle$  or  $\langle 111 \rangle$  directions. By contrast, a material such as cobalt with a hexagonal crystalline structure exhibits uniaxial anisotropy, and the anisotropy energy in this case is

$$E_K = \int_V \{K_1(1 - \gamma^2) + K_2(1 - \gamma^2)^2\} dV \quad (1.13)$$

where  $\gamma$  is the magnetisation component directed along the uniaxial symmetry axis (for a hexagonal crystal this corresponds to the c-axis). If  $K_1$  is large and positive an easy axis exists parallel to the anisotropy axis. If  $K_1$  is large and negative the preferred



magnetisation direction is any direction that is perpendicular to the anisotropy axis, and so an ‘easy plane’ exists perpendicular to the anisotropy axis.

Anisotropy can also be induced by the microstructure of the material even if there is no regular crystalline structure present. Most often this is uniaxial in nature, and is normally caused by the physical processing of the material. The shape of a magnetic object can also result in an anisotropy effect (i.e. a preferred direction of magnetisation), although in this case the cause is due to magnetostatic effects, and thus is not normally included in  $E_K$ . A review of the effects of shape anisotropy is given by Cowburn (2000), and the effects of processing magnetic material in different ways (specifically, evaporating thin films at different angles) is shown by McVitie *et al* (1999).

### 1.3.5 Magneto-elastic energy

A magnetic material will deform under the influence of magnetic effects, and this effect is termed magnetostriction. Conversely, applying stress to a magnetic material can change the magnetisation of the material. These magneto-elastic effects are small in ferromagnetic materials, with magnetostriction resulting in strains of around  $10^{-6}$  to  $10^{-3}$ , and this means that the elasticity is in the linear regime and thus can be described by Hooke’s law, which simplifies the analysis somewhat. The effect of large stresses on the material (of non-magnetic origin) does necessitate the inclusion of non-linear effects in the theory. In this case the magneto-elastic coefficients themselves depend on the strain of the material.

The magnetic properties of a ferromagnetic material all depend to some extent on the atomic arrangement of the material. However, the most significant contribution to the magnetostrictive energy is derived from the magneto-crystalline anisotropy. For single crystals the expressions for the magneto-elastic interaction energy involve a strain tensor, the magnetisation and a number of material parameters (the number of these parameters relates to the symmetry of the crystal). In the case of a uniformly magnetised isotropic material (polycrystalline or amorphous with no induced anisotropy) the expressions are somewhat simplified. For these materials the fractional change in length along the unit vector  $\mathbf{a}$  is given by

$$\frac{\delta l}{l} = \frac{3}{2} \lambda_s \left[ \left( \frac{\mathbf{M}}{M_s} \cdot \mathbf{a} \right)^2 - \frac{1}{3} \right] \quad (1.14)$$

where  $l$  is the length in the direction  $\mathbf{a}$  (when the material is in a paramagnetic state) and  $\lambda_s$  is the isotropic magnetostriction constant. This expression assumes that the material is

under no external stress, and is derived by combining the magneto-elastic energy with the elastic energy, and finding the minimum energy condition. Note that even if there is no net magnetisation ( $\mathbf{M}=0$ ) the material is still strained by the existence of domains, but in this case the strains are unordered. Hence there is still an increase (i.e.  $\delta l > 0$ ) in the material dimensions compared to the paramagnetic state. If the material is put under a uniaxial stress in the direction  $\mathbf{a}$  the magneto-elastic coupling energy  $E_{me}$  is written as

$$E_{me} = -\sigma \frac{\delta l}{l}. \quad (1.15)$$

Despite the small scale of these effects, magnetostriction can be very important in some situations. For instance, the humming noise produced by electrical transformers arises from the vibrations caused by the alternating magnetisation in the transformer core. It is also possible to use highly magnetostrictive films as strain gauges, as discussed by Karl *et al* (2000), as the magnetisation direction can be used as an indication of the strain the film experiences.

### 1.3.6 The micromagnetic equations

The energy terms described above together contribute to the total energy  $E_{tot}$  of the magnetisation distribution in a magnetic object

$$E_{tot} = E_{ex} + E_K + E_d + E_z + E_{me}. \quad (1.16)$$

To find a stable magnetisation pattern for a given sample and set of conditions, it is necessary to find the magnetisation distribution  $\mathbf{M}$  that results in a minimum (either a local or global) in the total energy. Using variational calculus it is possible to derive a set of differential equations known as the micromagnetic equations, which have  $\mathbf{M}$  as the only independent variable. These equations can be solved analytically in some cases, but when considering samples that are finite and inhomogeneous, numerical methods are normally used. The equations were originally given in full three-dimensional form by Brown (1963).

The above discussion does not take into account the magnetisation dynamics, and hence is only useful for the calculation of static magnetisation states. Magnetic moments have angular momenta associated with them, so if a magnetic field is applied the moments will precess around the direction of the field. Inside the sample we define an effective magnetic field  $\mathbf{H}_{eff}$  as

$$\mathbf{H}_{eff} = -\frac{1}{\mu_o} \frac{dE_{tot}}{d\mathbf{M}}. \quad (1.17)$$

The precession is then described by

$$\frac{d\mathbf{M}}{dt} = -\gamma \mathbf{M} \times \mathbf{H}_{eff} \quad (1.18)$$

where  $\gamma$  is the gyromagnetic ratio, which is given by

$$\gamma = \frac{\mu_o g e}{2m_e} \quad (1.19)$$

where  $m_e$  is the mass of the electron and  $e$  is the electronic charge. The Landé factor  $g$  is about 2.0 for a free electron, but can vary considerably. For example, the  $g$ -factor for  $\text{Fe}^{3+}$  can lie between 1.4 - 10, depending on the sample environment. These equations imply that the magnetisation will maintain a constant angle to the applied field direction, as no energy losses are taken into account. The Landau-Lifshitz-Gilbert (LLG) equation introduces a damping factor  $\alpha$  to model the effects of energy losses in the system

$$\frac{d\mathbf{M}}{dt} = \gamma \mathbf{M} \times \mathbf{H}_{eff} - \alpha \mathbf{M} \times (\mathbf{M} \times \mathbf{H}_{eff}). \quad (1.20)$$

The result of this is to allow the magnetisation vector to turn towards the field direction at a rate depending on the damping constant. For most cases the damping term is in fact dominant, and the gyromagnetic term only becomes significant at high (GHz) frequencies. It should be noted that the damping constant is purely phenomenological in nature, and explanations of the physical processes underlying damping are currently being investigated (see for example Suhl, 1998).

### 1.3.7 Micromagnetic simulation

Using the micromagnetic and LLG equations above, the magnetisation of a sample can be calculated in two ways. The simplest method is energy relaxation where the LLG equation is not used; instead the magnetisation vector in each cell is simply turned towards the direction of the effective field. The energy of the system is then recalculated along with the effective field, and the magnetisation in each cell is again turned towards the effective field direction. This process is continued until the system is in equilibrium, i.e. when the magnetisation lies in the same direction as the effective field in every cell. This condition corresponds to a system energy minimum (this can be the global minimum or a

local minimum). Such a method is useful when all that is required is the equilibrium magnetisation. To observe the dynamic behaviour of the system the LLG equation is used, and in this case each iteration of the system corresponds to a time step.

To simulate the magnetisation in small magnetic elements, discrete numerical methods are normally used. The sample is divided into small cells, and the magnetisation is assumed to be constant within each cell. The size of the cells is to some extent governed by the magnetic phenomena being investigated, and the computing power available. According to Rave and Hubert (2000) cells smaller than the exchange length parameter  $\sqrt{A/K}$  are required to find solutions that are independent of the mesh used (where  $A$  is the exchange length parameter and  $K$  is a relevant anisotropy constant). Typically cells of the order of 5 to 20 nm per side are used, which gives a reasonable simulation of the domain patterns of soft materials such as permalloy. The size of the simulated material is normally of the order of a few  $\mu\text{m}$ , to keep the total number of cells (and therefore the computation time) manageable. If detailed information is required on the magnetisation distribution in a domain wall, a smaller discretisation of the problem is required, which therefore limits the total size of the simulation. For much larger magnetic samples, the behaviour of the magnetisation is normally described using domain theory, as described in the following sections.

Micromagnetic simulations are useful when calculating the properties of small magnetic elements, but as noted there is a size limit on the samples, governed by the computing power available. For example, it would be useful to simulate the magnetisation patterns in the magnetic force microscope (MFM) tips introduced in Chapter 3. However, these tips take the form of a non-regular pyramidal structure 15  $\mu\text{m}$  in height. To simulate this with current desktop computers would take a prohibitive amount of time, and so most simulations of MFM tips tend to be restricted in size or detail. For instance, the simulations done by Tomlinson and Farley (1997) involved a four-sided pyramidal tip of height 1  $\mu\text{m}$  and also used a variable cell size to cut down the number of elements in the problem. As MFM tips will in future tend to reduce in size (for greater resolution and sensitivity, see for example Stipe *et al*, 2001) and computing power will certainly increase, at some point it may even become possible to simulate entire MFM tips using micromagnetic techniques.

In some cases micromagnetic simulations are performed using programs that are written specifically for the job in hand. There are also a few packages that can be used for general problems. One of these is called LLG<sup>TM</sup>, after the equations (<http://www.dancris.com/~llg/>). This is a commercial package that can perform full three-dimensional micromagnetic simulations of bodies of arbitrary (discretised into cubes)

shapes. There is also another simulation package referred to as the Object Oriented MicroMagnetic Framework, or OOMMF for short (<http://math.nist.gov/oommf/>). This has recently been upgraded to perform full three-dimensional simulations.

## 1.4 Domains and domain walls

The observation that a ferromagnetic material can display little or no net magnetic moment indicates that the magnetic moments of the material can be oriented in different directions, partly or wholly cancelling each other out. The parts of the material that are magnetised in different directions are called domains. The first evidence for domain structure was found by Barkhausen (1919), who monitored the magnetisation of samples by converting changes in the magnetisation (measured using induction coils) to audio signals. The magnetisation often changed discontinuously, resulting in clicks from the apparatus. These events appear in hysteresis loops as sudden changes in  $\mathbf{M}$ , and are known as Barkhausen jumps. At the time it was thought that these discontinuities were caused by domains switching directions, but it is now known that the cause is discontinuous domain wall motion.

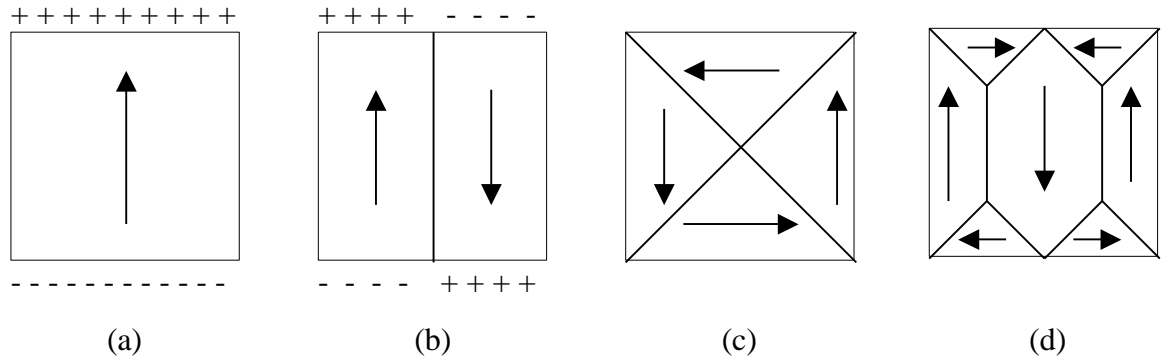
The first direct images of domain structure were shown by Bitter (1931) using a colloidal solution of fine magnetic particles. The particles tended to agglomerate in regions of high field gradient, which in most cases means domain walls. Although the images formed are difficult to interpret quantitatively, the patterns thus revealed by Bitter spurred further research into domain theory. An overall theory of domains was given by Landau and Lifshitz (1935), which stated that domain patterns are formed to minimise the total energy of the system.

### 1.4.1 Domains in thin films

We consider thin films here partly because the domain configurations are easier to visualise, and partly because thin films are important technological systems (magnetic thin films are used for the production of all the MFM tips studied in this thesis). The magnetisation states of thin films can also be observed using many different techniques. Two of these techniques that are discussed in Chapters 2 (transmission electron microscopy) and 3 (MFM) are extensively used in this thesis. To be described as thin, a magnetic film must have a thickness comparable to the width of the domain walls (discussed later), which for typical soft materials such as Permalloy ( $\text{Ni}_{20}\text{Fe}_{80}$ ) means less than 100 nm. In addition, when using electron microscopy the films must not be opaque to the electron beam; for 200 keV electrons this means a film thickness of <100 nm at most,

and preferably  $<50$  nm. In many thin films the magnetisation lies in-plane, as the magnetostatic energy associated with out of plane magnetisation is very large. For thin films to support out of plane magnetisation requires strong anisotropy (or applied field).

An equilibrium magnetisation state is reached when the total energy of the system reaches a local or absolute minimum, and thus the relative strengths of the energy terms dictate the form of this state. To illustrate the effect of each of the energy contributions consider a thin-film magnetic element. A set of hypothetical domain structures are shown in Fig. 1.3.



**Figure 1.3. Diagram illustrating various domain configurations of a square thin-film magnetic element. (a) Single domain, high stray field state. (b) Two domains magnetised in opposite directions with lower stray field energy than (a). (c) A flux-closure structure, minimal or no stray field. (d) A flux-closure structure where there is an easy axis parallel to the vertical direction.**

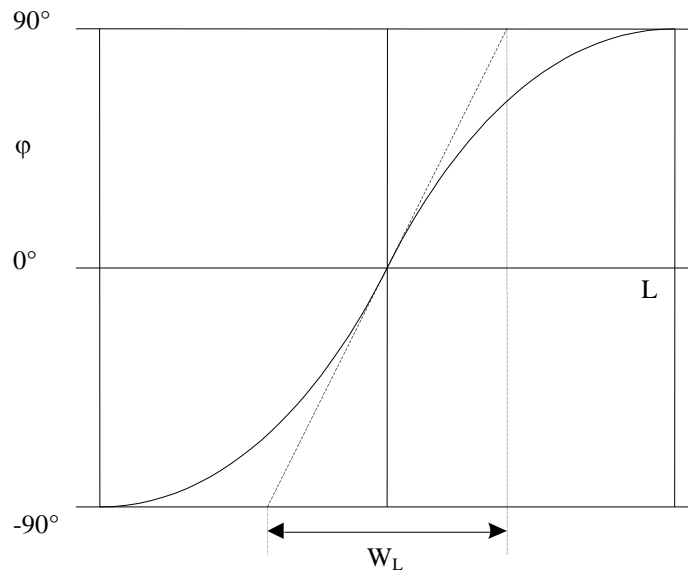
Fig. 1.3a shows a single domain state that gives a minimum in the exchange energy, but results in a very high stray field energy. This state is normally only seen either for very small particles, or where an external field acting on the element is high enough to saturate the magnetisation. This state could also be caused by a high uniaxial anisotropy, but in this case the configuration shown in Fig. 1.3b would also be compatible with high anisotropy, while also lowering the stray field energy. In cases where there is little anisotropy and external field the configuration shown in Fig. 1.3c may be preferred, as it has no stray field at all apart from that associated with the domain walls. If some degree of anisotropy is present this can then lead to modified flux closure configurations as shown in Fig. 1.3d. In this case the anisotropy is uniaxial, and the result is that domains magnetised parallel to the anisotropy axis are favoured. The anisotropy could be magnetocrystalline in nature, induced by other material properties or caused by a magnetostrictive stress.

It can be seen that the effect of magnetostatic energy is to cause the formation of domains, while the exchange energy tends to oppose domain formation. Anisotropy and external fields do not oppose domain formation *per se*, but tend to limit the possible orientations of these domains. In many cases the various energy contributions are similar

in magnitude, and hence the resulting magnetisation patterns can be considerably more complicated than shown in Fig. 1.3.

#### 1.4.2 Domain walls in thin films

If the transitions between the domains shown in Figs. 1.3c and d were infinitely thin these structures would be truly flux closed, with no stray field at all. The exchange interaction prevents this, and so the magnetisation rotation is continuous from one domain to the other. Due to the effects of the exchange energy, the direction of magnetic moment changes slowly from one atom to the next, and so the width of the domain wall normally extends over many atoms. Domain walls in thin films can be between a few nm to a few hundred nm in width, depending on the exchange length and the dimensions of the film. There are in fact several definitions of the width of a domain wall, but the most common measures are based on the rate of magnetisation change at the centre of the wall. The slope of the magnetisation angle  $d\phi/dL$  provides one measure of width that we term  $W_L$ , and the definition of this quantity is shown graphically in Fig. 1.4.

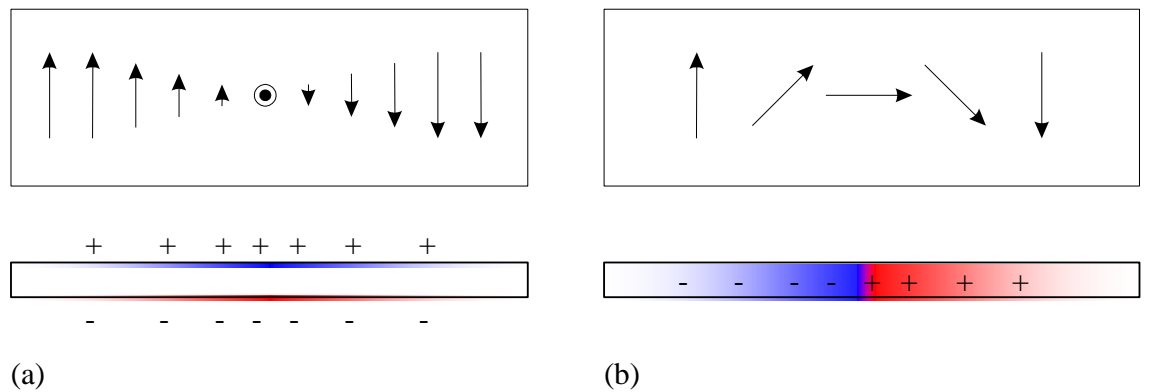


**Figure 1.1.4.** Illustration of the magnetisation wall profile of a  $180^\circ$  domain wall showing one definition of the wall width. The wall magnetisation angle  $\phi$  is shown, and the dashed line is the slope of the wall at the centre. The definition of the wall width  $W_L$  is shown.

As the change in magnetisation is continuous, it is of course possible to define the wall width in other ways as well if desired. Some magnetic transitions (particularly in the field of magnetic recording) can be modelled by suitable functions, and in these cases the wall width is given in terms of the model parameters. For example, the arctangent and hyperbolic tangent functions are often used for this purpose, in the forms  $\tan^{-1}(a/x)$  and  $\tanh(a/x)$ . In both cases the walls are centred at  $x=0$ , and  $a$  is the wall width parameter.

In bulk materials the width of the wall is primarily governed by the exchange energy and the anisotropy, but where thin films are concerned magnetostatic energy effects can also be important, depending on the type of wall present. Anisotropy energy can also influence the direction and type of a domain wall. In bulk materials the wall width usually depends on the quantity  $\sqrt{A/K}$ , where  $K$  is a relevant anisotropy constant. In thin films and particularly in patterned thin films, the dimensions of the material can also affect the wall width due to stray field considerations. In this case the stray field energy constant  $K_d = \mu_0 M_s^2/2$  is often much more important than the anisotropy constants.

There are two principal types of domain wall to consider, and these are termed the Néel wall (Néel, 1955) and the Bloch wall (Bloch, 1932). Fig. 1.5 shows the form of the magnetisation in the two wall types. One important difference between the two wall types is that the divergence of the magnetisation in a Bloch wall is zero, and hence in bulk material there is no charge and no stray field associated with a Bloch wall. However, if the material is in the form of a thin film then the intersection of a Bloch wall with the surfaces of the material creates surface charge, and hence stray field. A Néel wall does possess associated magnetic charge, and therefore has associated magnetostatic energy. Thus in bulk materials Bloch walls are usually preferred. However, Néel walls are unaffected by the thickness of the material, due to the symmetry of the wall. Hence for very thin films Néel walls are normally preferred. The film thickness at which the domain walls change in type depends on the domain wall width. As a rough guide, if the film thickness is lower than the width of the Bloch wall, then Néel walls are energetically favourable.



**Figure 1.5. Schematic representations of (a) a Bloch wall and (b) a Néel wall. The top views show the films from above and illustrate the magnetisation directions. The bottom views are cross-sections through the films, and show the charge distribution from each wall. Red represents positive charge, and blue represents negative charge.**

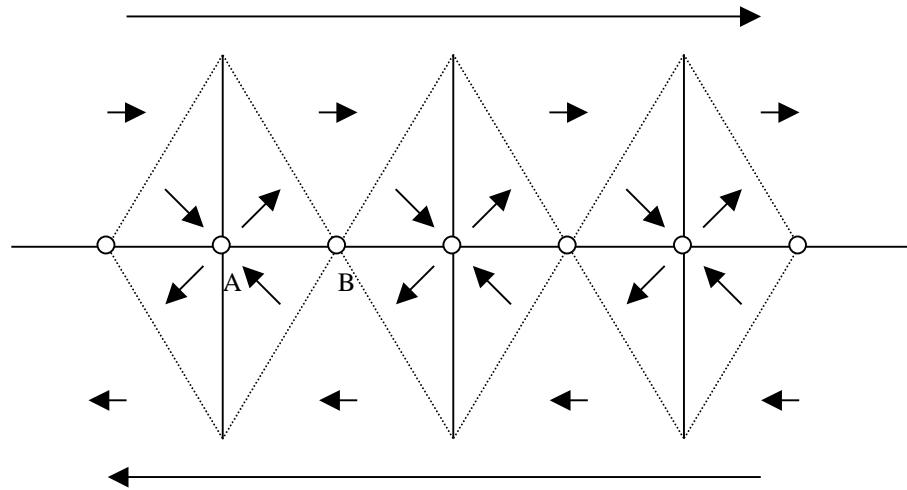
These two wall types form the basis of some more complex wall structures. The energy of a Néel wall varies rapidly with the angle between domain magnetisation directions, and the energy of a  $90^\circ$  Néel wall is around an order of magnitude smaller than a  $180^\circ$  Néel wall (Hubert and Schäfer, 1998). One result of this fact is that a simple  $180^\circ$



Néel wall can be replaced by a cross-tie wall, as illustrated in Fig. 1.6. The total length of this domain wall system is much longer than a simple straight wall, but the wall energy is smaller due to the reduction in the wall angles.

The circles in Fig. 1.6 indicate the position of Bloch lines. In continuum micromagnetic theory these are singularities, where the magnetisation direction is undefined. In reality the magnetisation points out of the plane of the film at the central point, and as the distance from the centre increases the magnetisation relaxes into the plane of the film. Point A in Fig. 1.6 is a cross Bloch line, and point B indicates a circular Bloch line (also referred to as a magnetic vortex). The cores of these structures (where the magnetisation points out of the plane) are normally small compared to the wall width, and are typically a few nm in size in soft (Fe, NiFe) thin films at the surface, although the width tends to increase away from the surface. It is actually a general result that for any simply-connected ferromagnetic body at least two singularities will exist on the surface of the body if a flux closure pattern exists, as shown by Arrott *et al* (1979). Thus any calculations of magnetic flux-closure distributions must take this fact into account.

One point to note about Bloch lines in cross-tie walls is that their direction (up or down) is normally undefined. Strictly speaking, the lowest energy state will be when the lines alternate in polarity, as this will minimise the magnetostatic energy. However, the magnetostatic interactions are so small in this case that the polarity of the Bloch lines is likely to be determined by the local magnetic history.

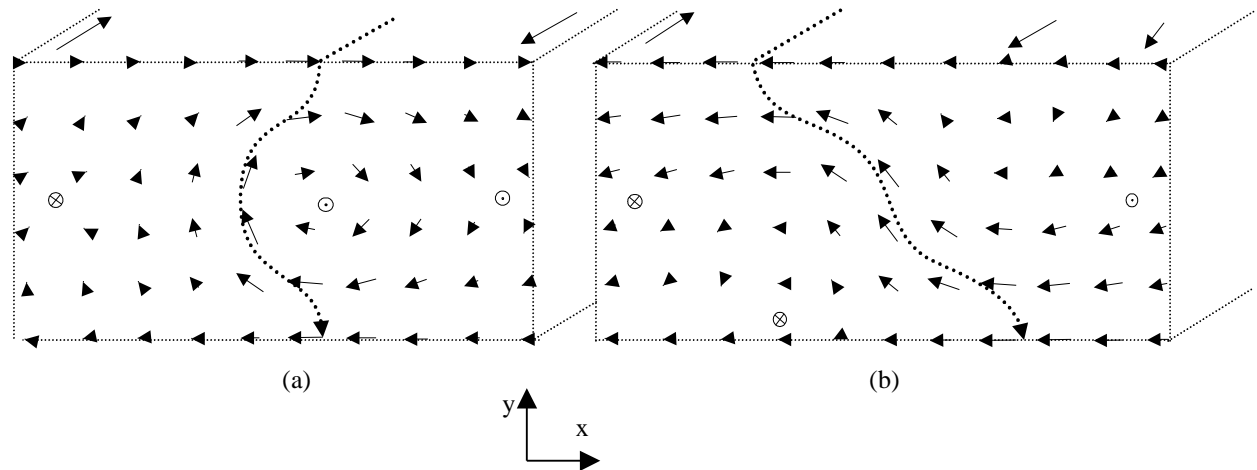


**Figure 1.6.** Schematic representation of the magnetisation in a cross-tie wall. The solid lines are  $90^\circ$  Néel walls, and the dotted lines are actually continuous transitions. The circles show the positions of the Bloch lines that intersect the wall. Point A is a cross Bloch line, and point B is a circular Bloch line, or vortex.

Another type of wall is possible in films that are not quite thick enough to support true Bloch walls. A vortex wall looks like a Néel wall on the surfaces of the film, but resembles a Bloch wall in the middle of the film. For this reason these walls are sometimes

referred to as Bloch walls with Néel caps. However, this description does not really describe fully the complexity of the vortex wall. These wall types are sometimes described as C-walls and S-walls, and it is obvious when examining the cross-sections of these walls how these descriptions arise.

Of the two walls shown in Fig. 1.7, the asymmetrical Bloch wall is favoured for small external fields, while the asymmetrical Néel wall is generally found when higher external fields are applied (Ramstock *et al*, 1996). The most important property of the vortex walls is that they contain little or no magnetic charge, and so the magnetostatic energy is reduced over the plain Néel or Bloch walls.



**Figure 1.7. Examples of vortex walls. (a) is an asymmetrical Bloch wall, while (b) is an asymmetrical Néel wall. The dotted line indicates the centre of the wall, that is, the point where the  $z$  magnetisation component changes sign (in this case  $z$  is in the plane of the film). This diagram is derived from Hubert and Schäfer (1998), and is based on model calculations for 100 nm thick Permalloy walls.**

#### 1.4.3 Other magnetic configurations of thin films

Magnetic vortices are found in cross-tie walls, but can also exist elsewhere. The domain structure shown in Fig. 1.3c has a vortex at the centre, for example. Far from the centre of the vortex the magnetisation simply rotates around the centre in the plane of the film. Closer to the centre of the vortex the radius of curvature decreases, thus the magnetisation rotation becomes tighter and the exchange energy increases. Near the centre the magnetisation begins to point out of the plane to reduce the exchange energy of the system, at a cost of some magnetostatic energy. At the centre of the vortex the magnetisation direction is perpendicular to the plane. As mentioned previously, Arrott *et al* (1979) showed that such singular points must occur in magnetic elements where a flux-closure domain structure exists.

Although domains are often thought of as uniformly magnetised, it is often possible to observe a magnetisation ‘ripple’ under close inspection. This effect is caused by the local variation of the easy axis of the film, which in polycrystalline films is due to the varying orientations of the crystal grains. This feature can be used to deduce the magnetisation direction, as will be illustrated in Chapter 3.

## 1.5 Conclusions.

The magnetic structure of a material is influenced by many factors, and the domain structure of magnetic materials is a result of the system relaxing into a minimum energy state. The energy of a particular configuration depends on the intrinsic material properties (exchange energy and magnetocrystalline anisotropy) and extrinsic properties (shape of sample, field applied). Domain structures and domain walls can be complex in nature, especially in the case of thin magnetic films. The observation of these magnetic structures is discussed in the following chapters (2 and 3).

## References

- Arrott A S, Heinrich B and Aharoni A (1979), “Point Singularities and Magnetisation Reversal in Ideally Soft Ferromagnetic Cylinders”, *IEEE Trans. Magn.*, **15**, 1228-1235
- Barkhausen H (1919), “Two phenomena, discovered with the help of the new amplifiers”, *Phys. Z.*, **20**, 401-403
- Bitter F (1931), “On inhomogeneities in the magnetization of ferromagnetic materials”, *Phys. Rev.*, **38**, 1903-1905
- Bloch F (1932), “On the theory of the exchange problem and the remanence phenomenon of ferromagnets”, *Z. Physik*, **74**, 295-335
- Brown W F (1963), *Micromagnetics*, Wiley
- Cowburn R P (2000), "Property variation with shape in magnetic nanoelements", *J. Phys. D: Appl. Phys.*, **33**, R1-R16
- Heisenberg W (1928), “On the theory of ferromagnetism”, *Z. Physik*, **49**, 619-636
- Hubert A and Schäfer R (1998), *Magnetic Domains: The Analysis of Magnetic Microstructures*, Springer
- Karl W J, Powell A L, Watts R, Gibbs M R J and Whitehouse C R (2000), “A micromachined magnetostrictive pressure sensor using magneto-optical interrogation”, *Sensors and Actuators A-Physical*, **81**, 137-141

- Landau L D and Lifshitz E (1935), “On the theory of dispersion of magnetic permeability in ferromagnetic bodies”, *Phys. Z. Sowjetunion*, **8**, 153-169
- McVitie S, Zhou L and Chapman J N (1999), "The effect of oblique incidence evaporation on the magnetic properties of thin film elements", *J. Phys. D: Appl. Phys.*, **32**, 2714-2720
- Néel L (1955), “Bloch wall energy in thin films”, *C. R. Acad. Sci. Paris*, **241**, 533-536
- Ramstock K, Hartung W and Hubert A (1996), “The Phase Diagram of Domain Walls in Narrow Magnetic Strips”, *Phys. Stat. Sol. A.*, **155**, 505-518
- Rave W and Hubert A (2000), “Magnetic Ground State of a Thin-Film Element”, *IEEE Trans. Magn.*, **36**, 3886-3899
- Stipe B C, Mamin H J, Stowe T D, Kenny T W and Rugar D (2001), “Magnetic dissipation and fluctuations in individual nanomagnets measured by ultrasensitive cantilever magnetometry”, *Phys. Rev. Lett.*, **86**, 2874-2877
- Suhl H (1998), "Theory of the magnetic damping constant", *IEEE Trans. Magn.*, **34**, 1834-1838
- Tomlinson S L and Farley A N (1997), “Micromagnetic model for magnetic force microscopy tips”, *J. Appl. Phys.*, **81**, 5029-5031
- Weiss P (1907), “The hypothesis of the molecular field and the property of ferromagnetism”, *J. de Phys. Rad.*, **6**, 661-690

## Chapter 2. Lorentz electron microscopy and tomography

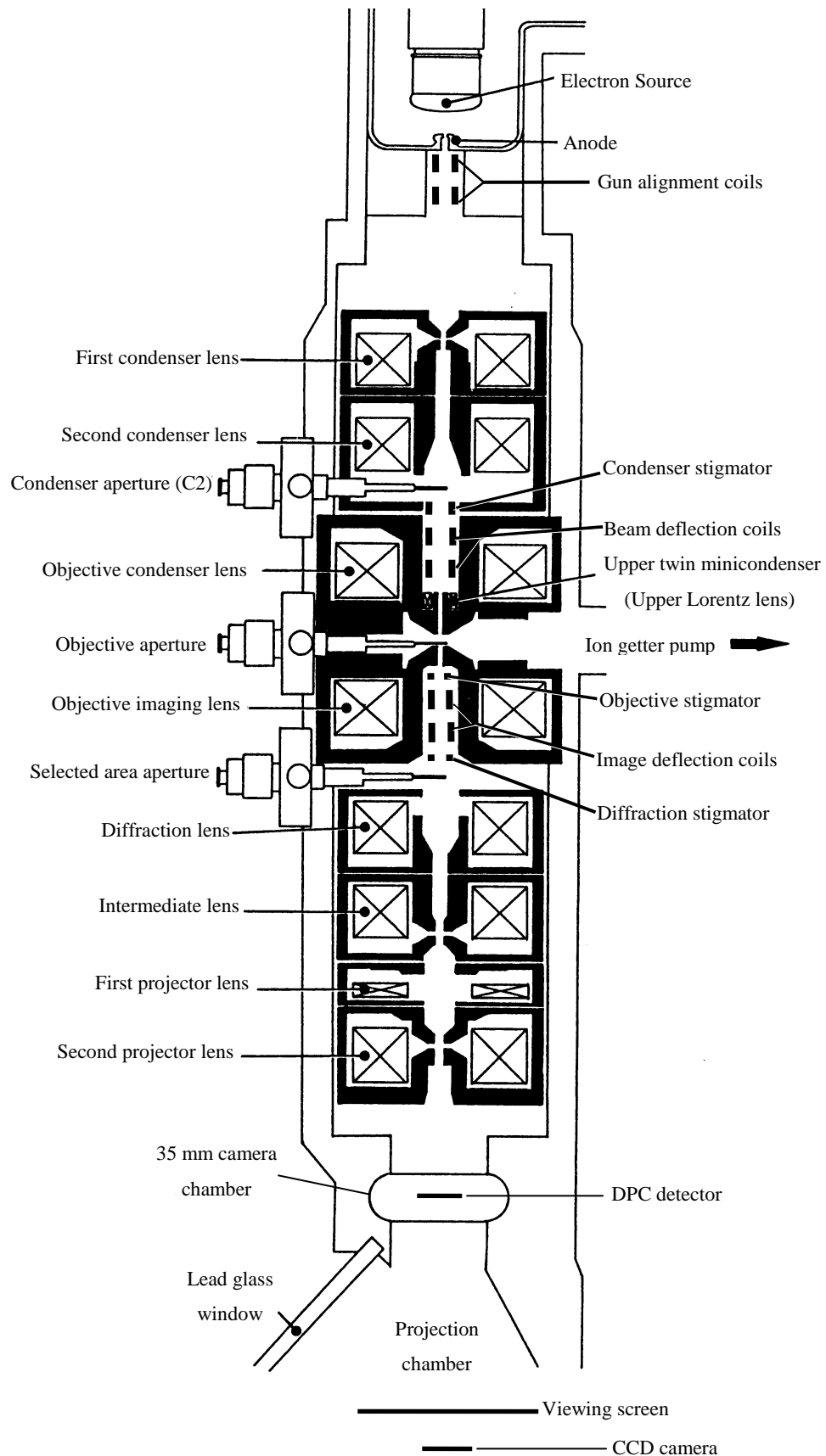
### 2.1 Introduction

Mapping the three-dimensional field (magnetic and/or electrostatic) from a sample with a resolution of a few nanometers is a formidable challenge. This can be achieved by the combination of phase imaging in the transmission electron microscope together with the technique of tomography.

In section 2.2 the transmission electron microscope is introduced, and the interaction of an electron beam with magnetic and electrostatic fields is described. In section 2.3 various ways of imaging these fields in the TEM are discussed. To find the full three-dimensional distribution of a field requires a tomographic procedure, and the application of tomography to Lorentz microscopy is covered in section 2.4. The implementation of the tomographic procedure is detailed in section 2.5, and some conclusions are given in section 2.6.

### 2.2 Electron microscopy

In some ways the electron microscope is a close analogue of the optical light microscope. In both cases there is a source of radiation, a series of lenses to focus the radiation onto and from an object and a detection system to display the resulting image. The main difference is that the resolution of the electron microscope is much higher than its light optical equivalent. There are two principle types of electron microscope, being the transmission electron microscope (TEM) and the scanning electron microscope (SEM). In the TEM a beam of electrons is used to illuminate a specimen, and post-specimen lenses then focus a magnified image onto a phosphor screen. In the SEM, the electron beam is focused onto the surface of a sample and scanned across it in a raster pattern. In this case electrons that are emitted from the beam-surface interaction are detected and displayed on a CRT, which is scanned at the same rate as the electron beam. The TEM can also be adapted to scan a beam of electrons across a sample in the manner of a SEM, and an instrument of this type is called a scanning transmission electron microscope (STEM). The instrument used for the work presented here is a Philips CM20 STEM that has been modified to image magnetic materials (Chapman, 1994). The general layout of this instrument is shown in Fig. 2.1.



**Figure 2.1.** The general layout of the electron optics and detectors of the CM20 STEM. This diagram is of a standard CM20, and thus does not show the lower Lorentz lens (lower twin minilens). The lower Lorentz lens sits just above the objective stigmator coils. The DPC detector, phosphor viewing screen and CCD camera can all be retracted from the path of the electron beam. The sample is placed in the centre of the objective lens gap, just above the objective aperture.

Microscopes that use lenses for imaging are limited in resolution to approximately half the wavelength of the radiation used. For visible light this equates to 200 – 400 nm. The electron microscope uses a beam of electrons accelerated by a potential that can range from a few kV to a few MV. Electrons accelerated through such potentials have wavelengths commonly measured in picometers, and so the electron microscope is theoretically capable of imaging down to the atomic scale and below. The full relativistic expression for the wavelength  $\lambda$  is

$$\lambda = \frac{hc}{\sqrt{eV(eV + 2m_0c^2)}} \quad (2.1)$$

where  $c$  is the speed of light,  $V$  is the acceleration voltage and  $m_0$  is the rest mass of the electron. Unlike light optical microscopes, the main limitation on the resolution of the electron microscope is the aberrations in the lenses. These aberrations normally limit the resolution of a transmission electron microscope (TEM) to a few Å. The purpose and function of the various components shown in Fig. 2.1 are discussed in the following sections.

### 2.2.1 The electron gun

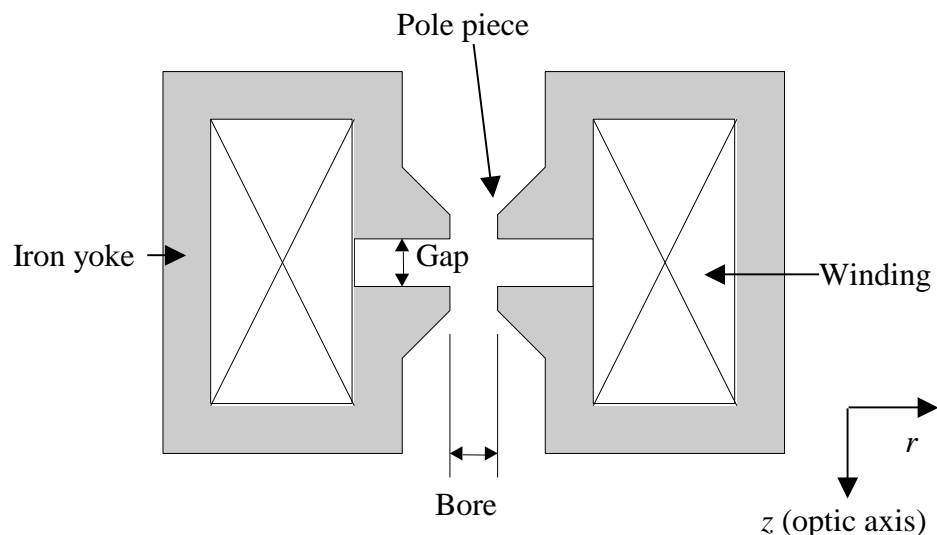
In a TEM electrons extracted from a small source are accelerated in the electron gun to form the electron beam. A series of anodes placed after the electron source accelerate the electrons in stages and also have a focusing effect. There are three main types of electron source; the tungsten filament, the LaB<sub>6</sub> crystal and the field emission gun (FEG). These different types of gun have different characteristics, such as the total beam current that they can produce, the energy spread of the beam and the vacuum conditions necessary to operate the gun. Another important factor is the brightness of the gun, defined as the current density per unit solid angle.

A tungsten filament gun consists of a thin tungsten wire that is bent to form a hairpin. This is heated to a high temperature (around 2500-3000K) by a current running through the wire. Electrons are ejected from the surface of the wire by thermionic emission. The LaB<sub>6</sub> source works on similar principles, but has better emission characteristics (brightness 20× greater than tungsten filament, ~1/2 the energy spread) and lasts longer than the tungsten filament. In this case the emitter is a pointed crystal of LaB<sub>6</sub>. The field emission gun uses a different mechanism for electron emission. A suitable material (often tungsten) is shaped to a very sharp point and placed in a strong electrostatic field gradient. At the tip of the FEG the field is strong enough to overcome the material

work function and extract electrons directly. The advantage of the FEG is the very high brightness ( $>1000\times$  greater than tungsten filaments) obtained, although this is at the expense of a lower beam current, which is typically a tenth of that from a tungsten filament. As discussed in later sections, the high brightness is an important requirement for studies on magnetic materials. For these reasons the CM20 is equipped with a thermally assisted FEG (the FEG is heated to assist electron extraction and stabilise the emission current). The tungsten needle in the FEG is also coated with zirconia to lower the work function of the needle and make electron extraction easier; this type of FEG is termed a Schottky emitter. The acceleration potential is set at 200 kV, and so the wavelength of the electron beam is 2.51 pm (from Eqn. 2.1).

### 2.2.2 Electron optical lenses

TEM lenses can be magnetic or electrostatic in nature, as both types of field will deflect electron beams. In practice most electron lenses are magnetic, as electrostatic lenses are susceptible to voltage breakdown due to the high voltage gradients required. A magnetic lens consists of a cylindrical wire winding surrounded by a magnetic yoke, as shown in Fig. 2.2. In the centre of the lens a pole piece is responsible for shaping the magnetic flux generated by current in the winding into the correct form in the lens gap. This field distribution then focuses the electron beam. The advantage of a magnetic lens compared to the light optical equivalent is that it is possible to change the strength of the lens by changing the current through the winding, and so it is not necessary to move the lens physically to change focus. The major problem with magnetic lenses in comparison to light optical lenses is that the lens aberrations are significant, and these in fact are the main limitation on the resolution of an electron microscope.



**Figure 2.2.** General layout of a magnetic lens. The view is a cross-section through the centre of the lens, which is cylindrical in form.



### 2.2.3 Lenses for imaging magnetic materials

In the (S)TEM, the sample is normally placed in or near the centre of the objective lens, and is thus immersed in the lens field. This is obviously not desirable for the study of magnetic specimens. In the CM20, this problem is solved by the use of two small lenses (normally called the Lorentz lenses) that are embedded in the main objective lens above and below the sample. These lenses can be used in place of the main objective lens, at the cost of resolution (the resolution is nonetheless sufficient to study most magnetic systems). The field in the lens gap is negligible using this system (the objective lens can generate a vertical gap field of 0.7 T at full excitation. The maximum remanent field when the objective lens is switched off is ~20 Oe, and using reverse current in the objective lens can reduce this to <0.5 Oe). Also, as the objective lens is not used for imaging it can be used as a field source, acting on the sample. At the sample the objective lens field lies along the optical (z) axis, perpendicular to the sample plane. Tilting the sample gives an in-plane field component that varies with the cosine of the tilt angle. This allows magnetising experiments to be performed on thin-film magnetic samples without the need for a special magnetising sample stage.

### 2.2.4 Magnetic lens aberrations

As stated previously, lens aberrations limit the resolution of the (S)TEM. There are many types of aberrations in magnetic lenses, but the most important are spherical aberration, astigmatism and chromatic aberration.

*Spherical aberration* arises because the focal length of the lens varies with the distance from the lens optical axis. Thus an image of a point object produced by a magnetic lens will be a disc, often referred to as the disc of confusion. If electrons leave the point object at angles from 0 to  $\alpha$  (measured from the optic axis) the resulting disc of confusion in the Gaussian image plane has radius

$$r_s = MC_s \alpha^3 \quad (2.2)$$

where  $M$  is the magnification of the lens and  $C_s$  is the (third-order) spherical aberration coefficient. Note that higher order spherical aberrations are also present in magnetic lenses, but these can normally be neglected. In some respects spherical aberration is the most important problem in electron optical systems, as there is no simple method to correct it. In most cases the spherical aberration of the microscope objective lens is the most important factor governing the microscope resolution. The CM20 objective lens has

a  $C_s$  of  $\sim 6.5$  mm. Note that when performing DPC on the CM20 the probe forming lens can be either the upper Lorentz lens ( $C_s \sim 0.5$  m) or the second condenser lens ( $C_s \sim 8$  m).

*Astigmatism* is caused by asymmetry in the lens field, which can be caused by asymmetries in the dimensions of the lens pole piece, or inhomogeneities in the material of the pole piece. The most important form of astigmatism is two-fold, where a conical ray entering the lens is brought to two line foci orthogonal to each other at different distances from the lens. The plane midway between these lines is the optimum focal position in this case, and an image from a point object forms a circle, which is termed the circle of least confusion. This form of astigmatism is normally corrected using a magnetic quadrupole system called a stigmator, which acts as a weak lens with adjustable astigmatism.

*Chromatic aberration* arises from the fact that the deflection of an electron by a magnetic field varies with the electron energy, so the focal length of the lens varies with electron energy. The energy spread of an electron beam can arise from two sources; the electron gun and the specimen. As all electron sources work at temperatures above absolute zero the electrons extracted from them will have some energy spread, governed by Boltzmann statistics. Instabilities in the electron gun voltage supply can also contribute to energy spreading. As the electrons interact with the specimen energy losses occur due to inelastic scattering events, and this also increases the energy spread of the emerging beam.

In this thesis the main TEM imaging mode used is the Fresnel mode (in Chapter 4), and this is only used at relatively low magnifications. The lens aberrations are therefore not overly important in this case. However, when DPC imaging is used the resolution is ultimately limited by the size of the electron probe, and so the aberrations are important. This is covered in more detail in the section on DPC imaging.

### 2.2.5 Detection of electrons

In the TEM an image of the sample is projected by the post-specimen lenses onto the image plane. To view this image there are three principal methods. Almost all TEMs are fitted with a viewing screen coated with a phosphor that glows when hit by electrons, providing a real-time view of the beam distribution. To record the image for later analysis photographic film is often used, as film can be exposed by direct exposure to the electron beam. It is also possible to use a modified TV camera to view and record images. In this case, a fluorescent screen is placed in front of the camera to convert the electron image into a light image, which is then imaged by the camera. In recent years charge-coupled device (CCD) chips have found widespread use, as these have the advantage that they can detect the electron distribution directly without an intermediate conversion stage as required for TV systems. The CM20 is equipped with all of the systems mentioned above,

as well as an eight-segment semiconductor detector for DPC imaging, which is described later.

### 2.2.6 Lorentz microscopy – classical description

The interaction of an electron beam with a magnetic specimen can be described classically in terms of the Lorentz force. An electron moving through magnetic induction  $\mathbf{B}$  with velocity  $\mathbf{v}$  will experience a force

$$\mathbf{F} = -e\mathbf{v} \times \mathbf{B} \quad (2.3)$$

where  $e$  is the electronic charge. If the electron with velocity  $\mathbf{v}$  directed along the  $z$  axis passes through a region of induction the resultant angular deflection  $\beta$  is given by

$$\beta_{x,y} = \frac{e\lambda}{h} \int_{-\infty}^{\infty} B_{-y,x} dz \quad (2.4)$$

where  $\lambda$  is the wavelength of the electron beam and  $h$  is Plank's constant. (The coordinate system is illustrated in Fig. 2.6, in Section 2.3.5.)

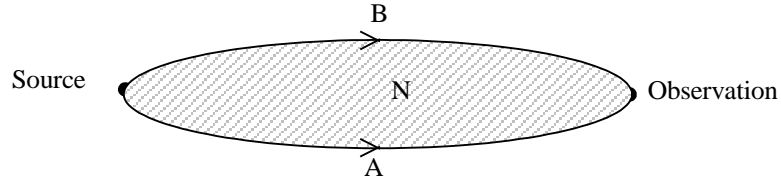
As an example, an electron with energy 200 keV passing through a 50 nm thick magnetic film with a saturation induction of 1 T (directed in the sample plane) will be deflected by approximately 30  $\mu$ rad. This is much smaller than typical Bragg deflections from crystalline materials, which are of the order of  $10^{-2}$  rad, and so Lorentz deflections can be easily differentiated from Bragg deflections.

### 2.2.7 Lorentz microscopy – quantum mechanical description

To understand the effects of interference in some imaging modes, such as electron holography, a quantum mechanical description of the beam – specimen interaction is required. For magnetic objects, Aharonov and Bohm (1959) showed that if two electron rays originate at one point and travel along the two different paths  $A$  and  $B$  before meeting again, the phase difference  $\Delta\phi$  between the two is

$$\Delta\phi = \frac{2\pi e}{h} N \quad (2.5)$$

where  $N$  is the magnetic flux through the surface bounded by the two electron ray paths  $A$  and  $B$ , as illustrated in Fig. 2.3.



**Figure 2.3. Illustration of the magnetic flux enclosed by two electron ray paths.**

In the case of a plane electron wave incident on a magnetic sample the  $x$ -component of the phase gradient of the emergent beam can be written

$$\frac{\partial \phi}{\partial x} = \frac{2\pi e}{h} \int_{-\infty}^{\infty} B_y dz. \quad (2.6)$$

The phase gradient is related to the deflection of the electron beam by

$$\beta = \frac{\lambda}{2\pi} \nabla \phi, \quad (2.7)$$

and so the Eqns. 2.4 and 2.6 are in fact equivalent.

### 2.2.8 Electrostatic phase microscopy

As will be explained in Chapter 6, when examining magnetic samples the results can be complicated by the effects of electrostatic charging, and so the effect of an electrostatic field on an electron beam is considered here. Given a specimen of thickness  $t$  and electrostatic field  $E$ , a plane wave incident on this specimen will undergo a phase shift between two points on the  $x$  axis of

$$\frac{\partial \phi}{\partial x} = \frac{\pi}{\lambda V} \int_{-\infty}^{\infty} E_x dz, \quad (2.8)$$

where  $V$  is the acceleration voltage of the beam. Again, the phase shift is related directly to the deflection of the electron beam. Taking this expression and combining with Eqns. 2.6 and 2.7 then gives the deflection from a sample with magnetic and electrostatic fields, which is

$$\beta_{x,y} = \frac{e\lambda}{h} \int_{-\infty}^{\infty} B_{-y,x} dz + \frac{1}{2V} \int_{-\infty}^{\infty} E_{x,y} dz. \quad (2.9)$$

Note that this equation does not involve the amplitude of the electron wave, i.e. the sample is treated purely as a phase object. This is certainly not true for thin-film samples where the electron beam passes through the material, as the beam amplitude will be altered

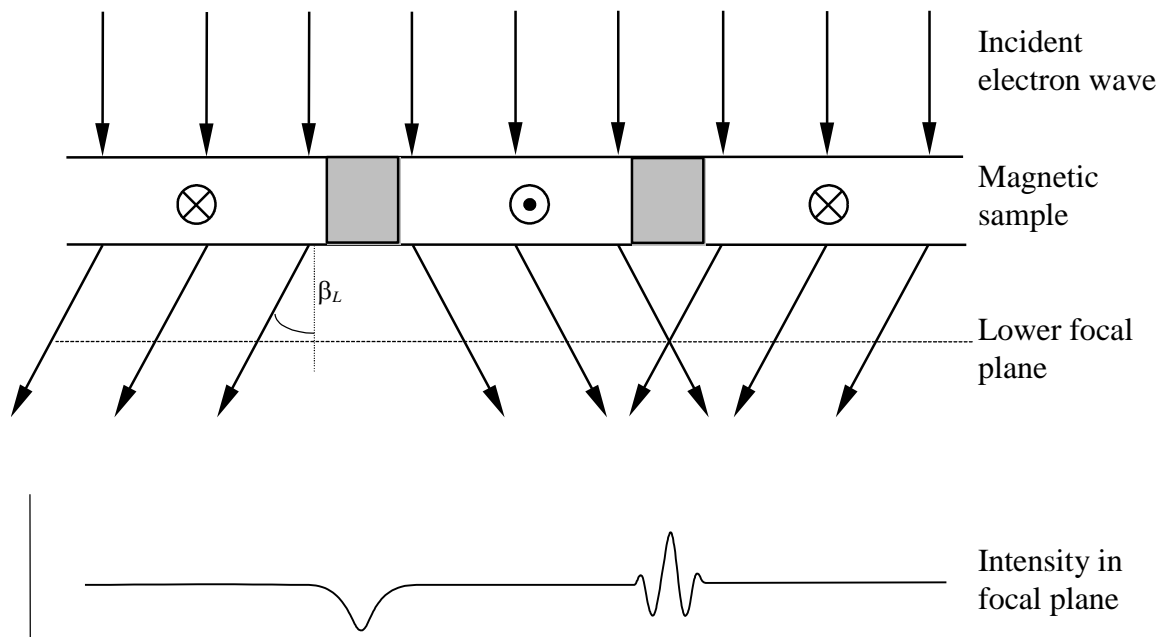
by large-angle scattering from the atomic potentials (which are excluded from the beam by apertures in the electron column). However, studies of the MFM tips covered in later chapters concentrate on the stray field from these tips, and so these samples can be counted as pure phase objects.

### 2.3 Imaging phase objects in the (S)TEM

All of the TEM detector systems mentioned previously detect the intensity of the electron wave, and so an in-focus image of a phase object in a conventional TEM will not reveal any phase information. Special imaging modes are therefore required to convert the phase variation of the electron wave into intensity variations that can be imaged. Some of these methods are covered below.

#### 2.3.1 Fresnel imaging mode

The simplest method to obtain contrast from phase objects is to defocus the imaging system such that the object plane of the instrument lies above or below the specimen. As illustrated in Fig. 2.4, when applied to a magnetic sample the result is that intensity variations occur in the image in areas where the beam converges and diverges. Light and dark lines in the image thus reveal the magnetic domain walls.



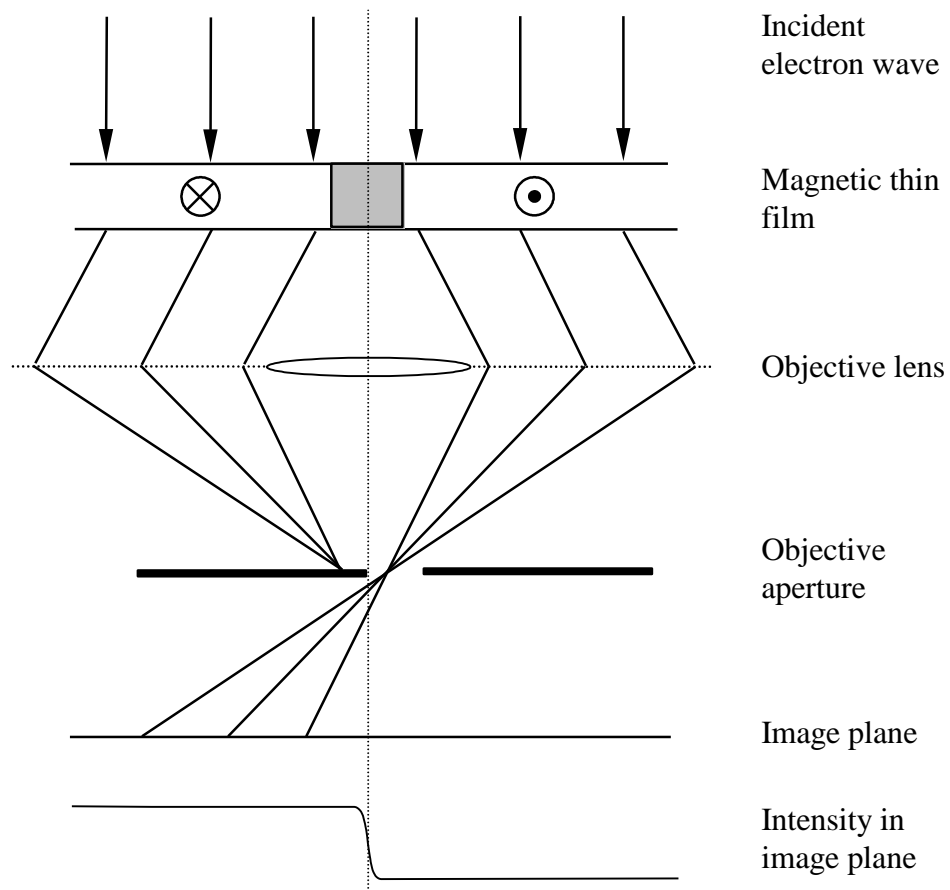
**Figure 2.4.** Diagram illustrating the formation of contrast from a magnetic specimen in Fresnel mode.

If a coherent electron source such as a FEG is used then it is also possible to observe internal structure where the electron beam converges. This is due to interference between the wavefronts from either side of the wall, and can be analysed to provide information on the wall structure. It is difficult to extract quantitative information using

this mode, as the imaging process is very non-linear (see Chapman *et al*, 1978 and references therein). However, the simplicity of the method does mean it enjoys widespread use, especially for dynamic magnetic studies.

### 2.3.2 Foucault imaging mode

In the Foucault imaging mode an aperture is placed in the back focal plane of the imaging lens to block electrons that have been deflected in particular directions. The aperture is positioned so that the edge is just to one side of the central spot in the diffraction plane, thus blocking approximately half of the deflected electrons (Fig. 2.5). This results in contrast relating to the direction of the magnetic induction parallel to the aperture edge. To reveal the full distribution therefore requires two images be taken with the aperture in orthogonal positions. As with Fresnel imaging, Foucault images have a non-linear dependence on the magnetisation. Extracting quantitative information is difficult, as the contrast mechanism is very sensitive to the positioning and quality of the aperture edge. Nevertheless, some success has been reported in quantifying magnetisation in thin films using this technique by Daykin and Petford-Long (1995).



**Figure 2.5.** Diagram illustrating the formation of contrast from a magnetic specimen in Foucault mode.

### 2.3.3 Coherent Foucault imaging mode

In this development of the normal Foucault mode, the objective aperture is used to introduce a phase shift between the Lorentz deflected electrons and a reference wave, usually part of the central (undeflected) diffraction spot (Johnston, 1995, Chapman *et al*, 1994). The different sections of the wave recombine at the image plane and interfere with each other. The result is an interference pattern that is directly related to the magnetisation of the sample, and can be readily quantified. The periodicity of the interference fringes is given by  $h/eBt$ , where  $t$  is the sample thickness. The aperture can be opaque as with normal Foucault imaging, or can be replaced by a special phase shifting aperture. The advantage of the phase shifting aperture is that electrons deflected in all directions contribute to the final image, and thus it is possible to obtain information on all magnetisation directions with a single image. The downside is that special apertures are used, which must be manufactured especially for the purpose, and also replace the normal TEM apertures so that the TEM cannot be used in the normal imaging modes.

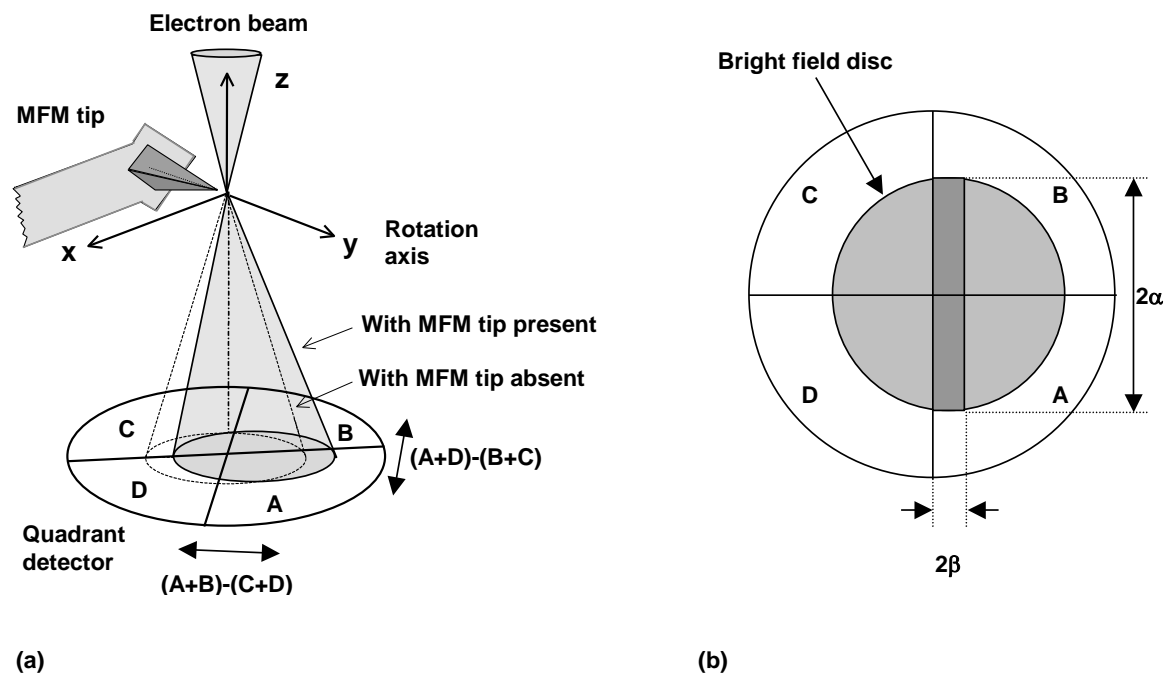
### 2.3.4 Electron holography

As with the coherent Foucault mode, electron holography relies on interference effects to reveal the phase of the electron wave. One method used is to place a positively charged wire in the path of the incident electron beam with grounded electrodes at either side, forming an electron biprism (see for example Tonomura, 1986). The two beams thus formed (called the object and reference beams) are bent towards each other and form an interference pattern. If a sample is placed in the path of the object beam it modifies the phase of that beam, which in turn alters the interference pattern, forming a hologram. This contains information on the amplitude and phase of the beam that passed through the sample. Unlike the coherent Foucault mode, the hologram cannot be interpreted directly, so the amplitude or phase information must be extracted by some means. Previously optical methods were used, but the advent of fast computers allows numerical reconstruction of the information, often at close to real-time speeds. For a recent review of this topic see Midgley (2001).

One drawback of this method is the requirement that a clear area exists to permit the passage of the reference beam undisturbed, meaning that continuous films are not suitable for this method. Also, thick samples introduce more inelastic scattering into the object beam, which destroys the coherence needed for the production of interference fringes.

### 2.3.5 Differential phase contrast

The concept of differential phase contrast imaging was introduced by Dekkers and de Lang (1974) for examining general phase objects, and was first applied to magnetic specimens by Chapman *et al* (1978). A general review is given by Chapman (1984). Unlike the modes described previously this is most conveniently implemented in a STEM. A convergent electron probe of half-angle  $\alpha$  is focused on the sample and is deflected by the angle  $\beta$  as defined in Eqn. 2.9. The deflected beam then falls on a detector situated in the far field that measures the deflection (Fig. 2.6). If the detector is split along the optic axis, the difference signal from the two halves of the detector provides a measure of the beam deflection. To measure the deflection in the two orthogonal directions a quadrant detector is used. The result is a pair of signals that are proportional to the orthogonal components of the beam deflection, which in turn are proportional to the integrated magnetic induction along the beam path. In addition, the signal summed from all four quadrants forms the standard incoherent bright field image, thus the structural information from the sample is collected in perfect registration with the deflection data.



**Figure 2.6.** (a) shows the general arrangement for DPC imaging. The convergence half-angle of the probe is  $\alpha$  and the beam deflection caused by the sample is  $\beta$ . (b) shows the deflected bright field disc on the DPC quadrant detector. The darkly shaded area corresponds to the difference signal  $(A+B)-(C+D)$ , which is approximately equal to  $2\alpha \times 2\beta$  for  $\beta \ll \alpha$ .

There are several conditions that must be fulfilled for successful DPC imaging. As a STEM technique, the resolution is limited by the size of the electron probe at the sample plane. The current in the probe must also be sufficient to allow images to be acquired in a reasonable time. There are also limits on the probe half angle  $\alpha$ , which can be explained as



follows. If  $\alpha$  is much larger than typical values of  $\beta$ , the difference between the two halves of the detector will be a small fraction of the total signal, and so the sensitivity of the system will be small. However, if  $\beta$  is comparable in size to  $\alpha$  the difference signal will become non-linear for large  $\beta$ . The ratio  $\beta/\alpha$  should therefore be  $<0.1$  (Chapman *et al*, 1978), giving reasonable linearity with sensitivity. Using the example given previously, if the maximum value of  $\beta$  expected is  $\sim 30 \mu\text{rad}$  then  $\alpha$  should be  $\sim 0.3 \text{ mrad}$ . This value is somewhat smaller than normal probe half angles used in STEM. To obtain a small probe with a thermionic electron source a large demagnification must be used in the probe forming lens system, giving a beam with a large value of  $\alpha$ . To reduce this to the value needed for DPC a small condenser aperture must be used, meaning that most of the beam is stopped by the aperture and thus the probe current is low. For moderate to high spatial resolution, high brightness sources are therefore preferred for DPC imaging, and the FEG is in most cases the best electron source to use.

The highest useful magnification of a DPC system is governed by the size of the electron probe as mentioned previously. The size of the probe in DPC mode depends on the spot size selected on the microscope and the size of the second condenser aperture. DPC on the CM20 is usually performed using a C2 aperture size of  $30 \mu\text{m}$ , and spot sizes between 5 and 9. The tomographic studies shown in this thesis have been done using a spot size of 7. In low magnification scanning mode the electron probe is formed by the C2 lens; the objective lens and Lorentz lenses are not used at all. A measurement of the probe size in this mode has been done by Lindsay (1998), giving figures of  $38 \text{ nm}$  for spot 7 and  $26 \text{ nm}$  for spot 8 (with an error of  $\pm 5 \text{ nm}$  in both cases). Spot size 8 would therefore be preferable for spatial resolution, but the probe current was found to be rather low, resulting in a significant amount of noise in the DPC signal. As spot 7 gave a signal level  $\sim 4\times$  larger than spot 8 it was used for all of the studies, despite the increased probe size. The  $30 \mu\text{m}$  aperture results in a value for  $\alpha$  of  $127 \mu\text{rad}$ .

The high magnification DPC mode utilises the Lorentz lenses to give increased resolution. The upper Lorentz lens is energised at a fixed value to give a smaller probe size, at the expense of a larger value of  $\alpha$  ( $830 \mu\text{rad}$  for a  $30 \mu\text{m}$  aperture). The reason the upper Lorentz lens is held at a fixed value is to minimise thermal drift (the upper Lorentz lens is quite close to the sample). The probe is focused using the C2 lens. In this case the probe size is expected to be considerably less than in the LM mode, and is certainly  $>25 \text{ nm}$ .

Ideally, in the absence of a sample the bright field disk should remain stationary as the electron probe scans across the sample plane. This state can be achieved by using the post-specimen lenses to make the detector plane conjugate with the beam rocking point (at

the scan coil position). Another method, which is in principle more flexible, is to use descans coils positioned after the specimen to compensate for the scanning motion. Both these methods have advantages and disadvantages, and the choice between them often depends on the details of the DPC setup on any particular microscope. The LM scanning mode in the CM20 uses the first method only, while in the HM scanning mode descans coils are used. The low end of the DPC magnification range is in fact limited primarily by the difficulty of descanning large scan fields. Conversely, accurate descanning tends to become easier at higher magnifications where, as discussed above, the probe size sets the magnification limit.

Post specimen lenses can be useful to aid with descanning, and are also required to match the size of the bright field disc with the size of the detector (the diameter of the current detector is 5.2 mm). The detectors used in the CM20 are photodiode devices, divided into quadrants by insulating dead zones, which are a few hundred  $\mu\text{m}$  wide. If the bright field disc is too small a large proportion of the signal will fall on the dead zone areas, leading to non-linearities in the difference signals. Conversely, if the bright field disc is of similar size to the detector, any movement of the disc will move it partly off the detector, again causing a non-linear response. The normal compromise is to set the camera length so that the diameter bright field disc is slightly larger than half the diameter of the detector, although for operational reasons this can vary somewhat.

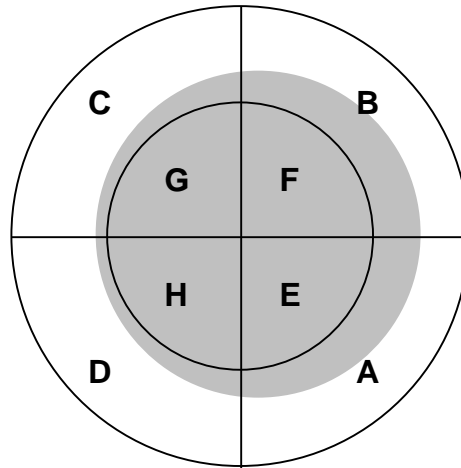
In the simple system shown in Fig. 2.6a the direction of the two orthogonal deflection components  $\beta_x$  and  $\beta_y$  corresponds to the scan field  $x$  and  $y$  axes. The use of post specimen lenses to change the camera length of the system also has the effect of rotating the deflection vectors. This rotation can be dealt with in several ways. One method is to adjust the post-specimen lens currents slightly, until a combination is found that aligns the two coordinate systems while maintaining a usable bright field disc size. Alternatively, the detector mounting can incorporate a rotation stage that allows the detector to be rotated around the optic axis. The detector in the CM20 incorporates such a mounting, and this is normally used for preference. A third way is to collect the data and then process the deflection components numerically to ‘virtually’ rotate the detector. However, with the current instrumentation it is not possible to do this in real time, and so it is preferable to physically rotate the detector.

The DPC system is normally used in one of two configurations called the ‘split’ and ‘quadrant’ configurations. In the ‘quadrant’ setup, the signals collected are (A-C), (B-D) and (A+B+C+D), being the two orthogonal deflection directions and the sum signals respectively. The ‘split’ setup is implied in Fig. 2.6b, where the signals collected are (A+B)-(C+D), (A+D)-(B+C) and (A+B+C+D). The ability to select either of these

configurations means that the detector rotation stage need only cover a range of  $>45^\circ$  to allow measurement of a beam deflection in any particular direction.

### 2.3.6 Modified DPC

When examining stray slowly varying magnetic fields in free space the standard four-quadrant DPC detector gives an accurate measure of the beam deflection. However, when examining polycrystalline thin films, it is found that non-magnetic ‘noise’ caused by differential scattering from the crystallites can often obscure the magnetic contrast. It was found that an annular quadrant detector can significantly suppress this ‘noise’ in DPC images (Chapman *et al*, 1990). In many samples the magnetic spatial frequencies are lower than the polycrystalline spatial frequencies, thus the magnetic information is enhanced. In most cases the annular detector is part of an eight-segment detector, which can be used as a solid or annular detector by selecting which signals are recorded. The layout of this detector is illustrated in Fig. 2.7. The diameter of the inner detector fitted to the CM20 is 5.2 mm (as mentioned previously), and the diameter of the outer detector is 10 mm.



**Figure 2.7. Layout of the modified dpc detector, showing that small shifts of the electron beam (shaded area) will not change the signals from the central portion (E – H).**

It is also simple to prove that the signal to noise ratio is enhanced using an annular detector. Consider the MDPC detector shown in Fig. 2.7. The differential signal in the horizontal direction is given by  $(A+B+E+F)-(C+D+G+H)$ . However, we can see that the inner quadrants are completely covered by the beam, so we assume that  $E=F=G=H$ . It can be seen that the difference signal can then be simplified to  $(A+B)-(C+D)$ . The noise of the signal simply depends on the total number of electrons detected. Therefore, the signal to noise ratio of the solid detector (i.e. adding A and E, B and F etc.) is

$$\frac{(A+B+E+F)-(C+D+G+H)}{\sqrt{A+B+C+D+E+F+G+H}} = \frac{(A+B)-(C+D)}{\sqrt{A+B+C+D+E+F+G+H}}. \quad (2.10)$$

When the inner quadrants E-H are removed, the signal to noise ratio becomes

$$\frac{(A+B)-(C+D)}{\sqrt{A+B+C+D}}. \quad (2.11)$$

Therefore, the only contribution of the inner detector is to the noise. The maximum signal to noise ratio is obtained when the bright field disc is just larger than the inner radius of the annular detector, but this means that small values of  $\beta$  are enough to move the disc partly off the outer detector. Thus the optimum size of the disc is given by  $\alpha+\beta$ .

## 2.4 Lorentz electron tomography

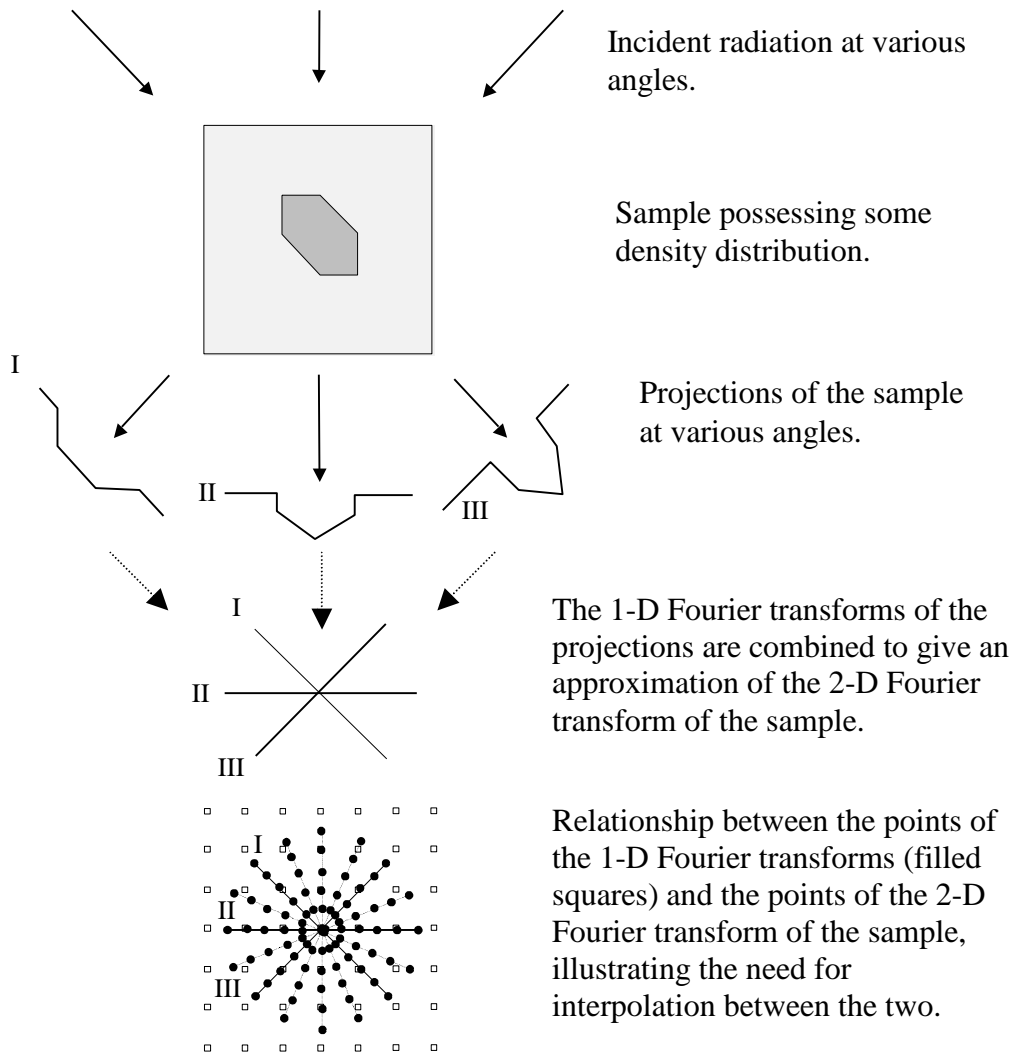
The techniques covered in the previous sections are all useful for the investigation of thin film samples, but all yield information only on the magnetic field integrated along the electron trajectory only. While this is often all that is needed to study thin films (which are essentially two-dimensional systems) other types of samples, such as MFM tips, pose more of a problem as they possess extended three-dimensional field distributions. The method used to reconstruct these field distributions from their projections is termed tomography.

### 2.4.1 Tomography fundamentals

The technique of tomography is used to reconstruct an n-dimensional object using many (n-1)-dimensional projections of that object. Examples include computerised axial tomography (CAT), positron emission tomography (PET) and electron tomography. All these methods are fundamentally the same, the only differences being the radiation used and the scale of the samples. For example, CAT and PET scanners are used to image the interior of human patients, allowing diagnosis of many ailments without the need for exploratory surgery. In the TEM, electron beam tomography has been performed to image biological structures such as chromosomes, where knowledge of the three-dimensional structure is essential in understanding the reactions of such molecules (DeRosier and Klug, 1968).

For simplicity, only examples of two-dimensional objects reconstructed from one-dimensional projections are shown as examples here. In this case the object is tilted around an axis perpendicular to the sample plane, and projections through the object are taken at

various tilt angles. The relation between the projections and the object is given by the central section theorem. This states that the one-dimensional Fourier transform of the projection is equal to a line section through the two-dimensional Fourier transform of the object (DeRosier and Klug, 1968). Therefore, given a series of projections taken at different tilt angles will enable the object to be reconstructed in Fourier space using interpolation. An inverse Fourier transform then yields the object. This process is illustrated in Fig. 2.8.



**Figure 2.8.** The principle of tomographic reconstruction using the central section theorem. The Fourier transforms of the projections of an object are combined to approximate the Fourier transform of the object. Inverse Fourier transformation then yields an approximation of the object density distribution.

The accuracy of the reconstruction depends on the angular spacing and range of the projections. In particular, it can be seen in Fig. 2.9 that the angular separation between projections is governed by the size of the region in Fourier space to be filled and the mesh size of the Fourier grid. In turn, these parameters are determined by the size of the object and the resolution desired, which leads to two constraints on the Fourier projection data. The mesh size of the Fourier space must be less than  $1/D$ , where  $D$  is the maximal

diameter of the object. Also, the diameter of the region of Fourier space to be filled has radius  $1/d$ , where  $d$  is the resolution desired. Taking all these factors into consideration, the minimum number  $N$  of projections required is given by Bracewell and Riddle (1967) as

$$N = \frac{\pi D}{d}. \quad (2.12)$$

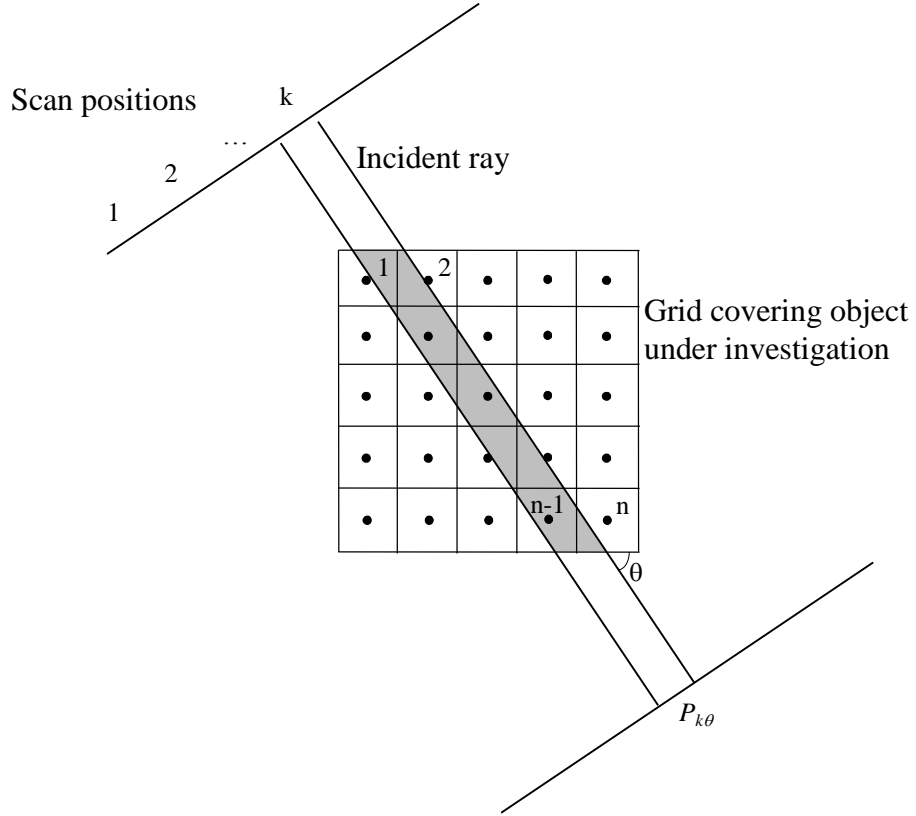
In fact, it has been found by Liu (1996) that it is possible to relax this restriction considerably when examining slowly varying functions such as magnetic fields, especially where the interesting detail is confined to the central portion of the reconstruction. For instance, when examining the stray field from a hard disk write head the diameter of the reconstruction was  $24.5 \mu\text{m}$ , and the resolution was  $0.25 \mu\text{m}$ . Using Eqn. 2.12, this implies that 308 projections are required. However, it was found that in practice, there was little improvement in the reconstruction accuracy for more than 36 projections.

The examples given above are examples of scalar tomography, where a scalar function (usually a density function) is reconstructed. The extension to vector tomography, where a vector field is reconstructed from the projections, can be envisaged simply by considering the vector field as several linked scalar fields. As well as direct Fourier transformation there are other algorithms that can be used for tomographic reconstruction of magnetic fields. Two such algorithms have been written specifically to reconstruct magnetic stray fields. The first of these algorithms is called the algebraic reconstruction technique (ART) and was used by Liu (1996) to investigate the fields from magnetic tape write heads.

#### 2.4.2 Conventional ART algorithm

The ART was introduced by Gordon *et al* (1970) as a simple and intuitive method for solving the tomographic problem. The technique has a simple basis; the projections from the reconstruction are compared with the projections of the actual object in question. Any error between the simulated and real projections is used to adjust the reconstruction such that the error decreases. This process is repeated iteratively for all projections until some convergence criteria are met.

In ART the space containing the density distribution (the sample) is divided into a discrete grid of the resolution required. A parallel beam of radiation will intersect a subset of these points as shown in Fig. 2.9



**Figure 2.9.** Illustration of how a portion of a wave incident on a region of space intersects a discrete grid covering that space.

The projection at a point  $P$  can then be written as the equation

$$P_{k\theta} = \sum_{(i,j) \in r(k,\theta)} w_{ij} f_{ij} \quad (2.13)$$

where  $\theta$  is the angle of the ray relative to the coordinate system and  $k$  is the scan point. The reconstruction function  $f$  at point  $(i,j)$  is modified by a weighting factor  $w$ . This is to account for the length of the electron beam in the element associated with the point. The object is to reconstruct  $f$  given  $P$ . Often  $f$  is initially set to zero at all points, but if the general form of the object is known  $f$  can be set to this form, to speed up the convergence of the algorithm. The first estimate of a projection point  $P_{k\theta}$  is then calculated using Eqn. 2.13. and is then compared to the corresponding experimental projection point. A proportion of the resulting error is then added to each element intersected by the beam. The proportion of the error added to each element normally depends on its weighting factor (normally proportional to the distance the beam travels through the element) and a global error multiplication factor (which essentially governs the convergence speed of the algorithm). The process is then repeated for the projections at the other angles. Once all the projections have been covered the new estimate of the function  $f$  is compared to its previous value. If the difference between the two is small enough to satisfy the

convergence criteria the process ends, otherwise the loop repeats. The choice of convergence criteria is normally a trade-off between accuracy and speed.

The advantage of ART algorithms is that a reasonable reconstruction can be obtained from sparse or incomplete data. This is an advantage in conventional electron tomography, where the tilt range is often limited to  $\pm 60^\circ$  or less. The main disadvantage of ART is the computing time required. To reconstruct an area divided into  $201 \times 201$  elements can typically take an hour or more, depending on the speed of the processor used and the noise level in the input data. It is possible to speed up the process by, for example, pre-computing and storing all the weighting factors to avoid the necessity of computing  $w$  for each iteration. However, this requires more memory.

### 2.4.3 RTM algorithm

The RTM (Radon Transform Method) tomographic algorithm was originally implemented by a group at the University of Duisburg; see Elsbrock *et al* (1985) and Steck (1990) for details. The algorithm is of the weighted back-projection type, where a convolution kernel is applied to the input projections, and the results are then back-projected onto the reconstruction space and added together to yield the reconstruction. The convolution kernels are derived using the relationship between the Radon and Fourier transforms, and the properties of magnetic fields in free space. Using different kernels it is possible to reconstruct all three field components from one component of the deflection data, hence using both deflection datasets yields two independent reconstructions of the field. Also, given measurements in a plane near the sample the field in the whole half-space beyond the measurement plane can be reconstructed using modified forms of the convolution kernels.

One interesting discovery by Gallacher (1999) was that the RTM algorithm can reconstruct a field distribution with good accuracy even if the reconstruction area does not cover the whole field region. Specifically, when using the  $x$  DPC deflection data, the reconstructions of the in-plane field components are very accurate, except for near the edge of the reconstruction region. The reconstruction of the out-of-plane field component is slightly less accurate in the centre of the reconstruction region, and the error then increases rapidly with increasing distance from the centre. When using the  $y$  DPC data the opposite case is true, that is the out-of-plane reconstructed field component is accurate and the in-plane components are less so. The error in the less-accurate reconstructions increases as the amount of integrated field outside the reconstruction radius increases. This effect was demonstrated by numerical modelling; there is currently no analytical explanation.



In previous investigations (Liu, 1996) the two reconstruction sets were usually averaged on the assumption that the accuracy would be improved and the noise reduced. As might be expected from the results covered above, this is not the case. In this thesis all results derived from reconstructions (such as peak field heights, full width at half maxima etc) are from the more accurate reconstruction components.

#### 2.4.4 Magnetic ART algorithm

The version of ART described previously is used to reconstruct scalar distributions, usually density distributions. The ART algorithm used in this work was originally written by Liu (1996) and was later modified slightly to increase execution speed. To modify ART for magnetic field reconstruction is quite simple. Instead of one scalar distribution, three are used to correspond to the three orthogonal components of the vector distribution. The  $y$  field component is reconstructed using the  $x$  DPC signal, and the in-plane field components are reconstructed using the  $y$  DPC signal. Otherwise the algorithm is a standard ART algorithm.

The accuracy of the magnetic ART algorithm has been investigated extensively by Liu and Gallacher (1999). Liu concluded that for reconstruction of the fields from magnetic recording heads the ART algorithm performed as well as the RTM algorithm. However, Gallacher showed that when reconstructing fields from MFM tips, the results were less accurate than the RTM results. In particular, it was shown that when reconstructing fields with long-range background contributions (that is, fields that extend outside the area of reconstruction) the ART algorithm gave very inaccurate results. Given that most of the studies of MFM tips in the following chapters do include long-range background fields (from the magnetic films covering the cantilever and substrate of these tips), the ART algorithm was not used for any of these studies.

### 2.5 Implementation of tomography on the CM20

The implementation of tomography in the CM20 STEM involves some modification, both to the microscope and the sample rods used. The microscope modifications have been covered previously, and the DPC imaging conditions used for tomography are given in section 2.3.5. The LM scanning mode was used in all cases except for the study of the high-coercivity tip in Chapter 5. The specific requirements for tomographic studies are discussed in the following sections.

### 2.5.1 Alignment of the DPC detector and the scan axes

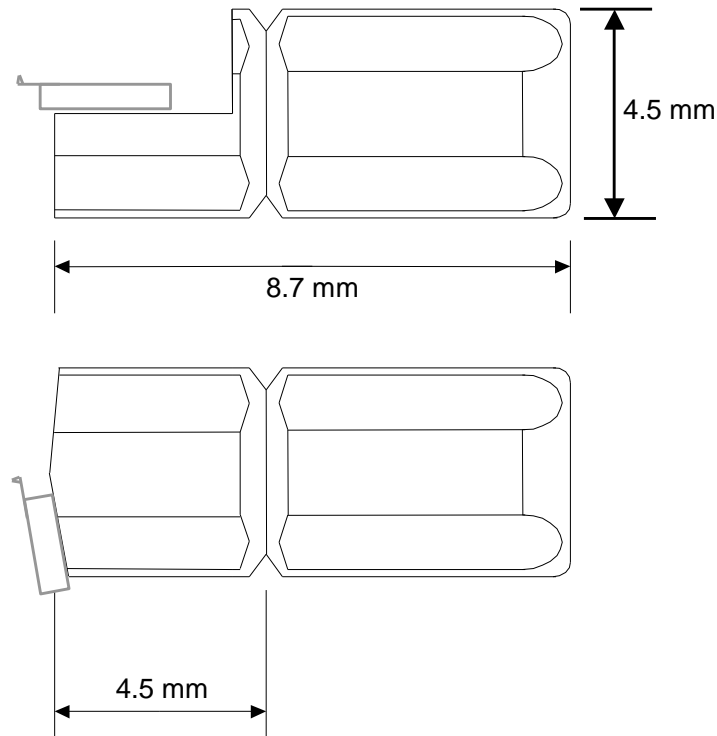
One problem that occurs in conventional electron tomography is the identification of the tilt axis in the projections, given that in a conventional TEM the orientation of the image with respect to the sample is usually undefined due to the image rotation caused by the magnetic lenses. In a STEM the orientation of the image is governed by the orientation of the scan coils, and so the orientation of the image is known. The problem of identifying the position of the tilt axis remains, and in the work of Liu (1996) and Munro (2000) the tilt axis was determined by using characteristic features of the field from the recording field heads. In the CM20, when using the low-magnification scanning mode (where the electron probe is formed by the condenser lenses only) the y scan axis is parallel to the tilt axis, so no special alignment is required. In the high-magnification scanning mode the upper Lorentz lens is energised at a fixed value, providing a smaller electron probe (at the expense of a larger convergence angle). As the upper Lorentz lens is located below the scan coils, the result is that the scan field is rotated by a fixed angle relative to the tilt axis. This can be counteracted by the scan rotation unit built into the CM20, which allows arbitrary rotation of the scan field axes. Therefore in both scan modes, the scan y axis is normally set parallel to the tilt axis.

It is also desirable in most cases to ensure that the DPC detector is oriented such that the components of integrated field detected are coincident with the scan field. As mentioned previously, this can be achieved either by rotating the detector physically, or altering the current in one or more of the post-specimen lenses to change the rotation applied to the beam. Both methods have been used in these studies, but in general rotating the detector is simpler from an operational perspective (as changing the lenses also alters the camera length), and is the preferred method. As it is possible to use either the ‘split’ or ‘quadrant’ configurations of the detector, the range of detector rotation only need be greater than  $45^\circ$ , and thus a simple design of rotation stage is required. The importance of correct detector alignment is investigated in Chapter 6.

### 2.5.2 Sample mounting for tomography

The goniometer on the CM20 is of standard design and the objective lens has a large gap of size 20 mm, giving an accessible tilt range of  $\pm 60^\circ$ . While tomographic studies can be done using this tilt range it is preferable to have access to  $180^\circ$  of rotation (indeed, one study covered in Chapter 6 required data taken over  $360^\circ$ ). This problem is solved by the use of a special sample rod, which accommodates sample stubs that can be mounted in various orientations (Ferrier, 1997). The rod has a v shaped groove near the

bearing end, with the bottom of the groove removed to permit passage of the beam. A wire clamp is provided which extends over the top of the groove. The sample stubs are square in section, with the corners rounded off, as shown in Fig. 2.10. The stub rests in the rod groove and is clamped by the securing wire. The stub can rest in any of four positions, and together with the goniometer rotation range this means that a sample mounted on the stub can be examined at any rotation angle. Thus for normal tomography (rotation range of  $180^\circ$ ) a complete dataset can be collected with only one change of stub position required.



**Figure 2.10. Diagram of the tomographic mounting stubs with MFM tips mounted on them. The top stub is a special flat mounting stub, and the bottom stub is a standard stub for tomographic imaging of MFM tips.**

For tomographic investigation of MFM tips, one end of a sample stub is rounded slightly, and a flat is ground at an angle of  $80^\circ$  from the stub/tilt axis. The tip is then attached to this flat using either thermosetting or epoxy adhesive, and silver DAG solution is usually applied to ensure electrical contact between the tip and the stub. In earlier investigations the tip and stub were also sputter coated with approximately 20 nm of Au in an attempt to prevent charging effects. This practice was later discontinued as it was found that the Au coating seemed to make little difference to the tip charging characteristics. The tip is mounted at an angle for two reasons. The first is to ensure that the cantilever or substrate does not block the beam, and the second is that this angle corresponds to the angle that the tip is mounted at in the AFM/MFM (as mentioned in Chapter 2, this is for sample clearance reasons). The plane of reconstruction (the  $x$ - $z$  plane) will therefore be parallel to the surface of a sample in the MFM.

The tips are usually mounted so that the tip apex is as close as possible to the stub axis. The maximum sample diameter permissible in the CM20 is about 7 mm. Standard MFM tips have substrate blocks of length 3-4 mm, so approximately 1.5 mm is trimmed from the end of the substrate to provide sufficient clearance. The stub is then placed in the v groove in the specimen rod, and inserted into the microscope. In a typical tomographic study, DPC images are taken between the goniometer rotation positions  $\pm 50^\circ$ , and the position of the sample stub is then changed by  $90^\circ$  and a second set of images are taken. Combining the two image sets then gives data over a range of  $190^\circ$ .

Some stubs have also been made with a mounting plane parallel to the rotation axis. These have been used to investigate the ultrasensitive MFM tip in Chapter 5, and also to mount tips so that field can be applied at varying angles to the tip axis. One advantage of these stubs is that there is no need to trim the tip substrates.

### 2.5.3 Extraction and alignment of linescans

As the goniometer in the CM20 is a standard manually controlled type, it is not possible to position the tip apex on the rotation axis with the precision required ( $>15$  nm). Therefore, instead of a single linescan an image is taken of the tip apex at each rotation position. For speed, the images are usually short in height; just enough to ensure the tip apex is included in the image. Image dimensions are typically  $256 \times 16$  pixels, with a pixel spacing of 25 to 30 nm. Along with each tip image, a background image in field free space is taken by moving the tip far away from the area being scanned. The background image is then subtracted from the tip image. This means that the electron beam does not have to be centred precisely on the DPC detector, and any residual descan effects are also subtracted out.

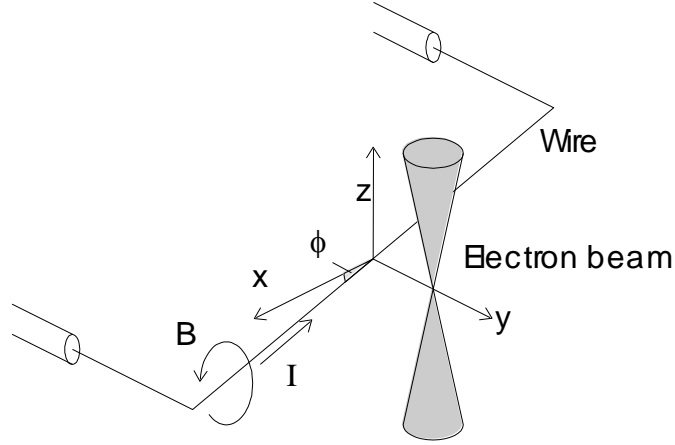
Once the tomographic dataset has been collected, linescans are extracted to form the actual reconstruction input data. The linescans are positioned as close as possible to the tip apex in each image, and for this the sum images are used. Each row of a sum image is examined, and the row that is closest to the tip, but does not actually encounter the tip apex is chosen. The other problem is to identify a common tilt axis in the images, so that the linescans can be centred. For MFM tips this is reasonably simple, given the shape of the tip apex. Most tips will have a point at the apex, and so examining the image row that just begins to encounter the tip will reveal a peak at the tip apex. This then gives the tilt axis position. In early investigations this procedure was performed manually, but later an image processing script was used, resulting in greater consistency and speed of execution.

The resulting datasets are then converted into the correct form for input to the tomographic reconstruction program. The reconstructions are usually output as binary

images, one for each field component. Analysis is usually concentrated on the  $y$  field component, as this component is perpendicular to the sample surface in the MFM, and therefore has the largest influence on the response of the MFM tip.

#### 2.5.4 Calibration of reconstructions

To calibrate the reconstructions it is necessary to calibrate the DPC response. This is done using a special sample, which consists of a straight current-carrying wire (McVitie *et al*, 1997). The geometry of this sample is illustrated in Fig. 2.12.



**Figure 2.11.** Illustration of current-carrying wire used for DPC calibration.

Using Ampère's Law, the field from a long straight wire carrying current  $I$  can be easily calculated. This field causes a deflection of the electron beam when the angle  $\phi$  between the wire and the  $x$  axis is non-zero. From symmetry arguments it can be shown that the total deflection due to the  $y$  component of the field is zero. The  $x$  component of the field is responsible for the deflection of the beam through the angle  $\beta$ . The expression for  $\beta_x$  is

$$\beta_x = \frac{e\lambda}{h} \int_{-\infty}^{\infty} B_y dz = \frac{e\lambda}{h} \frac{\mu_0 I}{2} \tan \phi. \quad (2.14)$$

Note that this expression only holds if the length of the wire is much greater than the distance between the electron beam and the wire. The angle  $\beta$  is only dependent on the angle  $\phi$  and the current in the wire  $I$ . To calibrate the DPC data, the wire is tilted to some angle (typically  $30^\circ$ ) and a current is passed through it. The DPC signal is recorded, and this value along with the calculated  $\beta$  allows the DPC data to be calibrated. The calibration of the reconstructions then follows.

## 2.6 Conclusion

Using the DPC method of Lorentz electron microscopy, it is possible to obtain accurate projections of the stray field of a magnetic sample. Collecting many projections at various angles allows accurate reconstructions of the field distribution in front of the sample. The RTM algorithm is the most accurate for this purpose, while the ART algorithm is currently not applicable to samples such as MFM tips.

## References

- Aharonov Y and Bohm D (1959), *Phys. Rev.*, **115**, 485
- Bracewell R N and Riddle A C (1967), “Inversion of fan-beam scans in radio astronomy”, *Astrophys. J.*, **150**, 427-434
- Chapman J N, Batson P E, Waddell E M and Ferrier R P (1978), “The direct determination of magnetic domain wall profiles by differential phase contrast electron microscopy”, *Ultramicroscopy*, **3**, 203-214
- Chapman J N (1984), “The Investigation of Magnetic Domain-Structures in Thin Foils by Electron-Microscopy”, *J. Phys. D: Appl. Phys.*, **17**, 623
- Chapman J N, Mcfadyen I R and Mcvitie S (1990), “Modified differential phase-contrast Lorentz microscopy for improved imaging of magnetic-structures”, *IEEE Trans. Magn.*, **26**, 1506-1511
- Chapman J N, Johnston A B, Heyderman L J, Mcvitie S, Nicholson W A P and Bormans B (1994), “Coherent magnetic imaging by TEM”, *IEEE Trans. Magn.*, **30**, 4479-4484
- Daykin A C and Petford-Long A K (1995), “Quantitative Mapping of the Magnetic Induction Distribution using Foucault Images formed in a Transmission Electron-Microscope”, *Ultramicroscopy*, **58**, 365-380
- Dekkers N H and de Lang H (1974), *Optik*, **41**, 452-456
- DeRosier D and Klug A (1968), “Reconstruction of three-dimensional structures from electron micrographs”, *Nature*, **217**, 130-134
- Elsbrock J B, Schroeder W and Kubalek E (1985), “Evaluation of Three-Dimensional Micromagnetic Stray Fields by means of Electron-Beam Tomography”, *IEEE Trans. Magn.*, **21**, 1593-1595
- Ferrier R P, McVitie S, Gallagher A and Nicholson W A P (1997), “Characterisation of MFM tip fields by electron tomography”, *IEEE Trans. Magn.*, **33**, 4062-4064
- Gallacher A (1999), “Theoretical Characterisation of Magnetic Force Microscope Tip Stray Fields”, *Ph.D. Thesis*, University of Glasgow

- Gordon R, Bender R and Herman G T (1970), “Algebraic reconstruction techniques (ART) for three-dimensional electron microscopy and x-ray photography”, *J. Theor. Biol.*, **29**, 471-481
- Johnston A B (1995), “Investigation of magnetic microstructures using novel transmission electron microscopy techniques”, *Ph.D. Thesis*, Glasgow University
- Lindsay R (1998), “TEM Investigation of Silicon Devices”, *Ph. D. Thesis*, University of Glasgow
- Liu Y (1996), Electron beam tomography of recording head fields”, *Ph.D. Thesis*, University of Glasgow
- McVitie S, Ferrier R P and Nicholson W A P (1997), “Absolute field strength determination of magnetic force microscope tip stray fields”, *Inst. Phys. Conf. Ser.*, **153**, 201-204
- Midgley P A (2001), “An introduction to off-axis electron holography” *Micron*, **32**, 167-184
- Munro T (2000), “The study of Stray Magnetic Fields from Digital Recording Heads for Tape Applications”, *Ph.D. Thesis*, University of Glasgow
- Steck M (1990), “Quantitative Bestimmung magnetischer und elektrischer Mikrofelder mit Hilfe der Elektronenstrahl-Tomografie”, *Doctoral Thesis*, Duisburg University
- Tonomura A, Matsuda T, Endo J, Arii T and Mihama K (1986), “Holographic interference electron microscopy for determining specimen magnetic structure and thickness determination”, *Phys. Rev. B*, **34**, 3397-3402

## Chapter 3. Scanning Probe Microscopy

### 3.1 Introduction

The concept of scanning a probe over a surface to ascertain some physical property is not new (here we define a scanning probe microscope as a system that uses a solid probe, so as to exclude scanning electron microscopy and other such techniques). However, only in the last two decades has it become possible to fabricate micron or even nanometer-scale probes and to control the position of these probes on the atomic scale. The invention by Binning *et al* (1982) of the Scanning Tunnelling Microscope (STM) was a great leap forward in the study of surfaces, allowing the imaging of detail down to atomic level. The invention of Atomic Force Microscopy (AFM) by Binning *et al* (1986) triggered an explosion in microscopy of surfaces that continues to this day. An offshoot of AFM, Magnetic force Microscopy (MFM) was first demonstrated by Martin and Wickramasinghe (1987) and has rapidly become one of the most widely used magnetic imaging techniques.

This chapter reviews briefly the history of scanning probe microscopy, leading up to the invention of MFM. The advantages and problems associated with MFM are presented along with the theory of MFM image formation. The MFM used at Glasgow is a Digital Instruments Dimension 3100 (hereafter referred to as the DI3100).

### 3.2 The SPM scanning system

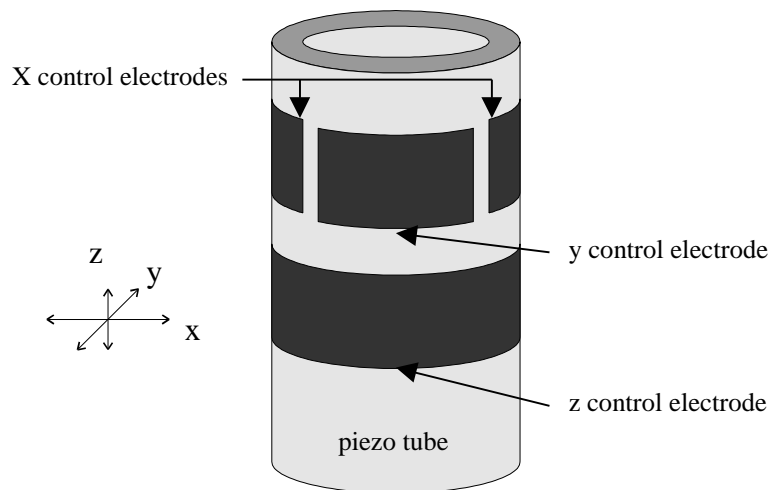
All scanning probe techniques depend on precise spatial control of a probe in three orthogonal directions. This is normally provided by piezo ceramic elements. When a voltage is applied across the piezo material it causes the material to expand or contract, depending on the sign of the voltage. The effect is small, and typically several hundreds of volts are required to cause a change of a few microns in the material dimensions. This effect can be used as the basis of a mechanical actuator that possesses a high spatial resolution.

There are two main disadvantages with the use of piezo actuators. The breakdown voltage of the material limits the total range of movement, typically to tens of microns at most. Also, the response of the material to voltage changes is hysteretic. If the piezo scanner is used in an open-loop system some characterisation of the piezo response is required to linearise the scan. The alternative is to use some form of feedback mechanism



in a closed-loop system, although the accuracy of this method naturally depends on the performance of the feedback sensors used.

The most common way to form a piezo-based scanner is to fashion the piezo material into a hollow tube (Fig. 3.1). Pairs of electrodes (on the inner and outer walls) are placed on either side of the tube. When these electrodes are biased appropriately one side of the tube expands and the other side contracts. This results in a bending of the tube, hence if one end is fixed the other end moves, resulting in the scanning motion. Two sets of electrodes 90 degrees apart allow motion in the x-y plane. A further pair of electrodes extending around the entire circumference of the tube cause an entire section of the tube to expand or contract, resulting in the free end of the tube moving parallel to the tube axis. The combination of all three sets of electrodes allows movement of the free end of the tube to be controlled very precisely in all three axes.



**Figure 3.1. Schematic of piezo tube with x, y and z control electrodes.**

There are two ways of exploiting this effect. A probe can be mounted on the moving end of the piezo tube and scanned over the sample in question. This can present difficulties when using probes that require optical detection of the parameter being measured, for example the bending of a cantilever, as the probe is a moving target. A simpler method is to mount the sample on the scanner tube and fix the probe to a stationary stage. This makes the transfer of information from the probe easier to implement, and also facilitates the design of rigid systems that have desirable resonance properties. The main drawback is that only small samples can be accommodated, as the piezo scanner cannot cope with the inertia of heavier samples. Hence when examining large (typically dimensions greater than 1cm) samples a scanned-probe design is indicated. The DI3100 is a scanned probe design, and has the capability to accommodate 8-inch wafers and samples of over 1 cm in height (although the maximum scan range of the piezo tube is  $\sim 80 \mu\text{m}$  in the xy plane and  $\sim 6 \mu\text{m}$  in the z direction). This allows a large variety of

samples to be imaged in this system, and also offers the possibility of incorporating magnetising stages or other such systems into the microscope.

Given the limited range of the piezo scanning system, most SPM systems also incorporate coarse positioning stages to position the probe over the area of interest of a sample. As mentioned previously, the DI3100 can accommodate large samples, and so a x-y translation stage is provided to move any sample area of interest under the piezo scanner. The piezo scanner is mounted in a scanning head that can move in the z direction. Stepper motors and lead screws are used to control all three of these movements with a precision of 2  $\mu\text{m}$  (for the x-y stage), or  $>0.1 \mu\text{m}$  (for the scanning head z movement).

### 3.3 Scanning Tunnelling Microscopy

The operating principle of the STM depends on the phenomenon of quantum tunnelling. This occurs when the wavefunction of an electron encounters a finite energy barrier. The wavefunction decays exponentially into the barrier region and therefore the function is non-zero at the other side of the barrier (assuming the barrier has a finite width). This results in a finite probability of the electron “tunnelling” through the barrier. This probability depends exponentially on the width of the barrier, and thus the barrier width must be very narrow to detect tunnelling currents.

In the STM, the point of a very sharp conducting needle is moved close to the surface of a (conducting) sample and a voltage bias between the two is applied, causing a tunnelling current to flow between tip and sample. The current depends on the tunnelling probability, which varies exponentially with the tip-sample distance, and so monitoring the tunnelling current gives a very sensitive indication of the tip-sample distance. Typically a bias of 1 V or less is used, resulting in a tunnelling current of a few nA when the tip-sample separation is under 1 nm. If the tip is sharp enough, there will be one atom at the tip that is slightly higher than the surrounding atoms, and it is from this atom that most of the tunnelling current originates. This is why the spatial resolution of STM is extremely high (sub-angstrom) in all three axes, which allows unambiguous imaging of surface atoms.

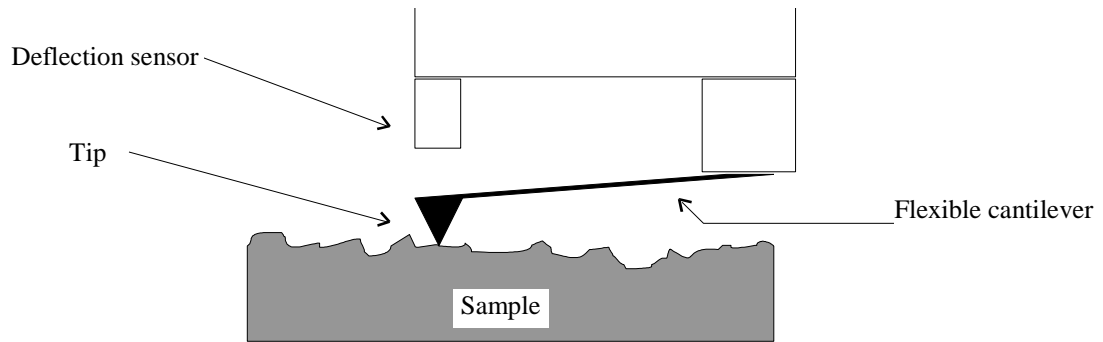
While STM is a powerful technique, there are some attendant problems. The most obvious is that the sample must be conductive, either a metal or a semiconductor. To image insulators requires coating with a layer of metal to provide the conduction path, which is of little use if the detailed surface properties are desired. While it is possible to use STM in air, most metal and semiconductor samples (and indeed the metal probe) tend to form oxide layers in air. These layers may only be a few monolayers thick, but this can be enough to necessitate dragging the tip through the oxide to bring the conductive

elements close enough to establish a tunnelling current, often damaging the tip. In addition, many samples tend to acquire a few monolayers of water in ambient conditions, which can short – circuit the tip – sample junction. For these reasons most STM imaging is performed in ultra-high vacuum conditions, with the sample preparation facilities and the STM system sharing the same vacuum system to prevent sample contamination.

It is possible to use STM for imaging magnetic samples. If the electrons in the probe are preferentially spin-polarised in one direction, the tunnelling probability will depend on the spin of the sample electrons at the surface, which depends on the magnetisation of the sample. Thus it is possible in theory to probe the magnetisation of individual surface atoms. If the probe current is polarised in one direction and then reversed, the difference between the two currents yields the component of magnetisation in that direction. The main problem with this method is controlling the spin polarisation of the probe current. One method employed by Nabhan and Suzuki (1998) is to use GaAs as the probe and illuminate it with circularly polarised laser light. The light causes the required spin majority in the conduction band of the GaAs. The polarisation direction depends on the rotation direction of the light, and thus can be reversed easily. Another method used by Bode *et al* (1999) is to use magnetic material on the probe itself (a thin coating of Fe in this case), and use an external field to magnetise the probe in the required direction prior to imaging (the sample imaged consisted of ~6 monolayers of Gd). Some results have been reported using both methods, but operational difficulties (particularly the requirement for UHV and clean samples) and difficult theoretical questions mean this type of magnetic microscopy is still in its infancy.

### 3.4 Atomic Force Microscopy

The concept of AFM is extremely simple, although the execution is often very sophisticated. A small (micron-scale) cantilever is held approximately parallel to the sample surface (Fig. 3.2). In the DI3100 the tip is held at an angle of 10° from the sample surface, to allow space for the mounting mechanism. The free end of the cantilever is shaped as a probe that interacts with the sample. The probe is normally in the form of a sharp tip (the different varieties of AFM probe are covered in section 3.5). Any force between the tip and the sample causes the cantilever to bend, and the resultant deflection is measured by some means. If the probe is brought into contact with a surface and then scanned over that surface, the profile of the surface can thus be measured with the resolution determined by the sharpness of the probe (often <10 nm).



**Figure 3.2. Diagram of basic AFM concept**

There are several methods that can be used to detect the cantilever deflection in AFM. There are three main requirements: (1) that the accuracy be high enough to detect deflections in the angstrom or even sub-angstrom range, (2) probes can be changed without requiring time-consuming realignment/calibration of the system, (3) the probe is not perturbed significantly by the measurement system. The main methods in use are discussed below.

### 3.4.1 AFM detection techniques

In a similar fashion to STM, tunnelling can be used to sense probe deflections. A small electrode similar to an STM tip is placed above the AFM probe and a bias applied between the two. The tunnelling current then is related to the probe deflection. This requires that the probe be conductive, at least along its back face. The tunnelling sensor is very sensitive, but only has a practical range of a few nanometers. Another concern is that the voltage difference applied exerts a considerable force on the cantilever. These handicaps mean that this method is not widely used.

If the back of the cantilever is approximately flat and conductive, placing another flat plate above it will form a capacitor. The capacitance will vary with the distance between the two surfaces, and can be measured using the usual methods. Again, the voltage difference between the electrodes can exert a significant force on the cantilever.

It is possible to manufacture strain gauges on the cantilever itself, allowing the strain in the cantilever to be measured directly. Obviously this means there are no alignment problems when changing probes, and sensitivity can be as high as with other methods. The downsides are that electrical connections need to be made to the probe, and the manufacturing complexity (and cost) is greater.

One popular optical technique uses laser interferometry. In this system the back of the AFM probe is used as one mirror in an optical interferometer. If the probe is deflected this has the effect of changing the path length of the interferometer arm, and hence causes fringe movement in the interference pattern. Generally the system is set up to monitor the

brightness of the central spot of the fringe pattern. This does require that when the probe is changed the system must be realigned so that the laser light hits the probe. The maximum deflection of the probe that can be measured with this system corresponds to the fully bright to fully dark transition of the central fringe spot pattern, as any further movement causes ambiguity (unless fringe counting is somehow incorporated). This corresponds to half the wavelength of the light used, meaning typically about 200 nm. Further problems arise if the probe is to be scanned, as this results in the path length changing constantly. For this reason, interferometric systems are usually found only on scanned-sample systems. An advantage over beam deflection systems (discussed below) is that the back of the probe does not necessarily have to be a perfect mirror, and thus wire probes etc. can be used. As this is an optical method, the force exerted on the cantilever is negligible. However, the focused laser light can heat up the cantilever, which can cause drift or otherwise affect the properties of the cantilever. This is not much of a problem when using typical single crystal silicon cantilevers, but if sensitive measurements in UHV conditions are required the effects of heating may cause difficulties.

The beam deflection method utilises the fact that the deflection of the AFM tip causes a change of angle at the free end of the cantilever. A beam of laser light is directed at the back of the cantilever so that the reflected beam is directed onto a split photodiode. When the cantilever bends the beam will be reflected through a different angle, causing the spot on the photodiode to move. This movement is detected by subtracting the signal from one half of the photodiode from the other half. As with the interferometric method, the laser beam must be aligned each time the probe is changed, and has the additional restriction that the back of the cantilever be flat and reasonably reflective. The advantage is that the system is very sensitive while being able to accommodate large cantilever deflections. There can also be heating problems (as with interferometric systems).

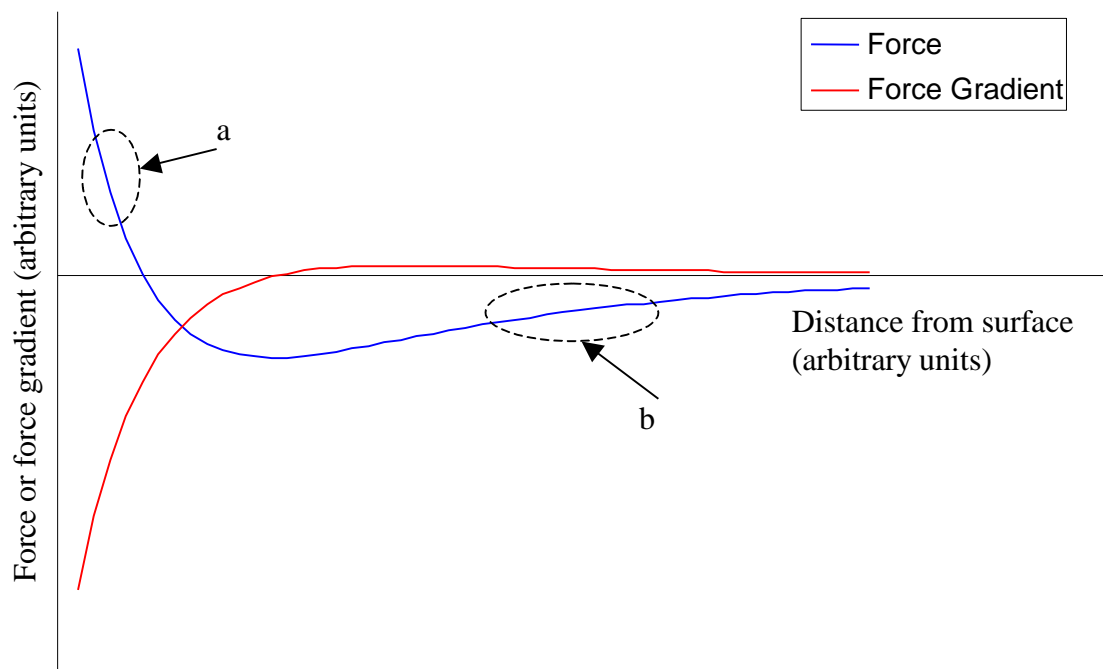
The DI3100 uses the beam deflection technique for cantilever movement detection. The beam, which is produced by a diode laser, passes down through the middle of the piezo tube to hit the back of the cantilever. The cantilever is mounted at an angle of  $\sim 10^\circ$  from the horizontal (see Fig. 3.2) and so the beam is reflected up at  $\sim 20^\circ$  to the vertical axis. A series of lenses and mirrors then steers the beam onto a quadrant photodiode. By combining the quadrant signals in different ways it is therefore possible to monitor the vertical and horizontal deflections of the reflected beam (the vertical deflection corresponds to the bending of the cantilever, while the horizontal deflection is caused by cantilever twisting).

### 3.4.2 Surface forces acting on AFM probes

As an AFM tip is brought close to a surface it experiences a total force which can be attractive or repulsive, depending on the distance and tip/surface properties. There are several components that contribute to the overall force, and the principal ones (for basic AFM) are:

- Atomic shell repulsion: Once the electron clouds of two atoms begin to overlap the Pauli exclusion principle requires that the overlapping electrons must have different quantum numbers from each other. This is achieved by increasing the energy states of some of the electrons, resulting in a repulsive force. This force is only effective over a very short range (about  $1 \text{ \AA}$ ) and increases very rapidly with decreasing interatomic distance.
- Van der Waals forces: These result from fluctuating charge distributions in the individual atoms of the surface and tip, causing transitory dipoles to be formed in the atoms. If such a dipole exists in one atom, it induces dipolar charges in other nearby atoms, and thus a force exists between them. The overall effect is an attraction between atoms, which can be effective out to a few hundreds of nm. The effect of Van der Waals forces is predominant in region *b* in Fig. 3.3.

The combination of these forces results in the force-distance graph shown in Fig. 3.3. Also shown in Fig. 3.3 is the corresponding force gradient curve.



**Figure 3.3.** Graph illustrating the form of the force and force gradient experienced by an AFM tip as a function of the tip-surface distance.

The effect of force on the tip causes the cantilever to bend, while force gradients alter the resonant properties of the cantilever (by effectively modifying the spring constant

of the cantilever). When performing AFM, the probe is usually moved close to the surface so that the tip comes into contact with the surface. This means that the main contribution to the force acting on the tip comes from the atomic shell interactions (region a in Fig. 3.3). However, if too much force is used (the tip moved too close to the surface) the surface and/or probe can be damaged, thus a compromise setting is usually used. It is also possible to image surfaces in ‘non-contact’ mode (note that this term is, confusingly, used by some literature to describe the AC imaging mode). In this case the attractive Van der Waals forces are used to track the surface geometry. In this case the cantilever actually bends towards the surface, but does not come into ‘contact’ with it (in the normal sense of the word).

In addition to these principal forces, there are other forces that may be present. In particular, when AFM is performed in ambient conditions most samples tend to acquire a few monolayers of water. When a tip encounters this water layer a meniscus can be formed between the sample and the tip, resulting in an additional attractive tip-sample force. This can significantly affect AFM measurements, and thus when attempting to measure surface properties with AFM it is important to take account of the humidity.

### 3.4.3 AFM imaging modes

There are a variety of operating modes that can be used in AFM to image surfaces. For example, the force (measured by the cantilever deflection) can be kept constant or varied during scanning. The three modes detailed here are the most common operating modes of the AFM.

*Variable deflection mode:* The simplest method of AFM imaging is to measure the deflection of the cantilever (using one of the methods detailed previously) as the tip is first brought into contact with the sample surface, and then scanned over the sample surface without changing the z position of the tip. While the simplicity of this mode makes it easy to implement there are some problems associated with it. The roughness of the surface cannot exceed the range of the deflection sensor used. This also implies that the surface must be reasonably level (i.e. within the limits of the cantilever detection system) with respect to the scanning system, particularly for large area scans (several tens of  $\mu\text{m}$ ). The force exerted on the sample surface by the tip, although small, is concentrated over an area of a few square nanometers or less. The resulting pressure can be enough to damage many softer materials, or if the sample is hard and rough the tip can be damaged. This limits the range of materials that can be studied. Also, the relation of sample height to AFM signal must be calibrated. This may only need to be done infrequently for an interferometer-based system, but a beam-bounce system must be calibrated for each new probe, as the

reflective properties of individual probes can vary. One advantage of this method is that scan rates can be higher than methods involving a feedback loop. This method is often used when attempting to obtain a lattice image of a near-atomically flat surface, where high scan speeds (tens of lines per second) must be used to counteract thermal drift.

*Constant deflection mode:* To avoid some of the problems of the variable deflection mode the z-piezo of the scanner can be used in a feedback system. The deflection signal from the probe is monitored and compared to a reference value (the *setpoint*). The error signal ( $= \text{deflection} - \text{setpoint}$ ) is calculated, and if it is non-zero the z piezo is extended or retracted, depending on the sign and magnitude of the error signal. The loop then repeats. In this case the force exerted by the tip on the sample is held nearly constant if the system is functioning properly. The signal to the z-piezo provides the measure of the sample height. This means only the z-piezo response needs to be calibrated, and the type of probe and detection system used is immaterial as long as the deflection signal from it is monotonic (and preferably linear).

Normally the setpoint is set so that the tip is in close contact with the surface, corresponding to region *a* in Fig. 3.3. As noted previously, this can damage soft samples, such as biological molecules. An alternative method is to tune the setpoint such that the tip is attracted by the surface, corresponding to region *b* in Fig. 3.3. The tip-sample force is lower and extended over a larger area in this case, so the risk of sample (or tip) damage is lower. However, the resolution is also lower in this case, as the tip is further away from the sample. This variant of the constant deflection mode is often called ‘non-contact’ mode (note that this term is, confusingly, used in some AFM literature to describe the constant gradient imaging mode described below).

*Constant gradient mode:* If the cantilever is made to oscillate at or around its resonant frequency, another imaging mode becomes possible, often referred to as AC imaging or ‘dynamic mode’. When the oscillating probe is brought near to the sample surface the tip begins to interact with the surface at the lower end of its travel (region *c* in Fig. 3.3). This dampens the oscillation, thus if the oscillation amplitude of the probe is measured the presence of a surface can be detected. In this case a feedback loop is set to maintain a constant tip oscillation amplitude, and thus the system tracks a constant force gradient surface. In this mode, tip-surface contact forces are much lower than for the DC or deflection mode case, so soft material such as biological samples can be imaged.

In an analogous fashion to the variable deflection mode, it is also possible simply to scan an oscillating probe over a surface and record the variation of the oscillation amplitude. This suffers from most of the drawbacks of the variable deflection mode, and is thus not generally used for AFM studies.



The DI3100 can operate in all of these modes described. The terms used by Digital instruments are Contact Mode (measuring the cantilever deflection) and TappingMode™ (measuring the cantilever oscillation amplitude). In both cases feedback loops are normally used (i.e. constant force or constant force gradient modes), as this means that the z-calibration of the system is independent of the tip used.

### 3.5 Probe manufacture for AFM

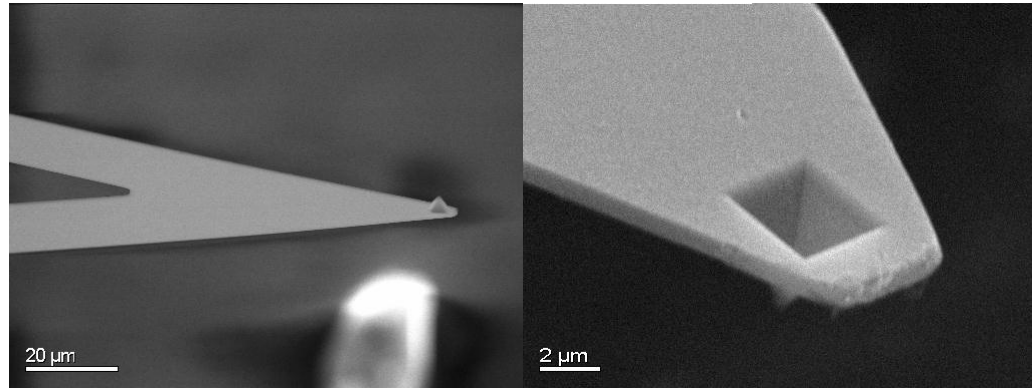
#### 3.5.1 Wire-based probes

Wire-based probes were a popular type of probe extensively used in earlier AFM studies, due to the fact that they can be made fairly simply. Typically the wire used is several tens of microns in diameter and made of Tungsten or Platinum-Iridium alloy; the main criteria being that the material is stable and resistant to oxidation. To obtain a sharp point the end of the wire is subjected to electrochemical etching, giving sharp and well-defined points. After etching, the sharp end of the wire is bent downwards, forming the AFM probe. This process can yield good tips with high aspect ratios and small tip radii [ $<30$  nm according to Rugar *et al* (1990)]. The process of etching and bending is performed manually, and thus consistency from one tip to another is usually poor. An alternative method of manufacturing wire probes is to stretch a portion of the wire to breaking point. Probe consistency is also variable using this method. Currently wire probes are used mainly for STM.

#### 3.5.2 Silicon Nitride probes

SiN probes are produced by first creating a mould by conventional lithographic techniques on a (100) oriented single-crystal silicon wafer. To define the tip, a pit is etched into the silicon through a lithographically defined square window using an anisotropic etchant such as potassium hydroxide. The sidewalls of the pit follow the (111) axes of the silicon. Silicon Nitride is then deposited into this mould and patterned to form the cantilever and tip. After a glass block is bonded to the rear end of the cantilever for handling purposes, the remaining Si is etched away, releasing the cantilever. An example of such a tip is shown in Fig. 3.4.

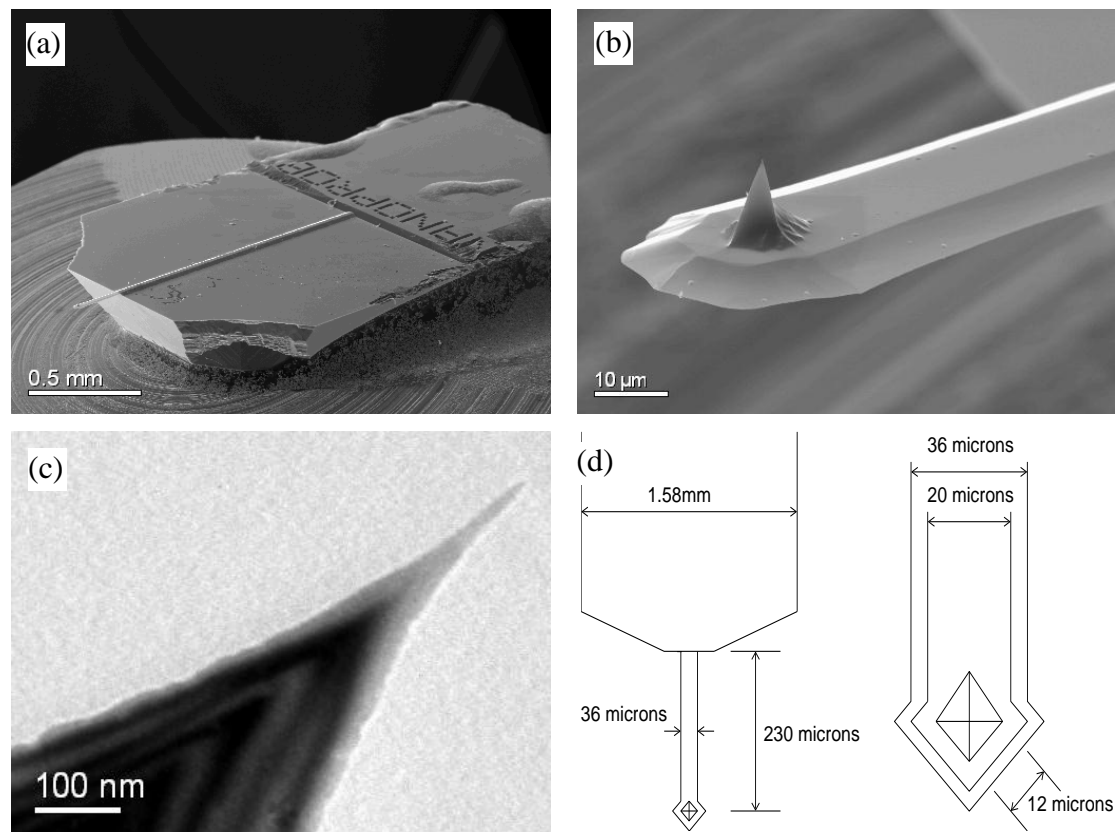
The tips produced by this method are square-based pyramids with sides that make an angle of  $45^\circ$  to the tip axis,. The tips produced by this method normally have apex radii of 20 to 50 nanometers, which is useful for lower resolution work. The production of SiN probes is covered in detail by Albrecht *et al* (1990)



**Figure 3.4.** Two views of a SiN AFM probe, showing the triangular cantilever and four-sided pyramidal tip.

### 3.5.3 Monolithic silicon probes

Using similar processes to those used in mould manufacture for SiN probes, complete probes can be fabricated directly from silicon as shown by Wolter *et al* (1990). The probes can take a variety of shapes depending on the application and the details of the manufacturing process. A typical general-purpose probe made by Nanosensors is shown in Fig. 3.5.



**Figure 3.5.** (a) SEM micrograph of probe substrate chip (DI MESP type). (b) SEM micrograph of cantilever and tip. (c) TEM micrograph of tip apex (uncoated tip). (d) Sketch of probe dimensions.

The tip is a four-sided pyramid with a (nominally) kite-shaped base. The tip radius is claimed by the manufacturer to be  $<10$  nm (when uncoated), easily small enough for all but the most demanding work. The cantilever is about  $3\text{ }\mu\text{m}$  thick,  $30\text{ }\mu\text{m}$  wide and  $225\text{ }\mu\text{m}$  long, giving a spring constant of  $1\text{--}4$  N/m and a resonant frequency of  $60\text{--}75$  kHz.

#### 3.5.4 Probe modifications for force detection

Normally, batch manufactured probes of Si or SiN are used in AFM. These are chosen for a variety of reasons. SiN and Si probes are easy to batch manufacture, and behave reasonably consistently. For basic AFM, the probes are usually used unmodified. Coating or otherwise modifying the probes can yield information on other fields or forces present, and is the main reason why AFM techniques have become so prevalent. For example, coating the probe with some hydrophobic species and scanning a sample can indicate which areas of the sample surface are hydrophobic/hydrophilic. This is one example of Chemical Force Microscopy, where the probe is coated or otherwise altered to respond to surface chemicals. Other examples include coating the probe with metal and applying a bias between it and the sample to map surface charges (Electrostatic Force Microscopy). It is this versatility that has been responsible for the rapid expansion in the use of AFM. We are mainly concerned here with another variant of AFM that allows magnetic microscopy, which is discussed below.

### 3.6 Magnetic force microscopy

If an AFM probe is made of, or coated with, a magnetic material the presence of magnetic fields from a sample will result in a force on the probe, and hence AFM can be used to detect and measure magnetic fields. This was realised soon after the invention of AFM, and is one of the first examples of the extension of AFM to measure more than just surface topography. The credit for inventing the MFM goes to Martin and Wickramasinghe (1987). MFM has rapidly become a popular technique to image surface magnetic microstructure. The spatial resolution of MFM is often quoted in the literature as  $<100$  nm. Abelman *et al* (1998) performed measurements on a variety of systems and claimed a maximum resolution (defined as the FWHM of the smallest feature seen) of  $30$  nm. Thus MFM does not have as high a resolution as Lorentz microscopy, but is certainly much better than Magneto-optical Kerr microscopy (where the resolution is limited by the wavelength of the light used). The resolution of MFM depends on the size of the magnetic probe, and also on the height of the probe above the sample. Smaller probes can yield higher spatial resolution, but at a cost of a lower signal to noise ratio. An

example of the forces involved is given by Grütter *et al* (1992). If two 10 nm particles of Fe are placed in contact with each other, the resulting force between them is  $4.9 \times 10^{-11}$  N, and the force gradient is  $1.9 \times 10^{-2} \text{ Nm}^{-1}$ . This assumes the particles are uniformly magnetised so as to maximise the force produced. The minimum force that can be detected by typical commercial AFM systems using is in the piconewton regime, and so it is possible to perform MFM using force detection methods. However, for typical cantilevers the force *gradient* sensitivity can be better than  $10^{-5} \text{ Nm}^{-1}$ , and so MFM work is normally done using the force gradient detection mode.

### 3.6.1 MFM probe types

There are a variety of ways that a MFM probe can be produced. Initially, wire probes prepared in the manner described in section 3.5.1 were used. The wire can be itself magnetic (Fe, Co or Ni) or non-magnetic but coated in magnetic material. Probes made from Ni wire are often used, as although the magnetic moment of Ni is rather lower than Fe, the resistance to corrosion is better. Etched wire probes usually have a very well defined magnetic anisotropy axis, as the large shape anisotropy of the probe supports domains oriented along the wire axis. As discussed by Grütter *et al* (1992), these tips can give good results when they are used to image samples such as hard disk media. However, the main problem with these tips is the difficulty of batch manufacture. Another problem is that these tips tend to generate a substantial stray field, which can cause problems when examining low-coercivity samples (this problem is discussed later in section 3.6.4).

As the MFM technique was refined the problems of batch manufacturing wire probes led, as with standard AFM, to the use of Si and SiN based probes. To make these probes sensitive to magnetic fields they are coated with some magnetic material, usually by sputtering or evaporation techniques. Most recent research has focused on the coating material, its thickness and the deposition method (see for example Babcock *et al*, 1994, Casey *et al*, 1999a, Heydon *et al*, 1999, Liou *et al*, 1997 and Liou and Yao, 1998). The choice of material depends on the desired probe coercivity and magnetic moment. The thickness of the material determines the magnetic moment of the tip, and often affects the coercivity as well. Other factors that can influence material choice include the resistance to oxidation (if used in air) and the wear resistance.

The coating method used can determine how much of the tip and cantilever is covered. Sputter coating results in an even coating over the entire tip, cantilever and substrate, and is the normal method used in commercial production of MFM probes. Using evaporation methods, the direction of evaporation can be chosen to coat selectively only certain facets of the tip, giving some flexibility compared to sputtering. This has been used

to advantage by Skidmore and Dahlberg (1997), for example. The microstructure of the material will depend on the coating conditions, and this can also affect the tip moment and coercivity.

Materials commonly used to coat MFM probes include Co, NiFe (Permalloy) and CoCr. Co and CoCr are used to produce probes with medium coercivity (typically around 400 Oe). CoCr is normally preferred as the resistance to oxidation is greater than for Co. NiFe coating gives a low coercivity probe. Low coercivity probes are commonly referred to as “soft” probes, and high coercivity probes are therefore termed “hard” probes. Note that these terms often refer to the probe coercivity *relative* to the magnitude of the stray field of the sample under investigation.

### 3.6.2 Basic MFM imaging theory

To simplify the analysis of MFM it is usually assumed that the cantilever is parallel to the sample surface plane, so that only the  $z$  components of the forces and/or force gradients are considered. Then according to Grütter *et al* (1992), a MFM probe in a magnetic stray field from a sample will experience a force;

$$F_z = -\mu_0 \int M_{z\_tip} \frac{\partial H_{z\_sample}}{\partial z} dV , \quad (3.1)$$

and a force gradient;

$$F'_z = -\mu_0 \int M_{z\_tip} \frac{\partial^2 H_{z\_sample}}{\partial z^2} dV , \quad (3.2)$$

where the integration is performed over the volume  $V$  of the magnetic material of the tip.  $M_{tip}$  is the magnetisation of the tip and  $H_{sample}$  is the stray field from the sample. Note that due to the principle of reciprocity, the tip and sample labels in Eqns. 3.1 and 3.2 can be switched, so that the interaction of the tip stray field with the sample magnetisation is considered. This point is considered in section 3.6.6.

In the DC imaging mode, the force  $F$  causes the cantilever to bend by an amount proportional to the force, causing a change in the signal from the cantilever deflection sensor. Hence the DC deflection signal is proportional to the convolution of the tip magnetisation with the first derivative of the sample stray field. In AC mode the probe is oscillated near the cantilever resonance frequency, usually by a small piezo stack on the probe holder. The resonant frequency with no external force gradient present is  $\omega_0$ . The presence of a force gradient will shift the resonant frequency of the probe by;

$$\Delta\omega = \omega_0 \frac{F'_z}{2k} \quad (3.3)$$

if the force gradient  $F'_z$  is small compared to the spring constant  $k$ .

This frequency shift can be measured in three ways; by monitoring the amplitude of the oscillation, the phase of the oscillation, or directly via a feedback system. As can be seen from Fig. 3.6, the amplitude of the probe oscillation changes with the resonant frequency shift when excited at a fixed frequency  $\omega_D$ . This frequency is usually chosen to be a point where the amplitude gradient  $dA/d\omega$  is large, so that changes in  $\omega_0$  will cause a large amplitude change. If the frequency  $\omega_D$  is chosen to be below  $\omega_0$  at the steepest part of the resonance curve then the resultant amplitude shift is given by

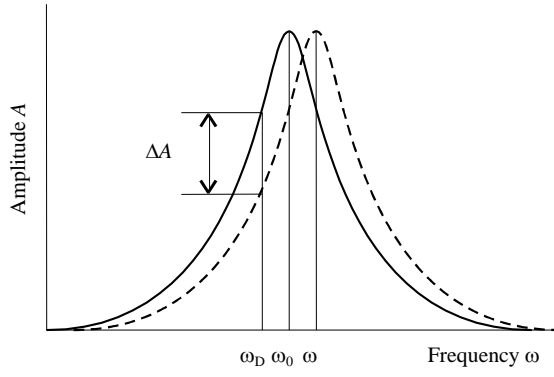
$$\Delta A = \frac{2A_D Q}{3\sqrt{3}k} F'_z \quad (3.4)$$

where  $Q$  is the quality factor of the resonance and  $A_D$  is the oscillation amplitude at  $\omega_D$ . The phase of the probe oscillation also changes rapidly around the resonant frequency. This can be measured in a similar fashion to the amplitude, again giving a signal proportional to the resonant frequency shift (Fig. 3.7). Near the resonance frequency the phase shift  $\Delta\phi$  is given by (Gomez *et al*, 1996)

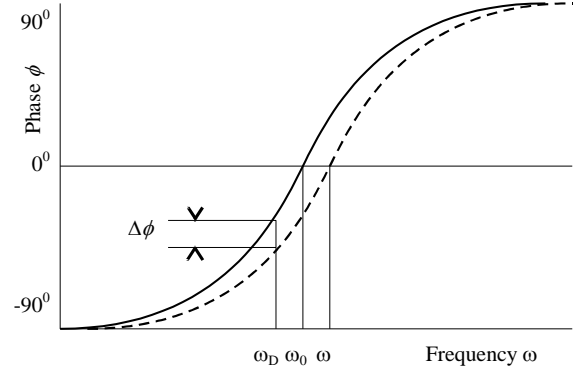
$$\Delta\phi = -\frac{Q}{k} F'_z. \quad (3.5)$$

The third measurement method utilises a feedback loop to track directly the resonant frequency shift. The amplitude (or phase) is monitored, and the driving frequency is altered to maximise the amplitude (or maintain the phase lag at a constant value), corresponding to the resonance condition.

Amplitude detection is the simplest method to implement; however phase or frequency measurements tend to be more sensitive and less susceptible to interference, and are preferred in most cases. Choosing between phase and frequency methods usually depends on the details of the hardware involved, as there is normally little difference in accuracy between the two. One factor in favour of the phase measurement method is the relative simplicity, as a simple measurement is performed. The frequency method requires a feedback loop, which introduces a little more complexity to the system. All the MFM images presented in this thesis are taken using the phase measurement method.



**Figure 3.6.** Graph illustrating the resonant frequency peak of an AFM probe. The solid curve is the oscillation amplitude vs. frequency when no external force gradient is present, while the dashed curve illustrates the effect of an external force gradient on the probe.



**Figure 3.7.** As Fig. 3.6 but with phase ( $\phi$ ) of cantilever oscillation (shifted so that phase =  $0^\circ$  at resonance)

### 3.6.3 Separation of topographic and magnetic effects in MFM

The introduction to MFM in the previous sections implicitly assumes that the magnetic tip is scanned over the surface but does not experience any of the other surface forces. This further implies that the tip is positioned far enough from the surface that the surface forces are negligible compared to the relatively long-range magnetic force (or in the case of the Van der Waals forces, to ensure that the force is reasonably constant with respect to the magnetic force). There are a variety of techniques that can be used to achieve this.

The simplest technique, at least in principle, is to engage the surface with the tip as in normal AFM, and then retract the tip by some distance and scan the area desired. The problem with this method is that the tip must be retracted far enough to avoid crashing into high points on the surface. In addition, the surface must be level and the system reasonably free from drift if accurate mapping of the stray field is to be achieved. A variant of this technique is described by Bode *et al* (1999), where AFM scans are taken around the edges of the area of interest. This data is then used to estimate the position of the sample surface in the area of interest, and the tip is scanned at a suitable height above this surface. Of course, the surface must be reasonably flat for this technique to work.

Another early technique was to control the height of the tip using a force-feedback loop similar to the surface-tracking loop used for AFM (Grütter *et al*, 1992). In this case the tip is scanned over the surface as usual, but the feedback loop setpoint is set so that the force maintained is lower than for normal AFM surface imaging. Thus the tip-sample

separation will be larger than normal, and the main contribution to the force on the tip will arise from the sample magnetic field. The result of this is a map of a surface of constant field. The main problem with this technique is the difficulty of ensuring the complete separation of magnetic and topographic contrast. In principle, this could be achieved by taking two scans, one with the magnetisation of the tip (or sample) reversed. In practice this is often difficult or impossible to achieve.

These difficulties led to the development of the LiftMode™ imaging mode, pioneered by Digital Instruments. In this mode one pass is made over the sample surface using normal repulsive-force AFM. Using the surface profile thus obtained, the tip is then retracted by a user-defined distance and the scan is repeated, with the tip height being varied to maintain a constant vertical separation between the tip and the surface. Normally this is done line-by-line, that is one line of topographic data followed by one line of data at the lift height. This is largely successful in separating the topographic and magnetic data, and is probably the most popular method in use at present.

#### 3.6.4 Interaction problems

Analysis of MFM data using Eqns. 3.1 and 3.2 is considerably simplified if the tip magnetisation is not perturbed by the sample stray field, and vice-versa. This ideal is only approached when the tip and sample susceptibilities are low. For example, imaging a hard disk track with a CoCr tip is unlikely to cause changes in the hard disk magnetisation, as the coercivities of the alloys used in hard disk media are high enough to prevent accidental erasure, and the field produced by a written track on a disk will not normally perturb CoCr alloy of 50 nm thickness (Babcock *et al*, 1994). However, using the same tip to image a soft magnetic sample such as a garnet film can cause problems, as demonstrated by Casey *et al* (1999a). The solution in this case is to use a tip with a lower stray field, either by making the magnetic film on the tip thinner or using a material with a lower magnetic moment. This unfortunately has the effect of decreasing the tip-sample force, and hence the signal.

In the case where the sample stray field approaches or exceeds the tip coercivity, there are two approaches to the problem. The most obvious method is to increase the tip coercivity by using a different coating material. There have been some results reported by Liou and Yao (1998) using CoPt tips, and an example of this type of tip is examined in Chapter 5. One obvious candidate for a high coercivity tip coating would be a NdFeB alloy. However, Gibbs (2000) reports that it has proven difficult to deposit high-quality NdFeB films onto the 3-D structure of the tip.



The other solution to the strong sample field problem is to create low-coercivity tips. The aim is for the tip magnetisation to be entirely dominated by the sample stray field, with little or no hysteresis present. The response of the tip to fields should then be predictable and not dependent on history. The disadvantage is that such a tip only gives information on the magnitude of the field or field gradient, while sign information is lost. Liou *et al* (1997) has produced tips coated with a superparamagnetic material, which consists of small (<10 nm) isolated Fe particles in a SiO<sub>2</sub> matrix and has essentially zero coercivity. Heydon *et al* (1999) have taken a different approach using an amorphous alloy (METGLAS®2605SC), and have produced tips with very low coercivity. Tips of this type are examined in Chapter 4.

### 3.6.5 MFM analysis using the point probe approximation

As indicated in Eqns. 3.1 and 3.2, to obtain quantitative information on the sample field the magnetisation distribution of the tip must be known. This is in practice a non-trivial problem, particularly with thin-film coated tips where the magnetic material extends over the entire tip and cantilever. Thus, even when assuming that there are no perturbation effects, the analysis of MFM images can be very difficult. Simplified models of tips are often used in MFM analysis; typically these models have several parameters that can be adjusted to approximate real tip behaviour. The simplest model is to assume that the tip acts as a point dipole or infinitely long dipole (i.e. effectively a monopole). For a point dipole it is found that the force and force gradient acting on the tip are

$$F_z = -\mu_0 \left( m_x \frac{\partial H_x}{\partial z} + m_y \frac{\partial H_y}{\partial z} + m_z \frac{\partial H_z}{\partial z} \right), \quad (3.6)$$

$$F'_z = -\mu_0 \left( m_x \frac{\partial^2 H_x}{\partial z^2} + m_y \frac{\partial^2 H_y}{\partial z^2} + m_z \frac{\partial^2 H_z}{\partial z^2} \right), \quad (3.7)$$

where  $m_i$  is the  $i$  component of the dipole strength (units are in Am<sup>2</sup>). As tips are normally magnetised vertically it is often assumed that  $m_x$  and  $m_y$  are zero, so  $\mathbf{m} = m_z$ , simplifying the equations considerably. In the case of a monopole the force and force gradient are

$$F_z = -\mu_0 p H_z, \quad (3.8)$$

$$F'_z = -\mu_0 p \frac{\partial H_z}{\partial z}, \quad (3.9)$$

where  $p$  is the monopole strength (in Am).

Using these point models for the tip, MFM images have been simulated for a variety of samples. The most common samples used are written data tracks in longitudinal and perpendicular magnetic media. These have been studied extensively using other methods, and can be modelled with reasonable accuracy (see for example Rugar *et al*, 1990). Other attempts have been made to characterise MFM tips using the field from micron-scale elements carrying electrical currents. The advantage of this method is that the fields (and derivatives thereof) produced by such elements can be accurately modelled. Babcock *et al* (1996) used a straight narrow current strip and analysed the response of the MFM as the probe was scanned over the strip to assign a dipole moment to the tip. Kong and Chou (1997) used lithographically defined current rings to fit a combined point monopole and dipole model to the tip response. Lohau *et al* (1999) later expanded on this work. However, using data on tip stray fields obtained by electron tomography, McVitie *et al* (2001) have demonstrated that point models have some limitations when applied to thin-film MFM tips. There are however some exceptions to this generalisation, such as the field ion beam milled tips studied in Chapters 5 and 6.

### 3.6.6 MFM analysis using reciprocity and the charge formulation

Wright and Hill (1995) observed that due to the principle of reciprocity, it is possible to switch the tip and sample labels in Eqns. 3.1 and 3.2, so that the force is due to the interaction between the tip stray field and the sample magnetisation. There are several advantages to this interpretation of the problem. The resolution of the system can be defined as the width (normally the full width at half maximum, or FWHM) of the stray field peak from the tip (or of the stray field gradient, depending on the imaging mode). Knowledge of the tip magnetisation, which is extremely difficult to obtain, is not required, instead the stray field distribution from the tip needs to be measured. This can be done using Lorentz electron tomography, as discussed in Chapter 2.

Hubert *et al* (1997) demonstrated that the tip-sample force can be interpreted in terms of magnetic poles in the sample, as these are the sources of stray field. The presence of magnetic poles is due to the divergence of the magnetisation in the sample (volume charges) and the intersection of the magnetisation with the sample boundaries (surface charges). As a result, Eqn. 3.1 can be rewritten as

$$F = \int_A \sigma_{sample} H_{tip} dA + \int_V \rho_{sample} H_{tip} dV ; \quad (3.10)$$

the integrations being performed over the surface  $A$  and the volume  $V$  of the sample. The volume charge of the sample is defined as

$$\rho_{sample} = -\nabla \cdot \mathbf{M}_{sample}, \quad (3.11)$$

and the surface charge is

$$\sigma_{sample} = \mathbf{M}_{sample} \cdot \mathbf{n}, \quad (3.12)$$

where  $\mathbf{n}$  is the surface normal vector. MFM can therefore be viewed as a form of charge microscopy, with the signal produced by the convolution of a probing function (the tip stray field or derivatives thereof) with the magnetic charges in the sample. This greatly facilitates the interpretation of MFM images. It should again be emphasised that if tip-sample perturbation effects are not negligible, the analysis becomes non-trivial.

### 3.6.7 Deconvolution of sample charge distribution

If the probe or response function of an MFM tip is known and the magnetisation of the sample is assumed to be invariant through its thickness, it is possible in principle to deconvolve the image to recover the actual magnetic charge distribution in the sample. Chang *et al* (1992) showed that this can be done quite simply in Fourier space. Consider the formation of the MFM image in real space. This involves a convolution of the MFM response function (the field or field gradient distribution) with the sample charge distribution

$$M(x, y, z) = C(x, y) \otimes A(x, y, z) \quad (3.13)$$

where  $C$  is the sample charge distribution averaged through the sample thickness,  $A$  is the tip response function,  $M$  is the MFM image and  $z$  is the tip-sample separation. In Fourier space this can be expressed as

$$\tilde{M}(k_x, k_y, z) = \tilde{C}(k_x, k_y) \cdot \tilde{A}(k_x, k_y, z). \quad (3.14)$$

Note that the Fourier transform is 2-dimensional, therefore only the  $x$  and  $y$  axes are transformed. The  $\sim$  denotes the Fourier transformed equivalents of  $M$ ,  $C$  and  $A$ . When Eqn. 3.14 is rearranged we find that

$$\tilde{C}(k_x, k_y) = \frac{\tilde{M}(k_x, k_y, z)}{\tilde{A}(k_x, k_y, z)}. \quad (3.15)$$

Hence the charge distribution  $C$  can be calculated using

$$C(x, y) = FT^{-1}[\tilde{C}(k_x, k_y)] = FT^{-1}\left[\frac{\tilde{M}(k_x, k_y, z)}{\tilde{A}(k_x, k_y, z)}\right]. \quad (3.16)$$

Note that in this case the charge distribution is only unique if the sample is two-dimensional, or if the charge is assumed to be invariant through the thickness of the sample. Vellekoop (1998) points out that given a field distribution above the surface of a three-dimensional sample it is possible to construct any number of charge distributions to generate that field. However, the magnetisation of a sample can in principle be reconstructed if some assumptions are made about the sample magnetisation, and if some additional information is available. This is discussed in the next section.

### 3.6.8 Magnetisation reconstruction from MFM and DPC data

Assuming that no free currents are present, the field from a magnetic sample can be written as

$$\mathbf{B} = \mu_0(\mathbf{H} + \mathbf{M}) \quad (3.17)$$

where  $\mathbf{B}$  is the magnetic induction,  $\mathbf{H}$  is the magnetic field strength and  $\mathbf{M}$  is the magnetisation of the sample. Now consider the special case where the magnetisation of the film is parallel to the plane of the film everywhere, and does not vary through the thickness of the film. If the in-plane vector components are denoted using the subscript  $\parallel$ , Eqn. 3.17 can be rearranged to form

$$\mathbf{M}_{\parallel} = \frac{\mathbf{B}_{\parallel}}{\mu_0} - \mathbf{H}_{\parallel}. \quad (3.18)$$

At this point we recall Maxwell's Equations, which for a sample with no free currents present can be written as

$$-\nabla \cdot \mathbf{H} = \nabla \cdot \mathbf{M}, \quad \nabla \cdot \mathbf{B} = 0, \quad (3.19a)$$

$$\nabla \times \mathbf{B} = \mu_0 \nabla \times \mathbf{M}, \quad \nabla \times \mathbf{H} = 0. \quad (3.19b)$$

Thus in Eqn. 3.18 the magnetisation of a sample is divided into divergence-free ( $\mathbf{B}_{\parallel}/\mu_0 = \mathbf{M}_{\parallel}$ ) and curl-free ( $-\mathbf{H}_{\parallel}$ ) components. Now if the sample is in the form of a film in the x-y plane and the magnetisation of the film does not vary through the film thickness

and is constrained to lie in-plane (i.e. only volume magnetic charges are present) then it can be then shown that

$$\mathbf{M}_{\parallel} t = \frac{1}{\mu_0} \int_{-\infty}^{\infty} \mathbf{B}_{\parallel} dz - \int_{-\infty}^{\infty} \mathbf{H}_{\parallel} dz \quad (3.20)$$

where  $t$  is the thickness of the magnetic sample (Beardsley, 1989). The divergence-free component involving  $\mathbf{B}_{\parallel}$  can be measured directly using Lorentz microscopy, as discussed in Chapter 2. The other component involves the curl-free  $\mathbf{H}_{\parallel}$ , which is directly related to the magnetic charge distribution. As stated in the previous section, the charge distribution of the sample can be calculated from MFM images if the MFM response function is known (Eqn. 3.16). To calculate the integrated curl-free  $H_x$  from the charge distribution we use

$$\int_{-\infty}^{\infty} H_x dz = FT^{-1} \left[ \frac{k_x}{i(k_x^2 + k_y^2)} \tilde{C}(k_x, k_y) \right], \quad (3.21)$$

and similarly for  $H_y$ . For an example of this see Mayergoyz *et al* (2001), although in this case the field sensor was a magnetoresistive read head, rather than an MFM tip.

Equations 3.20 and 3.21 imply that if we have DPC and MFM images of a sample, and we know the MFM response function, then it is possible in principle to reconstruct completely the in-plane magnetisation of the sample. Note that this only applies where only volume magnetic charges are present. If surface charges are also present (that is, a vertical component of magnetisation exists) it is still possible in principle to extract the magnetisation distribution. However, in this case MFM measurements above *and* below the sample are required, which in practice poses a formidable problem. It is also important to remember that the above analysis only yields the average magnetisation through the sample thickness, and thus is most useful for samples where the magnetisation does not vary with  $z$ . In the case of permalloy, for example, this implies a maximum thickness of  $\sim 30$  nm to ensure that only Neél walls are present.

To demonstrate this technique a numerical simulation was done by Wdowin *et al* (1998). The sample simulated was a small section of hard disk material, written with a longitudinal data track. DPC and MFM images were simulated using this model, and the authors then demonstrated that it was possible to use the data to reconstruct the magnetisation pattern with reasonable fidelity, so long as care is taken to filter out noise during the deconvolution process. An experimental study was done by Casey *et al* (1999b) of hard disk data tracks, where both TEM and MFM images of the same sample area were

obtained. However, no attempt was made to do a magnetisation reconstruction, probably because of the problems associated with spatially matching the TEM and MFM data.

### 3.7 Further uses of MFM

Although it is normally desirable that the tip and sample should not perturb each other in MFM, useful data can be obtained when such perturbations take place. In particular, the stray field from an MFM tip can be used to probe the effects of magnetic field on a sample, on a point-by point basis. Two such techniques are briefly reviewed here.

#### 3.7.1 Magnetic Dissipation Microscopy

As stated previously, it is desirable in most cases to ensure that the MFM tip and sample do not perturb each other. If the sample is affected by the tip stray field, artefacts can appear in the MFM image, such as domain walls suddenly jumping to different positions on different scan lines. If the tip is oscillating this can cause cyclic perturbations in the sample. If these perturbations are hysteretic, energy will be dissipated in the sample and this energy loss can be measured by monitoring the amplitude of the tip oscillation. This technique has been pioneered by Proksch *et al* (1999).

The opposite case, of the sample perturbing the tip, would appear to be of less utility (except where ultra-soft tips are used). It has been suggested by Hubert *et al* (1997) that dissipation in the tip might explain the origin of anomalous fine-scale (of the order of 20 nm or less) contrast in MFM images of permanent magnet materials, for example in the images obtained by Al-Khafaji *et al* (1996). Thus the appearance of sharp contrast features in MFM images should normally be interpreted with great care.

#### 3.7.2 Magnetoresistance Sensitivity Mapping

Write heads used to write magnetic media generate a stray field that can interact with a magnetic probe, and so MFM can be performed in the normal fashion on these heads. In contrast, read heads are designed to respond to changes in magnetic field (inductive heads) or the field itself (magnetoresistive heads). The performance of inductive read heads can be characterised by measuring the stray field produced when a current is sent through the device. Due to the different mechanism involved, magnetoresistive (MR) heads cannot be characterised in this fashion. To measure the response of MR heads, a MFM probe is scanned over the pole tips in the normal manner and the signal from the MR element is monitored. The MFM probe acts simply as a

localised field source, and as an AFM probe to correlate the pole tip topography with the MR response signal, thus mapping the sensitivity of the sensor on a point-by-point basis. This variant of MFM is termed Magnetoresistance Sensitivity Mapping (MSM). For an example of this technique see Song *et al* (1999).

### 3.8 Scanning Hall Probe Microscopy

The Hall effect occurs when a current flowing in a conductor passes through a magnetic field at right angles to the current. Due to the Lorentz effect a force acts on the moving electrons, directed at right angles both to the direction of current flow and the field direction. As the electrons are confined inside the conductor, the result is a voltage difference between the sides of the conductor. This is called the Hall voltage, and measuring this voltage gives a measure of the field acting on the conductor. Using standard lithographic techniques it is possible to fashion Hall probes of micron size or smaller. For example, Howells *et al* (1999) describe a system with a spatial resolution of 250 nm. Scanning these probes over a sample with an SPM system therefore gives a sensitive measure of one component of the stray field (the component direction depends on the orientation of the Hall sensor). This has the distinct advantage that it is a non-perturbative technique, as there is no field produced by the sensor (neglecting the field from the sensing current). The main drawback is that currently the resolution is limited to a few hundred nm, as this is the minimum size of the Hall sensor. Zhou *et al* (1999) have demonstrated functional Hall probes of 100 nm size, and indicate that the size can potentially be reduced to 50 nm. However, no data obtained with these probes has been published to date.

### 3.9 Conclusions

Scanning probe microscopy is a useful and highly versatile addition to the field of microscopy. MFM has proven to be a popular way to image magnetic samples, particularly samples which cannot be thinned to electron transparency but require characterisation on a scale of tens of nm. It has been demonstrated that MFM cannot by itself elucidate the magnetisation of a magnetic sample. However, using MFM together with Lorentz microscopy does, in principle, allow recovery of the complete magnetisation distribution of some types of thin film samples. In other cases it is likely that MFM imaging will form an important experimental test for micromagnetic simulations, especially in the case of semiconductor devices that incorporate small magnetic elements. One of the main challenges of MFM is to find an accurate and simple technique to

characterise MFM tips, preferably in the microscope itself. It has been suggested that a well-characterised hard disk track would form a useful standard reference sample for MFM. Rice *et al* (1997) have created such a sample and have characterised it using scanning electron microscopy with polarisation analysis (SEMPA). An example of this sample has been used extensively to characterise the tips in Chapter 4. The main problem with this sample type is that there is a limit to the width of transitions that can be written using normal inductive write heads in current magnetic media, and thus other types of samples are required if a demonstration of high resolution is needed. For example, magnetic multilayer systems used in magneto-optical data storage have been used as a potential high-resolution standard, as discussed by Abelman *et al* (1998). The work presented here suggests that it may be possible to use a well-modelled thin film to characterise MFM tips, and this seems a promising path to follow in future work. For example, van Schendel *et al* (2000) have used a multilayer thin film with strong perpendicular anisotropy as a model system, which allowed them to simulate what the MFM image should be. Using this they derived a tip response function that agreed well with the work done by McVitie *et al* (2001).

## References

- Abelman L, Porthun S, Haast M, Lodder C, Moser A, Best M E, van Schendel P J A, Stiefel B, Hug H J, Heydon G P, Farley A, Hoon S R, Pfaffelhuber T, Proksch R and Babcock K (1998), "Comparing the resolution of magnetic force microscopes using the CAMST reference samples", *J. Magn. Magn. Mater.*, **190**, 135-147
- Albrecht T R, Akamine S, Carver T E and Quate C F (1990), "Microfabrication of Cantilever Styli for the Atomic Force Microscope", *J. Vac. Sci. Technol. A.*, **8**, 3386
- Al-Khafaji M A, Rainforth W M, Gibbs M R J, Bishop J E L and Davies H A (1996), "The effect of tip type and scan height on magnetic domain images obtained by MFM", *IEEE Trans. Magn.*, **32**, 4138 - 4140
- Babcock K L, Elings V B, Shi J, Awschalom D D, Dugas M (1996), "Field-dependence of microscopic probes in magnetic force microscopy", *Appl. Phys. Lett.*, **69**, 705-707
- Babcock K, Elings V, Dugas M, Loper S (1994), "Optimization of Thin-Film Tips for Magnetic Force Microscopy", *IEEE Trans. Magn.*, **30**, 4503-4505
- Beardsley I A (1989), "Reconstruction of the Magnetization in a Thin Film by a Combination of Lorentz Microscopy and External Field Measurements", *IEEE Trans. Magn.*, **25**, 671-677



- Binning G, Quate C F and Gerber C H (1986), “Atomic Force Microscope”, *Phys. Rev. Lett.*, **56**, 930-933
- Binning G, Rohrer H, Gerber C H and Weibel E (1982), “Surface Studies by Scanning Tunnelling Microscopy”, *Phys. Rev. Lett.*, **49**, 57-61
- Bode M, Dreyer M, Getzlaff M, Kleiber M, Wadas A and Wiesendanger R (1999), “Recent progress in high-resolution magnetic imaging using scanning probe techniques”, *J. Phys.: Condens. Matter.*, **11**, 9387-9402
- Bradbury D L, Folks L and Street R (1998), “Interpretation of low-coercivity tip response in MFM imaging”, *J. Magn. Magn. Mater.*, **177** part 2, 980-981
- Casey S M, Lord D G, Grundy P J, Slade M and Lambrick D (1999a), “Single layer and multilayer tip coatings in magnetic force microscopy”, *J. Appl. Phys.*, **85**, 5166-5168
- Casey S M, Hill E W, Miles J J, Sivasamy P, Birtwistle J K, Middleton B K, Rose J and Chapman J N (1999b), "A study of recorded bit patterns using TEM and MFM", *J. Magn. Magn. Mater.*, **193**, 470-473
- Chang T, Lagerquist M, Zhu J and Judy J H (1992), “Deconvolution of Magnetic Force Images by Fourier Analysis”, *IEEE Trans. Magn.*, **28**, 3138-3140
- Digital Instruments, Veeco Metrology Group, 112 Robin Hill, Road Santa Barbara, CA 93117
- Gibbs M R J (2000), *private communication*
- Gomez R D, Burke E R and Mayergoyz I D (1996), “Magnetic imaging in the presence of external fields: Technique and applications (invited)” *J. Appl. Phys.*, **79**, 6441-6446
- Grütter P, Mamin H J and Rugar D (1992), “Magnetic Force microscopy (MFM)”, in: *Scanning Tunnelling Microscopy II*, ed. by Güntherodt HJ and Wiesendanger R, Springer-Verlag, Berlin), Chapter **5**, 151
- Heydon G. P., Rainforth W. M., Gibbs M. R. J., Davies H. A., McVitie S., Ferrier R. P., Scott J., Tucker J. W. and Bishop J. E. L. (1999), “Preparation and characterisation of a new amorphous tip coating for application in magnetic force microscopy”, *J. Magn. Magn. Mater.*, **205**, L131 – 135
- Howells G D, Oral A, Bending S J, Andrews S R, Squire P T, Rice P, de Lozanne A, Bland J A C, Kaya I, Henini M (1999), “Scanning Hall probe microscopy of ferromagnetic structures”, *J. Magn. Magn. Mater.*, **197**, 917-919
- Hubert A, Rave W and Tomlinson S L (1997), “Imaging magnetic Charges with Magnetic Force Microscopy”, *Physica Status Solidi B*, **204**, No.2, 817-828

- Kong L and Chou S Y (1997), “Study of magnetic properties of magnetic force microscopy probes using micronscale current rings”, *J. Appl. Phys.*, **81**, 5026-5028
- Liou S H and Yao Y D (1998), “Development of high coercivity magnetic force microscopy tips”, *J. Magn. Magn. Mater.*, **190**, 130-134
- Liou S. H., Malhotra S. S., Moreland J., Hopkins P. F. (1997), “High resolution imaging of thin-film recording heads by superparamagnetic magnetic force microscopy tips”, *Appl. Phys. Lett.*, **70**, 135 – 137
- Lohau J, Kirsch S, Carl A, Dumpich G and Wassermann E F (1999), “Quantitative determination of effective dipole and monopole moments of magnetic force microscopy tips”, *J. Appl. Phys.*, **86**, 3410-3417
- Martin Y and Wickramasinghe H K (1987), “Magnetic Imaging by Force Microscopy with 1000-Å Resolution”, *Appl. Phys. Lett.*, **50**, 1455-1457
- McVitie S, Ferrier R P, Scott J, White G S and Gallagher A (2001), “Quantitative field measurements from magnetic force microscope tips and comparison with point and extended charge models”, *J. Appl. Phys.*, **89**, 3656-3661
- Nabhan W and Suzuki Y (1998), “Ferromagnetic domains imaging with a spin-polarized STM using GaAs tips”, *Appl. Phys. A*, **66**, S101-105
- Proksch R, Babcock K and Cleveland J (1999), “Magnetic dissipation microscopy in ambient conditions”, *Appl. Phys. Lett.*, **74**, 419-421
- Rice P, Russek S E, Hoinville J, Kelley M (1997), “Optimizing the NIST magnetic imaging reference sample”, *IEEE Trans. Magn.*, **33**, 4065-4067
- Rugar D, Mamin H J, Guethner P, Lambert S E, Stern J E, McFadyen I and Yogi T (1990), “Magnetic Force Microscopy – General Principles and Application to Longitudinal Recording Media”, *J. Appl. Phys.*, **68**, 1169-1183
- van Schendel P J A, Hug H J, Stiefel B, Martin S and Guntherodt H J (2000), “A method for the calibration of magnetic force microscopy tips”, *J. Appl. Phys.*, **88**, 435-445
- Skidmore G D and Dahlberg E D (1997), “Improved spatial resolution in magnetic force microscopy”, *Appl. Phys. Lett.*, **71**, 3293-3295
- Song D, van Ek J, Amin N, Mao S N, Louder D, Schultz A (1999), “Magnetization in a spin valve head mapped by an MFM tip”, *IEEE Trans. Magn.*, **35**, 667-670
- Vellekoop B, Abelman L, Porthun S and Lodder C (1998), “On the determination of the internal magnetic structure by magnetic force microscopy”, *J. Magn. Magn. Mater.*, **190**, 148-151

- Wdowin M, Miles J J, Middleton B K and Aziz M (1998), "Magnetization reconstruction from differential phase contrast Lorentz microscopy and magnetic force microscopy", *IEEE Trans. Magn.*, **34**, 2324-2333
- Wolter O, Bayer Th and Greshner J (1991), "Scanning Force Microscopy with Micromachined Silicon Sensors", *J. Vac. Sci. Technol. B.*, **9**, 1353-1362
- Wright C D and Hill E W (1995), "Reciprocity in Magnetic Force Microscopy", *Appl. Phys. Lett.*, **67**, 433-435
- Zhou H, Mills G, Chong B K, Midha A, Donaldson L and Weaver J M R (1999), "Recent progress in the functionalization of atomic force microscope probes using electron-beam nanolithography", *J. Vac. Sci. Technol. A*, **17**, 2233-2239

## Chapter 4. Physical and magnetic properties of METGLAS coated MFM tips

### 4.1 Introduction

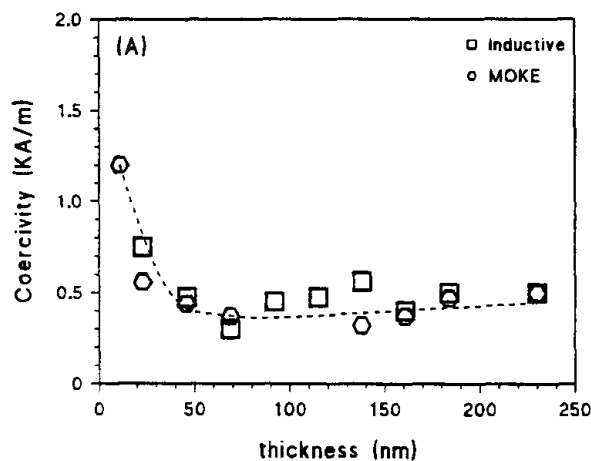
One problem encountered when imaging samples which have large ( $>0.5$  T) stray fields, such as hard disk writing heads, is that it can be difficult to find a MFM tip with a high enough coercivity to ensure that the tip is not significantly affected by the sample field. An alternative approach is to use a low coercivity tip, where the tip magnetisation aligns with the sample field. The ideal tip coating would be (super)paramagnetic in nature with zero hysteresis. The use of one type of superparamagnetic material, consisting of nanometer sized Fe particles embedded in a SiO matrix, has been investigated by Liou *et al* (1997). Other low coercivity materials such as Permalloy ( $\text{Ni}_{80}\text{Fe}_{20}$ ) have also been tried. These coatings do result in low coercivity tips which are useful in high field situations. The main problem with all of these materials is that they are crystalline in nature, and will have one or more crystallites at the tip apex. The orientation of these crystallites (and hence the magnetocrystalline anisotropy) will be difficult to control, causing inconsistencies between different tips. One solution to these problems is to use an amorphous material, which should possess a more consistent coating behaviour and will have zero magnetocrystalline anisotropy. One material which possesses these properties is the amorphous FeBSiC alloy METGLAS<sup>®</sup>2605SC, and the use of this material to coat MFM tips forms the subject of this chapter.

The physical and magnetic properties of the METGLAS alloy are discussed in section 4.2. Fresnel contrast microscopy is used to examine the magnetic behaviour of the METGLAS films in section 4.3. The physical structure of the METGLAS coated tips is examined using TEM in section 4.4, and the behaviour of the tips under applied field is covered in section 4.5 using differential phase contrast (DPC) microscopy. The stray fields from some of these tips are reconstructed using tomographic techniques (section 4.6) and the implications for MFM imaging are discussed. MFM images of a standard sample taken using METGLAS tips are shown in section 4.7 to illustrate the “real world” performance of these tips. Section 4.8 concludes with an evaluation of the advantages and disadvantages of METGLAS coated tips.

## 4.2 Physical and magnetic properties of METGLAS

The type of alloy used in these studies is called METGLAS®2605SC with composition  $\text{Fe}_{81}\text{B}_{13.5}\text{Si}_{3.5}\text{C}_2$ . This alloy is normally produced in ribbon or bulk form, and possesses high permeability and minimal hysteresis. To produce thin films to coat MFM tips, the material is obtained by sputtering from a melt-spun ribbon target. Heyderman *et al* (1995) and Shearwood *et al* (1996) showed that the sputtered material possesses low inherent coercivity in thin film form and is of an amorphous nature, similar to the original ribbon form. The coercivity of these films was found to depend on the film thickness, decreasing slowly with thickness down to ~40 nm, and then increasing rapidly below 40 nm (Fig. 4.1). It should be emphasised that these figures are for continuous planar films; patterning or deposition on tips would be expected to change the hysteretic properties due to the effects of shape anisotropy.

Despite being amorphous the material can possess uniaxial anisotropy, which can be induced by the presence of magnetic fields during the material deposition. It is thought by Ali *et al* (1998) that the magnetron in the sputtering system can generate enough field at the specimen to have this effect, and they suggest that in future studies a magnetising sample stage should be placed in the sputter chamber to produce a well-defined field direction, and thus a well-defined anisotropy in the material.

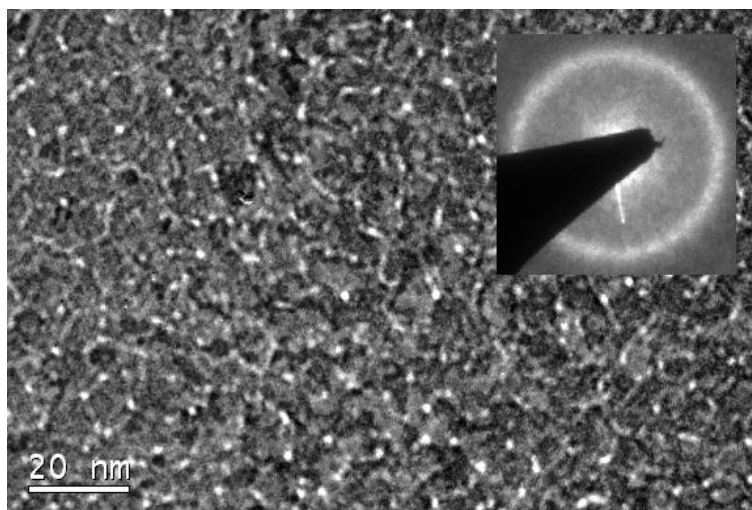


**Figure 4.1.** Measurement of METGLAS coercivity versus film thickness along the film easy axis. This data from Shearwood *et al* (1996).

The material studied in this chapter was produced by sputter coating by Dr Heydon at Sheffield University (Heydon *et al*, 1999 and Scott *et al*, 1999). The sputter target was a 150 mm diameter disc of METGLAS alloy. The target-substrate distance was 60 mm, and the sputtering conditions were 0.5 Pa Ar pressure and  $4.2 \text{ kW/m}^2$  power density. To produce very low-coercivity MFM tips, the thickness of the sputtered film should preferably be above 40 nm. However, the resolution of MFM tips generally varies with thickness, hence a thin coating is desirable. It was decided that a range of coatings with

different thicknesses should be produced and evaluated using MFM and Lorentz electron microscopy to try to determine the best coating thickness to use. To check the thickness of the films, glass slides were partially masked and were coated along with the tips, the mask being removed subsequently. The resulting step at the edge of the deposited film was then imaged by AFM and the height difference measured. One point to note is that in principle a sputter system should coat all surfaces evenly regardless of surface orientation. An MFM tip is however a fairly complex shape (see Chapter 3), so it is possible that the coating may not be entirely uniform and hence the film on the tip may well be thinner than the film measured on the glass slide. This point is examined in section 4.3 using TEM imaging.

An initial batch of MFM tips and SiN window substrates were coated with METGLAS of 10, 30 and 50 nm thickness. The physical and magnetic properties of the films were initially measured at Sheffield University, and X-ray diffraction was used to confirm that the films were amorphous. The magnetic properties were determined using MOKE, and this confirmed that the easy axis coercivity  $H_c$  of the films was of the order of 1-2 Oe when deposited on silicon. The MOKE data also showed that field required to rotate the magnetisation from the easy to the hard axis ( $H_k$ ) varied between ~10 to 20 Oe. As the research progressed some tips coated with 70 and 100 nm of METGLAS were produced, although no films were deposited on SiN windows for these thickness films. A TEM image and diffraction pattern from a 30 nm thick film are shown in Fig. 4.2. There is some structure evident in the micrograph, and it is thought this arises from the columnar growth of the film during deposition (Shearwood *et al*, 1996).



**Figure 4.2.** Bright field TEM image and (inset) diffraction pattern of a 30 nm thick METGLAS film sputtered onto a 50 nm thick SiN membrane.

Lorentz microscopy studies were done with the films deposited on the SiN windows mentioned above. These samples were investigated using the Fresnel imaging mode in the CM20, with the objective lens current set to produce a vertical field of a few tens of Oersteds. Using a tilt-rotate rod to hold the samples allowed the samples to be

rotated, therefore allowing the direction of the in-plane field component to be varied. Tilting the samples varied the magnitude of the in-plane field component.

### 4.3 Fresnel imaging of METGLAS films

#### 4.3.1 Measurement of anisotropy and coercivity

To check for the presence of magnetic anisotropy, the films were magnetised using the objective lens field in the CM20 while the Fresnel image of the sample was observed (The procedure is described in Chapter 2). The film was saturated in one direction and then the field was slowly reversed. The point at which domain walls first appeared was recorded, as a rough indication of the coercivity. The films were cycled in this manner for a few magnetisation loops, and this was done for a range of magnetisation directions. This allowed the confirmation of the presence of uniaxial anisotropy, and the direction of the easy axis. The results indicated that all the films possess uniaxial anisotropy. The points at which the films began to switch direction (field applied along the easy axis) are given in Table 4.1. These figures will of course be slightly smaller than the actual coercivity values.

Film thickness	Switching begins (Oe.)	$H_c$ (MOKE data, Oe)	$H_k$ (MOKE data, Oe)
10	2.4	1.5	9
30	8.4	1.7	7
50	4.9	1.5	15

**Table 4.1.** The points at which the magnetisation in the METGLAS samples begins to switch in the easy axis direction, measured using Fresnel imaging. The field values are the in-plane field components. Also shown for comparison are the values for  $H_c$  and  $H_k$  measured by MOKE at Sheffield.

It can be seen that these values are on average somewhat higher than those measured by MOKE, especially in the case of the 30 nm film. The reason for this is unclear, but there are two factors that will influence the TEM experiment. As noted previously, the in-plane field is produced by tilting the samples in a vertical field produced by the objective lens of the CM20. The field is usually set at a value that switches the film at tilt values between 0 – 20° (in all these experiments the value of the field was set at 24 Oe). Consequently, there is a component of field perpendicular to the plane of the film that can be many times larger than the in-plane component as the film is switching, and the presence of this component may well influence the switching mechanism.

Another point to consider is that the MOKE experiments were performed using sample films that were deposited onto silicon substrates, while the TEM samples were deposited on SiN windows. It is likely that the interfacial stresses would be somewhat different for these two sample substrates, and given the high magnetostriction (Ali *et al*, 1998) of METGLAS this could result in different magnetic properties. However, it should be noted that the coercivities of the TEM samples are still very low in absolute terms (comparable to Permalloy thin films, for instance).

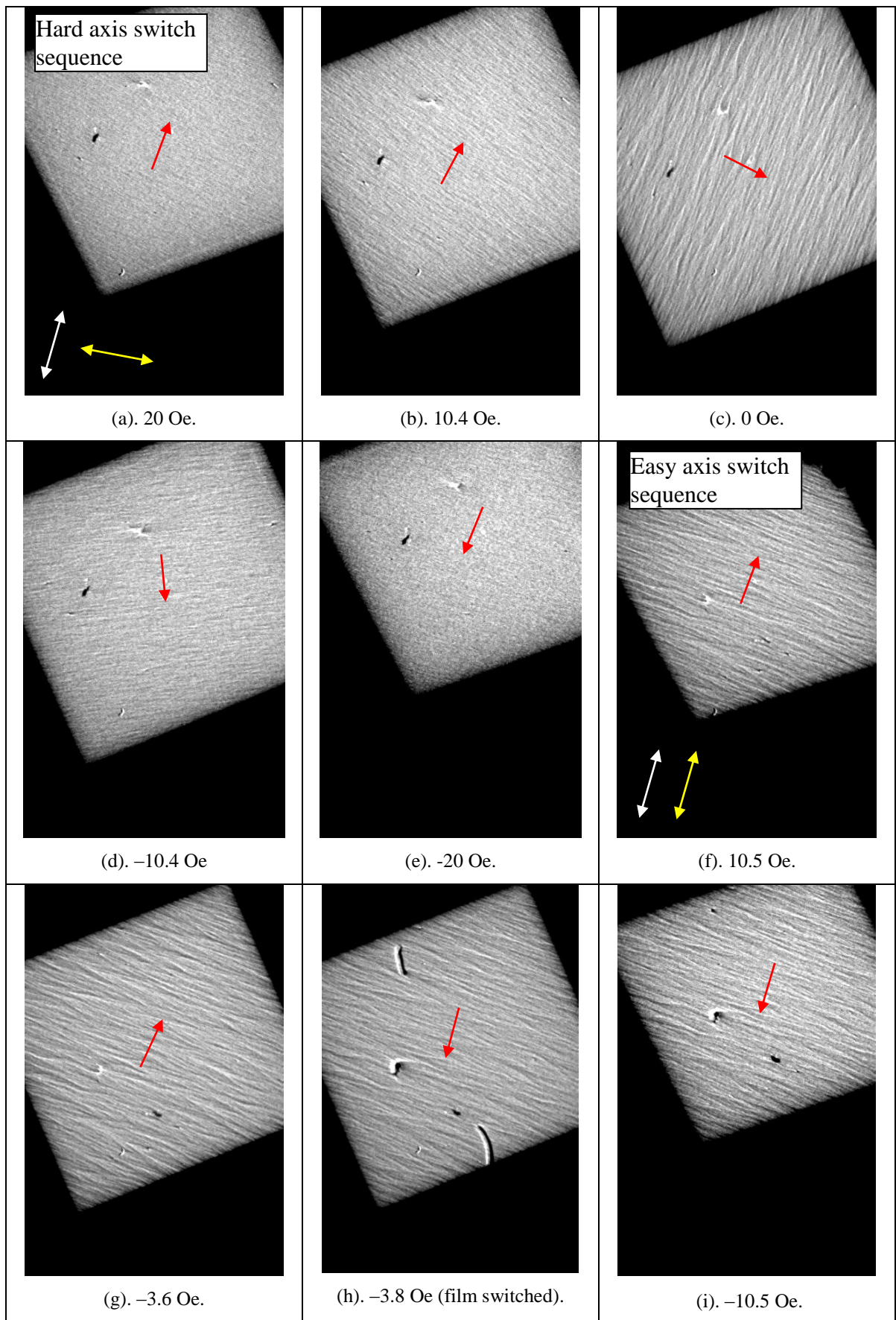
#### 4.3.2 Magnetisation processes in METGLAS films

Once the presence of uniaxial anisotropy in the films was confirmed, Fresnel images were taken for each film as the magnetising field was varied. Sequences were taken for fields applied in both the hard and easy axis directions. Selected images from these sequences are shown below in Figs. 4.3 to 4.5. When the field was applied along the easy axis direction, reversal of the magnetisation occurred by a single wall sweeping rapidly through the film. In some cases the motion of the wall was so rapid that it was not possible to catch it on camera, although it could be seen by close observation. Hence most of the images shown are of hard axis magnetisation sequences.

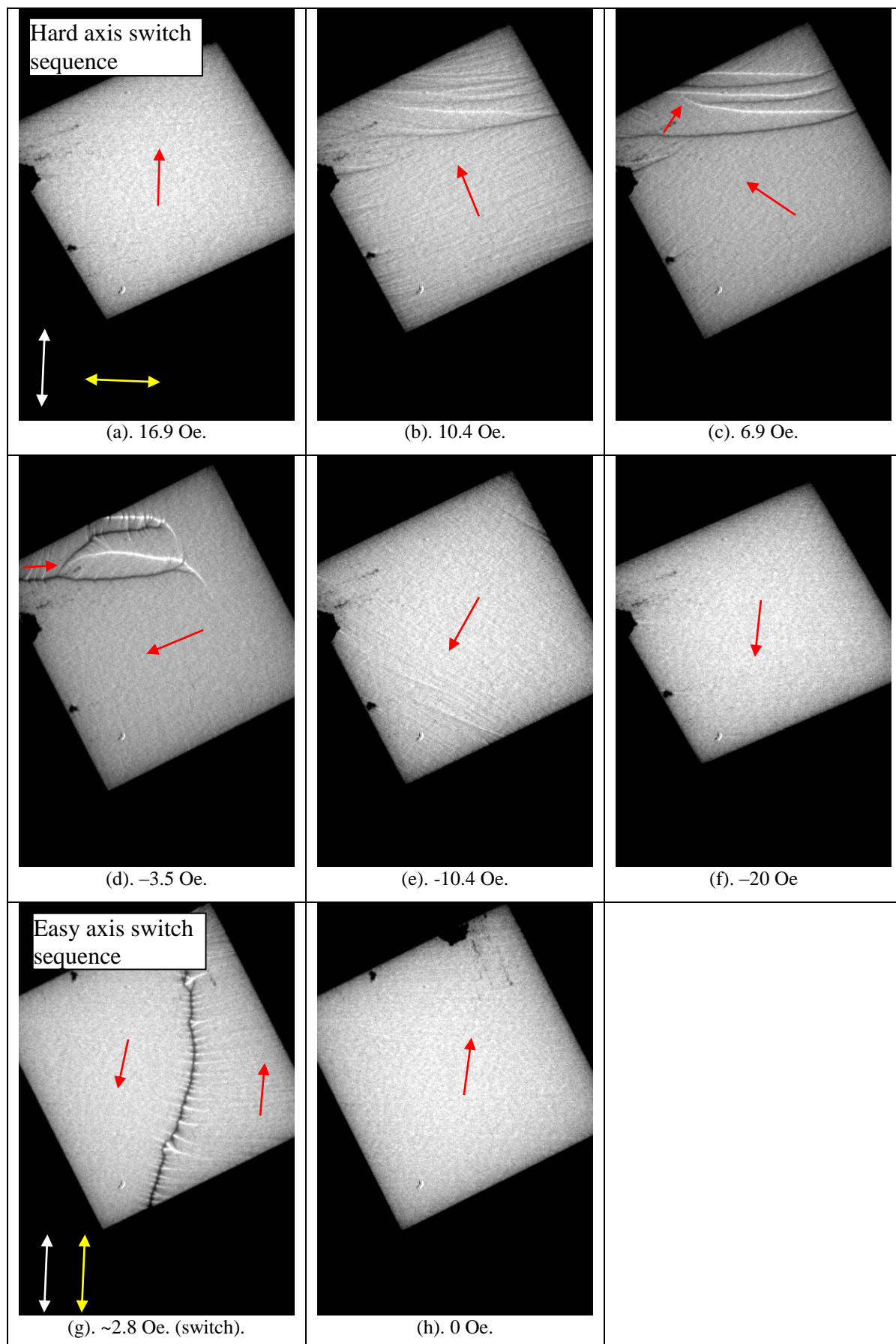
The magnetising sequence for the 10 nm thick METGLAS film was first done with the field applied parallel to the hard axis (Figs. 4.3a – e). In this case it can be seen that the magnetisation of the film rotates smoothly, passing through the easy axis at zero field. No distinct domain walls are observed anywhere in the sequence. There is a large amount of magnetisation ripple present at the zero field position, but this decreases with applied field. When a field of 20 Oe (in-plane) is applied the ripple almost vanishes. The uniform contrast at this point is only broken at inclusions in the film, which cause the magnetisation to deviate from homogeneity. The high dispersion of the film as observed here was also noted by Heyderman *et al* (1995).

The experiment was then repeated with the sample rotated by 90°, so that the applied field is parallel to the easy axis (Figs 4.3 (f) – (i)). The behaviour of the film in this case is markedly different due to the anisotropy. After saturation in one direction, the magnetisation remains parallel to the easy axis as the field is reversed. At the switching point, which is at ~2.5 Oe, a single domain wall oriented parallel to the applied field direction sweeps across the film very rapidly, and the magnetisation of the film is reversed in one step. This wall appeared to be a simple 180° wall rather than a cross-tie type, but due to the short observation time it is not possible to state this with complete confidence. After the switch a few 360° walls are visible. These walls are anchored by inclusions in the film, and eventually collapse when higher fields are applied.

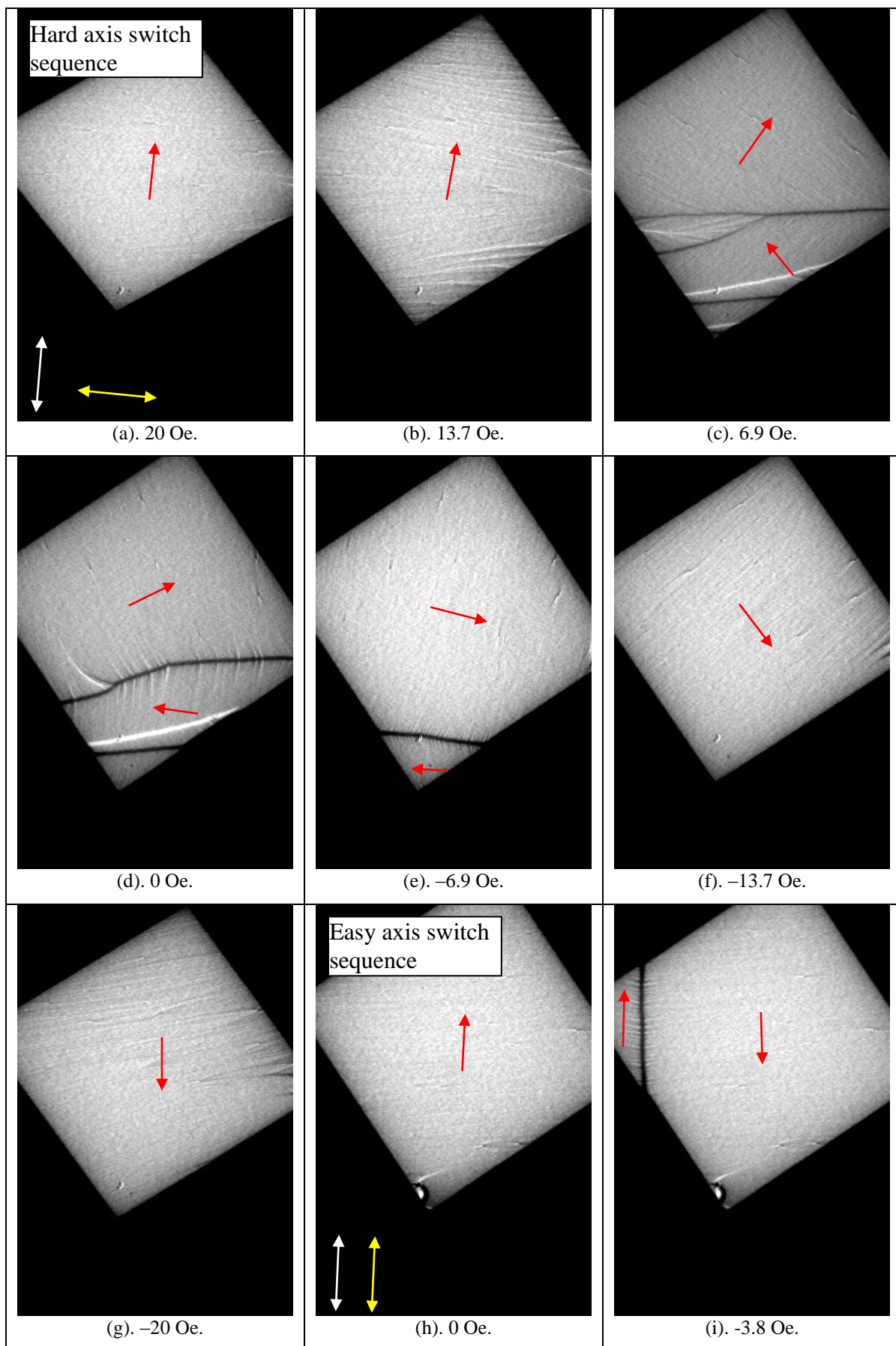




**Figure 4.3.** Fresnel images showing 10 nm thick METGLAS film undergoing magnetisation reversal for field applied (a) – (e) perpendicular to the easy axis and (f) – (i) parallel to the easy axis. The white arrows show the direction of applied field, the yellow arrows show the easy axis direction and the red arrows show the magnetisation direction. Due to the speed of the easy axis switch, only representative images before and after the switch are displayed.



**Figure 4.4.** Fresnel images showing 30 nm thick METGLAS film undergoing magnetisation reversal for field applied (a) – (f) perpendicular to the easy axis and (g) – (h) parallel to the easy axis. The white arrows show the direction of applied field, the yellow arrows show the easy axis direction and the red arrows show the magnetisation direction.



**Figure 4.5.** Fresnel images showing 50 nm thick METGLAS film undergoing magnetisation reversal for field applied (a) – (g) perpendicular to the easy axis and (h) – (i) parallel to the easy axis. The white arrows show the direction of applied field, the yellow arrows show the easy axis direction and the red arrows show the magnetisation direction.



The 30 nm film (Fig. 4.4) behaves slightly differently from the 10 nm film. The hard axis magnetisation sequence proceeds mainly by rotation but some domain formation is involved. As the field is reduced from saturation there is a marked increase in ripple contrast (Fig. 4.4b). This ripple structure coalesces into a domain pattern, and the ripple contrast greatly decreases (Fig. 4.4c). The magnetisation of the domains is oriented close to the easy axis direction. As the field is reduced further the magnetisation rotates towards the easy axis direction, until at zero field a complex domain structure forms, separated by  $180^\circ$  walls. Increasing the field eventually causes the unfavourable domains to collapse (Fig. 4.4e), and thereafter the magnetisation continues to rotate closer to the field direction as the field magnitude is increased.

The switching mechanism for the easy axis direction in the 30 nm film is similar to the 10 nm film, in that a single  $180^\circ$  wall sweeps rapidly through the film as the opposing field is increased. In this case the wall was pinned at several points, and thus it was possible for us to obtain an image of the wall. As can be seen in Fig. 4.4g, this wall has a complex cross-tie structure along its entire length.

The 50 nm thick film (Fig. 4.5) behaved similarly to the 30 nm film for both hard and easy axis magnetisation loops. Again, the easy axis switch was very rapid, and so only one image of part of the switching wall was imaged. Again, this proved to be a complex cross-tie wall.

All these experiments were performed using an objective lens field of 24 Oe, consistent with the requirement that the film magnetisation be saturated at  $\sim 30^\circ$  tilt. It was observed that the switching mechanism altered when higher (about 40 Oe) objective fields were used. Specifically, the increase in field caused the magnetisation reversal to proceed mainly by rotation, even at the easy axis position. This suggests that if an in-plane magnetising stage was used to provide the external field, rather than the microscope objective lens, the results might be slightly different from what is presented here.

#### 4.4 TEM studies of METGLAS tips

TEM studies of some of the METGLAS tips were performed to evaluate the physical structure of the tip coatings. This was done for tips coated with (nominally) 30 and 50, and 100 nm thick films (the single example of a 10 nm tip we possessed was found to be too badly damaged to obtain any meaningful results). It should be noted that tips will be referred to as 30, 50, 100 nm tips etc., even though the actual thickness of the tip coating may be slightly different from these values.

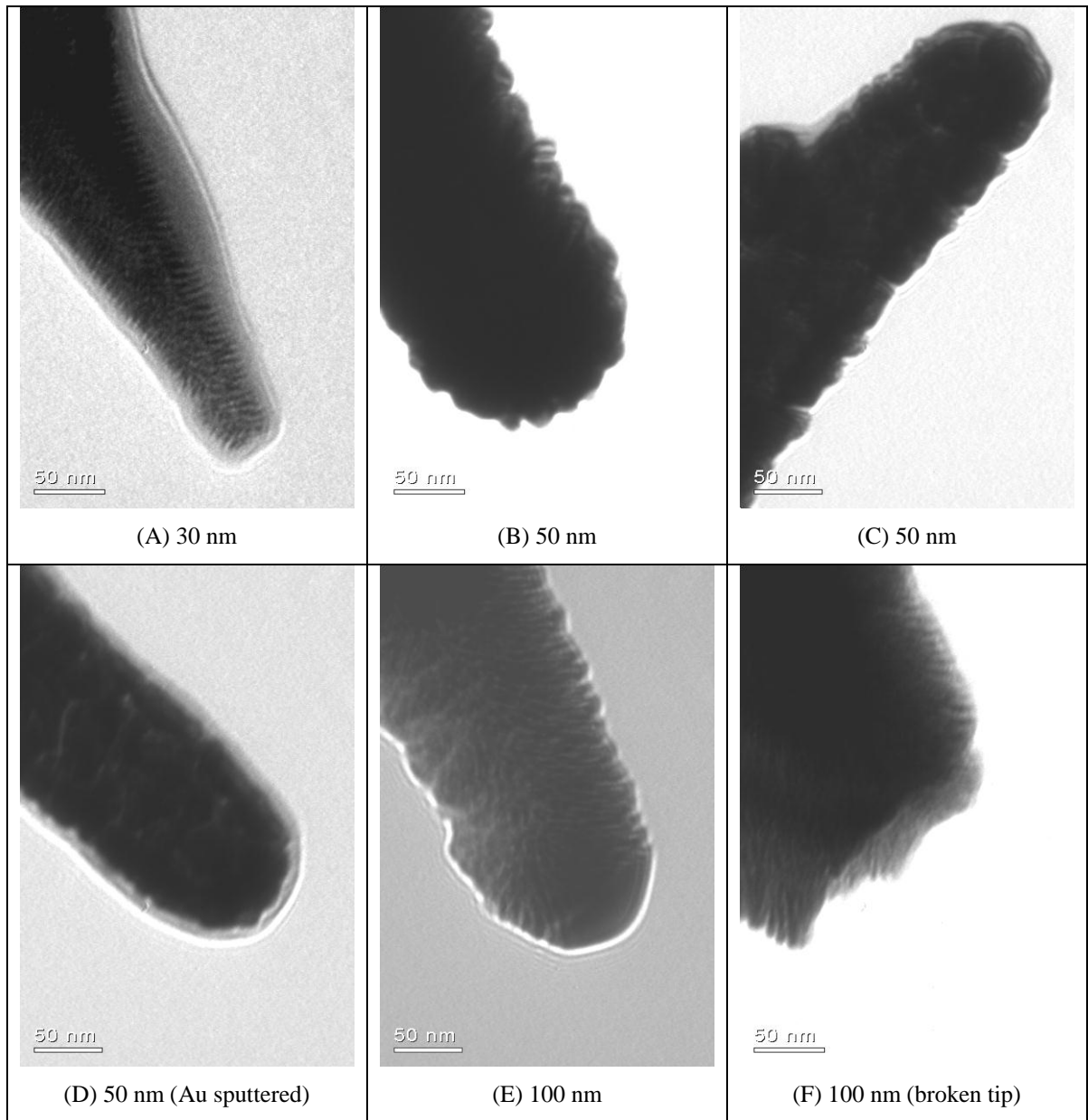
Images were taken at various magnifications. It can be seen (Fig. 4.6) that all the tips are similar in shape, the main differences occurring at the tip apex. For all the tips it

can be seen from the images that the coating is quite even, and has a uniform texture on the tip sides and apex. As expected, there is no obvious crystalline phase present. There are some differences in texture between the tips, however. The films on the 50 nm tips (B), (C) and (D) seem to be slightly lumpy in character, more so in the (B) tip than the (C). The third 50 nm tip (D), appears smoother, but this tip has been sputter coated with a few nm of gold. In comparison, the 30 and 100 nm tips have a smoother surface and a distinctly different texture. In both, the film seems to possess a columnar structure perpendicular to the surface of the film, with feature sizes ranging from 5 to 8 nm. It is possible that this may indicate how the film grows during deposition, although why this should occur for the 30 and 100 nm films, but not the 50 nm films, is unclear. The tip radii measured from these images are given in Table 4.2.

Tip	Film thickness (nm)	Tip radius (nm)	Tip radius as percentage of film thickness
(A)	30	25	83
(B)	50	80	160
(C)	50	50	100
(D)	50	50	100
(E)	100	65	65
(F)	100	N/A	N/A
Uncoated tip	N/A	<10	N/A

**Table 4.2.** Table showing the tip radii measured from the tips shown in figure 4.6. Also shown is the tip radius expressed as a percentage of the thickness of the film deposited on the tip. Note that the tip radius for the uncoated tip is quoted from the manufacturer's specifications.

It is interesting that the 30 and 100 nm tips possess tip radii somewhat smaller than would be expected for a simple isotropic coating model. The 50 nm tips are perhaps more in line with expectations. The difference in behaviour mirrors the difference in film texture between the 50 nm and 30/100 nm tips. The cause of this difference is not clear, but is probably to do with the precise conditions in the sputter system during film deposition. A much larger number of samples would have to be measured to give a true indication of the typical tip radii encountered, but the general observations about the film texture are probably valid for other tips coated in the same way. This is supported by the MFM studies carried out by Heydon *et al* (1999), where tips coated with the same thickness of film behaved similarly when imaging in the MFM. Results from these studies are presented and discussed in section 4.7.



**Figure 4.6.** TEM images of the apexes of some of the METGLAS coated tips. (A) is a 30 nm tip, (B) and (C) are two 50 nm tips, (D) is a 50 nm tip additionally coated with a few nm of Au, (E) and (F) are 100 nm tips [note that (F) is broken at the apex]. Also note the contamination on the tip apex in (D). Note that tip (A) is used for the switching experiments in Section 4.5.1, and also for the tomographic reconstructions in Section 4.6.2. Tip (D) is examined in section 4.6.3.

#### 4.5 DPC studies of METGLAS tip response to external field

The magnetisation of an ideal soft MFM tip should be dominated by the stray field of the sample in the MFM, and so it useful to measure the response of such tips to external fields. As demonstrated previously, the METGLAS films used to coat the tips have small, but finite coercivities and can also possess uniaxial anisotropy. When deposited on the MFM tip the effects of shape anisotropy will also become apparent, especially at the tip apex where the tip dimensions are comparable to the film thickness. The combination of these effects might be expected to complicate the response to external fields to a

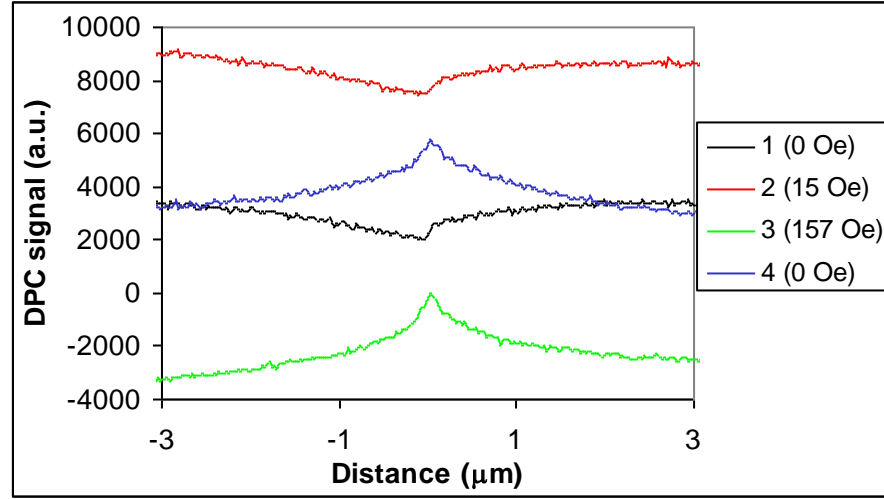
considerable degree. In particular, the shape anisotropy of the MFM tip will generally increase the coercivity of the tip compared to that of the flat film, as shown by Babcock *et al* (1996) and Carl *et al* (2001). Knowledge of the response of the MFM tip to applied fields is therefore desirable.

Tips mounted for tomographic imaging in the CM20 are positioned such that the tip axis makes an angle of  $10^\circ$  with the microscope goniometer rotation axis (see Chapter 2 Fig. 2.11). It is therefore possible to rotate the sample such that the tip axis makes an angle of  $80^\circ$  with the microscope optic axis. The microscope objective lens is used to generate a field parallel to the optic axis, causing a small component of field to act along the tip axis. This is similar to the method used to magnetise the thin films studied previously. The difference here is that the angle of the tip is held constant, and altering the objective lens current varies the field. For these METGLAS tips, the fields required were small enough that the objective lens excitation was very low, and hence the effect on the DPC imaging was minimal. It was found that the scan field was hardly affected in scale or rotation, and translational effects were small. The main effect was to shift the focal plane slightly, which could be easily compensated by refocusing.

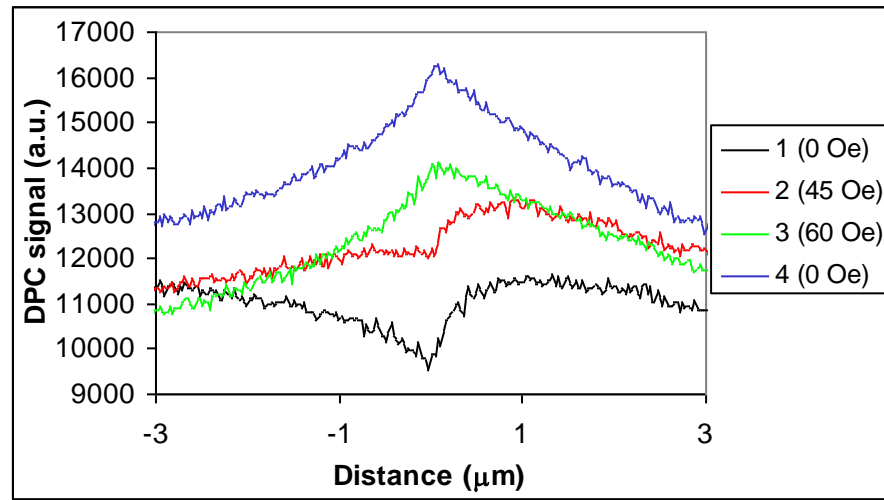
To monitor the effect of the applied field in real time, the tip apex was first centred on the CRT displays. The scan pattern of the microscope was then changed to a single horizontal line (that is, scanning along the x axis). The tip apex was then adjusted to a position as close as possible, but not touching, the scan line. The DPC linetraces were then monitored on the oscilloscopes as the field was slowly changed. Normal DPC images of the tip were recorded at various intervals in this process. Using this procedure, image sequences were obtained as the field was varied between positive and negative values sufficient to switch the tip magnetisation.

#### 4.5.1 30 and 50 nm tips

The DPC line traces from just above the tip apex were monitored as the objective lens field was increased and a reversal of the tip stray field parallel to the tip axis could clearly be observed on the oscilloscopes. It was found that the stray field of the 30 nm tip switched direction when the magnitude of the field was about 150 Oe (the component of field acting along the tip axis was therefore about 26 Oe). The 50 nm tip was switched at about one third of this value (50 Oe vertical, 8.5 Oe along the tip axis). Of course the component of field acting in the direction perpendicular to the tip axis is considerable and is expected to have a significant effect on these soft magnetic films. Even so it would appear that the shape anisotropy is still strong enough in the 30 and 50 nm thick films to support a net magnetisation along the tip axis. Switching events are shown in Fig. 4.7.



(a) 30 nm tip.

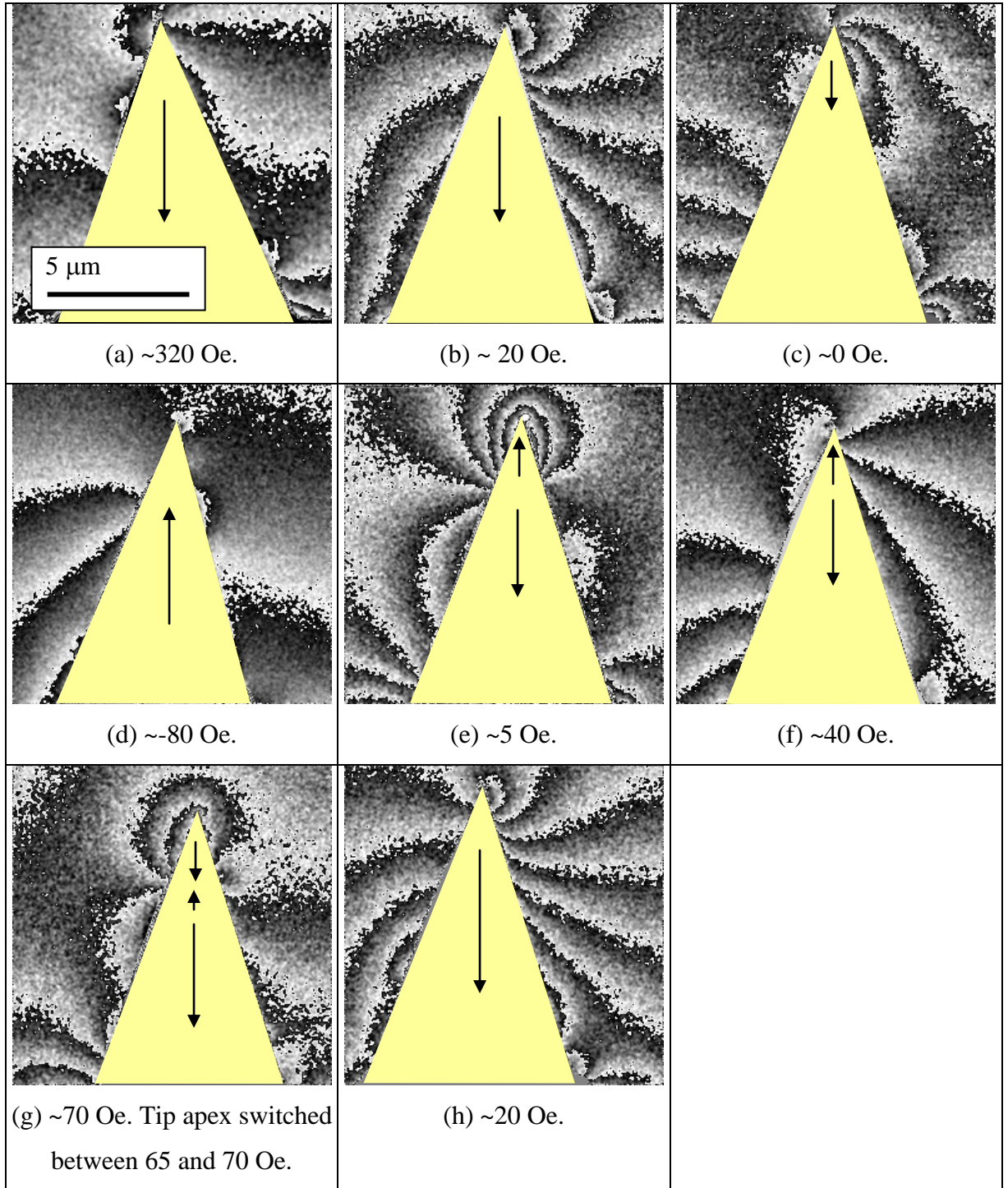


(b) 50 nm tip.

**Figure 4.7.** DPC linetraces showing the form of the  $y$  integrated field component just ahead of the tip apex as the tip is switched by the objective lens field. (a) is the 30 nm tip and (b) is the 50 nm tip.

The 30 nm tip was also imaged at low magnification while the field was applied. To show the results the magnitude of the DPC vector was calculated using the two orthogonal DPC component images. The resulting image is then displayed using a “pseudo-contour” colourmap, which results in a contour image of the integrated field (Fig. 4.8). This shows that there seem to be two main configurations of the tip magnetisation. In a few of the images (Figs. 4.8e, g and possibly c) there appears to be a clear indication of a domain of approximately 2  $\mu\text{m}$  in length at the tip apex, while the rest of the tip seems to be in a multi-domain state (judging by the field distribution along the edges of the tip). The other images would appear to indicate that the tip magnetisation is fairly uniform, apart from some small (1-2  $\mu\text{m}$ ) domains near the base of the tip.





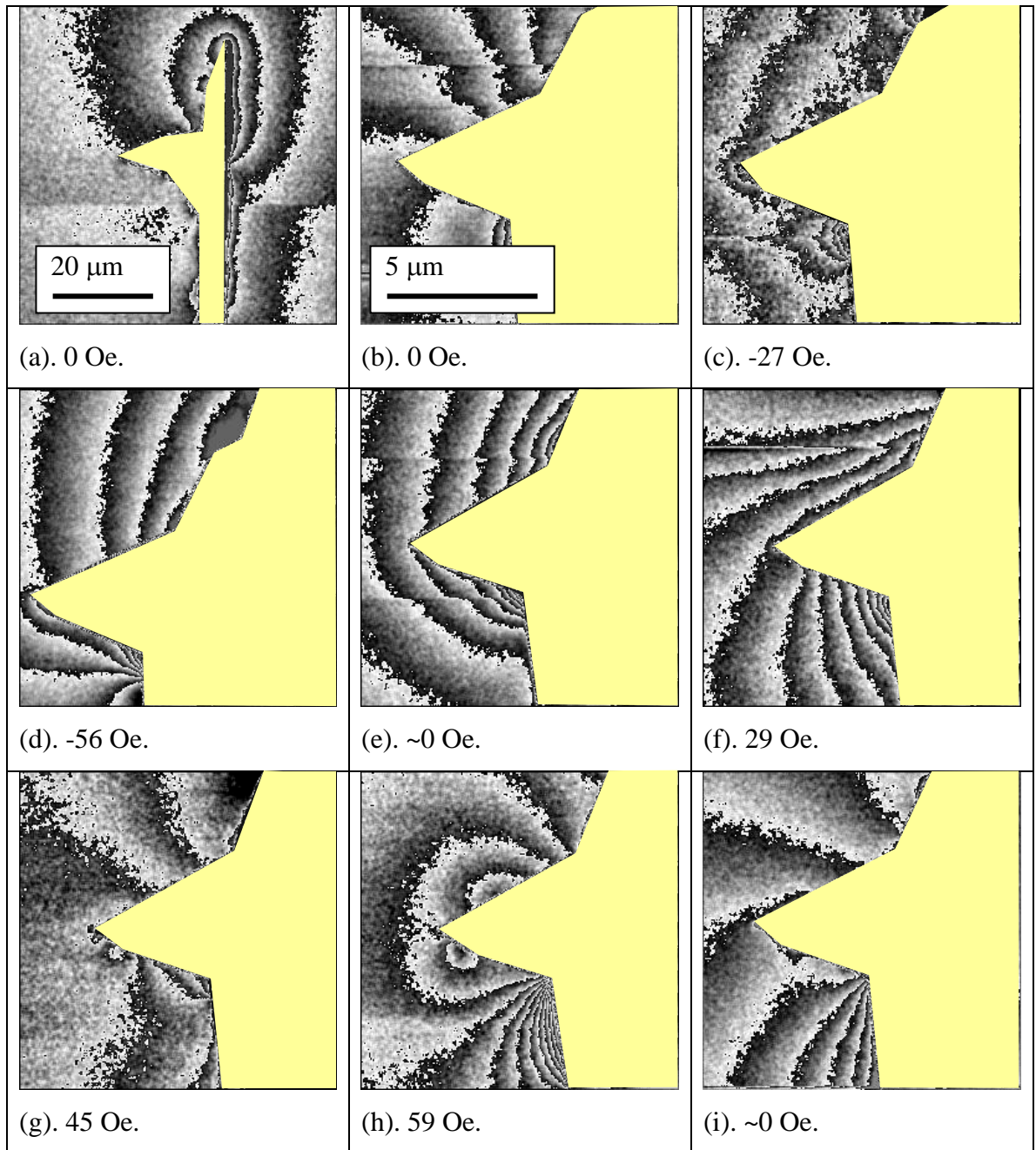
**Figure 4.8.** DPC images showing integrated field distribution around a 30 nm tip as the objective field is changed. These images represent the magnitude of the integrated field, displayed using a pseudo-contour colour scheme to illustrate the integrated field contours. The figures displayed are the values of the vertical field applied to the tip, the apex of which makes an angle of  $80^\circ$  to the field. The Yellow areas are the tip itself, and the arrows indicate the inferred magnetisation state of the tip.

#### 4.5.2 70 and 100 nm tips

The switching experiments were tried for the 70 and 100 nm tips. In both cases when the field was applied at  $80^\circ$  to the tip axis there was no observable magnetic field in the tip axis direction. Small fields (perhaps an order of magnitude smaller than observed with the 30 and 50 nm tips) were observed that did not change in magnitude or sign with applied field, and so could be identified as electrostatic in origin. Even when the objective field was set to zero after magnetising the tips, no magnetic signal from either tip was observed.

Another 70 nm tip was mounted on a flat sample stub with the cantilever pointing along the rotation (y) axis, allowing the optic-tip axis angle to be varied from  $0^\circ$  to  $90^\circ$  (see Chapter 2 Fig. 2.10). Of course, rotating the sample too far meant that the tip would be obscured by the cantilever. It was found that angling the tip at  $45^\circ$  allowed a reasonable portion of the tip to be observed, while still applying the field in a direction much closer to the tip axis than in the previous experiments. To give an overview of the tip, low magnification images of the tip were taken (Fig. 4.9).

The results of this experiment are rather inconclusive. Most of the images show a field from the cantilever (Fig. 4.9a), but very little from the tip. There does appear to be evidence of axial tip magnetisation in Fig. 4.9d, g and particularly h (at the tip apex). However, when the field is reduced to zero there appears to be no tip-specific field at all (Fig. 4.9b, e and i). It seems likely that this tip, in common with the first 70 nm tip, forms some type of flux closure structure in the absence of an external field. This is probably also true of the 100 nm tip. It also seems likely that when field is applied the magnetisation of the tip follows the field direction even for small fields, hence there is little DPC contrast (as the field and hence the tip magnetisation are directed along the z axis).



**Figure 4.9.** DPC images showing integrated field distribution around a 70 nm tip as the objective field is changed. These images represent the magnitude of the integrated field, displayed using a pseudo-contour colour scheme to illustrate the integrated field contours. The figures displayed are the values of the vertical field applied to the tip, the apex of which makes an angle of  $45^\circ$  to the field (apart from (a), where the tip axis is perpendicular to the field).

#### 4.6 Tomography of METGLAS tips

Following on from the Lorentz microscopy performed above, the next stage in the investigation was to study the different thickness tips in an axially magnetised state using electron beam tomography. As noted previously, the DPC signal strength from the 70 and 100 nm thick tips was very small, suggesting that these tips had a nearly zero net component of magnetisation along their axes. The 10 and 20 nm tips were examined, but

again they gave a very small DPC signal, probably due to the very small amount of magnetic material involved. The 30 and 50 nm tips did give a reasonable DPC signal, and therefore tomographic studies were performed on these tips. Two tips of each thickness were investigated.

Due to the softness of the magnetic films involved, care was required during DPC imaging that no stray fields affected the tip magnetisation. Indeed changes in the magnetic state of the tip were noted during acquisition of tomographic data in some early studies; it appeared that the weak remanent field from the objective lens was responsible (this observation was the impetus for the work discussed in the previous section). Using a Hall probe mounted in a modified sample rod, it was found that the remanent vertical field of the objective lens could be as high as 20 Oe (depending on the lens history), which would certainly be enough to affect the tip magnetisation. To counter this, a procedure was developed to ensure that the tip was in magnetic field free space before data collection. The objective lens current was set to maximum and was then reduced to zero. The direction of current was then reversed, and the current increased until the field was  $<0.5$  Oe in the sample region. The sample was then inserted, and the tomographic data was acquired in the usual manner.

In all these studies the Low Magnification Scanning (LMS) mode of the CM20 was used. The width of the scan in all cases was  $\sim 7$   $\mu\text{m}$ , and the resolution (governed by the electron probe size) was  $\sim 30$  nm. The pixel spacing was therefore set to  $\sim 30$  nm (256 pixels per line), and so the reconstructed fields are in a plane equivalent to the sample surface in the MFM, at a distance of  $\sim 30$  nm from the tip.

It was also found that there was a small amount of electrostatic charging of the tip during data collection. The origin of this charging is unclear, as METGLAS is expected to have a reasonable electrical conductivity, given that 81% of the material is composed of iron. In some cases the amount of charging was sufficient to distort the form of the field distribution significantly. The data was therefore analysed to determine the amount of charging present, and the effects were then removed before the reconstruction was done. The effect of charging of the tip on the reconstructions is discussed in detail in Chapter 6, along with the procedure used to remove the effects.

The tips were initially examined in the as-received state, and then magnetised in the direction of the tip axis using an NdFeB permanent magnet. (Digital Instruments recommends that tips be magnetised in this manner prior to use in the MFM). As these tips were obtained directly from Sheffield, it was hoped that the as-received state would correspond to the as-deposited state. However, given the sensitivity of these tips to stray fields, it was not possible to guarantee this.

## 4.6.1 30 nm tip #1

This tip was inadvertently magnetised prior to imaging, so there is no data on the as-deposited state. The tip was magnetised along the tip axis before imaging. The results are shown below in Figs. 4.10 and 4.11.

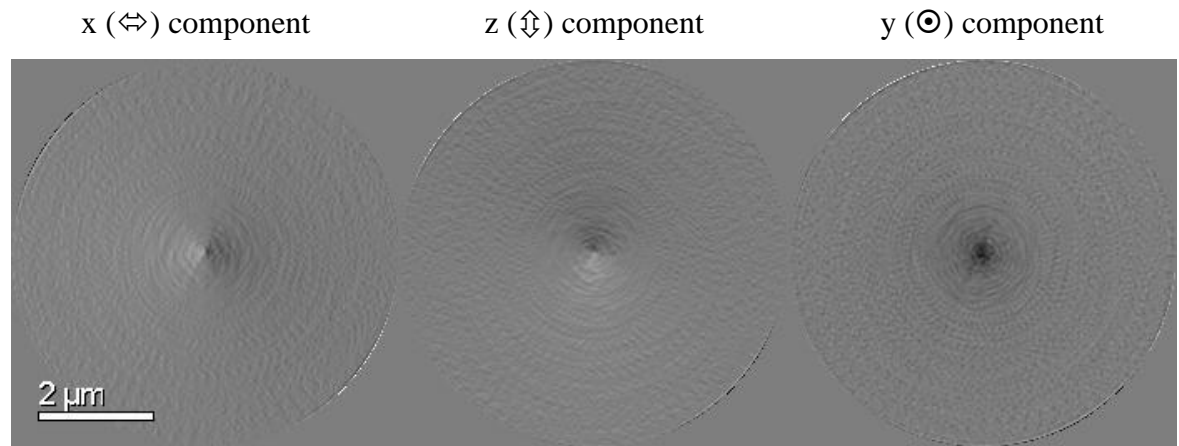


Figure 4.10. Field reconstruction of 30 nm tip #1 magnetised along the tip axis.

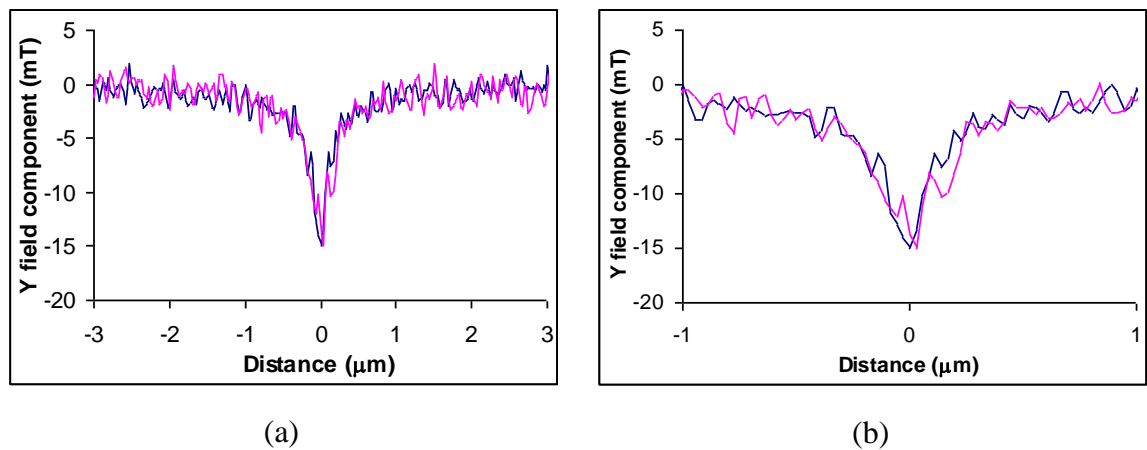
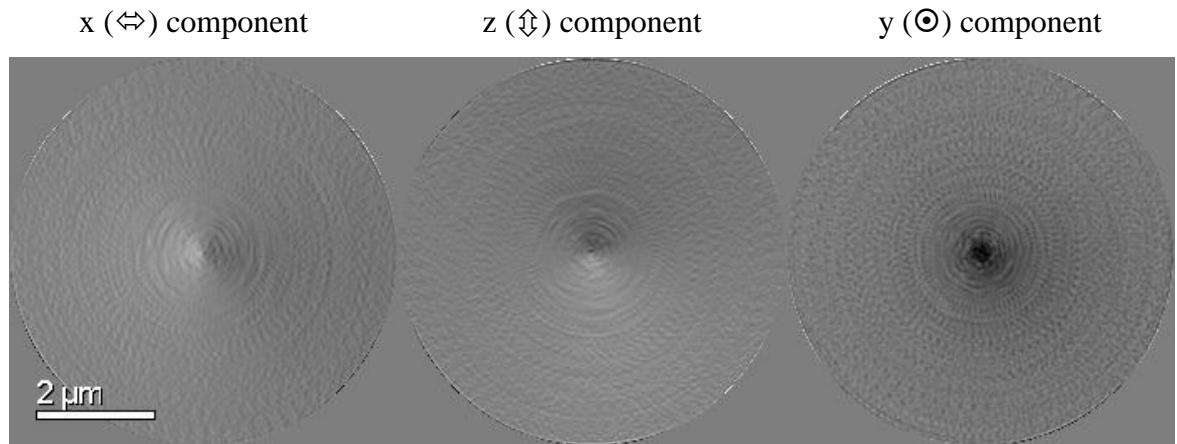


Figure 4.11. Linescans of the y field components of the field reconstruction in Fig. 4.10. The blue scans are taken along the x axis (horizontal), and the purple linescans are taken along the y axis (vertical). Almost the entire width of the reconstruction is covered by (a), while the detail of the field peak is shown in (b).

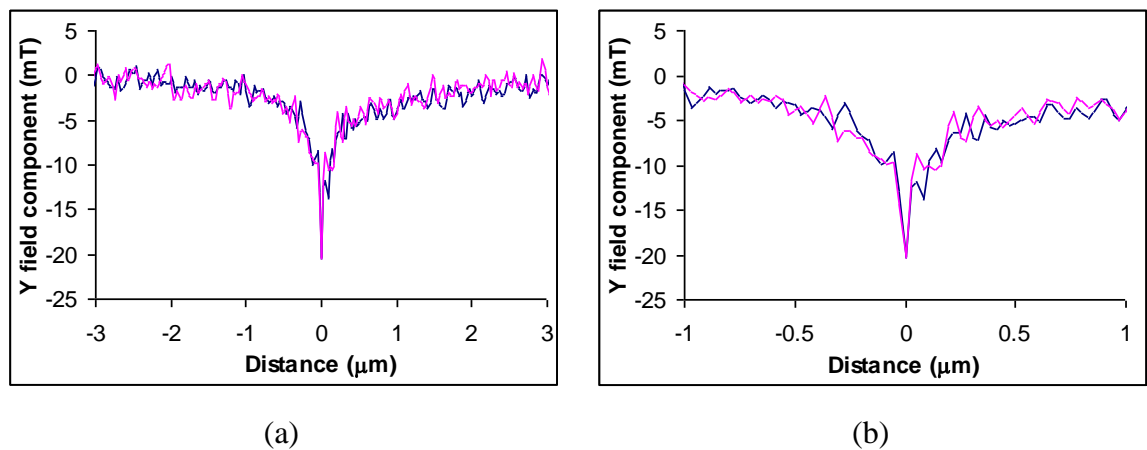


## 4.6.2 30nm tip #2

This tip was first studied as received, and the results are shown in Figs. 4.12 and 4.13. The tip was then magnetised and imaged again; the results are shown in Figs. 4.14 and 4.15. The tip was then magnetised in the opposite direction and imaged, however the signal was very low in this case and there were also some charging problems that could not be compensated for. The reconstruction contained no useful data and hence is not shown here.



**Figure 4.12.** Field reconstruction of 30 nm tip #1 magnetised along the tip axis.



**Figure 4.13.** Linescans of the y field components of the field reconstruction in Fig. 4.12. The **blue scans** are taken along the x axis (horizontal), and the **purple linescans** are taken along the y axis (vertical). Almost the entire width of the reconstruction is covered by (a), while the detail of the field peak is shown in (b).

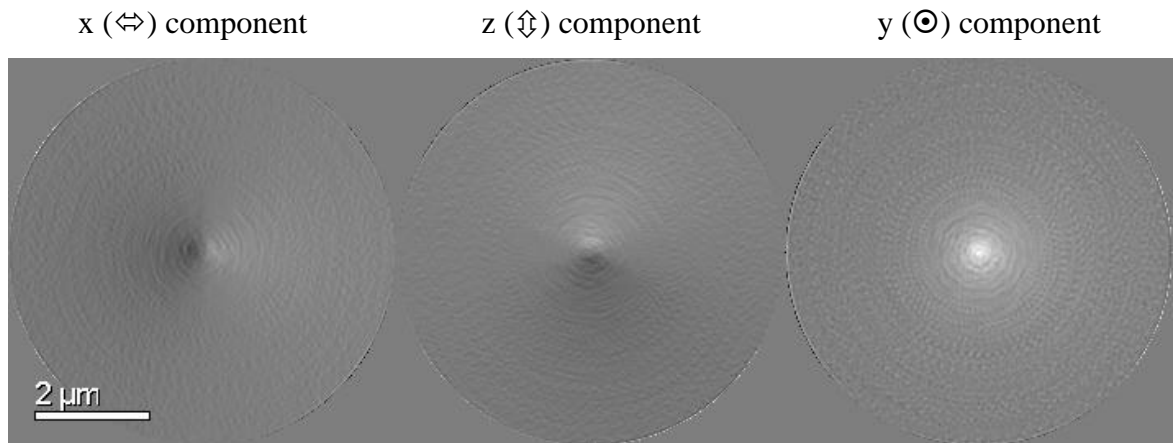


Figure 4.14. Field reconstruction of 30 nm tip #1 magnetised along the tip axis.

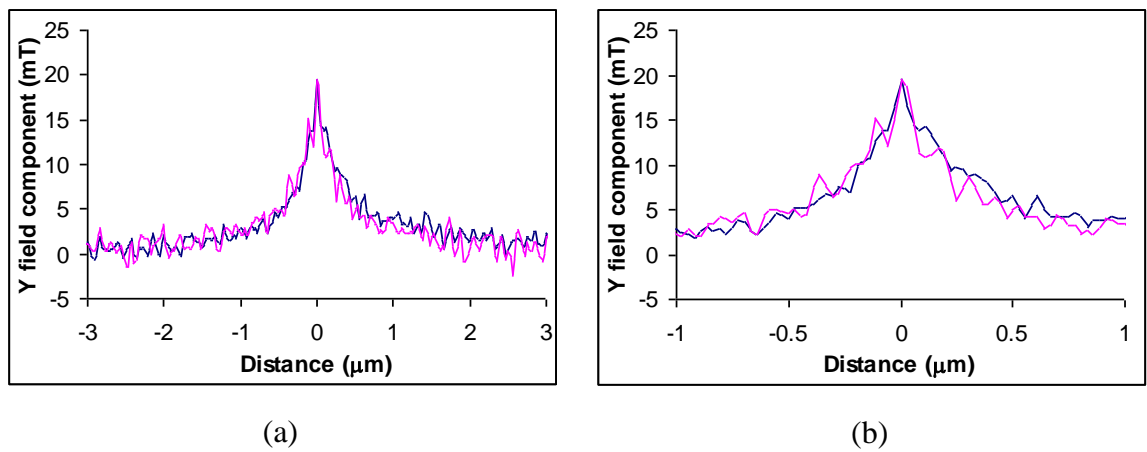


Figure 4.15. Linescans of the y field components of the field reconstruction in Fig. 4.14. The blue scans are taken along the x axis (horizontal), and the purple linescans are taken along the y axis (vertical). Almost the entire width of the reconstruction is covered by (a), while the detail of the field peak is shown in (b).

## 4.6.3 50 nm tip #1

This tip was first imaged as received, and the results are shown in Figs. 4.16 and 4.17. The tip was then magnetised along the tip axis and imaged again, and the corresponding reconstructions are shown in Figs. 4.17 and 4.18.

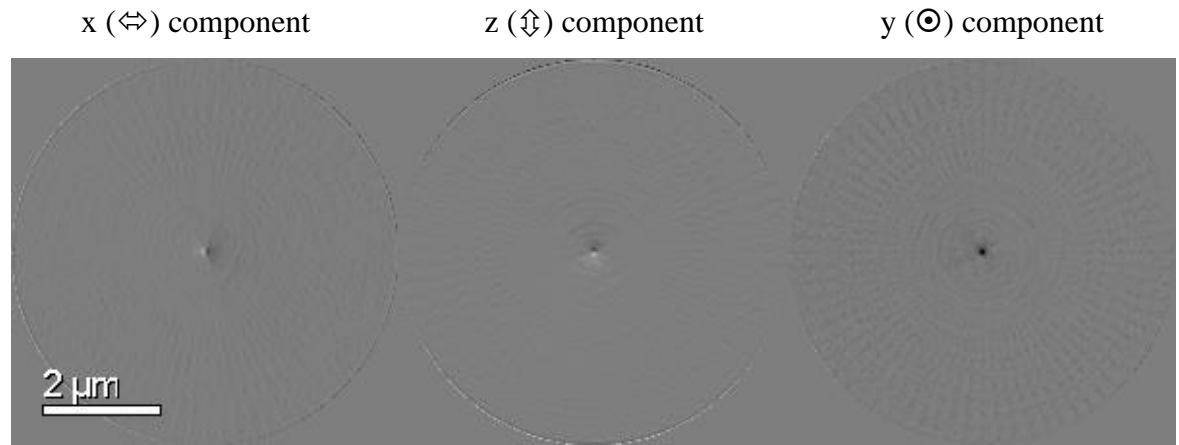


Figure 4.16. Field reconstruction of 50 nm tip #1 in the as received state.

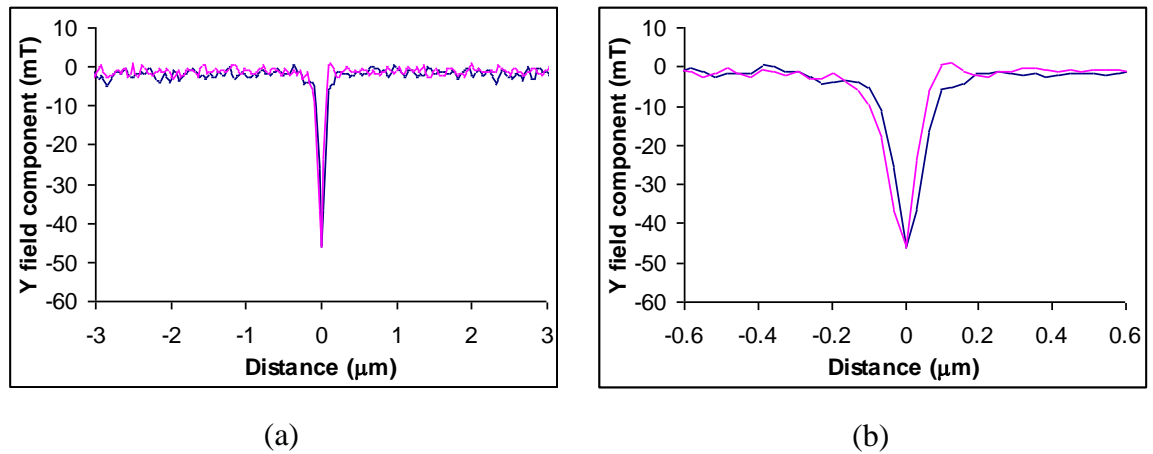
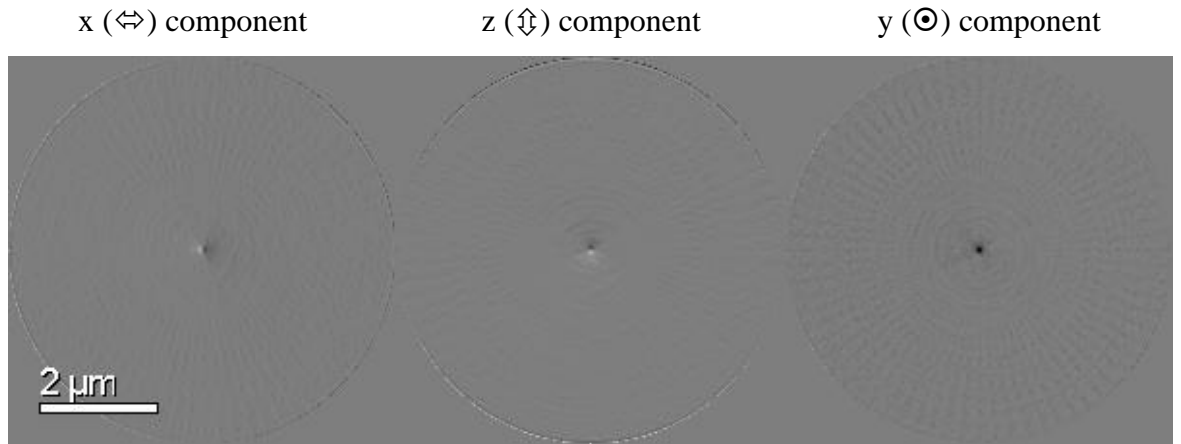
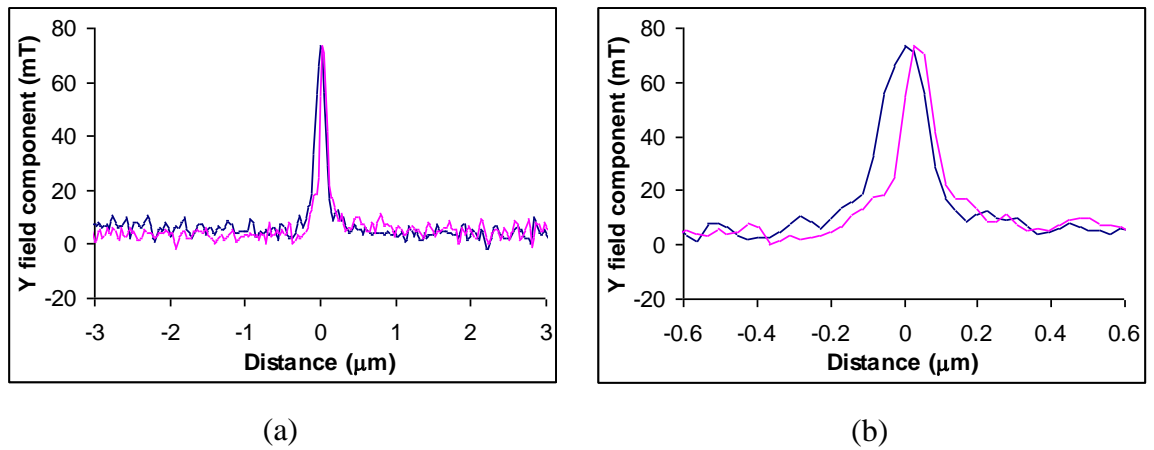


Figure 4.17. Linescans of the y field components of the field reconstruction in Fig. 4.16. The blue scans are taken along the x axis (horizontal), and the purple linescans are taken along the y axis (vertical). Almost the entire width of the reconstruction is covered by (a), while the detail of the field peak is shown in (b).





**Figure 4.18.** Field reconstructions of 50 nm tip #1 magnetised along the tip axis.



**Figure 4.19.** Linescans of the y field components of the field reconstruction in Fig. 4.18. The **blue scans** are taken along the x axis (horizontal), and **the purple linescans are taken along the y axis (vertical)**. Almost the entire width of the reconstruction is covered by (a), while the detail of the field peak is shown in (b).

## 4.6.4 50 nm tip #2

This tip initially gave only small DPC signals even when magnetised. It was then investigated during the switching experiments detailed in section 4.5. During the magnetisation sequence, the tip switched into a state that seemed to be axially magnetised. This state remained stable as the external field was reduced to zero. A tomographic study was then done to examine the state of the tip in more detail. The results are shown in Figs. 4.20 and 4.21.

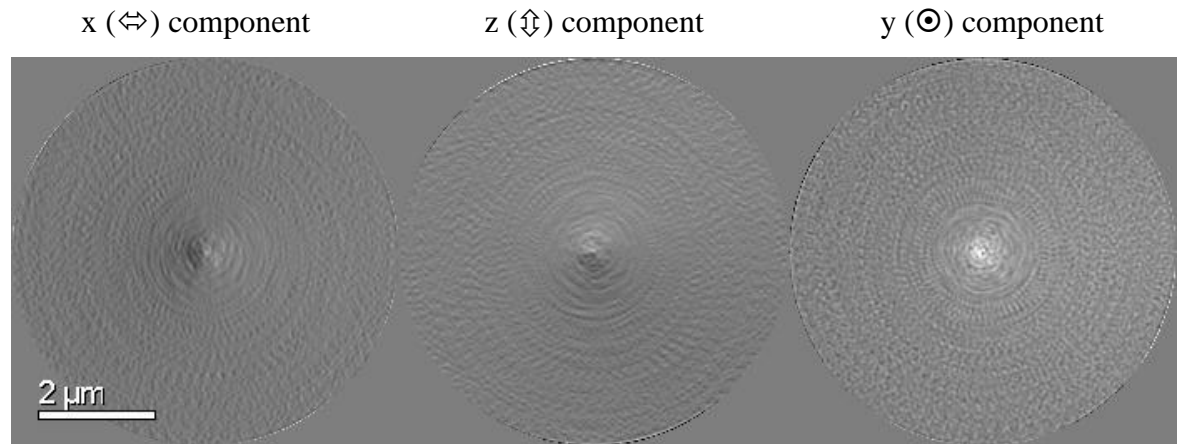


Figure 4.20. Field reconstruction of 50 nm tip #2 magnetised using the objective lens in the CM20.

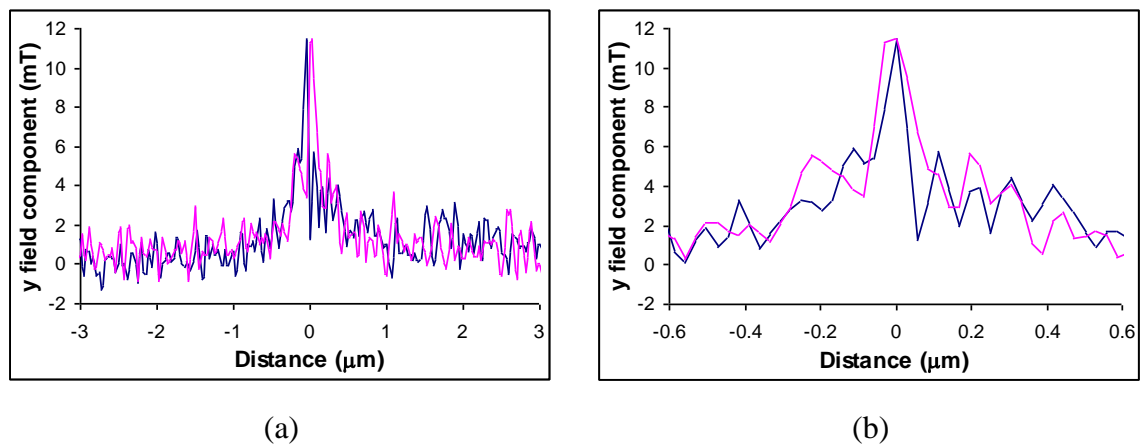


Figure 4.21. Linescans of the y field components of the field reconstruction in Fig. 4.20. The **blue scans** are taken along the x axis (horizontal), and the **purple linescans** are taken along the y axis (vertical). Almost the entire width of the reconstruction is covered by (a), while the detail of the field peak is shown in (b).

#### 4.6.5 Analysis of tomographic reconstructions

There are two main parameters of interest when analysing tip stray field distributions. The peak value of the axial ( $y$ ) field distribution gives a measure of the strength of the tip, and the full width at half maximum (FWHM) is a measure of the width of the field distribution. These values are tabulated in Table 4.3 for all the METGLAS tips shown above.

Tip	Peak field (mT)	FWHM (nm)
30 nm tip #1 magnetised	15	360
30 nm tip #2 as received	20	160
30 nm tip #2 magnetised	19	390
50 nm tip #1 as received	46	95
50 nm tip #1 magnetised	74	140
50 nm tip #2 magnetised	11	140 - 220

**Table 4.3. Peak field values and FWHM of  $y$  field components of METGLAS tip field reconstructions. In the case of the 50 nm tip #2, the peak field was found not to be symmetric around the tip axis, but elliptical in shape. The figures given refer to the short and long axis of the field distribution in this case.**

Comparing these reconstructions there are a number of points to note. The first 50 nm tip examined had higher peak fields than the 30 nm tips, as might be expected. The difference is however larger than would be expected given the nominal difference in thickness between the coatings. As shown previously, the actual tip radii (and by implication the amount of magnetic material at the tip apex) can vary somewhat from the nominal film thickness values, and the variation in peak field values is not inconsistent with this fact. The peak field from the second 50 nm tip is less than the 30 nm tips. This is probably due to the unusual method of magnetisation used in this case (i.e. the use of the objective lens to magnetise the tip as detailed in section 4.5).

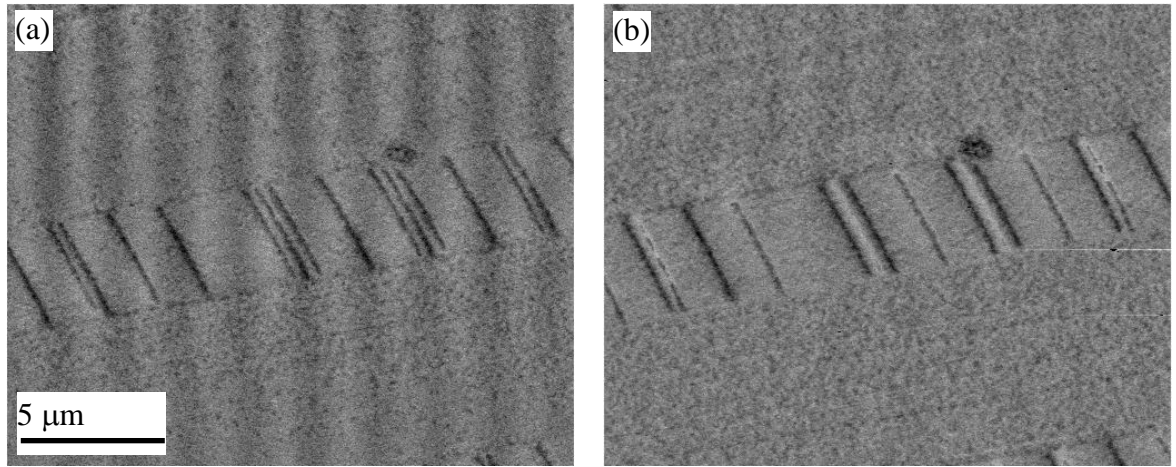
It is also apparent that both 50 nm tips possess narrower field distributions than the 30 nm tips, which is a rather surprising result. However, together with the fact that the FWHM increases when the tip is magnetised an explanation can be constructed. It is probable that the tip coating is not uniformly magnetised when the material is deposited. We would expect the magnetisation around the tip apex to be directed along the tip axis due to shape anisotropy effects (in the absence of external field). If the rest of the tip is in a multi-domain state, the fields from these domains will tend to cancel out over greater distances, and so the direction and size of the tip apex domain will dominate the character of the field above the tip apex. Magnetising the tip will result in a larger tip apex domain

extending further down the tip. This would be expected to give a wider and stronger field distribution, as is observed here. In all cases it appears that the 30 nm tips can support a larger axially magnetised tip apex domain than the 50 nm tips.

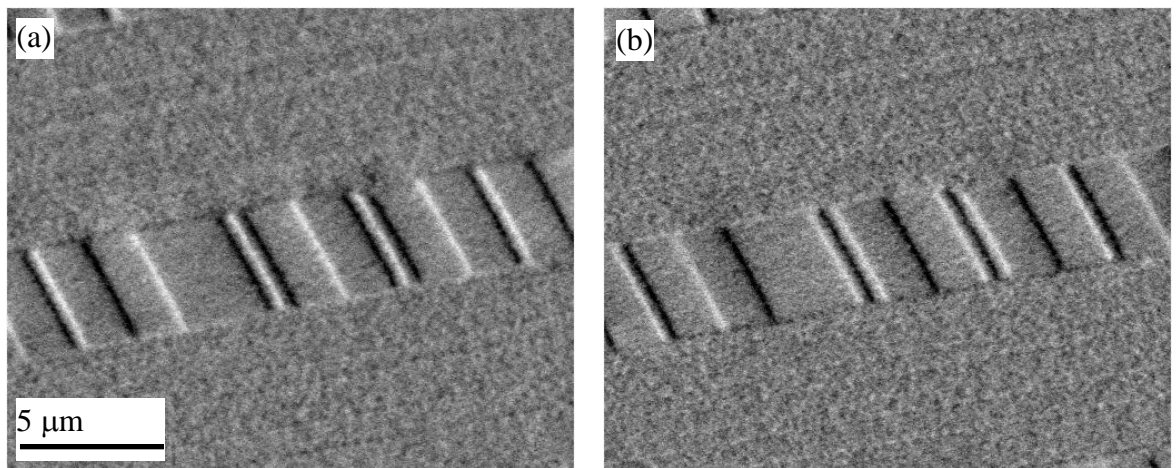
#### 4.7 Application of METGLAS tips to MFM

The METGLAS coated tips were characterised in the MFM by Dr Heydon at Sheffield University using a standard hard disk sample from NIST (Rice *et al*, 1997). Lithographically defined markers allowed the same area of the sample to be imaged each time, so images taken using different tips can be compared directly. Typical MFM images of this area are shown in Figs. 4.22 – 4.26. It can be seen that images taken using the 10 and 30 nm tips exhibit black/white contrast, indicating the presence of both attractive and repulsive interactions. The signal from the 30 nm tip is markedly stronger than the 10 nm tip, as might be expected. Images taken with this tip, with remanent magnetisation in the opposite direction, resulted in a reversal of the MFM contrast, indicating that the 30nm tips are relatively hard magnetically. The 10 nm tip appears to be slightly softer in one magnetisation state (Fig. 4.22a) than the reverse magnetised state. It was found that the 10 nm tips were quite inconsistent in behaviour, while most of the 30 nm tips behaved in a similar fashion to each other. The reason for the inconsistency of the 10 nm tips is unclear, although the variation of the coating behaviour with nominal film thickness noted earlier in section 4.4 suggests that for films as thin as 10 nm, the coating of the tips may be thinner than expected, and the coverage may possibly be patchy. Once the thickness of the film is greater than ~20 nm, the consistency of the tips seems to improve.

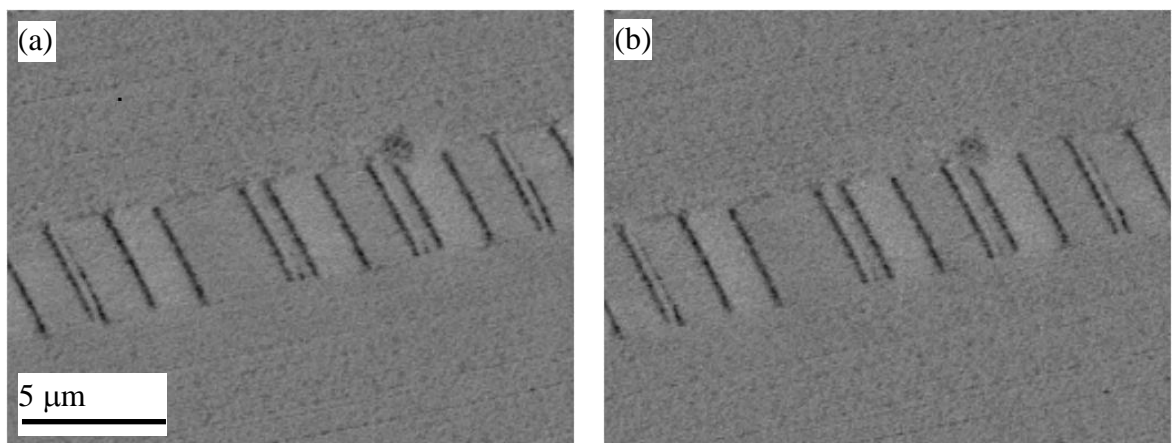
By comparison, the 50, 70 and 100 nm tips exhibited mainly black contrast, indicating that attractive interactions were predominant (Figs. 4.24 – 4.26). The main difference between these tips is that the 50 and 70 nm tips give some contrast between bits in opposite directions; this is absent for the 100 nm tips. To show the behaviour of the tips in more detail, linescans were taken along the direction of the written track in the sample area. Linescans for the 30, 50 and 100 nm tips are shown in Figs. 4.27 – 4.29. These tips were found to be reasonably consistent, as in general out of one coating batch (five tips) at least four were usable and gave similar and reproducible results. The images shown below are representative of each type of tip.



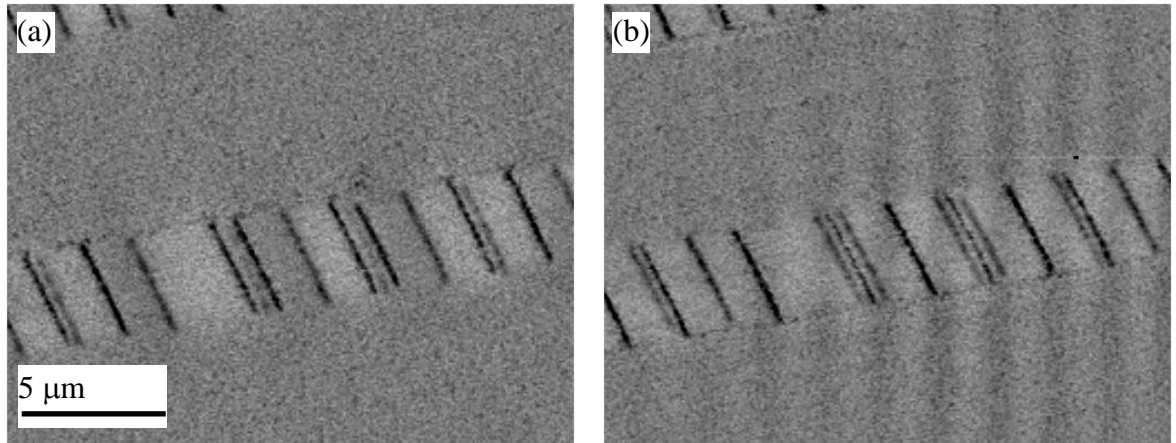
**Figure 4.22.** MFM images of the NIST standard hard disk sample taken using a tip coated with 10 nm of METGLAS. The tip flying height was 50 nm above the sample surface. The tip was magnetised for (a), and reverse magnetised for (b).



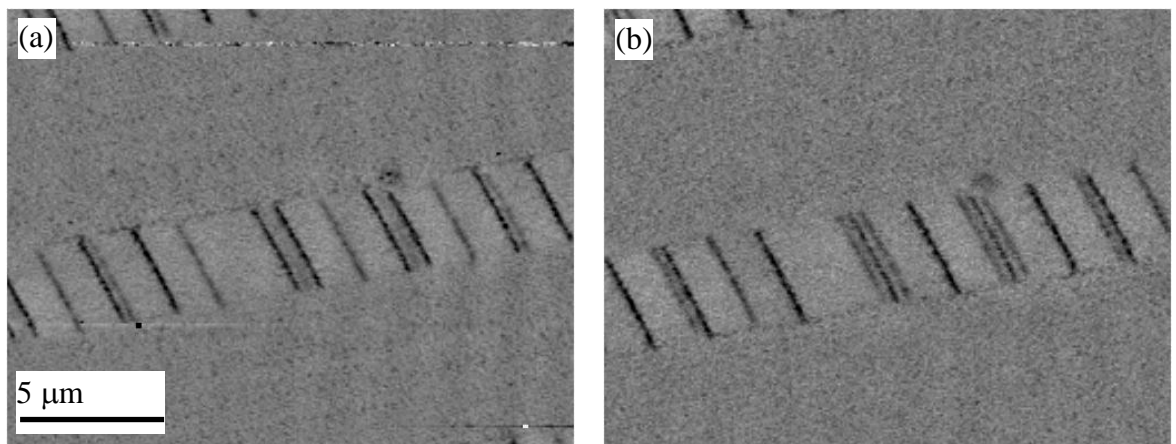
**Figure 4.23.** MFM images of the NIST standard hard disk sample taken using a tip coated with 30 nm of METGLAS. The tip flying height was 50 nm above the sample surface. The tip was magnetised for (a), and reverse magnetised for (b).



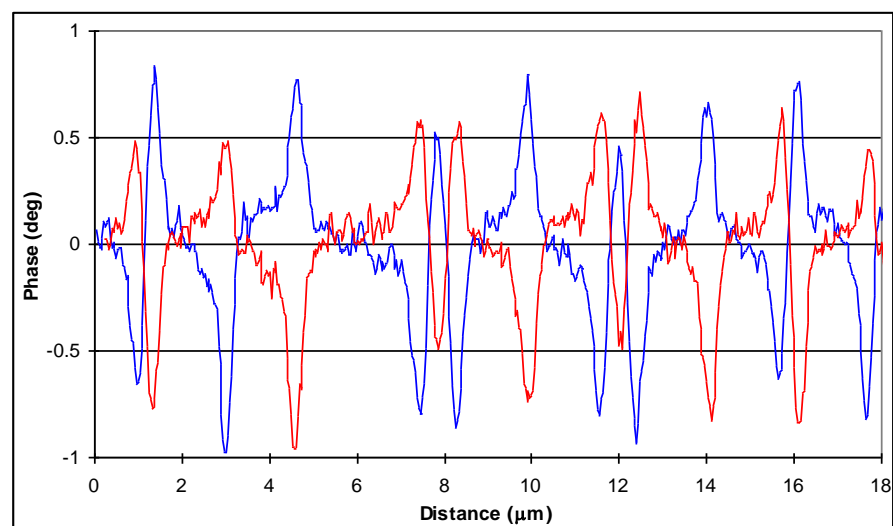
**Figure 4.24.** MFM images of the NIST standard hard disk sample taken using a tip coated with 50 nm of METGLAS. The tip flying height was 50 nm above the sample surface. The tip was magnetised for (a), and reverse magnetised for (b).



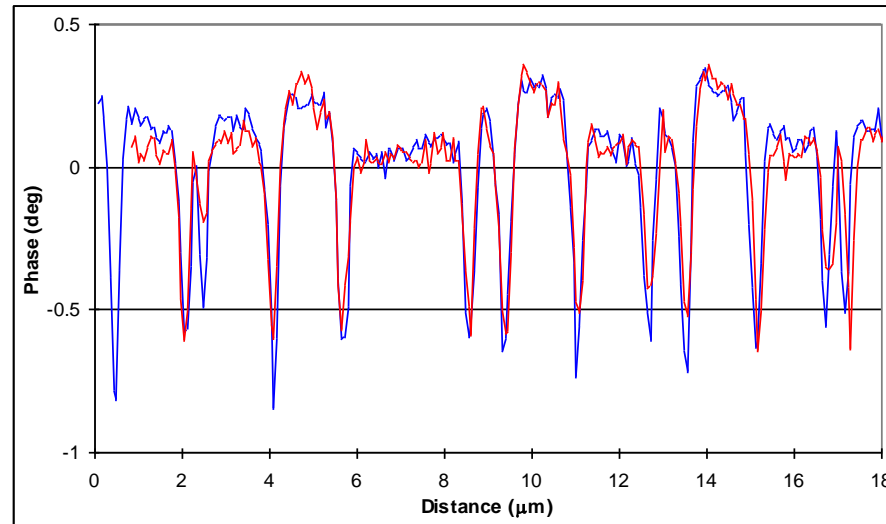
**Figure 4.25.** MFM images of the NIST standard hard disk sample taken using a tip coated with 70 nm of METGLAS. The tip flying height was 50 nm above the sample surface. The tip was magnetised for (a), and reverse magnetised for (b).



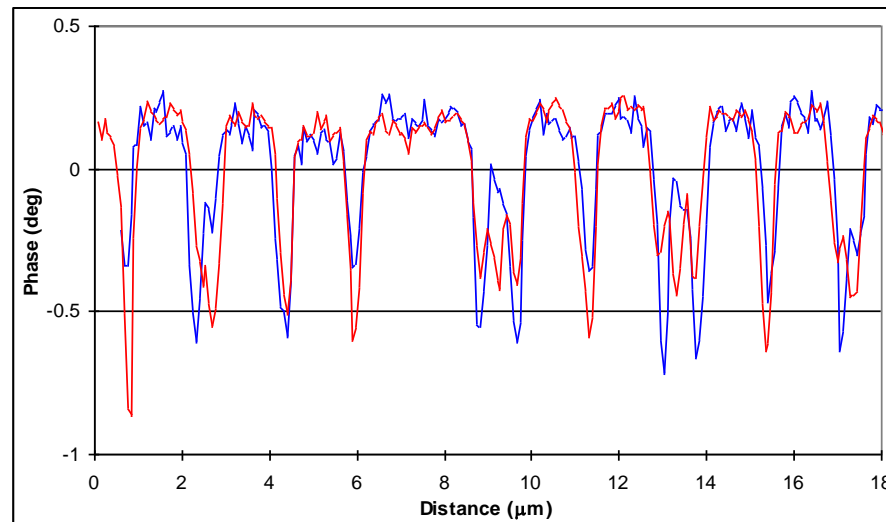
**Figure 4.26.** MFM images of the NIST standard hard disk sample taken using a tip coated with 100 nm of METGLAS. The tip flying height was 50 nm above the sample surface. The tip was magnetised for (a), and reverse magnetised for (b).



**Figure 4.27.** MFM linescans along a track of the NIST sample for a 30 nm tip. The blue linetraces were taken with the tips magnetised in one direction (along the tip axis), and the red linetraces were taken with the tips magnetised in the opposite direction.



**Figure 4.28.** MFM linescans along a track of the NIST sample for a 50 nm tip. The blue linetraces were taken with the tips magnetised in one direction (along the tip axis), and the red linetraces were taken with the tips magnetised in the opposite direction.



**Figure 4.29.** MFM linescans along a track of the NIST sample for a 100 nm tip. The blue linetraces were taken with the tips magnetised in one direction (along the tip axis), and the red linetraces were taken with the tips magnetised in the opposite direction.

It can be seen from the linescans taken along the track direction (Fig. 4.27) that the contrast from the 30 nm tip reverses almost completely when the tip is magnetised in the reverse direction, confirming that this tip behaves as a hard tip when applied to the NIST sample. The contrast from the 100 nm tip (Fig. 4.29) is largely unaffected by prior tip magnetisation, apart from the closely spaced double and triple transitions where some differences are evident. The 50 nm tip (Fig. 4.28) appears to be almost completely unaffected by prior magnetisation. However, there are clear differences in contrast between different bits.

To explain the differing behaviour of the 30 nm and 100 nm coated tips when imaging the NIST sample it is simply necessary to recall how the coercivity of METGLAS



varies with thickness. As noted earlier in section 4.2, the coercivity of these films on flat substrates is roughly constant down to a thickness of  $\sim 40$  nm, and then rises sharply for thinner films. The (relatively) high coercivity of the 30 nm tip can then be explained simply as a consequence of the inherent coercivity of this film thickness and the shape anisotropy.

Tips coated with films thicker than 40 nm have a lower inherent coercivity, resulting in exclusively attractive interactions in most cases. The 100 nm tip shown here also appears to be quite soft, but there are differences in the strength of the track transitions as the tip magnetisation is reversed. This can be clearly seen in both Figs. 4.26 and 4.29. The most likely explanation for this is the presence of a (relatively) high-coercivity region of the tip located at the tip apex. This region will be magnetised by the external magnet, but will not be affected by the stray field from the sample. This will result in a tip in which the high spatial frequency response (i.e. the sensitivity to small-scale features in the sample) changes sign when the tip magnetisation is reversed. The low frequency response (similarly, the response to large-scale sample features) will be governed largely by the magnetisation of the tip further up from the tip apex (simply because of the much greater amount of material spread over a large volume covering the rest of the tip as compared to the tip apex region).

The low frequency response will therefore not change sign when the tip is reverse magnetised, as the bulk of the tip acts as a soft tip in this case. The image is then composed of low spatial frequency components that do not change sign on reverse magnetisation, and high spatial frequency components that do. Thus the bit contrast (low frequency) does not change significantly when the tip magnetisation is reversed, while the transitions do change somewhat. The transitions do not actually change sign, but do change in magnitude. This is because in this case the signal from the transitions is a combination of the low (which does not change sign) and high (which does change sign) frequency response.

This is probably a simplified model of the tip behaviour. It may be the case that there are several regions of the tip that have different coercivities. However, the two-region model does adequately explain the observed data.

It can be said that the 100 nm coated tip does not behave exactly as an ideal paramagnetic tip. However, for higher field samples such as permanent magnet materials or recording heads the coercivity of the tip will be so low (compared to the sample field strength) that it can probably be neglected for most purposes. One possible way to achieve even lower coercivity would be to anneal the tip, to minimise any magnetostrictive stress in the coating. This was not done here due to lack of time.



The 50 nm thick films are expected to have approximately the same inherent coercivity as the 70 and 100 nm films, so it would be expected that the 50 nm coated tips would display the same sort of behaviour. In practice, the 50 and 70 nm tips do appear to behave as soft tips, although some contrast between oppositely magnetised magnetic bits is apparent. The simplest model for this behaviour is the opposite of that postulated for the 100 nm tips. That is, the low frequency response of the tip has a high coercivity nature, while the high frequency response has a low coercivity nature. This would imply that the tip apex region was low coercivity and the rest of the tip (or a substantial portion thereof) was high coercivity. There are two main problems with this model. The magnetisation experiments performed on a 50 nm tip (section 4.5.1) suggest that the tip apex is the high coercivity region of the tip. Also, the bit contrast does not reverse when the tip is reverse magnetised. This would suggest that if a large high coercivity region of the tip does exist, it is not reversed by the permanent magnet used for this purpose. Given the properties of the other tips investigated, this is extremely unlikely.

As noted previously, when examining the TEM images shown in section 4.4 it is apparent that the texture of the 50 nm films differs markedly from the 100 nm (and 30 nm) films at the tip apex. It may be that this difference in texture is the reason for the anomalous behaviour of the 50 nm tips. The most likely explanation is that there are many different regions of the tip with different coercivities, and thus the magnetisation behaviour of the tip is quite complex. As it is difficult to directly measure the tip magnetisation, this may be a problem that would benefit from micromagnetic simulation.

The behaviour of the 70 nm tips in the MFM appears almost identical to the 50 nm tips. The magnetisation experiments performed in section 4.5.2 suggest the coercivity of the 70 nm tips is similar to the 50 nm tips, with the caveat that the 70 nm tips do not sustain an external stray field at remanence, unlike the 50 nm tips.

## 4.8 Conclusions

As explained in the introduction to this chapter, the motivation for the production of these METGLAS coated tips was to create a MFM tip with very low coercivity, high sensitivity and high consistency between tips. The 30 nm tips can be dismissed, as their coercivity is too high to act as a soft tip when imaging hard disk tracks. They could be used as soft tips while imaging samples with high stray fields such as hard disk write heads, but as tips with thicker coatings can also be used for this purpose there is little point in doing so. The 100 nm tips at first glance appear to be very soft in character, but it has been shown that they seem to have a hard component in their response to field. However, they are probably still suitable for examining samples with high stray fields. Tips coated

with 50 to 70 nm are probably also suited to high field investigations. Where samples with lower stray fields (such as hard disk media) are encountered these tips should probably not be used, given the results shown here. However, in this case tips with high coercivity can be used, so this is not a serious problem. It can be said that tips coated with greater than 30 nm are quite consistent in their behaviour (this is where the value being able to image the same area of an MFM sample becomes evident), and so would be suited to batch production. The consistency probably arises from the thickness of the coating involved, as small thickness variations (say  $\pm 5$  nm) will not have a large effect on the tip properties.

The question of resolution is more difficult to address, given the data here. As stated before, the NIST sample is not intended as a high-resolution MFM test (the transitions in the NIST sample are at least 300 nm apart). Certainly the thicker tips can resolve the three closely separated transitions on the NIST sample clearly, and the resolution does not appear to be worse compared to the thinner tips. The results from the tomographic reconstructions do suggest that increasing film thickness does not necessarily result in wider remanent field distributions. However, the resolution of a soft MFM tip is difficult to define, as the response function of the tip (related to its stray field distribution) depends on the stray field of the sample. Therefore to test the resolution of soft MFM tips really requires an appropriate sample that possesses detailed magnetisation patterns (patterned ferromagnetic films, for example, or narrow current-carrying wires).

## References

- Ali M, Watts R, Karl W J, Gibbs M R J (1998), "The use of stress for the control of magnetic anisotropy in amorphous FeSiBC thin films - a magneto-optic study", *J. Magn. Magn. Mater.*, **190**, 199 – 204
- Babcock K L, Elings V B, Shi J, Awschalom D D, Dugas M (1996), "Field-dependence of microscopic probes in magnetic force microscopy", *Appl. Phys. Lett.*, **69**, 705-707
- Carl A, Lohau J, Kirsch S and Wassermann E F (2001), "Magnetization reversal and coercivity of magnetic-force microscopy tips", *J. Appl. Phys.*, **89**, 6098-6104
- Heyderman L. J., Chapman J. N., Gibbs M. R. J. and Shearwood C. (1995), "Amorphous melt spun ribbons and sputtered thin films – investigation of the magnetic domain structures by TEM", *J. Magn. Magn. Mater.*, **148**, 433 – 445

- Heydon G. P., Rainforth W. M., Gibbs M. R. J., Davies H. A., McVitie S., Ferrier R. P., Scott J., Tucker J. W. and Bishop J. E. L. (1999), “Preparation and characterisation of a new amorphous tip coating for application in magnetic force microscopy”, *J. Magn. Magn. Mater.*, **205**, L131 – 135
- Liou S. H., Malhotra S. S., Moreland J., Hopkins P. F. (1997), “High resolution imaging of thin-film recording heads by superparamagnetic magnetic force microscopy tips”, *Appl. Phys. Lett.*, **70**, 135 – 137
- Rice P, Russek S E, Hoinville J and Kelley M (1997), “Optimizing the NIST magnetic imaging reference sample”, *IEEE Trans. Magn.*, **33**, 4065-4067
- Scott J., McVitie S., Ferrier R. P., Heydon G. P., Rainforth W. M., Gibbs M. R. J., Tucker J. W., Davies H. A. and Bishop J. E. L. (1999), “Characterisation of FeBSiC coated MFM tips using Lorentz electron tomography and MFM”, *IEEE Trans. Mag.* **35**, 3986
- Shearwood C., Mattingley A. D. and Gibbs M. R. J. (1996), “Growth and patterning of amorphous FeSiBC films,” *J. Magn. Magn. Mater.*, **162**, 147-154

## Chapter 5. Magnetic properties of special purpose MFM tips

### 5.1 Introduction

The imaging properties of a thin-film MFM probe are determined by the shape of the probe and the properties of the material used to coat it. In this chapter several modified tips are characterised using DPC and tomographic reconstruction. In section 5.2 a standard silicon MFM tip modified by focused ion beam (FIB) milling to give a localised in-plane field at the tip apex is examined. This type of tip has been used to map the response of a magnetoresistive read head. Another use of FIB milling is to make spike tips that, when coated with a magnetic film will potentially have very sharp field distributions, and can also be used to probe deep recesses in surfaces, and these are examined in section 5.3.

There is interest in designing MFM tips with high force sensitivity, allowing smaller magnetic moments to be detected. A tip designed for this purpose is described and characterised in section 5.4. At the other end of the scale, to image materials with high stray fields requires ideally a high coercivity tip. A tip coated with a hard magnetic material for this purpose is characterised in section 5.5. Overall conclusions on the tips and their properties are given in section 5.6.

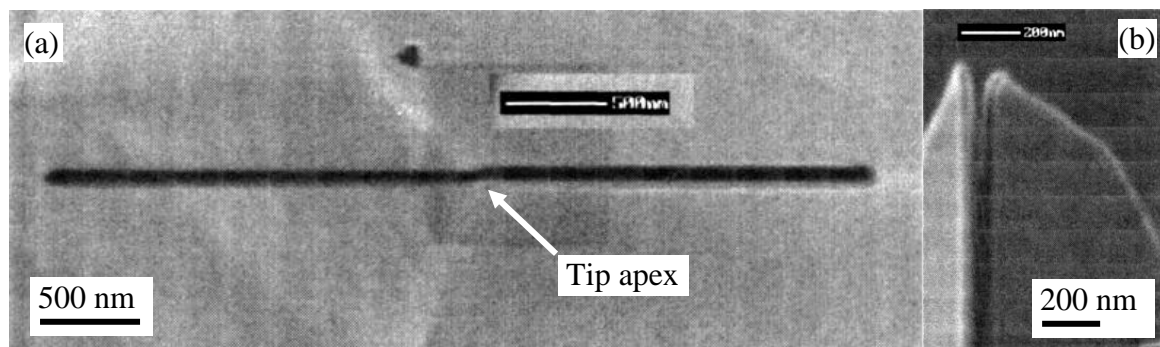
### 5.2 Seagate ion beam milled tips

Read heads for magnetic recording media are designed either to respond to magnetic field  $H$  (magnetoresistive heads) or temporal changes in magnetic field  $dH/dt$  (inductive heads). The performance of inductive read heads can be characterised by measuring the stray field produced when a current is sent through the device. Due to the different mechanism involved (the resistance of the device varies with the value of the field), magnetoresistive (MR) heads cannot be characterised in this fashion. To measure the response of MR heads, a MFM probe is scanned over the pole tips in the normal manner, but the signal from the MR element is measured as a function of the probe position. In this case the MFM probe acts simply as a localised field source (although it also measures the topography of the pole tips as well). This variant of MFM is termed Magnetoresistance Sensitivity Mapping (MSM).

MSM can either be applied to the air bearing surface of a read head, or to the surface of the isolated MR element. In the latter case a normal MFM tip is unsuitable when magnetised along the tip axis. This is because the component of the tip stray field in the sample plane (which governs the magnetoresistance) will be radial in character. The

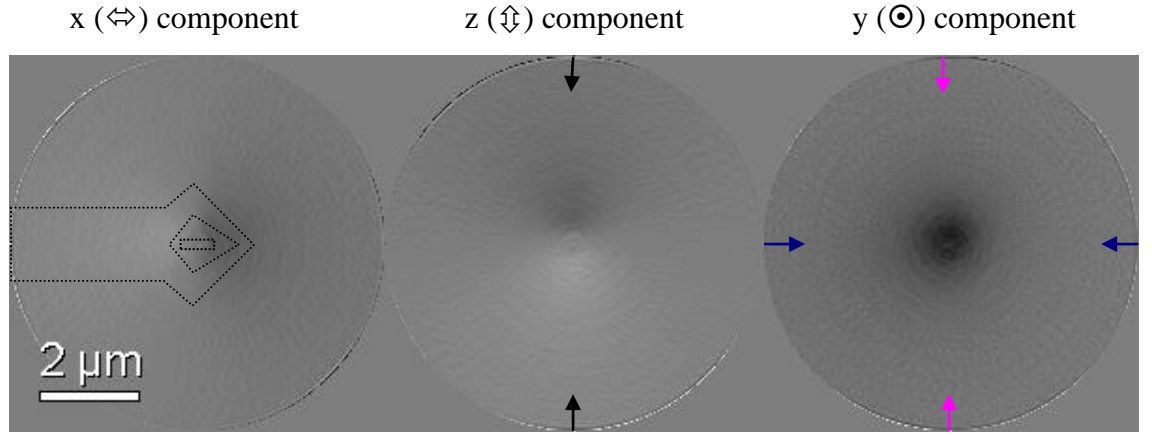
response of the MR element to this type of field is difficult to interpret. If the tip is horizontally magnetised (i.e. in the plane of the sample) the in-plane stray field component of the tip will be stronger in one direction. This will make the MR response pattern much easier to interpret, as shown by Song *et al* (1999). However, as shown by Rice and Russek (1999) standard MFM tips are difficult to magnetise in the direction perpendicular to the tip axis due to the effect of shape anisotropy, and the stray field from a horizontally magnetised tip is small. To increase the strength of the stray field the tip shape can be modified by FIB milling. In this section one example of such a tip is examined.

The modified tip was obtained from Dr Dian Song of Seagate Technology and was based on a standard Nanoprobe tip (model MESP). Before the tip was coated, a groove was cut across the tip apex using FIB milling. The groove was approximately 200 nm wide and 200 nm deep, and extended about 6  $\mu\text{m}$  down the sides of the tip (SEM micrographs of the groove are shown in Fig. 5.1). The tip was then sputter coated with 80 nm of CoCrPt on top of a 20 nm Cr seed layer. In theory, when magnetised perpendicular to the groove direction this should result in magnetic charges occurring at the edges of the groove, resulting in a strong horizontal field in the gap region and a similar fringing field above the gap.

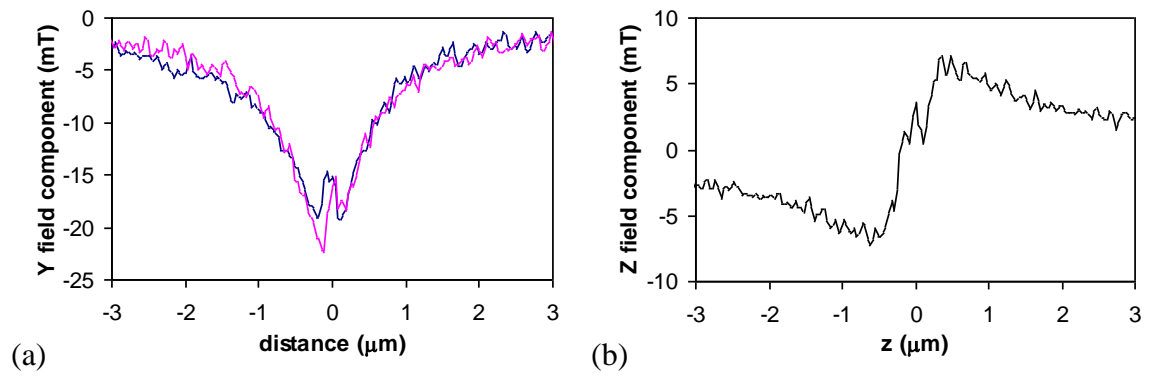


**Figure 5.1.** SEM micrographs of the FIB milled tip before coating. (a) is a top-down view, showing the length of the FIB milled groove in the tip, and (b) is a side-on view of the tip apex. Images courtesy of Dian Song, Seagate Technology.

The tip was first magnetised along the tip axis. The results of the tomography are shown in Fig. 5.2. The general form of the field is what would be expected from a blunt MFM tip fully magnetised along the tip axis. However, at the centre of the reconstruction there is a dip in the  $y$  field component, which can be seen clearly in the linescans (Fig. 5.3a). Examining the  $z$  field component (Fig. 5.3b), the general form is again similar to a blunt axially magnetised MFM tip. There is a small peak in this component at the centre of the linescan, which suggests that there is a small horizontal component of magnetisation at the tip apex. The field distribution however indicates that most of the tip is magnetised in the direction of the tip axis.



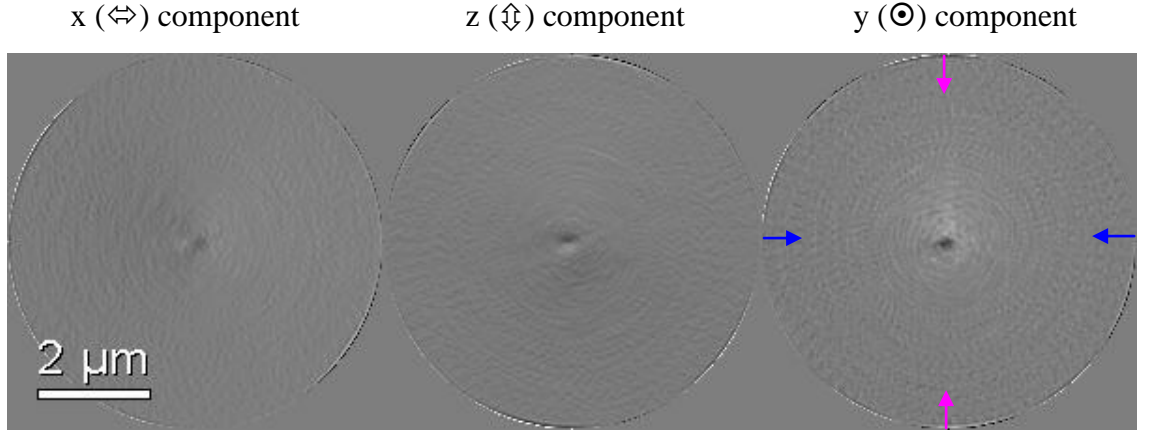
**Figure 5.2.** Field reconstruction from the Seagate FIB modified tip magnetised along the tip (y) axis. The orientation of the cantilever, tip and groove is indicated on the x field component, and the arrows on the z and y field components show where the linescans are taken from.



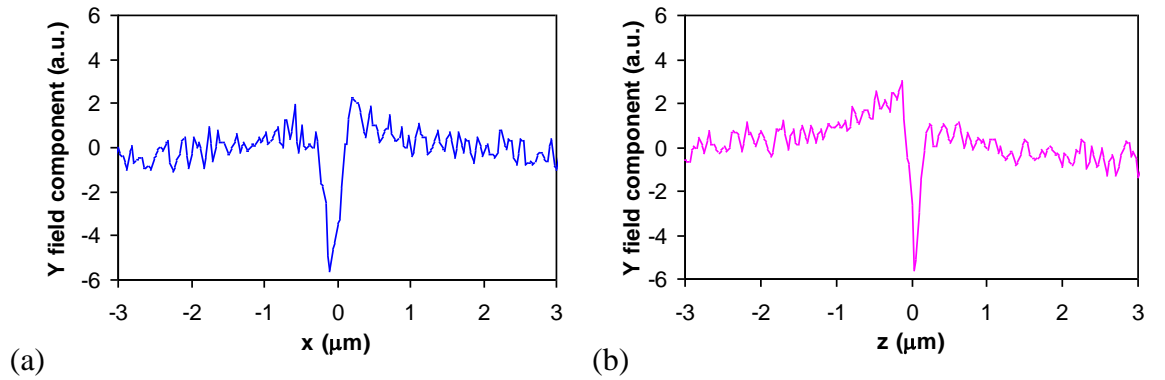
**Figure 5.3.** Linescans of field reconstruction of the Seagate FIB modified tip magnetised along the tip (y) axis. (a) shows the linescans of the y field component; the blue linescan is taken along the x axis, and the purple linescan is taken along the z axis. (b) shows a linescan of the z field component taken along the z axis.

The tip was then magnetised along the cantilever axis (i.e. along the y axis) using the objective field in the CM20. The reconstruction of the field is shown below in Fig. 5.4. The main feature present is a field peak in the y component reconstruction, with a FWHM of 200 nm in the x direction and 100 nm in the z direction.

In this study there was a slight degree of electrostatic charging present, which could not be subtracted as there was insufficient data. However, as the charging DPC signal was somewhat less than the magnetic signal, the reconstructed peak magnitude is probably within 50% of the actual value at least. The slight asymmetry in the z axis linescan (Fig. 5.5b) is probably caused by the charging present. Note that the field strength is not calibrated, as the DPC calibration was not done for this study.

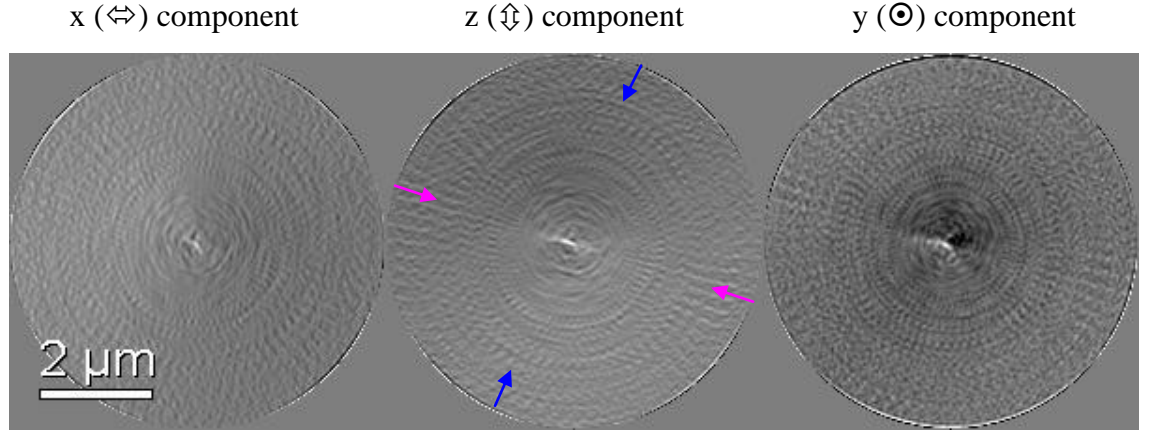


**Figure 5.4.** Field reconstruction of the Seagate FIB modified tip magnetised along the x axis. The orientation of the cantilever is the same as shown in Fig. 5.2, and the arrows on the z and y field components show where the linescans are taken from.

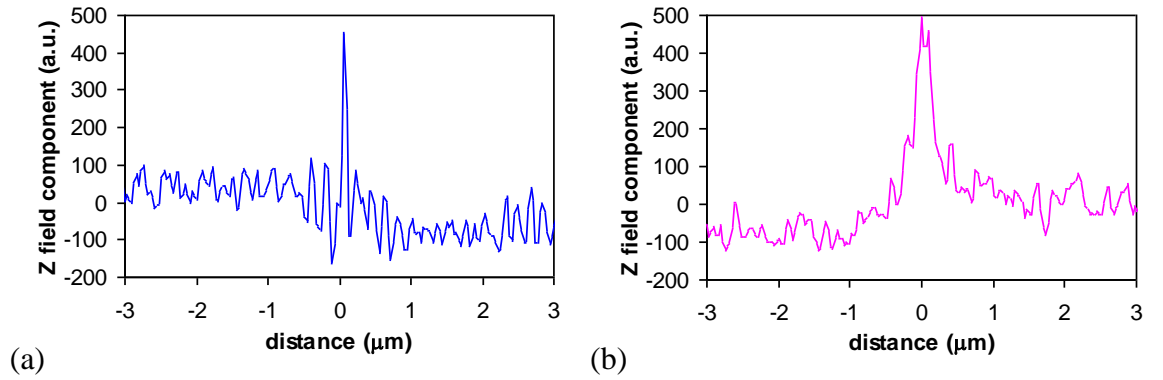


**Figure 5.5.** Linescans of the y field component of the Seagate FIB modified tip magnetised along the x axis. (a) is taken along the x axis, and (b) is taken along the z axis.

The tip was then magnetised in the plane of the cantilever but perpendicular to its length, i.e. across the cut groove. The objective lens field was again used for this purpose. In this state the magnetisation is expected to result in positive magnetic charges on one side of the groove, and negative charges on the other side, resulting in a dipolar field distribution. The reconstruction of the tip field is shown in Fig. 5.6, and it can be seen that there does appear to be a dipolar field at the tip apex. This is most evident when examining the z field component, and from this it can be seen that the in-plane field component from the tip forms a line angled at about  $20^\circ$  from the cantilever direction (and from the groove direction). Linescans taken along the direction of the line of field and across it are shown in Fig. 5.7. The FWHMs of the z field component are 260 nm along the long axis of the distribution, and  $\sim 60$  nm along the short axis. The field is therefore similar to what would be expected from a dipolar line charge. However, the narrowness of the distribution is somewhat surprising, given that the groove was measured to be  $\sim 200$  nm wide.



**Figure 5.6.** Field reconstruction of the Seagate FIB modified tip magnetised along the z axis. The orientation of the cantilever is the same as shown in Fig. 5.2, and the arrows on the z and y field components show where the linescans are taken from.



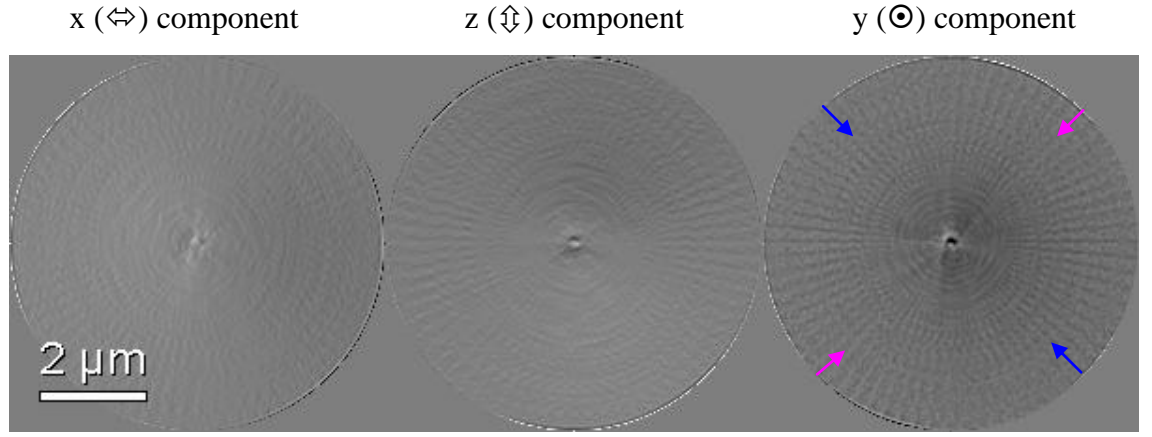
**Figure 5.7.** Linescans of the z field component of the Seagate FIB modified tip magnetised along the z axis. (a) is taken at an angle of  $67^\circ$  from the x axis, and (b) is taken at an angle of  $-23^\circ$  from the x axis.

These results suggest that the simple picture of opposite charges on either side of the groove may not be valid, given the fairly complex geometry of the tip (where the groove intersects the tip apex).

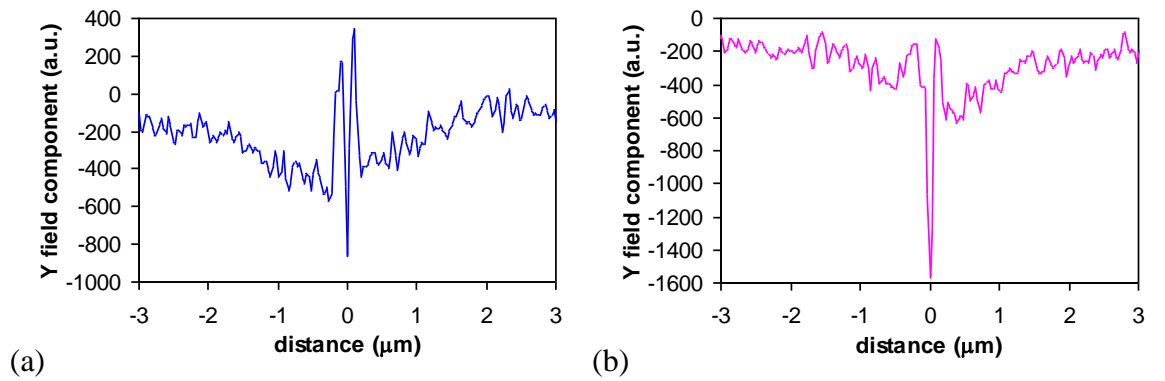
The method of subtracting the electrostatic charging from the tomographic data was not developed until some time after this tip was examined. At the time there was some concern over the character of the data taken for the previous reconstruction, and so another dataset was taken a few days later. The tip was not magnetised before this study, and was therefore expected to be in the same state as previously. The resulting reconstruction is shown in Fig. 5.8.

Examining this reconstruction, it can be seen immediately that the field distribution is quite different from the previous case. The main feature is a sharp central peak in the y field component, surrounded by a region of opposite field polarity. This can be seen more clearly in the linescans shown in Fig. 5.9. The FWHM of the peak is  $\sim 60$  nm in all directions. Given that the tip was not subjected to strong magnetic fields between the studies, this result suggests that the state of the tip in the previous study was not stable.





**Figure 5.8.** Field reconstruction of the Seagate FIB modified tip magnetised along the z axis, after several days relaxation time. The orientation of the cantilever is the same as shown in Fig. 5.2, and the arrows on the z and y field components show where the linescans are taken from.



**Figure 5.9.** Linescans of the y field component of the Seagate FIB modified tip magnetised along the z axis, after several days relaxation time. (a) is taken at an angle of  $45^\circ$  from the x axis, and (b) is taken at an angle of  $-45^\circ$  from the x axis.

To conclude; the FIB modifications of this tip have certainly changed the magnetic behaviour of the tip. However, it is questionable if the modifications have had the desired effect, namely the production of a localised field in the plane of the cantilever. The third study of the tip seemed to suggest that this was achievable, but the stability of this state does not appear to be high. Ironically, the main effect of the modifications appears to be that the tip could produce very localised fields in the direction of the tip axis, as is particularly evident in Figs. 5.6 and 5.8. However, to achieve these states the tip had to be magnetised in the plane of the cantilever, as magnetising along the tip axis produced the field which appears in the first study, which although interesting, is not particularly useful for MFM. It is also worth noting that the study by Song *et al* (1999) used tips that had not been modified by FIB milling (although they were coated in the same way as this tip) but nevertheless could be horizontally magnetised. The value of this type of FIB modification is therefore questionable. A different type of FIB modification performed by Folks *et al* (2000) should also be mentioned here. In this case a FIB was used to produce tips with holes in the magnetic coating of between 20 – 50 nm diameter at the tip apex, resulting in

a horizontal fringing field at the tip apex. This modification was used to improve the resolution of these tips, illustrated by imaging 50 nm period magnetic data tracks. Currently these tips have not been used for MSM studies.

### 5.3 IBM ion milled spike tips

One problem with standard Si AFM and MFM tips arises when the sample to be imaged has steep or perpendicular sidewalls. The maximum slope that can be measured by AFM is governed by the tip geometry. For Nanoprobe tips these maximum slopes (relative to the sample plane) are between  $90^\circ$  and  $55^\circ$ , depending on the orientation of the tip relative to the feature. This means that the geometry of structures such as etched or milled holes or trenches in semiconductor devices cannot be measured accurately. In addition, if holes or trenches are narrow enough the tip may not be able to reach the bottom of the feature, and so the true depth of the feature cannot be measured. In these cases a tip of high aspect ratio is required, often referred to as a ‘spike’ tip. One method of producing these tips is to utilise electron assisted deposition in a SEM to produce a sharp spike on top of a standard AFM tip, as demonstrated by Rührig *et al* (1996). This can produce spikes of small (10s of nm) diameter, and the length can be controlled by varying the exposure time. One problem with this method is that the quality of the spike depends on the stability of the electron optics and mechanical systems of the SEM. The stability becomes more critical for longer exposure times.

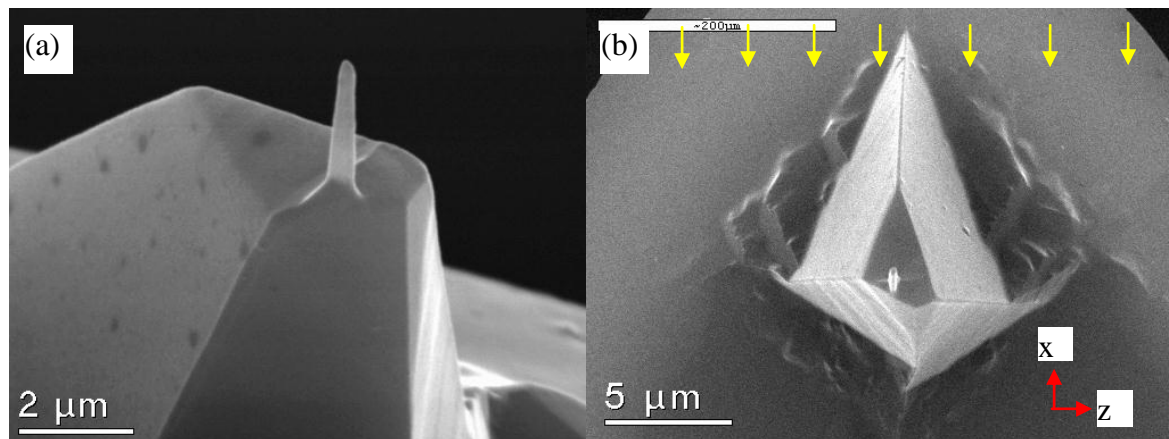
Another method to produce spike tips can be realised by using FIB milling to alter the shape of a standard AFM tip. In this case most of the material near the tip apex is milled away to leave a spike, which can be machined to the dimensions required. In general FIB milled spikes are not as sharp as deposited spikes, but the control achievable using the FIB is usually better, and so longer spikes can be milled with greater precision. It is worth noting that both these techniques process a single tip at a time, and so commercially available spike tips tend to be much more expensive than standard batch processed tips. One other drawback of spike tips is that, as might be expected, they tend to be more fragile than standard tips. This is not a problem for the third type of spike tip, which is produced by attaching a carbon nanotube to a tip, creating a very sharp and resilient spike tip. Again, the problem with this tip type is that each tip has to be produced individually, as discussed by Stevens *et al* (2000).

Coating a spike AFM tip with magnetic material gives a MFM tip, which in addition to the advantages already mentioned above, is well-suited to MFM use. The shape anisotropy effect conferred by the spike portion of the tip means that the magnetisation of the spike should be constrained to the long axis of the spike, i.e. either up or down. In the

ideal case, the spike should act as a small bar magnet, with magnetic charges only at the ends. The result of this would be a MFM tip with a localised magnetic charge at the tip apex, meaning that the tip could effectively act as a monopole, and thus the point probe approximation could be used to analyse the signal, as described in Chapter 3. There will be a compensating charge distribution of opposite sign at the other end of the spike, of course, but if the spike is long enough this could be ignored in many cases.

The localisation of the magnetic charge also implies that the resolution of spike MFM tips is potentially higher than normal MFM tips. Another advantage of a spike MFM tip is that the volume of magnetic material is less than for a comparable pyramidal tip. Thus magnitude of the stray field from the spike tip will tend to be lower, which is desirable when imaging low coercivity samples (although the signal from a spike tip will be lower as well as a consequence).

These advantages have motivated several groups to investigate spike MFM tips. For examples of results obtained using such tips see Hug *et al* (1998) or Skidmore and Dahlberg (1997), and references therein. Here we examine spike MFM tips that have been supplied to us by Liesl Folks at the IBM Almaden Research Centre. These tips have been made using FIB milling to machine a spike out of a standard Nanosensors single crystal silicon AFM tip. The geometry of the tips is shown by the SEM micrographs in Fig. 5.10.



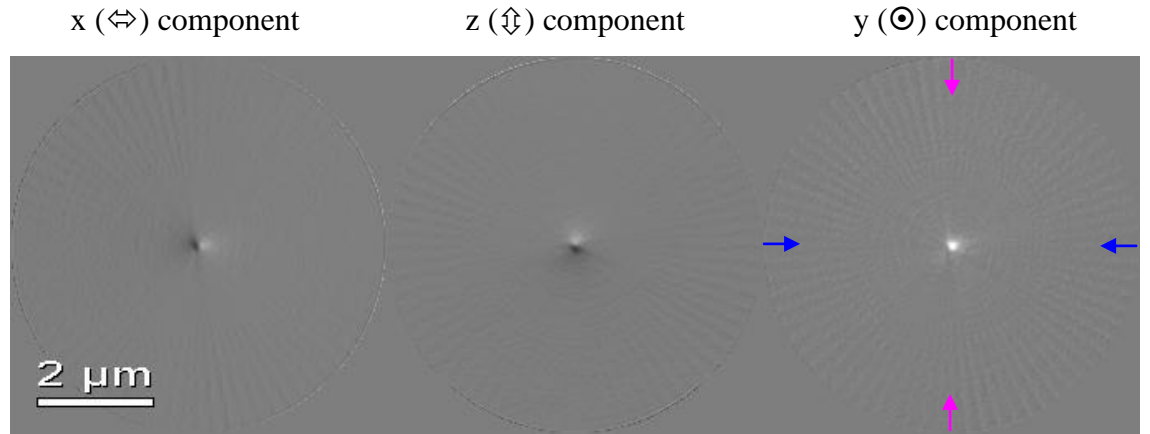
**Figure 5.10.** SEM micrographs of a spike MFM tip produced by FIB milling. The spike is  $\sim 250$  nm wide, and has been coated with 25 nm of Co, on the front-facing parts of the tip only (The yellow arrows in (b) show the direction of the incident Co flux). The coordinate system shown in (b) corresponds to the coordinate axes in the following reconstructions (i.e. in the reconstructions the tip is rotated  $90^\circ$  anticlockwise relative to (b)).

The spike on this tip is approximately 2  $\mu\text{m}$  in length and 250 nm wide. After the FIB milling the tips were coated by evaporation with 25 nm of Co. The evaporated metal was incident on the front side of the tip, i.e. in Fig. 5.10b the evaporated metal would travel in the  $-x$  direction. Thus the spike was coated on one side only. The tomographic field reconstructions from two of these tips are presented here. A third tip of this type was

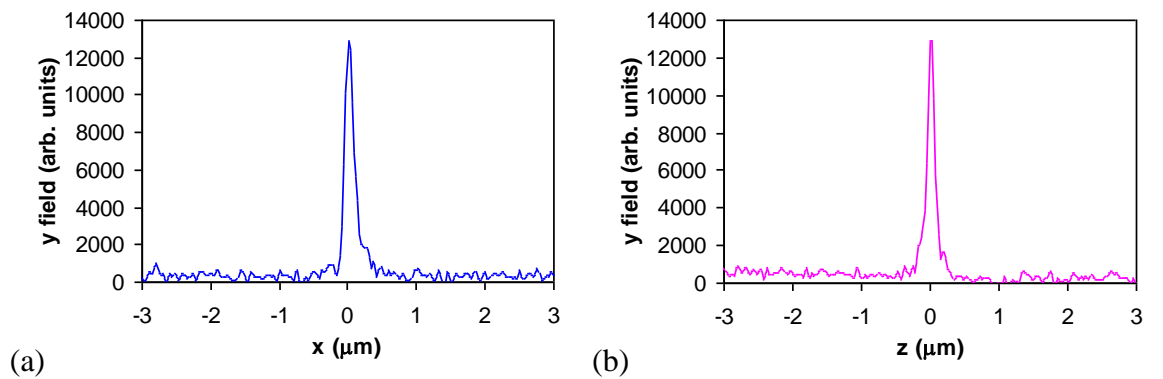
also examined, and used to investigate the effect of electrostatic charging on the reconstruction process. The results for that tip can be found in Chapter 6.

### 5.3.1 Spike tip 1

This tip was magnetised along the tip axis by an NdFeB permanent magnet before imaging. Tomographic data for this tip was taken over a rotation range of  $270^\circ$ , as there was initially some worry about the consistency of the data. Thus when the data was later analysed for evidence of charging an overlap range of  $90^\circ$  could be used. This resulted in a determination of the electrostatic DPC signal over the  $90^\circ$  range, and helped confirm the hypothesis discussed in Chapter 6, namely that given identical imaging conditions tips tend to exhibit the same charging behaviour. The electrostatic DPC signal in this case was roughly equal in magnitude and shape to the magnetic signal, in other words a non-negligible contribution. The reconstruction of the tip field is shown in Fig. 5.11, and linescans are shown in Fig. 5.12.



**Figure 5.11.** Field reconstruction of spike MFM tip (tip #1) magnetised along tip (y) axis. The orientation of the cantilever is the same as shown in Fig. 5.2, and the arrows on the z and y field components show where the linescans are taken from.

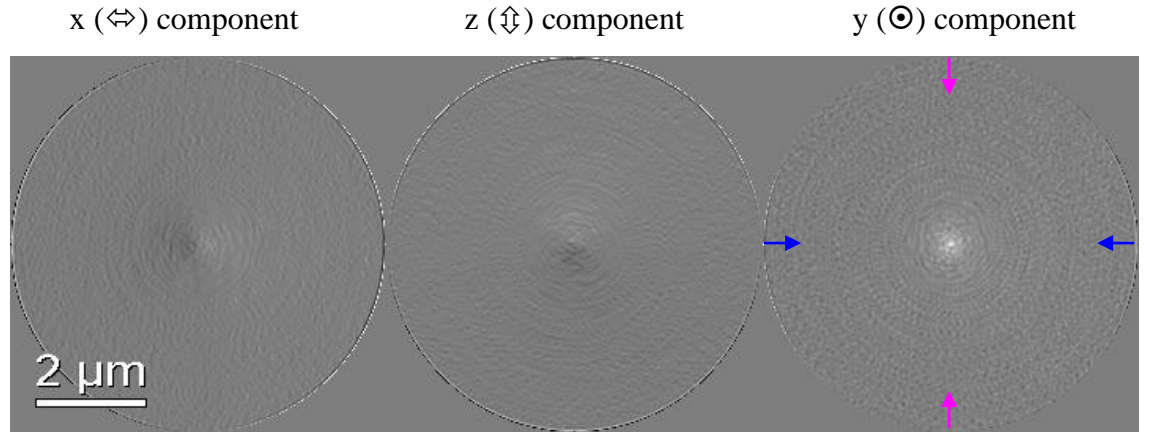


**Figure 5.12.** Linescans of the y field component of the spike MFM tip (tip #1) magnetised along the y axis. (a) is taken along the x axis, and (b) is taken along the z axis.

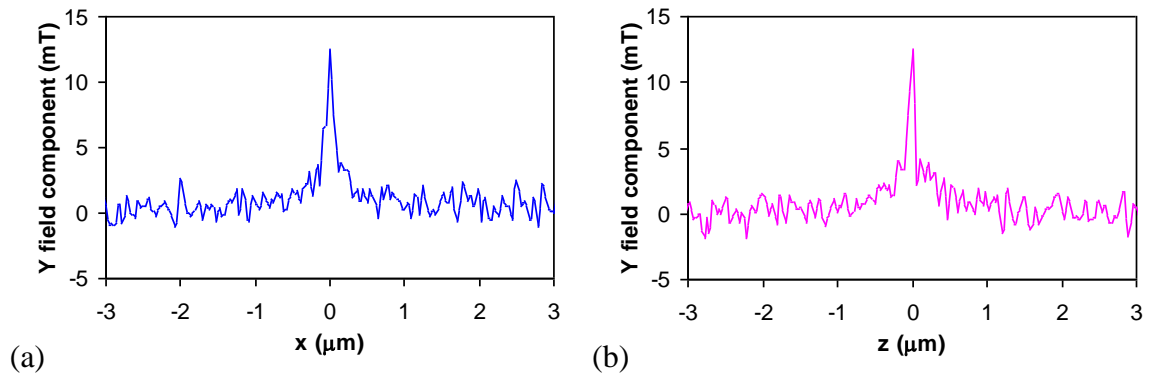
Field calibration data was not available for this study, but the results are still of interest. There is a sharp and well-defined peak in the centre of the reconstruction, with y field component FWHMs of 170 nm in the x direction and 140 nm in the z direction. The magnitude of the field is not calibrated, but comparison with the other two tips of this type (in the next subsection and in Chapter 6) suggests a peak field of 10 – 20 mT. One other notable feature of this tip is the almost complete absence of background field. Although all forward facing parts of the tip and cantilever were coated, the lower part of the tip and the cantilever do not seem to contribute significantly to the tip field.

### 5.3.2 Spike tip 2

This tip was magnetised in the same manner as the previous example, and a normal tomographic dataset was taken. In this instance there was significant electrostatic charging of the tip, however, when this was removed the field from the tip was found to consist of a sharp, localised peak. The field reconstruction is shown in Fig. 5.13, and linescans are shown in Fig. 5.14.



**Figure 5.13.** Field reconstruction of spike MFM tip (tip #2) magnetised along tip (y) axis. The orientation of the cantilever is the same as shown in Fig. 5.2, and the arrows on the z and y field components show where the linescans are taken from.



**Figure 5.14.** Linescans of the y field component of the spike MFM tip (tip #2) magnetised along the y axis. (a) is taken along the x axis, and (b) is taken along the z axis.

As noted, the main feature present is a sharp peak in the y field component. The maximum y field value is ~12 mT in this case, and the peak has FWHMs of 110 nm in the x direction and 170 nm in the y direction. In this case there is some field present out to a radius of 1  $\mu\text{m}$ , this may be due to field sources further down the spike. As with the previous FIB'ed tip, the cantilever does not appear to contribute significantly to the field at the level of the tip apex.

### 5.3.3 Conclusions

The ion milling of the tips studied here has certainly not compromised the sharpness of the stray field distribution, and therefore the magnetic spatial resolution. Indeed, in the case of tip 2 the modifications may have actually increased the resolution compared to a standard MFM tip. Another benefit of these tips is the comparative lack of background field. As already mentioned, this is due to the fact that the Co deposited on the spike feature acts as a high aspect ratio magnetic element, and is expected to be magnetised along the long axis (=tip axis) due to the effect of shape anisotropy. Thus magnetic charges will only occur at the ends of the spike. As the charge at the base of the spike is relatively far away (~2  $\mu\text{m}$ ) it will not contribute significantly to the field at the tip apex. Thus the tip can be considered as an approximation to a monopole.

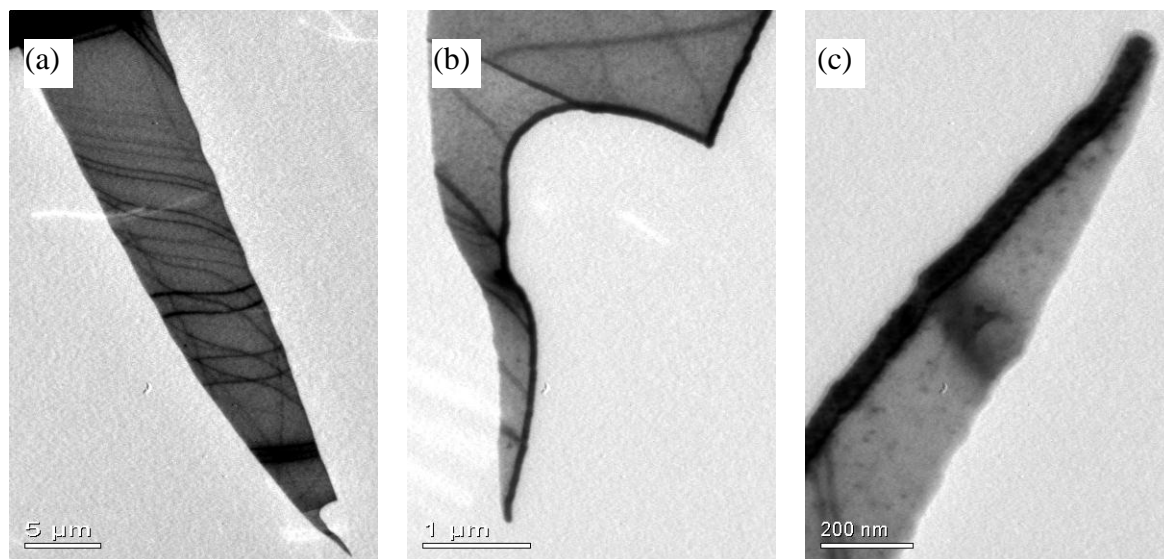
The magnitude of the field generated by these tips is generally about four times less than standard MESP tips (McVitie *et al*, 1997), and this would make them suitable for imaging low coercivity samples. The shape of the tips also means that they can be used to image in narrow trenches or similar, and this could be of benefit when imaging samples such as MRAM devices, where the magnetic elements are part of a complex structure. As discussed previously, these tips are produced individually, and so are more expensive to make. One additional problem specific to this type of spike tip is the loss of mechanical strength entailed by the removal of tip material. Thus these tips will be somewhat fragile, and so are not well suited to general usage.

## 5.4 IBM ultrasensitive tip

The force sensitivity of AFM and MFM probes is related to the spring constant of the cantilever. The benefit of using low spring constant probes for MFM is that lower forces or force gradients can be detected. This means that magnetic materials with low saturation magnetisation values can be imaged, where standard cantilevers might not yield adequate results. Alternatively, MFM tips with smaller stray fields than normal could be used to image low-coercivity samples, where standard tips tend to perturb the sample

magnetisation. Also, it has been proposed that MFM could be used to detect single-spin magnetic resonances, in a technique termed magnetic resonance force microscopy (MRFM) - see Züger *et al* (1996) for an introduction to this technique. MRFM requires detection of forces in the attonewton ( $10^{-18}$ ) regime, and for this purpose thinned single crystal silicon cantilevers have been produced by Stowe *et al* (1997), amongst others. Stipe *et al* (2001) have used these cantilevers to measure dissipation in nanometer sized ferromagnetic particles and wires. H J Mamin of IBM Almaden provided two tips of this type for study. Unfortunately one was broken in transit, but the other tip was unharmed and is studied here.

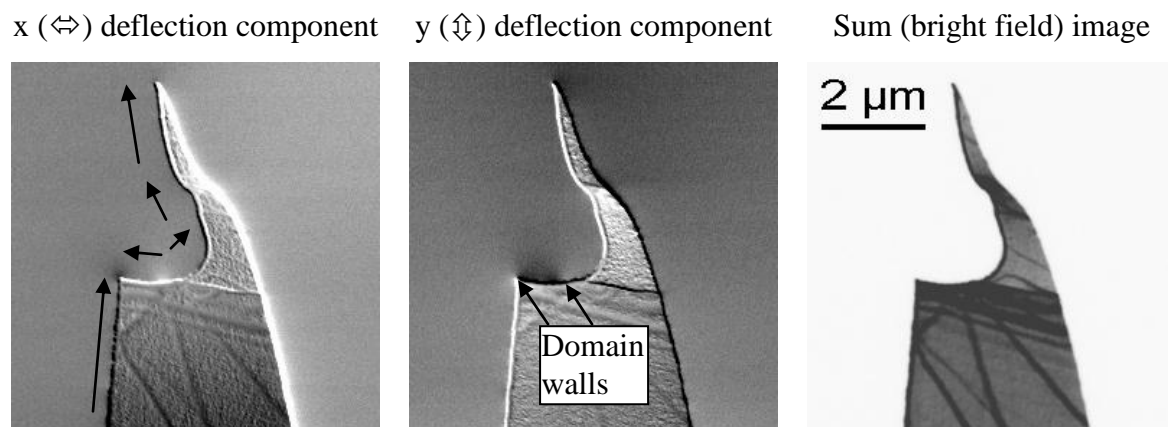
The cantilever studied was etched from a single crystal silicon substrate, and consists of a blade of material about 40  $\mu\text{m}$  long, 9  $\mu\text{m}$  wide at the base and tapering to a point at the free end. TEM micrographs of the cantilever are displayed in Fig. 5.15. The thickness of the cantilever at the tip is about 30 nm. The sidewall of the cantilever was coated by evaporation with Co, and capped with a few nm of Pt to inhibit oxidation. This resulted in a Co wire running down one side of the cantilever, and this can be seen as a dark line in the TEM images. The width of the wire is approximately 60 nm, and the tip radius at the end of the cantilever is about 30 nm. There appears to be a piece missing from the end of the cantilever, resulting in a very narrow cantilever width for a distance of  $\sim 5$   $\mu\text{m}$  from the apex. This shape is not intentional; the cantilever should be essentially triangular, as shown by Stowe *et al* (1997).



**Figure 5.15. TEM micrographs of ultrasensitive tip.** The dark feature along the edge of the cantilever is a Co nanowire, capped with Pt (can be seen in (b) and (c) only). In image (a) the edge of the substrate that the cantilever projects from can just be seen (top right corner). The white marks on the images are artefacts of the CCD camera.



The cantilever was magnetised along its long axis in a field of 1 T. DPC images of the cantilever subsequent to this show the magnetisation of the Co wire (Fig. 5.16). It was found that the wire was magnetised in one direction for most of its length. However, an oppositely magnetised domain of just under 1  $\mu\text{m}$  in length was found at the corner 5  $\mu\text{m}$  from the tip apex. This can be seen clearly in Fig. 5.16b, as the stray field changes sign just above the domain walls. The inferred direction of magnetisation of the wire is shown using arrows in Fig. 5.16a. Some images taken after subsequent reverse magnetisations (again along the main cantilever axis) exhibited several domains in this area, but in all cases the segments of wire close to the magnetisation direction were uniformly magnetised.



**Figure 5.16.** DPC images of the ultrasensitive tip magnetised along the tip axis (the y axis in these images). The inferred magnetisation of the Co nanowire is shown by the arrows on the x deflection image. The strong x deflection signal on the uncoated (right) edge of the cantilever is due to electrostatic charging.

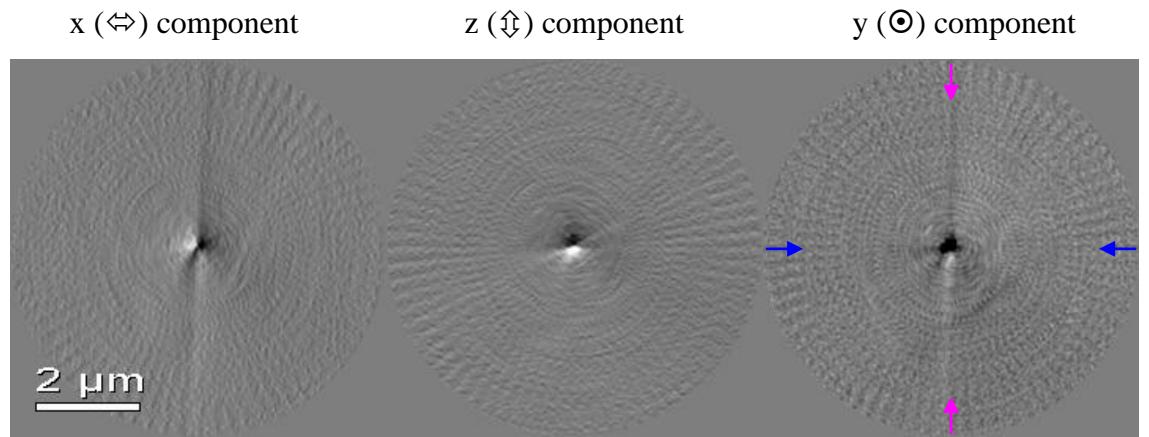
Also evident in Fig. 5.16a is a significant degree of electrostatic charging, running down the uncoated (right hand) edge of the cantilever. It was felt that any further coating with Au to try and reduce the charging was not practicable, as this could easily bend or even break the cantilever.

Despite the evident charging a tomographic study of the tip was performed. In the event the magnitude of charging was not as great as feared, probably because during the study the electron beam was confined to the tip apex region of the sample, which as can be seen in Fig. 5.15c was predominantly composed of Co metal. Unfortunately, the electrostatic charging was found to be centred off the rotation axis, and so it was not possible in this case to subtract the electrostatic effects. This problem could have been solved by obtaining a 360° tomographic dataset. However, this study was performed some time before the method of separating out electrostatic and magnetic effects was developed (discussed in Chapter 6), and so the required data was not taken. The magnitude of the electrostatic DPC signal was approximately 2/3 of the magnetic signal.

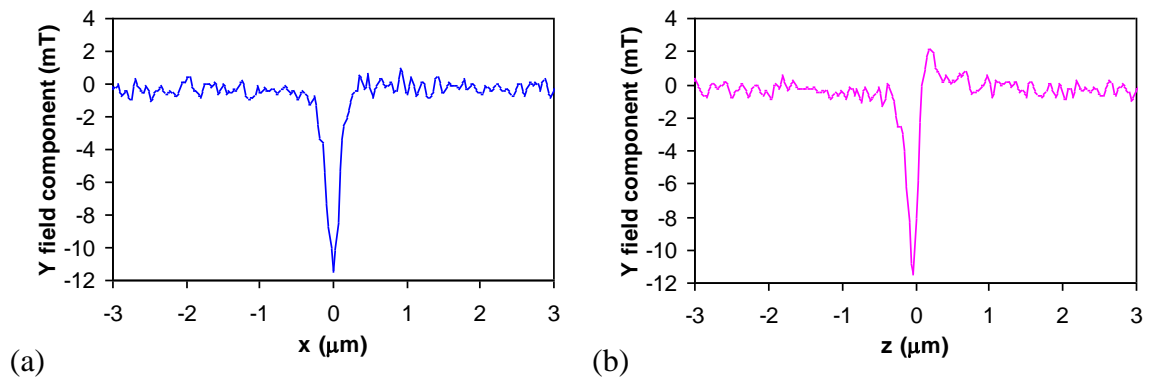


Nonetheless, the results of this study are still useful. The reconstructions of the cantilever tip field are shown in Fig. 5.17, and the linescans are shown in Fig. 5.18. There is an obvious field peak in the centre of the reconstruction, in addition to the vertical ‘tails’ characteristic of electrostatic charging artefacts. The FWHMs of the field peak are 200 nm in the x direction and 180 nm in the y direction. Note that the y FWHM value is likely to be affected by the charging artefacts. The peak magnitude is about 11 mT, although the charging present will affect this value it should still be accurate to somewhat less than an order of magnitude.

This tip therefore seems to be well suited to high sensitivity MFM and MRFM. One study that has been performed with this tip type is discussed by Stipe *et al* (2001). In this case the properties of the magnetic material on the tip itself were investigated, rather than using the tip to investigate other materials. Actual MRFM studies are rare at the moment, given the instrumental requirements and the novelty of the technique.



**Figure 5.17.** Field reconstruction of the ultrasensitive tip, magnetised along the tip axis. The vertical streaking in the images is caused by electrostatic charging.

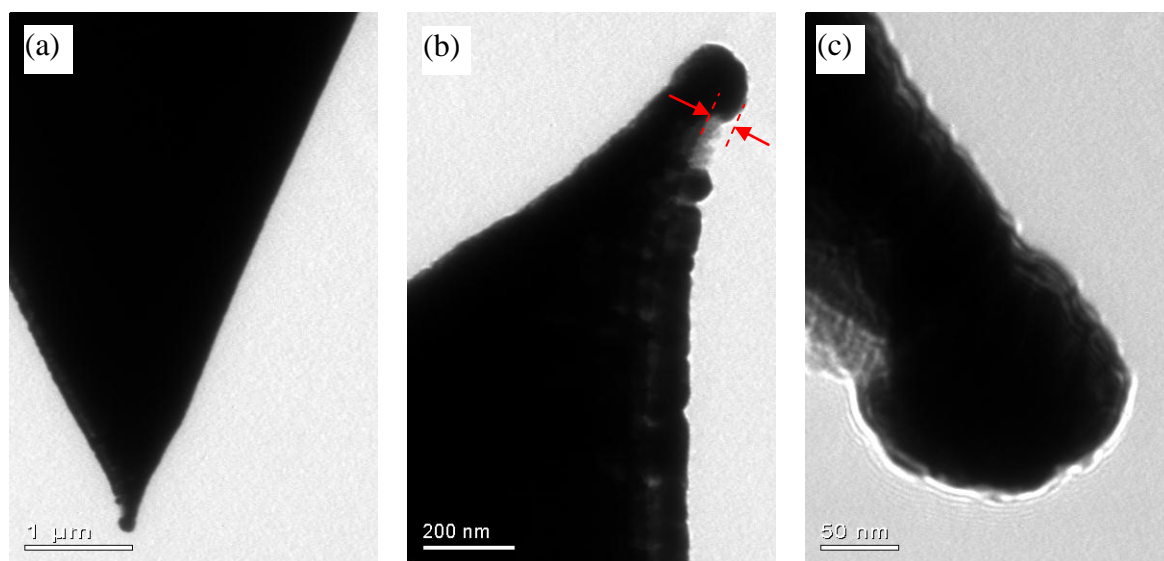


**Figure 5.18.** Linescans of the y field component of the ultrasensitive tip, magnetised along the tip axis. (a) is taken along the x axis, and (b) is taken along the z axis.

### 5.5 High $H_c$ tip

As discussed in Chapter 3, the analysis of MFM data normally rests on the assumption that the magnetisation of the tip and the sample do not affect each other (or more realistically, that any perturbations are negligible compared to the noise of the system). When imaging samples such as hard disk media it is usually the case that the field from the tip is not strong enough to perturb the sample magnetisation, and vice-versa. However, the coercivity of standard CoCr coated MFM tips has been measured by Babcock *et al* (1996) as about 400 Oe. For some types of samples (such as hard disk write heads or NdFeB permanent magnet materials) there is a danger that the coercivity of the tip will be approached or exceeded, resulting in hysteresis artefacts in the MFM image. Clearly, a tip coating with higher coercivity than CoCr is desirable for these cases. One obvious choice would be an NdFeB-based material, however this material is difficult to deposit on three-dimensional shapes such as tips. The tip examined was kindly supplied by S H Liou of Nebraska University, and is coated by sputtering with a CoPt alloy which has a saturation magnetisation of  $800 \text{ kAm}^{-1}$  in bulk form, and about  $400 \text{ kAm}^{-1}$  for films of  $\sim 100 \text{ nm}$  thickness. The coercivity of the tip has been measured as 1.5 T. Details of the development of this tip are given by Liou and Yao (1998). The tip had been magnetised after manufacture in a field of 5.5 T, directed along the tip axis.

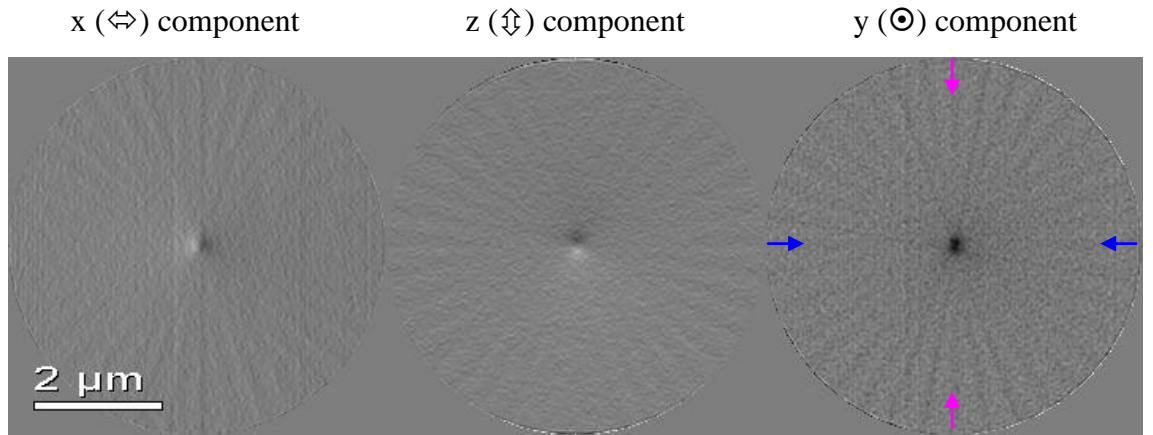
TEM micrographs of the tip are shown in Fig. 5.19. The radius of curvature of the tip apex was measured as 70 nm. As the coating is missing on one side of the tip (just below the tip apex) it was also possible to measure the film thickness at this point; the thickness is 70 nm.



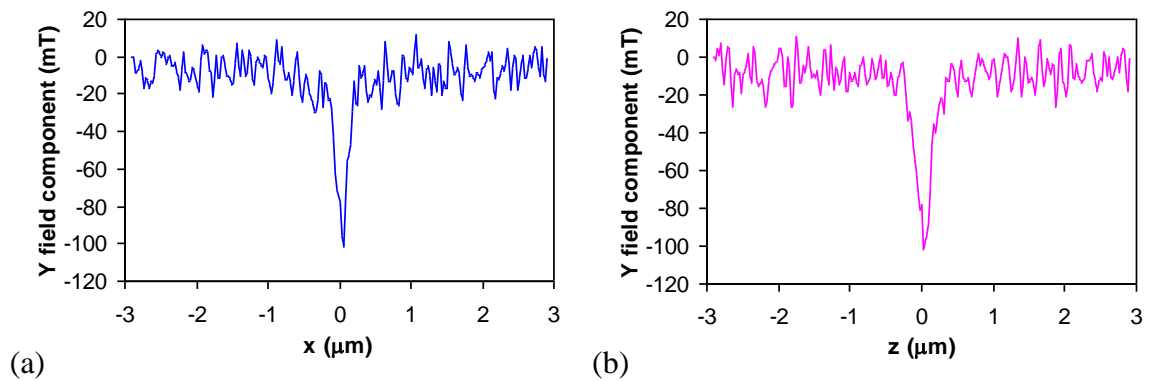
**Figure 5.19. TEM micrographs of the high  $H_c$  tip. The arrows in (b) show where the thickness of the coating was measured.**

The tomographic study of this tip is notable for several reasons, not least the fact that the HM (high magnification) scanning mode was used. As discussed in Chapter 2, this

mode differs from the normal LM mode (which was used for all other tomographic studies in this thesis) by utilising the small pre-specimen lens (the upper Lorentz lens) embedded in the main objective lens of the CM20 to give a smaller probe size. The disadvantage of this mode is that as the probe convergence angle is larger than in the LM mode, the HM DPC mode is less sensitive to field (the interplay of probe size, convergence angle and sensitivity is discussed in Chapter 2). This mode was used in this case partly as an experiment, as no tomographic studies had been performed with HM mode previously. In particular, it was felt that in future, higher resolution tomographic studies would be desirable, and this would not be possible with the LM DPC mode, as in this case the minimum usable probe size is  $\sim 30$  nm, i.e. approximately the same size as the resolution used in the proceeding tomographic studies. Hence reducing the pixel size in LM mode would not provide much benefit. As this tip was expected to have a strong stray field given the properties and thickness of the coating, it was felt that it would be an ideal first subject for the lower sensitivity HM DPC mode. The resulting field reconstructions bear this out; these are shown in Fig. 5.20, and the corresponding linescans are shown in Fig. 5.21.



**Figure 5.20.** Field reconstruction of the high  $H_c$  tip, magnetised along the tip ( $y$ ) axis. The orientation of the cantilever is the same as shown in Fig. 5.2, and the arrows on the  $z$  and  $y$  field components show where the linescans are taken from.



**Figure 5.21.** Linescans of the  $y$  field component of the high  $H_c$  tip, magnetised along the tip axis. (a) is taken along the  $x$  axis, and (b) is taken along the  $z$  axis.

The peak field is 100 mT, and the FWHM is ~200 nm for both x and z directions. Thus, despite the thickness and roughness of the magnetic coating, the results indicate that this tip would give reasonable MFM resolution. Another notable feature of this tip was that there was no observable electrostatic charging present, and so a correction for charging was not required in this instance. It is suspected that the absence of charging may be due to the thickness of the coating, resulting in a highly conductive tip.

One further point to note is the relatively high noise level in the reconstructions. Again, this is a consequence of the smaller probe convergence angle  $\alpha$ , as discussed above and in Chapter 2.

## 5.6 Conclusions

Various tips that have been shaped or coated for a specific purpose have been studied here. The purpose of the FIB-modified tip from Seagate is to provide a localised field source approximately parallel to the sample plane in the MFM. The results shown here seem to indicate that this state can be achieved, but there is a question mark over the magnetic stability of this configuration. Another tip of this type was also studied, but in this case the effects of electrostatic charging were severe, and so the results from this tip are not shown here.

Three spike MFM tips produced by FIB milling have been studied, and the results have been presented here and in Chapter 6. In all cases the field was found to be smaller in magnitude than standard MFM tips, with a very low background field. The spatial resolution of these tips appears to be as good or better than standard tips. Thus the modifications made are largely beneficial. The main challenge with these tips is to make the production process more economical.

The ultrasensitive tip is an example of a completely different design of tip, intended to increase the sensitivity of MFM by orders of magnitude. The magnetic properties of this tip are satisfactory, with what is effectively a small monopole at the tip of a thin cantilever. In the example studied there appeared to be a piece missing from the end of the cantilever, resulting in a sharp corner in the deposited Co nanowire. When the tip was magnetised this resulted in a multidomain configuration around the corner region, which resulted in stray field from the area. However, due to the distance (~ 5  $\mu\text{m}$ ) separating these field sources from the tip apex they would probably not affect the imaging properties of the tip significantly.

The CoPt coated tip is the only example here of a tip of conventional shape but novel coating. The results indicate that this is a tip of reasonable resolution and strong stray field. The strength of the stray field could be a problem when imaging samples, and

ideally would be decreased by depositing thinner coatings on the tip. However, the TEM images of this tip indicate that the CoPt film is quite lumpy in texture, implying that thinner coatings could result in incomplete or uneven coverage of the tip. Nonetheless, an attempt to produce a thinner coating would seem a worthwhile experiment.

## References

- Babcock K L, Elings V B, Shi J, Awschalom D D and Dugas M (1996), "Field-dependence of microscopic probes in magnetic force microscopy", *Appl. Phys. Lett.*, **69**, 705-707
- Folks L, Best M E, Rice P M, Terris B D, Weller D and Chapman J N (2000), "Perforated tips for high-resolution in-plane magnetic force microscopy", *Appl. Phys. Lett.*, **76**, 909-911
- Hug HJ, Stiefel B, van Schendel PJA, Moser A, Hofer R, Martin S, Guntherodt HJ, Porthun S, Abelman L, Lodder JC, Bochi G and Handley RC (1998), "Quantitative magnetic force microscopy on perpendicularly magnetized samples", *J. Appl. Phys.*, **83**, 5609-5620
- Liou S H and Yao Y D (1998), "Development of high coercivity magnetic force microscopy tips", *J. Magn. Magn. Mater.*, **190**, 130-134
- McVitie S, Ferrier R P and Nicholson W A P (1997), "Absolute field strength determination of magnetic force microscope tip stray fields", *Inst. Phys. Conf. Ser.*, **153**, 201-204
- Qian C X, Tong H C, Liu F H, Shi X, Dey S, Proksch R B, Nielson P and Hachfeld E (1999), "Characterization of high density spin valve recording heads by novel Magnetic Force Microscope", *IEEE Trans. Magn.*, **35**, 2625-2627
- Rice P and Russek S E (1999), "Observation of the effects of tip magnetization states on magnetic force microscopy images", *J. Appl. Phys.*, **85**, 5163-5165
- Rührig M, Porthun S, Lodder J C, McVitie S, Heyderman L J, Johnston A B and Chapman J N (1996), "Electron beam fabrication and characterization of high-resolution magnetic force microscopy tips", *J. Appl. Phys.*, **79**, 2913-2919
- Skidmore G D and Dan Dahlberg E (1997), "Improved spatial resolution in magnetic force microscopy", *Appl. Phys. Lett.*, **71**, 3293-3295
- Song D, van Ek J, Amin N, Mao S N, Louder D and Schultz A (1999), "Magnetization in a spin valve head mapped by an MFM tip", *IEEE Trans. Magn.*, **35**, 667-670

- Stevens R, Nguyen C, Cassell A, Delzeit L, Meyyappan M and Han J (2000), "Improved fabrication approach for carbon nanotube probe devices", *Appl. Phys. Lett.*, **77**, 3453-3455
- Stipe B C, Mamin H J, Stowe T D, Kenny T W and Rugar D (2001), "Magnetic dissipation and fluctuations in individual nanomagnets measured by ultrasensitive cantilever magnetometry", *Phys. Rev. Lett.*, **86**, 2874-2877
- Stowe T D, Yasumura K, Kenny T W, Botkin D, Wago K and Rugar D (1997), "Attonewton force detection using ultrathin silicon cantilevers", *Appl. Phys. Lett.*, **71**, 288-290
- Züger O, Hoen S T, Yannoni C S, and Rugar D (1996), "Three-dimensional imaging with a nuclear magnetic resonance force microscope", *J. Appl. Phys.*, **79**, 1881-1884

## Chapter 6. Artefacts in Lorentz electron tomography

### 6.1 Introduction

In this chapter some of the operational difficulties that can arise when performing Lorentz electron tomography will be discussed. In section 6.2 the effects of electrostatic charging of the sample will be simulated, to illustrate the influence these effects have on tomographic reconstruction. A method for separating electrostatic and magnetic effects is presented in section 6.3, and an experimental case study is shown in section 6.4. In section 6.5 the effects of angular misalignment of the DPC detector are discussed. Section 6.6 illustrates the problems incurred when both charging is present and the DPC detector is misaligned. Conclusions are drawn in section 6.7.

### 6.2 Modelling electrostatic charging artefacts

As with other methods of electron microscopy, electrostatic charging of samples can cause problems in Lorentz microscopy. Charging can occur if the sample itself is poorly conductive, or if the sample is contaminated with poorly conducting debris. Most MFM tips are coated with some form of reasonably conductive metallic alloy such as Co, CoCr, NiFe etc. Even metallic glassy alloys such as the METGLAS compound ( $\text{Fe}_{81}\text{B}_{13.5}\text{Si}_{3.5}\text{C}_2$ ) used to coat the tips examined in Chapter 4 are expected to be reasonably conductive, given the concentration of Fe present. One coating type that might be expected to cause charging problems would be the superparamagnetic-like coatings used by Liou *et al* (1997), as these consist of small magnetic particles surrounded by a insulating matrix. (It should be pointed out, however, that performing tomographic studies on this type of tip would be a pointless exercise, as a true superparamagnetic tip would have no remanent stray field to image.)

A more common cause of charging arises from contamination of the sample. If a tip has previously been used in the MFM, it is quite common to observe small particles of dust attached near the end of the tip (picked up from dust on sample surfaces in the MFM). If these particles are poorly conductive they can charge in the electron beam and cause severe charging problems. Contamination can also occur if the beam of the electron microscope is scanned over a small area of the tip for long periods, causing electron beam induced material deposition from residual gases in the microscope vacuum system. The presence of moderate or heavy contamination is usually obvious when inspecting the

bright field images of the tip. However, the vacuum in the CM20 STEM is normally good enough that with care, beam-induced contamination can be minimised.

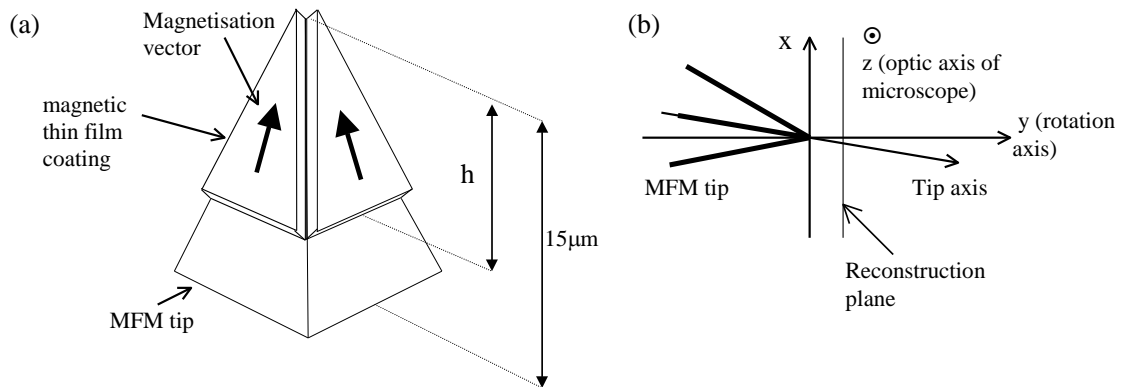
As stated in Chapter 2, when performing DPC in a STEM, the deflection signals depend on the interaction of an electron beam with the magnetic and electrostatic fields produced by the sample. The relevant equation is repeated here for reference (see Chapter 2 for the relevant symbols and coordinate system).

$$\beta_{x,y} = \frac{e\lambda}{h} \int_{-\infty}^{\infty} B_{y,x} dz + \frac{1}{2V_{accel}} \int_{-\infty}^{\infty} E_{x,y} dz. \quad (6.1)$$

In any individual DPC image it is often impossible to separate the magnetic and electrostatic effects, making interpretation of these images difficult. In the following sections these problems are illustrated by numerical modelling.

### 6.2.1 The model MFM tip

The magnetic DPC data used in this section was calculated by Gallacher (1999) using a simple tip model. This model consists of a number of thin triangular prisms assembled to form a pyramidal tip, as can be seen in Fig. 6.1. The prisms can be uniformly magnetised in various directions, but for the purposes of this investigation a simple configuration was used, whereby the magnetisation of each prism lay in the plane of the prism, and pointed towards the tip apex.



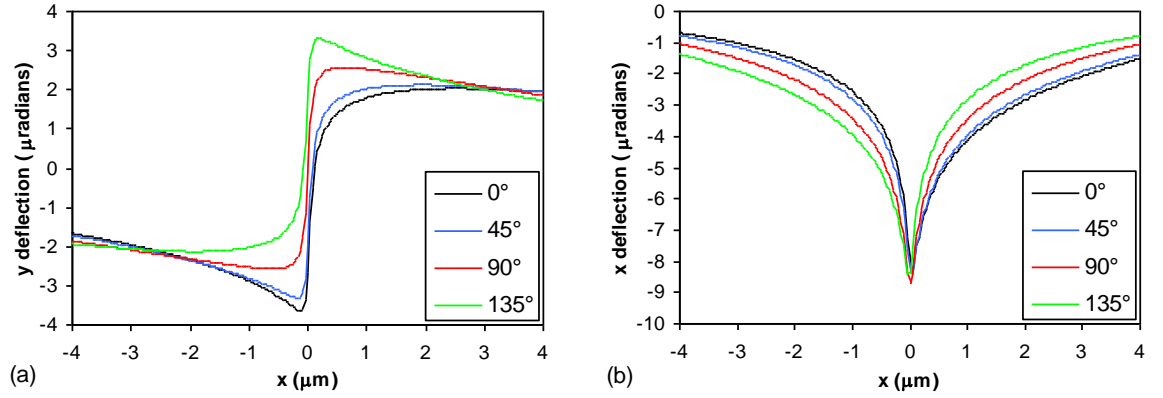
**Figure 6.1.** Diagram showing (a) configuration of model MFM tip used for simulations and (b) orientation of tip in the STEM for tomography. The tip axis makes an angle of 12.5° with the y (rotation) axis.

The magnetostatic charges resulting from the magnetisation were calculated using the equation

$$\rho = \mathbf{M} \cdot \mathbf{n} \quad (6.2)$$



where  $\rho$  is the charge density on the surface concerned,  $\mathbf{M}$  is the magnetisation vector and  $\mathbf{n}$  is the surface normal. From the resulting charge distribution the stray field from the tip could be calculated at any point. Integrating the field over the appropriate path then allows the DPC signal to be calculated. The MFM tip apex was located on the rotation axis at a distance 60 nm from the reconstruction plane in the model used here. Selected linescans from the resulting DPC dataset are shown in Fig. 6.2.



**Figure 6.2.** DPC linescans calculated for a distance of 60 nm in front of the model tip described in section 6.2.1, for tip rotations of 0°, 45°, 90° and 135°; (a) is the beam deflection in the y direction, and (b) is the beam deflection in the x direction.

### 6.2.2 The electrostatic model

To simulate the effects of electrostatic charging of the tip described in the previous section, a point monopole model was used for simplicity. More complex models were also considered, but the experimental study presented in section 6.4 shows that a point model appears to be a reasonable simplification of the tip charge distribution. The field from an electrostatic monopole (in Cartesian coordinates) located at the origin is,

$$E_x = \frac{Qx}{4\pi\epsilon_0(x^2 + y^2 + z^2)^{3/2}}, \quad (6.3)$$

where  $Q$  is the charge and  $E_x$  is the x electric field component. There are equivalent expressions for the y and z components. To calculate the analytical DPC response from this charge the above expression is put into equation 6.1 to yield (after integration),

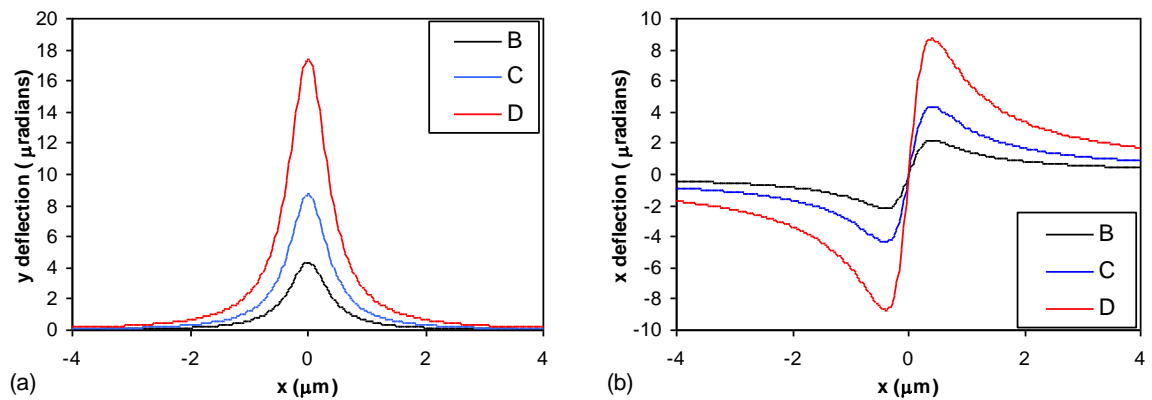
$$\beta_x = \frac{1}{2V_{accel}} \frac{Qx}{2\pi\epsilon_0(x^2 + y^2)}, \quad (6.4)$$

where  $V_{accel}$  is the accelerating voltage of the electron beam. This expression and the equivalent for  $\beta_y$  were used to calculate the DPC signal due to the charge.

The parameters of the electrostatic model were chosen so that the resulting DPC data was of similar character to experimental data taken in previous studies where charging was obviously present, due to tip contamination by charging particles. The charge was located on the rotation (y) axis, at a distance of 400 nm from the reconstruction plane. This distance gave DPC linescans with FWHMs similar to the DPC linescans from the magnetic tip model. As the charge was located on the rotation axis the DPC signal distribution was the same for all rotation angles. Charges of varying magnitude were used, as shown in Table 6.1. The DPC linescans from these charges are shown in Fig. 6.3.

Model	Electrostatic charge magnitude (C)
A	0
B	$-3.8 \times 10^{-17}$
C	$-7.8 \times 10^{-17}$
D	$-15.5 \times 10^{-17}$

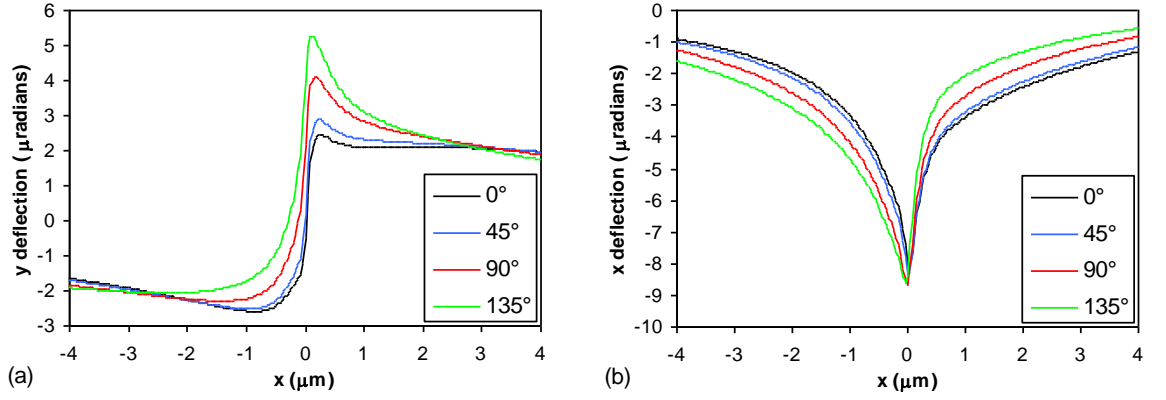
**Table 6.1.** Magnitude of electrostatic charges added to MFM model tip.



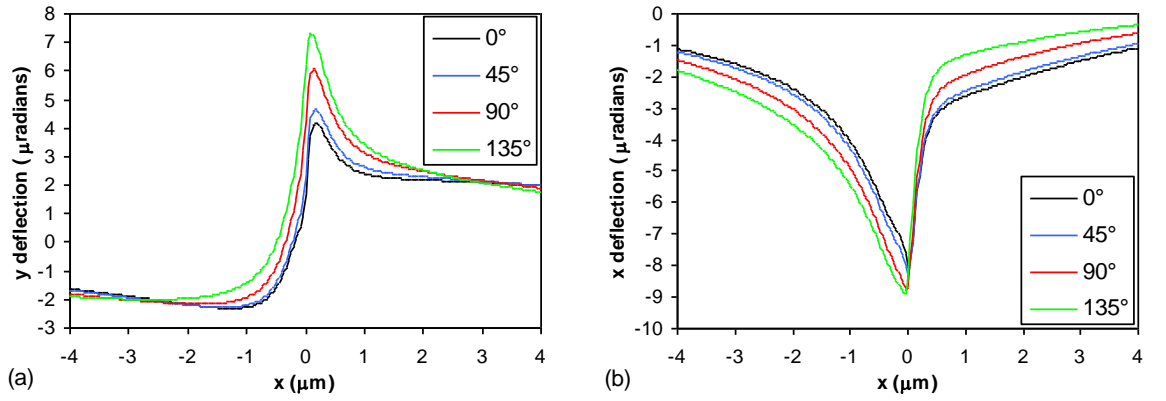
**Figure 6.3.** DPC linescans taken at a distance of 400 nm from point electrostatic charges of (B)  $-3.8 \times 10^{-17}$ , (C)  $-7.8 \times 10^{-17}$  and (D)  $-15.5 \times 10^{-17}$  C; (a) is the beam deflection in the y direction, and (b) is the beam deflection in the x direction.

The electrostatic DPC data were combined with Gallacher's magnetic data to form the complete tomographic datasets for the electrostatic charged models. Selected linescans from the resulting datasets are displayed in Figs. 6.4 – 6.6.

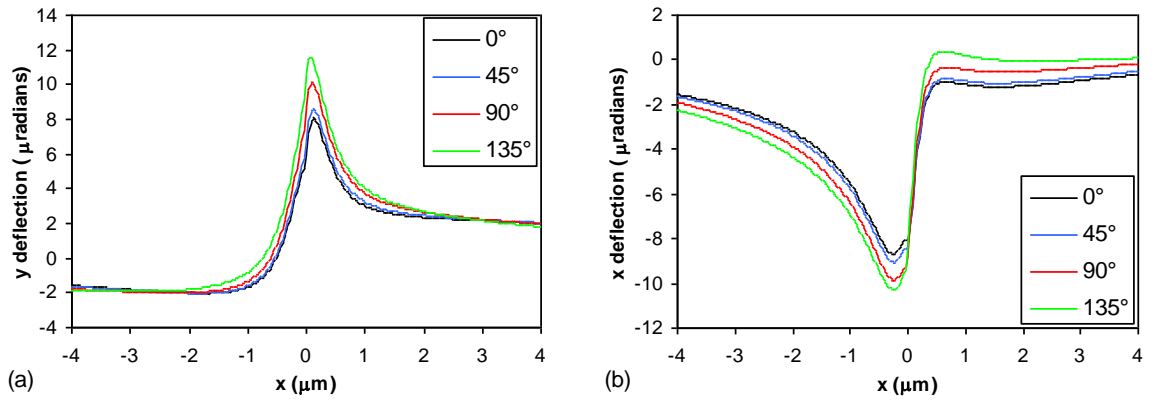
It is easy to see the increasing distortion caused by the increasing electrostatic charge. On casual inspection, the character of the linescans would appear to indicate a misaligned DPC detector (see section 6.5.1 for examples of DPC linescans where the detector is misaligned). This highlights the importance of aligning the DPC detector correctly.



**Figure 6.4.** DPC linescans from model tip B, combining the magnetic DPC traces shown in Fig. 6.2 with those from an electrostatic point charge of  $-3.8 \times 10^{-17}$ ; (a) is the beam deflection in the y direction, and (b) is the beam deflection in the x direction.



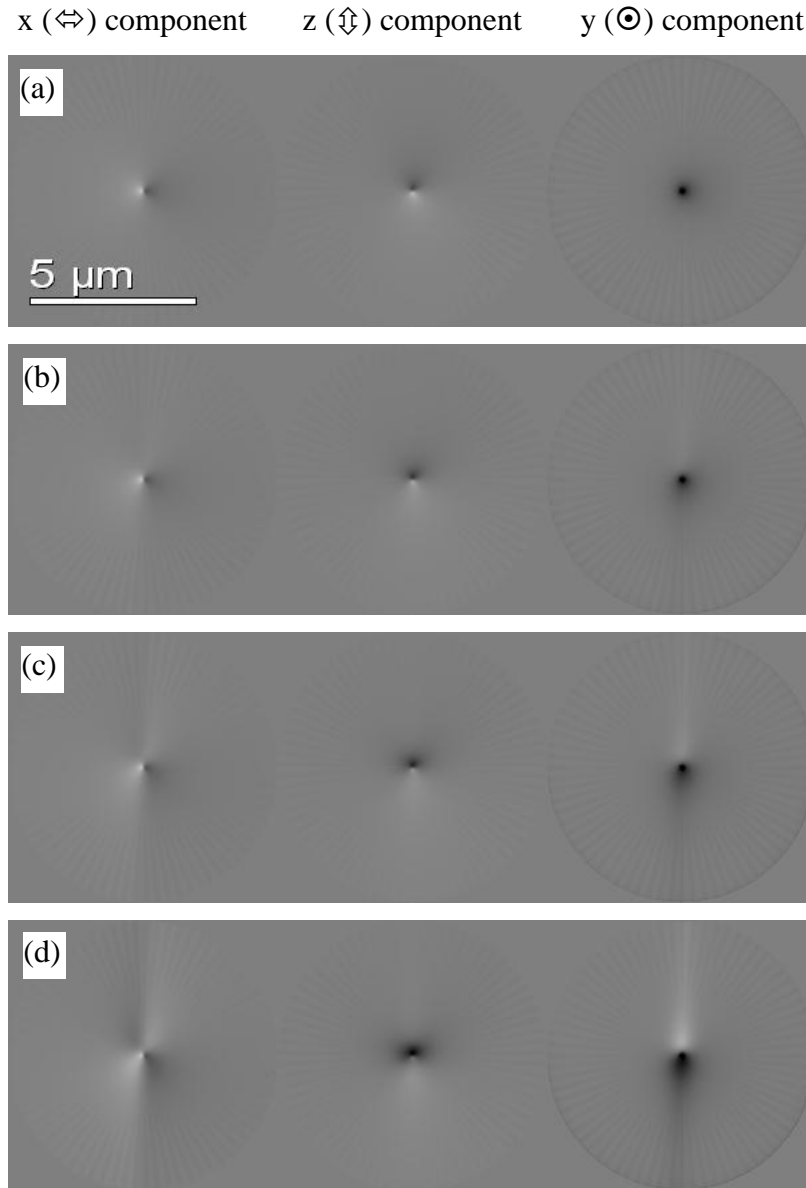
**Figure 6.5.** DPC linescans from model tip C, combining the magnetic DPC traces shown in Fig. 6.2 with those from an electrostatic point charge of  $-7.8 \times 10^{-17}$ ; (a) is the beam deflection in the y direction, and (b) is the beam deflection in the x direction.



**Figure 6.6.** DPC linescans from model tip D, combining the magnetic DPC traces shown in Fig. 6.2 with those from an electrostatic point charge of  $-15.5 \times 10^{-17}$ ; (a) is the beam deflection in the y direction, and (b) is the beam deflection in the x direction.

### 6.2.3 Effect on tomographic reconstruction

The DPC data from these models were input to the RTM tomographic algorithm. The data was treated as though it were purely magnetic in origin, i.e. the y deflection signal was fed to the y input channel of the algorithms, and similarly for the x signals. The “magnetic” fields from the models were reconstructed for all four of the datasets shown above (Figs. 6.2, 6.4 – 6.6). The reconstructed field distributions are shown in Fig. 6.7 for all four models.

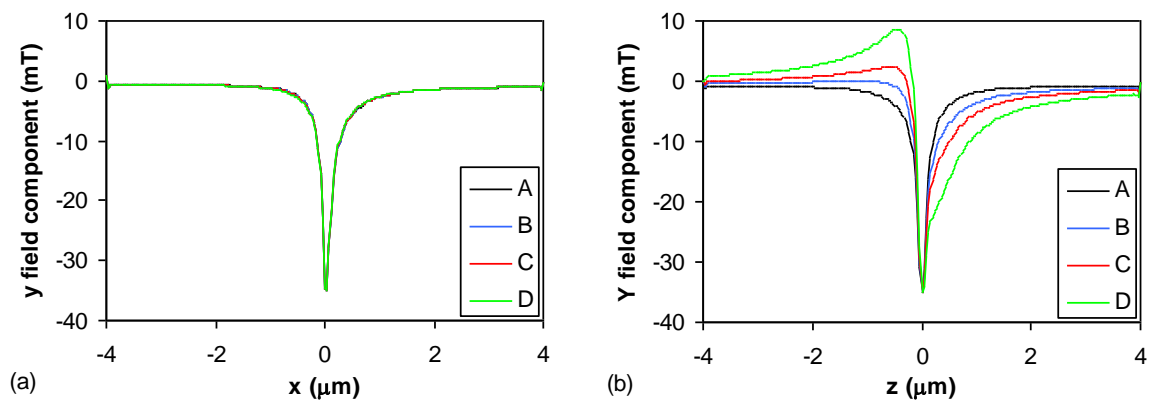


**Figure 6.7. Reconstructions of the fields from the electrostatically charged model MFM tips; (a) is the reconstruction from the uncharged tip A, (b) is for model B, (c) is for model C, (d) is for model D. Field components are (from left to right) x ( $\leftrightarrow$ ), z ( $\uparrow$ ), y ( $\odot$ ).**

As discussed in Chapter 2, Gallacher (1999) showed that the reconstruction error for the field magnitude is less than 5% using the RTM algorithm, and so the reconstruction of the magnetic-only tip model A is faithful to the actual model stray field. By contrast, it is obvious that there are significant artefacts in the reconstruction of the model with charge

added. All three reconstructed field components show a characteristic streaking effect along the  $z$  axis. As might be expected, the artefacts become more prominent with increasing electrostatic charge, and in the case of the model D, the effect dominates the field distribution. In fact, the form of the reconstructed field from tip model D could almost be interpreted as the field from a tip magnetised in the  $z$  direction. The one feature inconsistent with this interpretation is the extended tails that reach almost to the edges of the reconstruction region. Given the structure of the tip (i.e. a steep pyramid), it is very difficult to envisage a tip magnetisation distribution that would give these tails, and so this feature could be confidently labelled as an artefact, even if the field distribution of the tip was not known in advance.

Linescans of the  $y$  field component along the  $x$  and  $z$  axes of the reconstructions are shown in Fig. 6.8 for all four tip models. These linescans are taken from the  $y$  field distributions reconstructed from the  $y$  deflection DPC data. As discussed in Chapter 2, this should give the most accurate results, although in this case there is actually little difference between the reconstructions from the  $x$  and  $y$  deflection datasets, as can be seen in Fig. 6.7. The linescans along the  $z$  axis clearly illustrate the increasing distortion of the reconstruction with charge magnitude. One result, which is not obvious from inspection of the reconstructions in Fig. 6.7, but is clearly shown by the linescans in Fig. 6.8(a), is that the field reconstruction along the  $x$  axis is unaffected by the presence of electrostatic charge. Note that the asymmetry of the field that can be seen in the  $x$  axis is due to the tilt of the tip as illustrated in Fig. 6.1b.



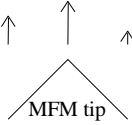
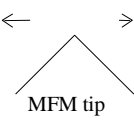
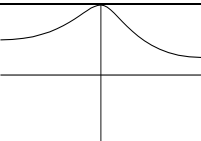
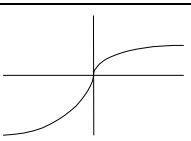
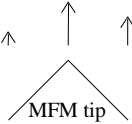
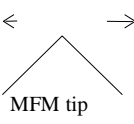
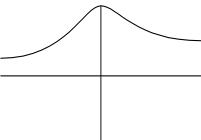
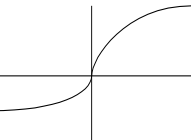
**Figure 6.8.** Linescans along (a) the  $x$  axis and (b) the  $z$  axis of the reconstructed  $y$  field components from models A – D.

### 6.3 Separation of magnetic and electrostatic effects

It is obviously desirable to be able to separate magnetic and electrostatic effects in Lorentz microscopy. Other authors (Frost and Jenkins, 1996 and Tonomura *et al*, 1986)

have discussed several solutions to this problem. The method used by both authors is to utilise the effect of time reversal on the phase contrast of the specimen. The simplest way to achieve this is to take two images of the specimen, turning the specimen upside down for the second image. Using these two images the magnetic and electrostatic contributions to the phase contrast image can be separated. This can be explained as follows.

Consider a point on a thin sample at coordinates  $(x_0, y_0)$ . At this point the deflection of the electron beam in the  $x$  direction ( $\beta_x$ ) is proportional to the integrated  $x$  electrostatic field component ( $E_x$ ) and the integrated  $y$  magnetic field component ( $B_y$ ). If the sample is then rotated  $180^\circ$  around the  $y$  axis, the point of the sample under consideration will now be located at  $(-x_0, y_0)$ . At this point  $E_x$  will reverse in direction, while  $B_y$  will still point in the same direction as before. This is illustrated in Table 6.2.

	Y ( $\uparrow$ ) field component	X ( $\rightarrow$ ) field component	Linescan of Y field component	Linescan of X field component
Tip at $0^\circ$ position				
Tip at $180^\circ$ position				

**Table 6.2. Illustration of the behaviour of the integrated field produced by a sample during  $180^\circ$  rotation about the  $y$  axis.**

Hence, we can say that the sign of the electrostatic contribution to  $\beta_x$  changes with the sample rotation, while the sign of the magnetic contribution stays the same. Adding and subtracting the  $\beta_x$  signals taken at  $0^\circ$  and  $180^\circ$  then yields  $2B_y$  and  $2E_x$  respectively at the point of the sample under consideration. Similarly, the  $\beta_y$  signals yield  $2E_y$  and  $2B_x$ . The derivation of this result is covered in more depth in Appendix A.

It should be noted that this procedure is only valid if the electrostatic and magnetic field distributions are the same for both sample positions. It is certainly possible for even small fields ( $<10$  Oe) to perturb some magnetic materials, and this was found to be the case for the METGLAS tips analysed in Chapter 4. To avoid this problem, care was taken to cancel the objective remanent field in these cases, to a level less than 1 Oe. If the DPC imaging is performed in these (almost) magnetic field-free conditions, it is certainly the case that any disturbance of the tip magnetisation will be negligible.

It is more difficult to state that the amount of charging in each image will be the same, as sample charging is generally a dynamic process. However, given that the imaging conditions (beam current and size, scan speed and size) are the same for both images, it

might be expected that the amount of charging should at least be quite similar. The charging characteristics may be different if contamination of the sample occurs between acquisition of the images, but this problem can usually be avoided if care is taken to minimise the exposure of the tip to the electron beam, and the sample environment is clean.

There are other methods that can be used to separate the magnetic and electric components in DPC imaging. One method was discussed by Frost and Jenkins (1996), and utilises the fact that the ratio of magnetic to electric contributions in the DPC signal changes with the electron beam accelerating voltage. Thus, in principle, obtaining two DPC images at different accelerating voltages allows separation. However, as the imaging conditions in the microscope also change with the accelerating voltage, this method is usually impractical to implement and is not considered here.

Another method suggested by Tonomura *et al* (1986) is to take another micrograph of the sample at a temperature higher than the Curie point of the material in question, which in principle should give an electrostatic signal only. One disadvantage of this method is that the charging characteristics of the sample are likely to change with temperature, given that the sample resistance will change. Also, any contaminants present would probably be driven off the sample, which would again change the charging characteristics. A further problem is the requirement for a heating rod, which might be difficult to reconcile with the sample mounting requirements for tomography.

## 6.4 Experimental case study

To test the effectiveness of the separation procedure outlined above, an extended tomographic dataset was taken for a MFM tip. The tip used was a NANOSENSORS™ MFM tip modified by ion beam milling (a SEM micrograph of this tip is shown in Fig. 6.9). This tip possesses a spike several microns long, and was coated by evaporation on the front side of the spike with 25 nm of Co. It was felt that this thickness of Co, along with the spike geometry would result in a stray field of smaller magnitude than standard Nanosensors MFM tips, hence allowing easier observation of any charging effects.

The tip was magnetised along the spike axis by a 1 T field before being placed in the STEM. DPC images were taken every 10° as the tip was rotated from 0° to 350° about the y axis. This required four sample stub position changes, and one concern was that the tip could be contaminated during these changes, resulting in different charging characteristics at different points in the experiment. However, checking the data at the overlapping sample positions before and after the changes indicated that the field distribution appeared to be largely unaffected by these changes.

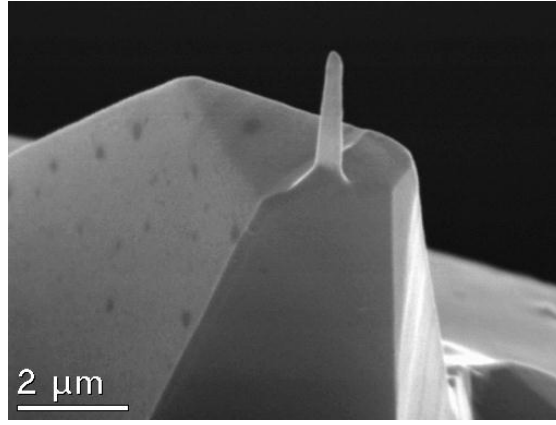


Figure 6.9. SEM micrograph of the FIB modified MFM tip.

Sample linescans are shown in Figs. 6.10a and c, taken at the  $90^\circ$  and  $270^\circ$  rotation positions. It can be seen that the form of these linescans is not what would be expected from an axially magnetised spike tip. Indeed, at first glance the linescans have the form that would be expected from a tip magnetised along the cantilever axis, i.e. across the tip. The data was analysed using the procedure outlined earlier. Each linescan was subtracted from its counterpart taken from the diametrically opposite position. Sample results from this processing stage are shown in Figs. 6.10b and d.

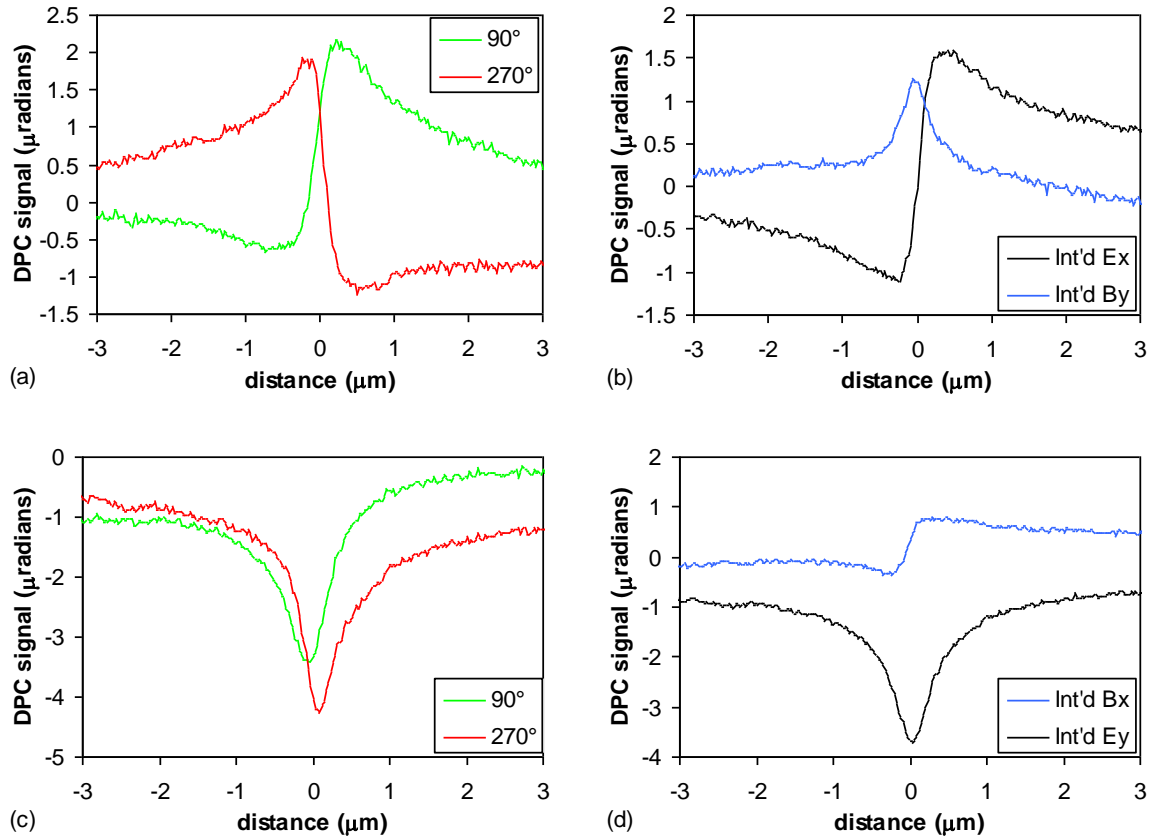
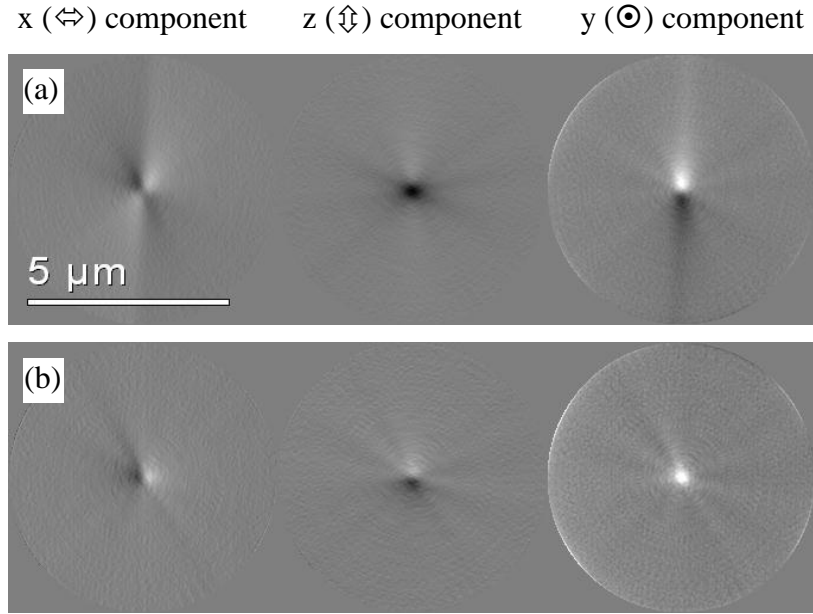


Figure 6.10. Sample of DPC data taken from modified MFM tip. (a) Original x deflection signal linescans taken at  $90^\circ$  and  $270^\circ$  sample rotations. (b) linescans separated into magnetic ( $B_y$ ) and electrostatic ( $E_x$ ) components. (c) Original y deflection signal linescans taken at  $90^\circ$  and  $270^\circ$  sample rotations. (d) linescans separated into magnetic ( $B_x$ ) and electrostatic ( $E_y$ ) components.



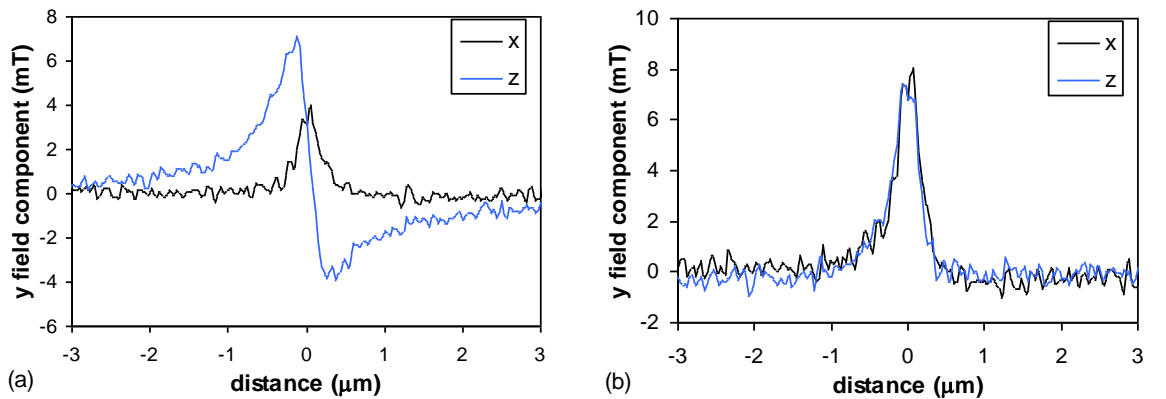
There are a number of points of interest in this data. Examining the relative sizes of the peaks in Figs 6.10 (b) and (d), it is apparent that the magnitude of the DPC signal due to electrostatic effects is about twice as large as the magnetic signal. It is also notable that the electrostatic peak is centred almost exactly at the origin and is symmetrical about the origin, implying that the electrostatic charge is distributed symmetrically over the tip. Examination of the full electrostatic dataset confirms this point, as the shape and position of the electrostatic peak remains similar over the  $180^\circ$  range of rotation. The shape of the peak is similar to the DPC signal calculated from the point charge model used earlier, implying that the charge is concentrated at or near the tip apex. The magnetic signal, although smaller than the electrostatic signal, is also well defined. The magnetic peak is quite localised, which is consistent with what would be expected from a spike tip magnetised along its long axis.

These results indicate that there can be a significant amount of electrostatic charging present in tomographic studies, even if the MFM tip is considered to be reasonably conductive (as would be expected in this case, given that half of the tip is coated with Co. Another point that becomes apparent when examining the complete data sets is that the average level of the unprocessed data (the d.c. shift) varies markedly with sample position. When the data is processed most of the d.c. shift is contained in the magnetic data, with the baseline of the electrostatic data remaining at a constant level. The cause of these d.c. shifts (for the magnetic case) has been investigated by Gallacher (1999), and was attributed to the fields from the magnetic material coating the cantilever and supporting substrate of the tip. The fields produced by these elements are usually of low magnitude at the reconstruction plane. However, the spatial extent of these fields is much greater than that of the tip (in the case of the substrate coating, the field produced can extend over a few mm). As DPC imaging integrates the field over the whole beam path, the cantilever and substrate fields can produce a large, albeit slowly varying contribution to the DPC data. However, as noted earlier, reconstructing the  $y$  field component from the projections of the  $x$  field component results in high accuracy. Gallacher (1999) showed that this is true even with large level shifts in the DPC data, and so we can be confident that the reconstructions presented here are true descriptions of the field distribution, assuming that the input data are purely magnetic in origin. The reconstructions of the tip stray field are shown in Fig. 6.11 for (a) the original unprocessed data and (b) the separated magnetic data.



**Figure 6.11.** Field reconstructions from (a) the unprocessed DPC data and (b) the processed DPC data. Field components are (from left to right) x ( $\leftrightarrow$ ), z ( $\updownarrow$ ), y ( $\odot$ ).

As expected, the reconstructions from the unprocessed data exhibit a smearing effect in the  $z$  direction, consistent with the charged simulations examined in the previous section. The form of the field in the centre of the reconstruction could potentially be due to a magnetic dipole oriented parallel to the  $z$  axis at a short distance from the reconstruction plane (corresponding to the tip being magnetised perpendicular to the spike direction). However, the long tails extending from the centre of the reconstruction are entirely inconsistent with the geometry of the tip. Linescans of the  $y$  field components of these reconstructions along the  $z$  axis are shown in Fig. 6.12.



**Figure 6.12.** Linescans of field reconstructions shown in Fig. 6.11, along the  $x$  and  $z$  axes. (a) is from the reconstruction of the unprocessed  $x$  deflection data. (b) is from the reconstruction of the processed  $B_x$  data.

These linescans illustrate the severe distortion induced by the electrostatic effects in the  $z$  direction. The reconstruction from the processed data shows a field distribution much closer to that expected from an axially magnetised spike tip, with a peak field of 8.1 mT and a full width at half maximum (FWHM) of 290 nm (for the  $y$  field component).

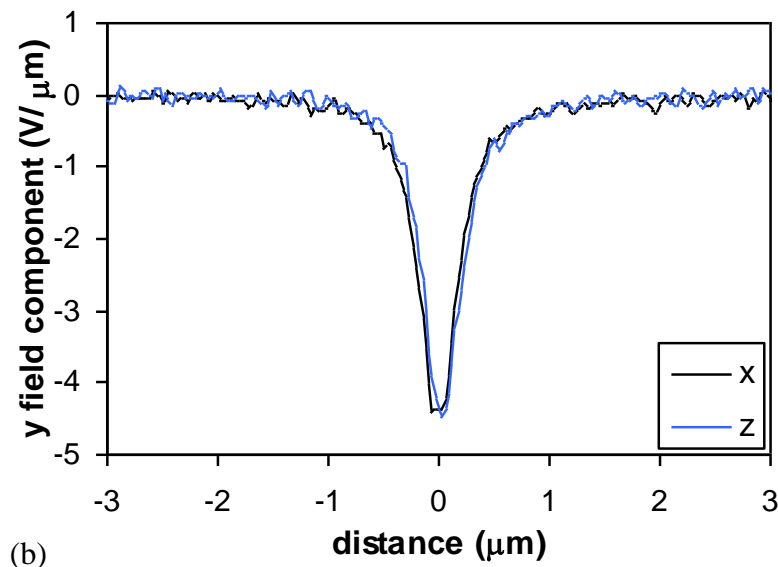
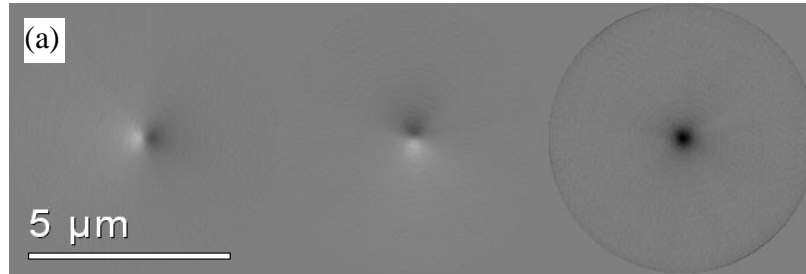
The separation procedure used here yields as a by-product the DPC data set due to the electrostatic field only, also over a rotation range of  $180^\circ$ . It is possible to reconstruct electrostatic fields using the same tomographic algorithm as used for magnetic data, as the mathematical properties of magnetic and electric fields are the same in vacuum. That is to say;

$$\nabla \cdot \mathbf{B} = 0, \nabla \times \mathbf{B} = 0, \quad (6.5a)$$

$$\nabla \cdot \mathbf{E} = 0, \nabla \times \mathbf{E} = 0, \quad (6.5b)$$

assuming no time variation. In this case the only difference in behaviour between magnetic and electrostatic fields are that different units are involved. The other important difference is that for the electric field, the x integrated field component is related to the x DPC signal and the y integrated field is related to the y DPC signal. Thus care must be taken to input the deflection components the correct way round into the tomographic reconstruction algorithm. The reconstruction of the electric field from the tip is shown in Fig. 6.13 together with the appropriate linescans.

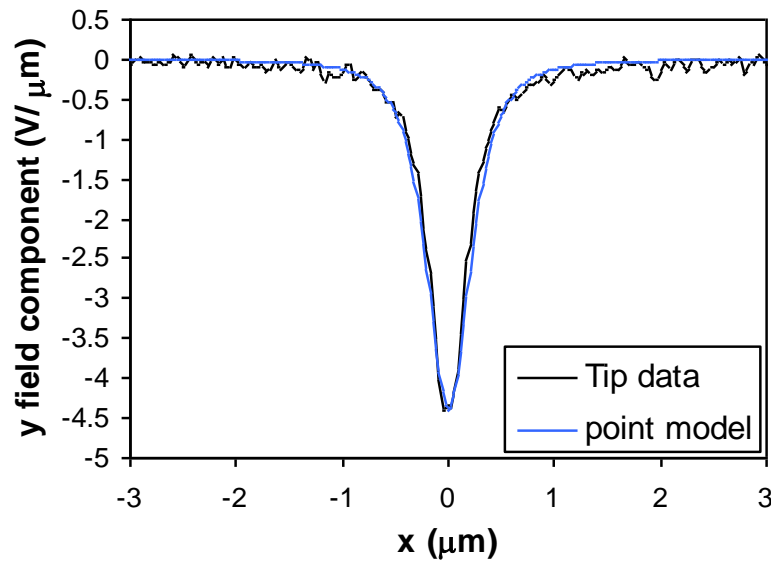
x ( $\leftrightarrow$ ) component      z ( $\updownarrow$ ) component      y ( $\odot$ ) component



**Figure 6.13.** (a) is the reconstruction of the electric field distribution from the FIB modified tip. Field components are (from left to right) x ( $\leftrightarrow$ ), z ( $\updownarrow$ ), y ( $\odot$ ). (b) is the y field component linescans along the x and z axes.

The electrostatic field distribution is centred on the rotation axis, and more detailed analysis shows that the field is roughly circularly symmetric. The peak height is approximately  $-4.5 \text{ V}\mu\text{m}^{-1}$  and the FWHM is 400 nm. The width of the peak and the absence of background field suggest that the electrostatic charge on the MFM tip is indeed concentrated near the tip apex, possibly within a few hundred nm.

To test this hypothesis a point charge model was fitted (using the least-squares method) to the electrostatic data, the two fitting parameters being the distance of the charge to the reconstruction plane and the magnitude of the charge. A very close fit (Fig. 6.14) was obtained for a point charge of  $-5 \times 10^{-17} \text{ C}$  at a distance of 320 nm, which compares favourably with the parameters used for the simulations in the previous section. The charge on the tip will not, of course, be in the form of a single point, but as the electric field can be approximated using a point charge model the implication is that most of the charge is located within a few hundred nm of the tip apex.



**Figure 6.14.** Graph comparing fit of point electrostatic charge model to the reconstructed electrostatic field of the FIB tip. The charge that gave the best fit was  $-5 \times 10^{-17} \text{ C}$ , at a distance of 320 nm from the reconstruction plane.

The electrostatic effects in this study are slightly larger than anticipated; other tomographic studies of MFM tips performed previously by Ferrier *et al* (1997) and Scott *et al* (1999) have not exhibited such extreme effects. However, careful examination of the data given by Scott *et al* (1999) for the 50 nm METGLAS tip (for example) does reveal evidence for some charging, centred on the rotation axis. Re-examination of the deflection data used in that study indicates that the magnitude of the Lorentz deflection signal due to electrostatic charge was slightly less than half than that of the magnetic signal, roughly equivalent to tip model B in section 6.2.2. The effect is not readily apparent in the linescans of the reconstruction shown in that work, mainly because the linescans were

taken along the  $x$  axes of the reconstructions. As illustrated earlier, if the electrostatic charge of the tip is centred on the rotation axis, the linescan along the  $x$  axis of the reconstruction is unaffected. Furthermore, the magnetic peak was much sharper than the electrostatic, so the electrostatic signal acted more as a spurious background signal. Thus the linescans shown by Scott *et al* (1999) still represent the character of the tips in that study, although the values of the field peaks may not be as accurate as first thought. The reconstructions of the tips examined by Scott *et al* (1999) are shown in Chapter 4 with the electrostatic contributions subtracted (sections 4.6.1 and 4.6.4). In both cases the  $x$  axis linescans of the  $y$  field components are very similar to those shown in Scott *et al* (1999).

The degree of charging present in this study (i.e. electrostatic DPC signals of twice the magnitude of the magnetic DPC signals) is therefore somewhat atypical, and can be probably be considered as an extreme case. Nevertheless, this analysis shows that the ability to separate the magnetic and electrostatic components in tomography is very useful, and should probably be done as routine, especially when imaging tips with small magnetic moments and stray fields. Charging problems will not be as apparent when imaging high magnetic moment tips, simply because the large magnetic fields will dominate the DPC data in these cases (as long as the amount of charging is less than or equal to this study). For example, the field reconstruction of the CoCr coated MFM tip by Ferrier *et al* (1997) exhibits no obvious charging artefacts (i.e. there are no ‘tails’ present in the reconstruction).

The main disadvantage of the separation method used here is the requirement that a full  $360^\circ$  tomographic dataset be taken, as opposed to the  $180^\circ$  datasets normally used. This requires several hours of data collection and necessitates four sample position changes (see Chapter 2 for details). However, the symmetry and central location of the charge distribution suggests that it may only be necessary to find the electrostatic components of the DPC signal at one or two angular positions. Assuming that the charge distribution is indeed symmetric about the rotation axis, the electrostatic signal thus found can then be subtracted from the data over the entire range of rotation, leaving the magnetic components only. This assumption allows the analysis to be carried out on previous studies, as in most cases data for tomography was collected over a range of  $190^\circ$  (the total rotation range accessible with one change of the sample stub position). Initial analysis of tomographic data acquired in earlier experiments indicates that in most cases there is some degree of charging (even when the tip has been gold coated to try and prevent this problem), and the electrostatic contribution is usually symmetric about the rotation axis. This will therefore allow us to improve the accuracy of studies already performed, confirming that this analysis should be done as routine, particularly for tips with low

magnetic moments. This method has therefore been applied to most of the tomographic studies covered in this thesis.

## 6.5 DPC detector misalignment

Another potential cause of inaccuracy in the tomographic reconstruction process is the misalignment of the DPC detector. The usual method used to align the DPC detector is described in Chapter 2, and utilises micron-scale patterned magnetic thin film elements, which are usually made of polycrystalline cobalt or permalloy. DPC images taken of these elements contain noise due both to the intrinsic shot noise of the electron beam, and the contrast due to the crystallites of the elements. This noise means that there is some uncertainty involved with the DPC alignment. The maximum angular error on a properly set up DPC system is thought to be at least  $<5^\circ$ , and probably  $<2^\circ$ . In this section the effects of angular misalignment of the DPC detector are examined, to determine the tolerance of the tomographic process to this error. A scheme for determining the presence of angular misalignment is given.

### 6.5.1 Effect on DPC data

To simulate the effect of DPC detector misalignment, the model dataset described in section 6.2.1 was again used. As the detector is rotated the axes of the detector coordinate system obviously change. To transform the original data into the new coordinate system we use the relations

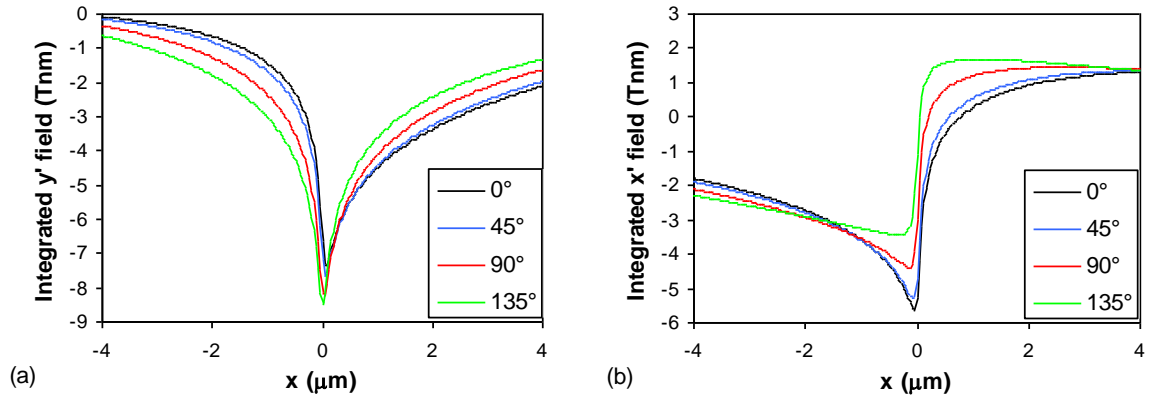
$$\beta'_x = \beta_x \cos \theta - \beta_y \sin \theta \quad (6.6a)$$

$$\beta'_y = \beta_y \cos \theta + \beta_x \sin \theta \quad (6.6b)$$

where  $\beta_x$  and  $\beta_y$  are the original DPC signals,  $\theta$  is the rotation angle and  $\beta'_x$  and  $\beta'_y$  are the transformed signals. The effect on the DPC data is shown in Fig. 6.15 for a misalignment angle of  $15^\circ$  (see Fig. 6.2 for the original dataset).

It can be seen that the DPC data produced by a misaligned detector is similar in character to data influenced by electrostatic charging as shown previously, and so it might be expected that tomographic reconstructions using this data would contain the same sort of artefacts as seen in section 6.2.3. To test this theory DPC datasets were generated for detector misalignment angles of  $5^\circ$ ,  $10^\circ$  and  $15^\circ$ . It was felt that the maximum error possible in the DPC detector orientation was  $\sim 10^\circ$ , even with a hurried alignment

procedure. Tomographic reconstructions were then calculated using these transformed datasets.

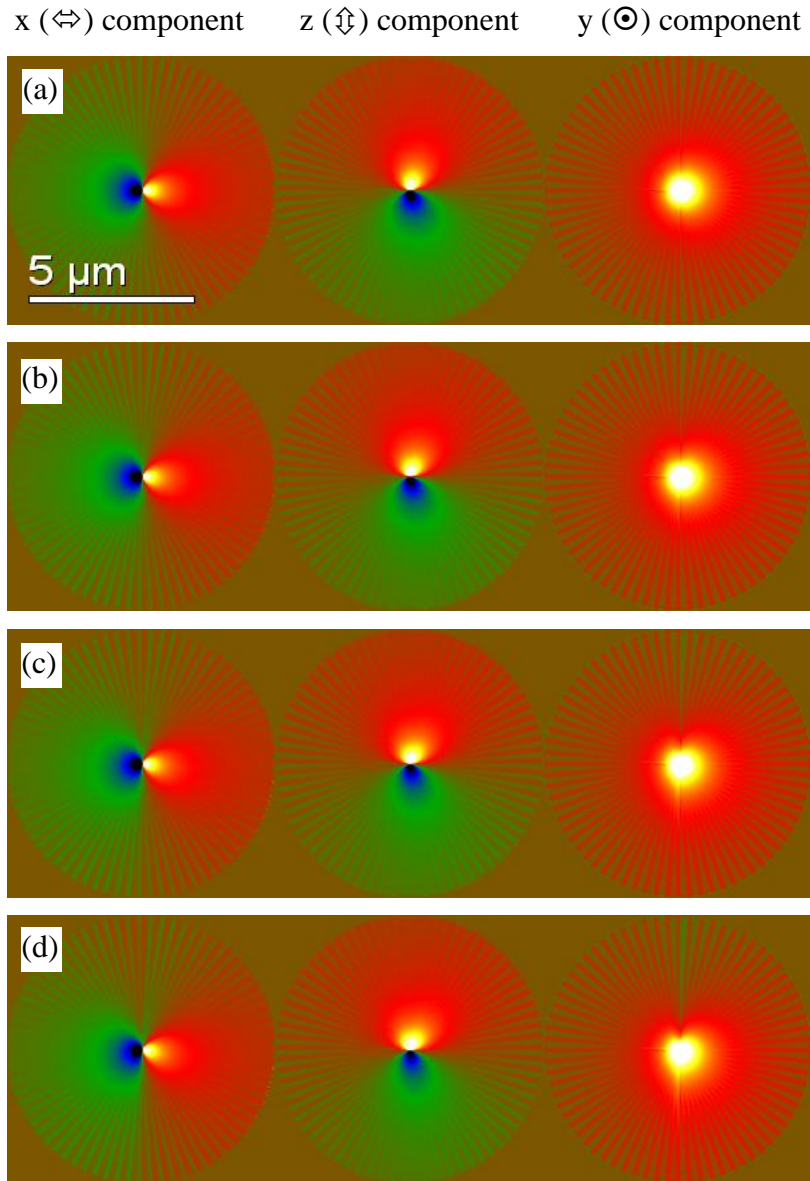


**Figure 6.15.** Selected linescans from DPC data of model MFM tip, with the DPC detector rotated  $15^\circ$  from the model coordinate system. (a) is the beam deflection in the  $y'$  direction and (b) is the beam deflection in the  $x'$  direction.

### 6.5.2 Effect on tomographic reconstructions

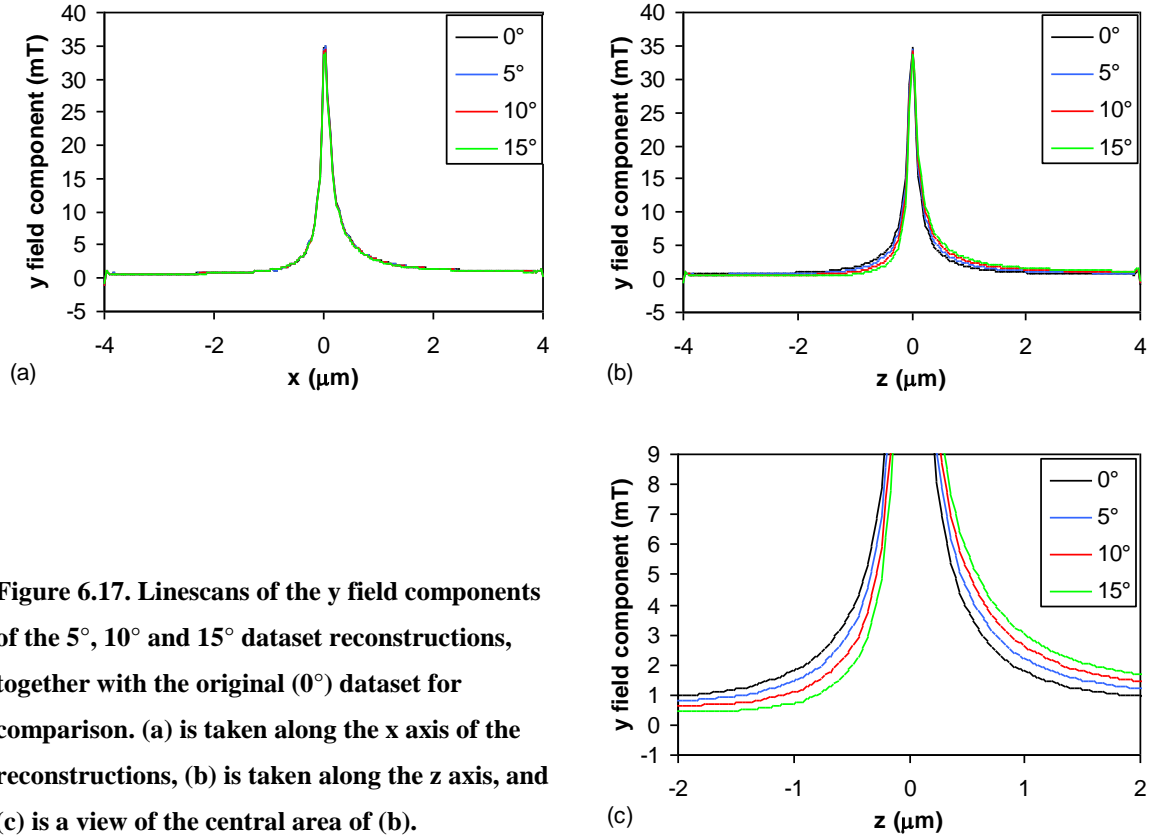
The tomographic reconstructions for the  $5^\circ$ ,  $10^\circ$  and  $15^\circ$  transformed DPC datasets are shown in Fig. 6.16, together with the reconstruction of the original dataset. In this case the changes are quite subtle, so the reconstructions are displayed using a temperature colour scale to emphasise the differences. It can be seen that the reconstructions exhibit the same type of artefact as the electrostatically charged simulations, specifically the vertical tails extending from the reconstruction centre of the  $y$  field component, although in this case the effect is much less prominent. As before, we will concentrate on the  $y$  field component for detailed analysis. The linescans of the  $y$  field components along the  $x$  and  $z$  axes of the reconstructions are shown in Fig. 6.17.

These figures show that the field peak becomes increasingly asymmetrical in the  $z$  axis direction as the DPC detector misalignment angle increases. However, as with the charging case, the peak shape along the  $x$  axis is almost unaffected. (The model tip is tilted in the  $x$  direction for these reconstructions, hence the asymmetry in Fig. 6.17a. The model is symmetrical with respect to the  $z$  axis, so any asymmetry is due to the DPC detector rotation in this case.) One point to note is that the peak field does decrease slightly with increasing misalignment, although this is not immediately apparent in the linescans. In fact, the peak field scales with  $\cos\theta$ , and the reason for this is discussed below in section 6.6.



**Figure 6.16.** Tomographic field reconstructions of (a) the original dataset, (b) the 5° dataset, (c) the 10° dataset and (d) the 15° dataset. Note that the contrast setting is high to emphasise the vertical “tails” in the reconstructions. Field components are (from left to right)  $x (\leftrightarrow)$ ,  $z (\updownarrow)$ ,  $y (\odot)$ .





**Figure 6.17.** Line scans of the  $y$  field components of the  $5^\circ$ ,  $10^\circ$  and  $15^\circ$  dataset reconstructions, together with the original ( $0^\circ$ ) dataset for comparison. (a) is taken along the  $x$  axis of the reconstructions, (b) is taken along the  $z$  axis, and (c) is a view of the central area of (b).

### 6.5.3 Determination of misalignment angle

Assuming that the DPC detector is misaligned, this can be detected using the same general method used for the charging case i.e. by adding and subtracting diametrically opposed views of the sample. It can be shown using similar arguments to the charging case that adding and subtracting diametrically opposed views yields the separated  $x$  and  $y$  integrated field components. If we know  $\beta_x$  and  $\beta_y$  it is then possible to solve equation 6.6 for  $\theta$ . To find the unknown  $\theta$  the following equations are used;

$$\theta_1 = \tan^{-1} \left( \frac{{}^0\beta'_y - {}^{180}\beta'_y}{{}^0\beta'_x - {}^{180}\beta'_x} \right), \quad (6.7a)$$

$$\theta_2 = -\tan^{-1} \left( \frac{{}^0\beta'_x + {}^{180}\beta'_x}{{}^0\beta'_y + {}^{180}\beta'_y} \right), \quad (6.7b)$$

where  ${}^0y'$  is the  $y$  deflection signal obtained from the DPC detector at the  $0^\circ$  sample position, etc. A full derivation of this result is given in Appendix A.

The angles  $\theta_1$  and  $\theta_2$  can be calculated for any one pair of DPC data points. However, when dealing with real data that contains noise it is obviously better to calculate  $\theta$  over a larger range of the data to reduce the uncertainty. Assuming that there is no

charging present, the values of  $\theta$  should be constant for all points on the DPC linescan, apart from noise variations. Having obtained  $\theta$  in this way, the misaligned data can then be transformed using Eqn. 6.6 to compensate for the detector misalignment.

## 6.6 Similarity between charging and misalignment

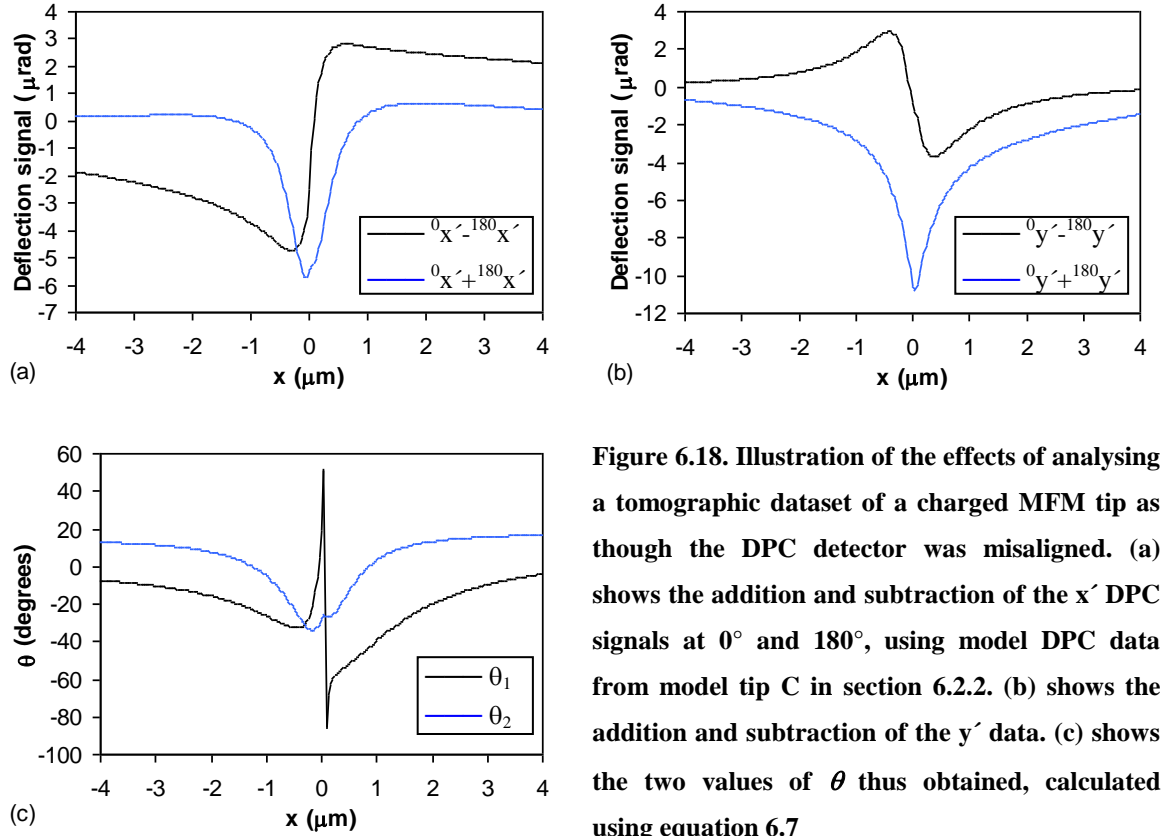
In the previous sections it was assumed that either charging or detector misalignment was present. If both effects are present simultaneously the problem of correcting the data becomes much more difficult. For instance, suppose the DPC detector is misaligned, and no electrostatic charging is present. If we were to analyse this as though charging was present (and assuming that the detector was aligned perfectly) the result would be separated ‘magnetic’ and ‘electrostatic’ components. However, in this case the ‘magnetic’ component is the actual magnetic integrated field multiplied by a factor of  $\cos \theta$ . The ‘electrostatic’ component is the actual magnetic integrated field rotated by  $90^\circ$  and multiplied by a factor of  $\sin \theta$ .

To examine the problem the other way round, suppose there is a MFM tip that is also electrostatically charged, as in section 6.2. As the effects of electrostatic charge work at right angles to magnetic effects, electrostatic charges can be made to look like magnetic charges by rotating the DPC detector by  $90^\circ$ . Thus, if an electrostatic monopole (for example) is added to a magnetic monopole and both charges give equal DPC signal magnitudes (and both give fields of roughly the same shape), the effect could be interpreted as a detector rotation of  $45^\circ$ . As an example, take the charged model MFM tip C (section 6.2.2). The DPC data from this model is analysed assuming that there is no charging but the detector is misaligned, using equations 6.7a and b. If this is done for each point of the data we obtain a graph of the ‘rotation’ ( $\theta$ ) at each point. The results are shown in Fig. 6.18.

It can be seen that the effect of the charging on the analysis is to simulate the effect of detector rotation, although in this case the angle varies with scan position. The effect of any actual detector rotation on this analysis would be to add a DC shift equal to the detector rotation angle to the linescans shown in Fig. 6.18c. Of course, if there was no charging present then the graphs of  $\theta_1$  and  $\theta_2$  would be straight and level, and would equal each other.

Therefore it seems that it will be difficult in most cases to separate charging and detector misalignment effects. Indeed, if the analysis is done at a single point it is impossible to separate the effects, as the problem becomes one of four equations and five variables (see Appendix A). Given the value of  $\theta$  over the whole scan range however, it

might be possible to separate the effects if some assumptions are made. The example above could be analysed by assuming that the electrostatic charge present was of the form of a single monopole. By varying the monopole parameters (position and magnitude) it should be possible to reduce or eliminate the variation of  $\theta$  over the scan range. The remaining constant  $\theta$  will then correspond to the detector misalignment angle.



**Figure 6.18.** Illustration of the effects of analysing a tomographic dataset of a charged MFM tip as though the DPC detector was misaligned. (a) shows the addition and subtraction of the  $x'$  DPC signals at  $0^\circ$  and  $180^\circ$ , using model DPC data from model tip C in section 6.2.2. (b) shows the addition and subtraction of the  $y'$  data. (c) shows the two values of  $\theta$  thus obtained, calculated using equation 6.7

With real experimental data it may not be valid to assume that the charging can be approximated by a monopole. Furthermore, the effects of noise will make it more difficult to fit a charge distribution to the data. In general, then, if both detector misalignment and charging are present in DPC data, it is not feasible to separate the two effects with any degree of accuracy.

## 6.7 Conclusions

It has been shown that electrostatic charging and DPC detector misalignment can distort tomographic field reconstructions from magnetic samples if these two effects are not accounted for. Both effects cause a characteristic distortion of the field, and thus it is normally easy to see if there is a problem. If either effect is present exclusively, it is possible to detect and correct for, although this requires that twice as much data be acquired compared to normal DPC and tomographic studies. An experimental case study has shown that charging effects can be detected and subtracted from real DPC data. As has

been shown, it is difficult to subtract charging effects when the DPC detector is also misaligned. Given the difficulty in eliminating all charging from MFM tip samples, it is therefore essential to align the DPC detector correctly when performing tomographic studies, as described in Chapter 2. Given that real tomographic reconstructions contain some degree of noise, an error of  $\sim 5^\circ$  in the detector alignment can be tolerated. Alternatively, a separate measurement of the angular position of the DPC detector can be performed, and this can then be used to correct the DPC data. However, the DPC detector was aligned properly (to within  $<5^\circ$  error or better) for all data presented in this thesis.

Examination of the raw DPC data taken from the MFM tips covered in Chapters 4 and 5 reveals that charging effects are present in almost every case, in varying magnitudes. All the results presented in these chapters have been analysed for charging effects, and the charging subtracted as necessary.

## References

- Ferrier R. P., McVitie S., Gallacher A. and Nicholson W. A. P. (1997), "Characterisation of MFM tip fields by electron tomography," *IEEE Trans. Magn.*, **33**, 4062
- Frost B. G. and Jenkins T. L. (1996), "On the interpretation of magnetic and electric fields imaged by low-magnification off-axis electron holography", *J. Microsc.*, **187**, 85
- Gallacher A. (1999), "Theoretical Characterisation of Magnetic Force Microscope Tip Stray Fields", *Ph.D. Thesis*, Glasgow University
- Liou S. H., Malhotra S. S., Moreland J., Hopkins P. F. (1997), "High resolution imaging of thin-film recording heads by superparamagnetic magnetic force microscopy tips", *Appl. Phys. Lett.*, **70**, 135 – 137
- Scott J., McVitie S., Ferrier R. P., Heydon G. P., Rainforth W. M., Gibbs M. R. J., Tucker J. W., Davies H. A. and Bishop J. E. L. (1999), "Characterisation of FeBSiC coated MFM tips using Lorentz electron tomography and MFM", *IEEE Trans. Mag.* **35**, 3986
- Tonomura A., Matsuda T., Endo J., Ariei T. and Mihama K. (1986), "Holographic interference electron microscopy for determining specimen magnetic structure and thickness determination", *Phys. Rev. B*, **34**, 3397

## Chapter 7. Conclusions and future work

### 7.1 Conclusions

The work presented in the proceeding chapters has demonstrated that tomographic reconstruction of MFM tip stray field distributions is a viable method of characterising MFM tips. This method can only measure the remanent stray field of the tip, but as discussed in Chapter 3, this is all that is required to characterise the MFM response. As illustrated by the MFM images in Chapter 4, the response of soft MFM tips to field can be complex. However, it can be said that the project to develop soft MFM tips based on METGLAS alloy coatings has been broadly successful. As discussed in Chapter 4, there are some subtle effects present in the MFM images taken with tips coated with 50 and 70 nm of METGLAS, for which there is no suitable explanation. This may be worthy of further investigation.

Of the tips investigated in Chapter 5, it is clear that creating spike MFM tips using FIB milling results in good magnetic properties, and these tips would appear to be eminently suited for MFM on samples that contain deep holes or trenches with steep sidewalls. However, they do not appear to have significantly better magnetic resolution than normal pyramidal MFM tips, so their use as routine is not indicated. The tips containing a FIB milled groove do show some potential, but were somewhat inconsistent in behaviour when magnetised in the cantilever plane (as required for their intended application). It should be noted that the maximum field that we could apply ( $\sim 1$  T) may not be enough to magnetise properly a tip in the plane of the cantilever.

The ultra-sensitive tip examined in Chapter 5 appears to be a successful attempt to create a close approximation to a point monopole tip. Unfortunately the charging problems encountered while imaging this tip mean that it is not possible to check whether the stray field is truly monopole-like. Given the techniques discussed in Chapter 6, it is probable that future work on tips of this type will be more fruitful.

The concept of separating magnetic and electrostatic charging in DPC images is not a new one. However, the implementation of this concept discussed in Chapter 6 is a fairly uncommon example, and is mainly possible due to the nature of the samples involved. It is also something of a curiosity that some MFM tips suffer from charging during DPC imaging, despite the fact that these tips are nominally quite conductive.

## 7.2 Future work on DPC imaging

### 7.2.1 Separation of magnetic and electrostatic DPC data

As discussed in Chapter 6, it is difficult to separate the magnetic and electrostatic contributions to a DPC image when only one view of the sample is available. This problem with DPC imaging (and phase microscopy in general) has been recognised since the early days of electron microscopy. The method used in Chapter 6 (recording views of the sample from the top and bottom of the sample) has the advantage that in many cases, it is easy to mount the sample upside down in (S)TEM sample holders. However, the method does rely on obtaining the correct spatial registration between the two images, otherwise artefacts will be present in the results. The benefit of having an MFM tip as the sample is that it is normally easy to align the two views of the tip, as the image of the tip itself forms only a small part of the image. Furthermore, as the field distribution varies smoothly and slowly with increasing distance from the tip apex, small errors in the registration of the two images are not critical.

One problem with current investigations of magnetic materials, and in particular small magnetic elements, is the phase contrast generated by the structure of the material. For example, one material that is often used to make small magnetic elements is permalloy, which can be deposited by thermal evaporation or sputtering. The crystallite size in this case is normally in the range 5 to 10 nm. As described in Chapter 2, one way of reducing the phase contrast of the crystallites in DPC is to use an annular quadrant detector. This has the effect of filtering out high spatial frequency phase contrast, and thus tends to enhance the magnetic phase contrast relative to the crystallite contrast. However, this assumes that the magnetisation of the sample varies much less rapidly than the electrostatic contrast (which is due in most cases to the inner potential of the material). This assumption begins to break down when examining the fine structure of domain walls, or even the structure of magnetic vortices. To study these structures properly requires that the resolution be equivalent to the exchange length of the material (as with micromagnetic simulations). For permalloy thin (thickness  $<50$  nm) films this implies a resolution of  $<5$  nm, that is, comparable to the crystallite size. In this case there is little advantage in using an annular DPC detector over the normal solid quadrant type.

In principle, by using the two-image method described in Chapter 6 it is possible to separate the crystallite and magnetic phase contrast in any DPC image. One problem, as with MFM tips, is to ensure that any charging is minimised and is the same in both images. This can be achieved by ensuring that the sample environment in the electron microscope is clean (to avoid contamination buildup) and that the sample is coated with

conductive material (to minimise charging). The major problem to be solved is the spatial registration of the two images (normally using the bright field images acquired with the DPC data). As noted above, images of MFM tips need only be aligned precisely at the tip apex itself, while small mis-registrations elsewhere in the image can be neglected. However, when dealing with images of polycrystalline thin films the entire area of the two images must be accurately aligned. This implies that the scan system must provide an accurate raster scan. This problem is quite formidable, but may need to be addressed if the fine structure of domain walls and vortices is to be accurately measured.

As a side note, it is also obvious that to align the images it is necessary to know the orientation of the sample rotation axis. It is probably desirable in this case to ensure that the scan axes are aligned with the rotation axis, as described in Chapter 2. Furthermore, aligning the DPC detector so that the DPC component axes are aligned with the scan axes is also a desirable convenience.

### 7.2.2 Improved DPC detectors

As discussed by both Waddell (1978) and Morrison (1981) the ideal DPC detector would be a first moment detector, that is, a detector that would return the center of mass of the electron distribution. A quadrant (or split) DPC detector can be viewed as a very rough approximation to this ideal. It has been suggested by Waddell (1978) that a pixel detector could be used to provide a better approximation to a first moment detector. In this case the image of the beam would be read out, and then analysed to determine the centre of the resulting distribution. The main challenge with this method is to ensure that the data from the pixel detector can be read out quickly enough to permit a reasonable scanning rate. For instance, a  $256 \times 256$  pixel DPC image displayed at a frame rate of 1 Hz requires a detector bandwidth of  $\sim 65$  kHz. If the detector is of size  $64 \times 64$  pixels, then this implies a read out rate of  $\sim 270$  MHz. This speed is unlikely to be achieved by CCD devices, but may be reachable by other types of pixel detector. For instance, hybrid pixel detectors operating at 10 MHz have already been designed for high energy physics applications, and 100 MHz devices are planned (see Faruqi, 2001)

## 7.3 Tomography

The results shown in this and previous theses (Gallacher, 1999) have indicated that Lorentz electron tomography is ideally suited for the characterisation of the remanent fields from MFM tips. The main drawback with tomography is not the quantity of data required (which is fairly modest compared to medical tomography, for example) but the

time required to acquire that data. As described in Chapter 2, it is not practicable to construct an accurate tilting stage in the STEM due to space constraints, and so for each tilt angle the tip apex must be centred in the scan range and focused. In addition, the sample is usually moved away from the scan region so that a background image can be taken. This process serves two purposes; the beam can be centred on the DPC detector in (approximately) field free conditions, and when the background images are subtracted from the sample images this removes any residual descanned effects. As sample tilt and movement are performed manually on the CM20, this process does take some time, and so a normal study requires a minimum of ~4 hours to do (including microscope alignment, DPC calibration and sample changes). For a microscope with a motorised sample stage (which is standard on most modern analytical (S)TEMs) it should be possible to automate most of the data collection process, which would considerably reduce the time required and would allow more studies to be done.

## 7.4 Future directions in MFM

### 7.4.1 Creating approximations to point or line charge MFM tips

One way of quantifying MFM data is to find an accurate model for the tip. Another approach is to modify the MFM tip such that it more closely approximates the tip model. In particular, there is interest in creating a tip that would act as a point dipole or monopole, as this would considerably simplify the analysis of MFM data. The most obvious way to create a point dipole tip is simply to have a small (preferably spherical) particle of magnetic material on the tip, preferably at the tip apex. This has been attempted by Liou *et al* (1999), where a MFM tip is coated with magnetic material and then FIB milled, so that all the magnetic material was removed except for a protected region at the tip apex. Another method used is to create small particles of magnetic material by some process and then attach one to a tip (see for example Stipe *et al*, 2001).

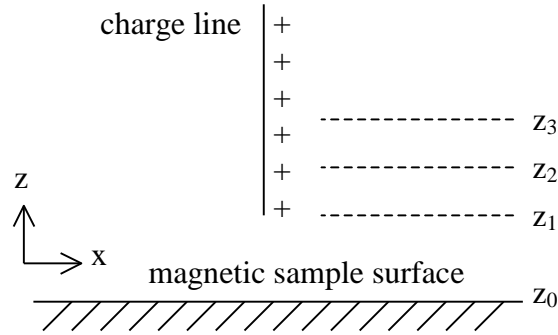
An approximation to a point monopole tip can be constructed by using a wire of magnetic material that terminates at the tip apex, so long as the wire is in a single-domain state. The other end of the wire should terminate reasonably far from the tip apex (this system is, strictly speaking an extended dipole). The ultra-sensitive tip examined in Chapter 5 is an example of this type. The FIB milled spike tips could also be considered as point monopole tips.

Data taken using such tips is relatively simple to analyse, as the theory relating to point tips discussed in Chapter 3 can be used (so long as the size of the magnetic features



examined is greater than the actual size of the ‘point’ tip). One disadvantage of these tips is that the tip has an extremely small magnetic charge compared to normal MFM tips, and so the signal from point-like tips will be correspondingly weaker.

Another type of model tip is the charge-line tip. In this case there is a line of magnetic charge that extends from the tip apex to some length, ideally infinity (a method to generate an approximation to this ideal will be considered below). Consider such a line that extends from some point  $(x,y,z_1)$  above a magnetic sample to  $(x,y,z_N)$ , as illustrated in Fig. 7.1.



**Figure 7.1.** Diagram illustrating the geometry of a magnetic charge line above the surface of a magnetic sample.

Now a *single* point charge attached to a tip will yield a signal proportional to

$$\frac{\partial H_z}{\partial z} \quad (7.1)$$

when the AC imaging mode is used (from Chapter 3, Eqn. 3.9). To find the signal from the line of charge we integrate the signal from the point charge over the line;

$$\int_{z_1}^{z_N} \frac{\partial H_z}{\partial z} dz = H_{z_1} - H_{z_N} . \quad (7.2)$$

Now if  $z_N$  is located at infinity (where the field  $\mathbf{H}$  is zero by definition), this becomes;

$$\int_{z_1}^{z_\infty} \frac{\partial H_z}{\partial z} dz = H_{z_1} . \quad (7.3)$$

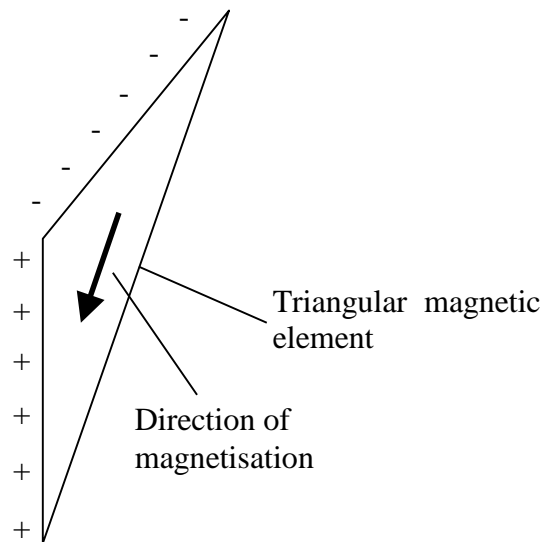
Therefore, a MFM tip possessing a line of charge running from the point  $(x,y,z_1)$  to infinity (along the  $z$ -axis) will yield a signal proportional to  $H_z$  at that point, when operated in AC mode.

For a real tip, the line of charge will be of finite length. The signal will be proportional to the difference of the field strengths at the start and end of the charge line (Eqn. 7.2). However, the field strength at (say)  $15 \mu\text{m}$  above the sample surface will be

negligible for many samples (such as hard disk media or nanometer scale magnetic elements). Thus a tip possessing a charge line 15  $\mu\text{m}$  long should give a signal closely resembling  $H_z$  at the tip apex.

Of course real MFM tips do not usually have one single line of magnetic charge running up them. If the simple model of the axially magnetised four-sided pyramidal tip is considered (as describe in Chapter 6), then there exist four lines of charge along the four edges of the pyramid, and four lines of opposite charge forming the base of the pyramid. Assuming the charges at the base of the pyramid are far enough removed from the sample, the AC MFM signal will depend on the charge lines running down the pyramid edges. These lines are not parallel to the vibration direction, but are close enough to it that the signal should approximate the field component (in the vibration direction) at the end of the tip. This is in fact what is often seen in MFM images, the signal tends to resemble  $H_z$  rather than  $dH_z/dz$  or  $d^2H_z/dz^2$  as might naively be expected.

An approximation to a charge line tip could be constructed in the following manner. If a triangle of magnetic material is magnetised parallel to one of the edges of the triangle the magnetic charge will be distributed along the other two edges of the triangle as illustrated in Fig. 7.2.



**Figure 7.2.** The magnetic charge distribution in a triangular magnetic element, where the magnetisation lies parallel to the hypotenuse.

If this triangular magnetic element was incorporated onto an AFM tip this would approximate the ideal line charge MFM tip, with one edge of the triangle yielding the charge line. There is of course another charge line present in this model, and so the triangle would have to be large enough so that these charges would be far enough removed from the sample to have minimal influence. One important feature of this model is that for the magnetisation of the magnetic material to lie in the direction shown would require a uniaxial anisotropy in that direction.

### 7.4.2 Active Q factor control

One problem when performing AFM or MFM in air is the damping effect of the air, which can reduce the Q factor of a cantilever by several orders of magnitude. This problem is even more pronounced when using AFM in a liquid environment (which is required when examining DNA structures, for example). In liquids the Q factor is typically in single figures. This means that the sensitivity to force gradients is similarly reduced. Anczykowski *et al* (1998) describe how this problem can be countered by ‘artificially’ increasing the Q of the system by adding a feedback loop that essentially monitors the cantilever oscillation and adds a signal of the same frequency (but with variable phase and gain) to the cantilever oscillation input. The result is a system that can be tuned to give a specific Q value. This allows more sensitive force gradient measurements in liquid, and this area is where the technique was originally used. However, as the technique makes AFM more sensitive to any force gradient, it is obvious that it could be applied to MFM studies. In particular, when imaging high permeability magnetic samples such as permalloy, a tip with low stray field must be used to avoid perturbing the sample magnetisation. This results in a low signal to noise ratio for such studies, thus the ability to increase the Q value of the cantilever would be of obvious benefit here.

It should also be noted that it is sometimes beneficial to decrease the Q of a cantilever. This is because a high Q system takes longer to respond to a change in force gradient than a low Q system. Decreasing the Q value can therefore speed up the response of the AFM to force gradient changes. In particular, it can allow an increase in the scanning speed. This is obviously of benefit, not only for MFM but also for AFM in general. It is therefore possible to envisage performing MFM with the Q being reduced for the topographic scan (for speed) and increased for the lift scan (for sensitivity). This would allow faster frame rates, which would be useful for dynamic experiments in particular.

### References

- Anczykowski B, Cleveland J P, Krüger D, Elings V and Fuchs H (1998), “Analysis of the interaction mechanisms in dynamic mode SFM by means of experimental data and computer simulation”, *Appl. Phys. A*, **66**, S885–S889
- Faruqi A R (2001), “Prospects for hybrid pixel detectors in electron microscopy”, *Nucl. Instr. and Meth. in Phys. Res. A*, **466**, 146-154
- Gallacher A (1999), “Theoretical Characterisation of Magnetic Force Microscope Tip Stray Fields”, *Ph.D. Thesis*, Glasgow University

- Liou S H (1999), "Comparison of magnetic images using point and thin-film magnetic force microscopy tips", *IEEE Trans. Magn.*, **35**, 3989-3991
- Morrison G R (1981), "The observation of magnetic domain structure in a transmission electron microscope", *Ph.D. Thesis*, University of Glasgow
- Stipe B C, Mamin H J, Stowe T D, Kenny T W and Rugar D (2001), "Magnetic dissipation and fluctuations in individual nanomagnets measured by ultrasensitive cantilever magnetometry", *Phys. Rev. Lett.*, **86**, 2874-2877
- Waddell E M (1978), "Phase contrast in the electron microscope", *Ph.D. Thesis*, University of Glasgow

## Appendix A. Analysis of charging and detector rotation in Lorentz microscopy

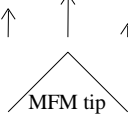

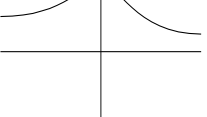
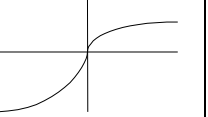
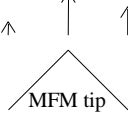

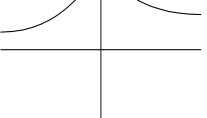
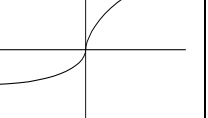
### A.1 Separation of electrostatic and magnetic DPC signals

#### A.1.1 Simple argument

As stated in chapter 2, the equation

$$\beta_{x,y} = \frac{e\lambda}{h} \int_{-\infty}^{\infty} B_{y,x} dz + \frac{1}{2V_{accel}} \int_{-\infty}^{\infty} E_{x,y} dz \quad (\text{A.1})$$

describes the deflection  $\beta$  of a beam of fast electrons with magnetic  $\mathbf{B}$  and electrostatic  $\mathbf{E}$  field distributions. Note also that  $e$  is the electronic charge,  $V_{accel}$  is the acceleration voltage of the beam and  $\lambda$  is the electron wavelength. The problem is to separate the contributions of  $\mathbf{B}$  and  $\mathbf{E}$ . A simple scheme to accomplish this can be found by noting that the  $\mathbf{B}$  and  $\mathbf{E}$  contributions to any directional component of  $\beta$  are at  $90^\circ$  to each other. That is to say, the deflection signal  $\beta_x$  is produced by the y component of the integrated magnetic field, and the x component of the integrated electric field. Now consider the effect on a vector field produced by a sample which is rotated by  $180^\circ$  about the y axis. Viewing the integrated field distribution, both field components are of course mirrored about the y axis. However, in addition the direction and therefore sign of the x field component also changes, while the y field component remains the same sign. This is illustrated below in Table A.1

	Y ( $\uparrow$ ) field component	X ( $\rightarrow$ ) field component	Linescan of Y field component	Linescan of X field component
Tip at $0^\circ$ position				
Tip at $180^\circ$ position				

**Table A.1. Illustration of the behaviour of the integrated field produced by a sample during  $180^\circ$  rotation about the y axis.**

Hence, if the linescans from the second ( $180^\circ$ ) field distribution are mirrored about the y axis again to compensate for the original spatial transform, the y component

linescans will then appear identical, while the second x component linescan will be inverted compared to the first.

Now consider the case where there are electrostatic and magnetic fields present. Taking the signal  $\beta_x$  for example, we know that the field components  $B_y$  and  $E_x$  contribute to this signal. Using the argument outlined above, the sign of the field component  $B_y$  will not be affected by the rotation of the sample by  $180^\circ$  (around the y axis). The sign of the  $E_x$  field component will change, however. Hence adding the two  $\beta_x$  signals will cause the  $E_x$  integrated field components to cancel, leaving the  $B_y$  component only. Similarly, subtracting the second  $\beta_x$  signals from the first will yield the  $E_x$  integrated field component.

#### A.1.2 A more quantitative argument.

Consider the field (magnetic or electrostatic) from some material. The DPC signal  $\beta$  from the distribution will be:

$$\beta_x = \frac{1}{2V_{\text{accel}}} \int_{-\infty}^{\infty} E_x dz + \frac{e\lambda}{h} \int_{-\infty}^{\infty} B_y dz, \quad (\text{A.2a})$$

$$\beta_y = \frac{1}{2V_{\text{accel}}} \int_{-\infty}^{\infty} E_y dz + \frac{e\lambda}{h} \int_{-\infty}^{\infty} B_x dz. \quad (\text{A.2b})$$

Now when a field  $\mathbf{V}$  is rotated 180 degrees around the y axis, the field components transform as:

$$V_x(x, y, z) \rightarrow -V_x(-x, y, -z), \quad (\text{A.3a})$$

$$V_y(x, y, z) \rightarrow V_y(-x, y, -z), \quad (\text{A.3b})$$

$$V_z(x, y, z) \rightarrow -V_z(-x, y, -z), \quad (\text{A.3c})$$

i.e, the coordinates of any particular point are transformed, and in addition the x and z field components reverse in direction, and hence in sign.

The projections of the field  $\mathbf{V}$  (along the z axis) therefore transform as:

$$P_x(X, Y) = \int_{-\infty}^{\infty} V_x(x, y, z) dz \rightarrow \int_{-\infty}^{\infty} -V_x(-x, y, -z) dz = -P_x(-X, Y), \quad (\text{A.4a})$$

$$P_y(X, Y) = \int_{-\infty}^{\infty} V_y(x, y, z) dz \rightarrow \int_{-\infty}^{\infty} V_y(-x, y, -z) dz = P_y(-X, Y), \quad (\text{A.4b})$$

where  $P(X, Y)$  is the projection of the field  $V$ . If we denote the projections of the electrostatic and magnetic fields by  $e$  and  $b$ , then the DPC signal  ${}^0\beta$  at the  $0^\circ$  position will be:

$${}^0\beta_x(X, Y) = e_x(x, y) + b_y(x, y), \quad (\text{A.5a})$$

$${}^0\beta_y(X, Y) = e_y(x, y) + b_x(x, y). \quad (\text{A.5b})$$

The DPC signal when the field distributions are rotated through  $180^\circ$  around the y axis will be:

$${}^{180}\beta_x(X, Y) = -e_x(-x, y) + b_y(-x, y), \quad (\text{A.6a})$$

$${}^{180}\beta_y(X, Y) = e_y(-x, y) - b_x(-x, y). \quad (\text{A.6b})$$

Hence, to separate the  $e$  and  $b$  components:

$${}^0\beta_x(X, Y) + {}^{180}\beta_x(-X, Y) = e_x(x, y) + b_y(x, y) - e_x(x, y) + b_y(x, y) = 2b_y(x, y), \quad (\text{A.7a})$$

$${}^0\beta_x(X, Y) - {}^{180}\beta_x(-X, Y) = e_x(x, y) + b_y(x, y) + e_x(x, y) - b_y(x, y) = 2e_x(x, y), \quad (\text{A.7b})$$

$${}^0\beta_y(X, Y) + {}^{180}\beta_y(-X, Y) = e_y(x, y) + b_x(x, y) + e_y(x, y) - b_x(x, y) = 2e_y(x, y), \quad (\text{A.7c})$$

$${}^0\beta_y(X, Y) - {}^{180}\beta_y(-X, Y) = e_y(x, y) + b_x(x, y) - e_y(x, y) + b_x(x, y) = 2b_x(x, y). \quad (\text{A.7d})$$

Note that the effects of the coordinate transform are also included in these equations. Thus the same point on the sample is being considered for both sample orientations.

This procedure can be applied to a real sample as follows. First obtain two DPC image pairs of the sample at two positions  $180^\circ$  apart. Take the second image pair and flip them around the y axis, i.e. so that the coordinates are transformed  $x \rightarrow -x$ . Some matching will generally then be required to bring the image pairs into spatial registration (for DPC, the sum images are usually employed for this purpose). Adding and subtracting the images

will then yield the separate electrostatic and magnetic field components. Note that these resulting images must be divided by 2 to yield the correct signal magnitudes – examine Eqns. A.7 a to d to appreciate this point.

Of course, as discussed in chapter 6 this procedure assumes that the electrostatic (and magnetic) field distributions do not change between acquiring the two image pairs.

## A.2 Effects of angular misalignment of DPC detector

Assume that the DPC detector is rotated by an angle  $\theta$  away from the correct position. The deflection signals obtained from the detector will be related to the correct (i.e. aligned with the microscope coordinate system) signals by the relations

$${}^0\beta'_x = \beta_x \cos \theta - \beta_y \sin \theta, \quad (\text{A.8a})$$

$${}^0\beta'_y = \beta_y \cos \theta + \beta_x \sin \theta, \quad (\text{A.8b})$$

where  ${}^0\beta'_x$  and  ${}^0\beta'_y$  are the signals from the rotated DPC detector. (note that  $\theta$  is a clockwise rotation). We know that the x components of these signals will reverse in sign. Therefore when the sample is rotated by  $180^\circ$  the DPC signals at equivalent points will be

$${}^{180}\beta'_x = -\beta_x \cos \theta - \beta_y \sin \theta, \quad (\text{A.9a})$$

$${}^{180}\beta'_y = \beta_y \cos \theta - \beta_x \sin \theta. \quad (\text{A.9b})$$

Hence, adding and subtracting the signals in the same manner as previously, we obtain

$${}^0\beta'_x + {}^{180}\beta'_x = \beta_x \cos \theta - \beta_y \sin \theta + (-\beta_x \cos \theta - \beta_y \sin \theta) = -2\beta_y \sin \theta, \quad (\text{A.10a})$$

$${}^0\beta'_x - {}^{180}\beta'_x = \beta_x \cos \theta - \beta_y \sin \theta - (-\beta_x \cos \theta - \beta_y \sin \theta) = 2\beta_x \cos \theta, \quad (\text{A.10b})$$

$${}^0\beta'_y + {}^{180}\beta'_y = \beta_y \cos \theta + \beta_x \sin \theta + (\beta_y \cos \theta - \beta_x \sin \theta) = 2\beta_y \cos \theta, \quad (\text{A.10c})$$

$${}^0\beta'_y - {}^{180}\beta'_y = \beta_y \cos \theta + \beta_x \sin \theta - (\beta_y \cos \theta - \beta_x \sin \theta) = 2\beta_x \sin \theta. \quad (\text{A.10d})$$

To find the unknown angle  $\theta$  the relation



$$\tan \theta = \frac{\sin \theta}{\cos \theta} \quad (\text{A.11})$$

is used. Applying this to equations A.10 a to d, we obtain the relations

$$\frac{{}^0\beta'_x + {}^{180}\beta'_x}{{}^0\beta'_y + {}^{180}\beta'_y} = -\tan \theta, \quad (\text{A.12a})$$

$$\frac{{}^0\beta'_y - {}^{180}\beta'_y}{{}^0\beta'_x - {}^{180}\beta'_x} = \tan \theta. \quad (\text{A.12b})$$

Hence we have two measures of the angle  $\theta$ . If there is no electrostatic charging present,  $\theta$  should be constant for all points in the DPC scan, except for noise effects. Averaging over all values of  $\theta$  thus obtained should then yield a fairly accurate value for the detector misalignment angle. Using this value the data can then be corrected (using the relations in Eqns. A.8 a and b).

### A.3 Effects of charging and detector rotation

When both electrostatic charging is present and the DPC detector is misaligned the separation problem becomes much more intractable. The signals are calculated by substituting the values of  $\beta$  in Eqns. A.5a, A.5b, A.6a and A.6b into the Eqns. A.8a, A.8b, A.9a and A.9b. This then yields

$${}^0\beta'_x = (e_x + b_y) \cos \theta - (e_y + b_x) \sin \theta \quad (\text{A.13a})$$

$${}^0\beta'_y = (e_y + b_x) \cos \theta + (e_x + b_y) \sin \theta \quad (\text{A.13b})$$

$${}^{180}\beta'_x = -(-e_x + b_y) \cos \theta - (e_y - b_x) \sin \theta \quad (\text{A.13c})$$

$${}^{180}\beta'_y = (e_y - b_x) \cos \theta - (-e_x + b_y) \sin \theta \quad (\text{A.13d})$$

In this case we have a system with four measurements and five variables. Hence we cannot solve the problem uniquely.